A MULTI-PRONGED ASSAULT ON NEW PHYSICS AT THE LARGE HADRON COLLIDER

BY MICHAEL PARK

A dissertation submitted to the

Graduate School—New Brunswick

Rutgers, The State University of New Jersey

In partial fulfillment of the requirements

For the degree of

Doctor of Philosophy

Graduate Program in Physics and Astronomy

Written under the direction of

Professor Scott Thomas

And approved by

_____

_____

_____

_____

_____

New Brunswick, New Jersey

October, 2014

ABSTRACT OF THE DISSERTATION

A Multi-Pronged Assault on New Physics at the Large Hadron Collider

by Michael Park

Dissertation Director: Professor Scott Thomas

With the completion of Run I at the Large Hadron Collider, the primary directive of the high energy phenomenology community now lies in evaluating the lessons learned in order to formulate an optimal strategy for potential discoveries in Run II. Given the challenges to our theoretical biases presented by Run I, we argue for an approach to Run II that makes minimal assumptions about what new physics may lie at the electroweak scale outside of what has already been discovered. The overwhelming evidence for a Standard Model-like Higgs boson with a mass of approximately 125 GeV is undoubtedly of central importance for our considerations.

The first section of this dissertation focuses on developing a model independent strategy for parameterizing theories of new physics by the possible decay topologies of heavy new particle states. Connections between this parameterization and theories like supersymmetry are also detailed. The second section focuses on exploring the newly discovered Higgs sector for possible non-Standard Model-like behavior. This includes the search for additional Higgs doublets as well signs of potential flavor violation induced by the Higgs sector. The final section is dedicated to new methods for extracting theoretical parameters from decay topologies that arise in a wide range of possible theories of physics beyond the Standard Model.

Preface

This dissertation contains a detailed summary of selected work that I completed as a doctoral candidate, under the supervision of professor Scott Thomas, with the New High Energy Theory Center at Rutgers University. The work presented here focuses on the search for physics beyond the Standard Model at the Large Hadron Collider experiment.

The timing of my graduate fellowship appointment, with respect to Run I of LHC operation, was extremely fortuitous. Entering the research group just as soon as preprations were ramping up, I was fortunate to have been able to work on an extraordinarily wide range of topics related to high energy collider physics, at almost every stage of development. It is this breadth and comprehensiveness that I hope is conveyed in this thesis, which is organized as follows: Part I describes early work on searches for heavy new particle states in the context of supersymmetry and simplified models. Part II is dedicated to a long-term project applying multi-lepton search strategies to various aspects of Higgs searches. Part III describes a number of post-discovery projects related to the extraction theoretical parameters from data using kinetmatic variables.

Understanding that doctoral dissertations are rarely read after they are written; I hope that this thesis stands, however silent, as an accurate reflection of how truth was sought in this endeavor.

Acknowledgements

How surreal. It was around this time 8 years ago that I quit my office job and, with only a vague memory of my high school coursework, decided to jump down a rabbit hole to see what this "physics" mess was all about. At the time, I honestly did not project it to be likely that I would make it to this point. At the time it seemed obvious that such a thing would require an outrageously fortuitous sequence of occurences. However, due to all of the wonderful people I have met along the way, this sequence of occurences was realized.

I should first thank Amit Lath. For saying yes when one brilliant undergraduate physics student and one washed up college flunky knocked on his door asking if there was any opportunity for research. Also thanks to Tim Lou, the brilliant undergraduate physics student who egged me on to join him on his walk around the physics department knocking on random doors begging for research opportunities. I would also like to thank the members of the CMS group at Rutgers who have provided me with invaluable guidance over the years. Especially Sunil Somalwar, Eva Halkiadakis, and Steve Schnetzer.

I would also not have survived this journey if not for the constant support of my closest friends. Although they did not provide answers to my physics questions, they were a constant source of support for me when the answers I sought seemed unattainable. Special thanks to Brian Soames, Jason Kim, John Lin, Brian Lau, Gerard Reddy, Phil Youn, Danny Choi, Ed Cho, Shorti Kim, Matt Liu, Joe Yi, Hojo Wang, Justin Lee, and all those I've missed. Special thanks to David Dolan for always coming through with the extra help.

Perhaps most directly important to this acheivement were my peers in the theoretical community who would always overlook the naivety of the question that I lacked the

confidence to ask my professors. Especially Simon Knapen, Pietro Longhi, Gordan Krnjaic, Yoni Bentov, Aria Basirnia, Daniel Egana, Sebastian Macaluso.

Penultimately, I would like to thank my family for being an unrelenting source of love and support. Thank mom, dad, and K-Sue.

Finally I would like to give a special thanks to my advisor Scott Thomas, who took me on as a student when there was no strong justifiable reason to do so. The impact that this had on my life is immeasurable.

Dedication

To my parents,
who have always supported me **unconditionally**

Table of Contents

Abstract ii

Preface iii

Acknowledgements iv

Dedication vi

1. Introduction 1

1.1. Historical Context 1

1.2. Symmetries and Scalars 5

1.3. Hierarchies and the Higgs 7

I The First Prong: Model Independent Searches for Heavy New States **9**

2. Simplified Models 10

2.1. Effective Lagrangians 12

2.2. Simplified Model Parametrization 14

2.3. Combining Topologies 15

2.4. Supersymmetry to Simplified Models 17

2.5. Phenomenological Structure of Gauge Mediation 18

3. Topologies with a Neutralino NLSP 22

3.1. Bino NLSP 24

3.2. Wino NLSP 26

3.3. Z-rich Higgsino NLSP 28

4. Topologies with a Slepton NLSP 30
4.1. GMSM Inspired Benchmark Spectra 32
4.2. Slepton-coNLSP 33
4.3. Stau-(N)NLSP 35

II The Second Prong: Exploring the Higgs Sector with Multi-Leptons **39**

5. The Minimal Standard Model Higgs at the LHC 40
5.1. Multi-Lepton Higgs Searches 43
5.1.1. Multi-Lepton Signal Channels 43
5.1.2. Simulation Details 45
5.2. Multi-Lepton Signals of the Higgs 46
5.3. Towards a Dedicated Multi-Lepton Higgs Search 49
5.4. Going Forward 50

6. Extended Higgs Sectors at the LHC 52
6.1. Parameterizing the Space of Two-Higgs Doublet Models 55
6.2. Multi-lepton Signals of Two Higgs Doublet Models 60
6.3. Benchmark Spectra 62
6.4. Search Strategy and Simulation Tools 65
6.4.1. Signal Channels 69
6.4.2. Simulation 70
6.5. Results 74
6.5.1. Spectrum 1 75
Types I & III 76
Types II & IV 81
6.5.2. Spectrum 2 84
Types I & III 84
Types II & IV 84

6.5.3. Spectrum 3 . . . 86
Types I & III . . . 89
Types II & IV . . . 90
6.5.4. Spectrum 4 . . . 92
Types I & III . . . 96
Types II & IV . . . 96
6.6. Towards a Dedicated Multi-Lepton 2HDM Search . . . 97

7. Rare Flavor Processes involving Higgs . . . 100
7.1. Effective Operator Description of $t \to ch$ . . . 102
7.2. A Multi-Lepton Search for $t \to ch$ . . . 104
7.2.1. Multi-Lepton Signal Channels . . . 104
7.2.2. Simulation Details . . . 105
7.2.3. Results . . . 106
7.3. Going Forward . . . 110

III The Third Prong: Post-Discovery **112**

8. Particle Masses from Cascade Decays . . . 113
8.1. The Phase Space of Sequential On-Shell Cascade Decays . . . 116
8.2. Kinematic Features of Cascade Decays in Dalitz Space . . . 118
8.3. From Three Dimensional Dalitz Parameters to Particle Masses . . . 123
8.3.1. Combinatoric ~~Confusion~~ Clarity . . . 124
8.4. Extracting Masses from the Dalitz Distribution . . . 125
8.5. NNOMET Masses: A Supersymmetric Example . . . 128
8.6. Going Forward . . . 132

9. Particle Masses from Displaced Tracks . . . 134
9.1. Kinematics of Displaced Vertices . . . 136
9.1.1. Counting the Unknowns . . . 136

9.1.2. Parameterizing the Unknowns . . . 138
9.2. Monte Carlo Simulations for Displaced Tracks . . . 142
9.2.1. Weight Functions . . . 143
9.3. Examples with a Massless LSP . . . 144
9.3.1. Measurable Displaced Vertices . . . 145
9.3.2. Measurable Displaced Tracks . . . 146
9.3.3. Can We Do Better? . . . 147
9.4. Examples with a Massive LSP . . . 150
9.4.1. Measurable Displaced Vertices . . . 151
9.4.2. Measurable Displaced Tracks . . . 153
9.4.3. Can We Do Better . . . 155
9.5. Going Forward . . . 157

10. Testing Discrete Symmetries of the Higgs Sector . . . 161
10.1. Four-Body Kinematics . . . 163
10.1.1. The T-Odd Observable . . . 163
10.1.2. Matrix Elements . . . 165
10.2. Simulation and Validation . . . 169
10.3. Results . . . 171
10.4. Fermion Electric Dipole Moments . . . 172

Chapter 1

Introduction

At the time of the writing of this thesis, the field of particle physics stands at something of a cross road. The Standard Model (SM) of particle physics has stood firm since the 1970's as an extremely robust description of nearly all the interactions (with the exception of gravity) that are known to occur between the observed fundamental building blocks of matter. The experimental consequences born from the structure of the SM are so vast in number, and (again with a few notable exceptions) have been verified with such veracity, that the dearth of experiments providing new insight has become the central bottle-neck to theoretical progress in this field. While it is entirely possible that the broader theoretical framework of quantum field theory (QFT), within which the SM sits as a specific construction, stands equipped to potentially address every observable phenomenon in this universe; there are clear indications that the validity of the SM itself does not extend to all known scales. Although the SM is an elegant and fully consistent theory, the omission of a description of gravity, an explanation for neutrino masses, and a specification of the identity of dark matter, stand as obvious phenomenological obstructions to viewing the SM as a candidate theory of everything that is valid up to Planckian energies M_{Pl}. While all of these ommisions can be accounted for within the modern paradigm of effective field theory (EFT), a great challenge still lies in finding a broader theoretical framework to explain these phenomena.

1.1 Historical Context

Roughly speaking, the paradigm of EFT can be viewed as exactly this acquiscence to the fact that our theoretical understanding of nature has a limited regime of validity. This regime is commonly defined by the existence of a "cut-off distance" L: a length scale

below which yet unknown laws of physics presumably subsume the laws we currently understand. Because of the wave-like nature of matter, this cut-off length scale L is associated with a corresponding "cut-off energy" scale called Λ, which is the energy at which matter waves would have to collide in order to resolve structures of size L. This Λ is simply given by the compton wavelength relation $\Lambda = hc/L$ and represents the energy above which our effective theories lose their validity and/or predictivity.

Despite the problems mentioned with the SM, there are empirical reasons to suspect that the more general framework of QFT is applicable at least to some energy scale above which the SM breaks down. It is therefore natural to interpret the SM as an EFT with an energy range of applicability demarcated by some cutoff scale Λ, representing the energy scale above which we expect the predictions of the SM to diverge from nature. With the power of hindsight, a historical account of the progress in theoretical physics over the last century through the modern lens of EFT, paints a sharp picture of the central issue facing our field today.

The first indication of the existence of such a cut-off distance came from considerations of Maxwell's theory of electromagnetism. Recall that in Maxwell's theory, the electrostatic potential energy U_E between an electron e^- and a positron e^+ separated by a distance r, is inversely proportional to this separation distance:

$$U_E(r) \propto \frac{1}{r} \tag{1.1}$$

With no empirical evidence for a non-zero radius of the electron (or positron), Maxwell's theory clearly allows for arbitrarily small separation distances, which in turn allows for the existence of infinite energy densities as $U_E \to \infty$ when $r \to 0$. Indeed it was known that a minimum distance of separation $L = r_e$, commonly referred to as the "classical electron radius", must be included as an ad-hoc input to this theory in order to prevent such a nonsensical prediction. Demanding that the potential energy attributed to an electron be bound by its total rest energy (given by its mass via Einstein's equation $U_E = m_e c^2$), gives a cut-off minimum distance for $r_e \sim 10^{-15}$ m, or equivalently a cut-off maximum energy scale $\Lambda \sim 1$ GeV. Below distances of about 10^{-15} m, or above energies of about 1 GeV, the Maxwellian picture produces non-sensical results,

indicating that some new phenomena should appear upon probing this distance or energy scale.

In fact, the new phenomena appeared far sooner than expected. When particle colliders began probing atomic distances of about $r \sim 10^{-10}$ m (collision energies of 10 keV), all kinds of phenomena that were incompatible with Maxwell's theory were discovered in what eventually led to the development of quantum theory. In particular, it was found that the quantum mechanical phenomenon of vacuum polarization (the screening of electric charge due to particle-antiparticle pair creation) modified the form of U_E in a way that removed the nonsensical behavior. We now know that at distances comparable to atomic radii, quantum-electrodynamics (QED) subsumes classical Maxwellian electrodynamics as the new effective theory.

Shortly after the development of quantum mechanics, another cut-off energy was encountered with the peculiar phenomenon of neutron decay. After a time of about $\tau_n \sim 900\ s$, an isolated neutron (n) was observed to disintigrate into a proton (p), electron (e), and an anti-neutrino ($\overline{\nu}$), in a phenomenon that became known as β-decay. The existence of this four-fermion interaction

$$\frac{G_F}{\sqrt{2}}\ \overline{\nu}\gamma^{\mu}e\ \overline{p}\gamma_{\mu}n \tag{1.2}$$

had the troubling property that it necessitated the existence of *inverse* β-scattering, and it predicted that the probability of *inverse* β-scattering $\mathcal{P}(\overline{\nu}p \to e^{+}n)$ occuring in high energy collisions behaved as

$$\mathcal{P}(\overline{\nu}p \to e^{+}n) \propto G_F^{\,2}s \tag{1.3}$$

where s is the squared center-of-mass energy with which the particles collide. The quadratic dependence of $\mathcal{P}(\overline{\nu}p \to e^{+}n)$ on the center-of-mass energy meant that at some high energy, the probability of particle collisions would exceed unity thus violating unitarity. Since we cannot make sense of a theory that predicts probabilities greater than unity, the cut-off energy for this theory finds an upper bound at the center of mass energy at which unitarity is violated. For this four-fermion interaction this is around

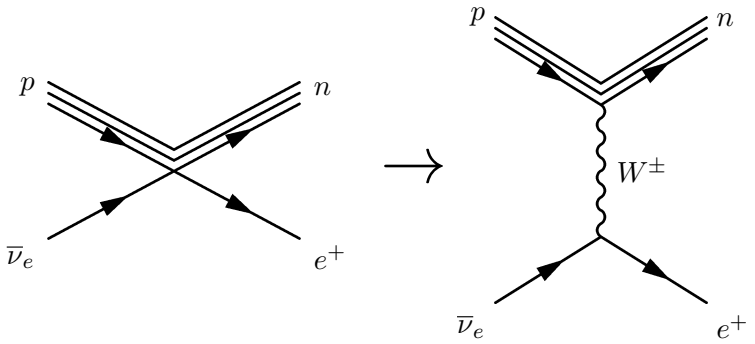

Figure 1.1: Inverse β-scattering via exchange of a $W^\pm$ boson.

$\Lambda \sim 100$ GeV.

Once again, particle collider experiments far below this energy scale revealed that at *very* small distances $r \sim 10^{-17}$ m, the four-fermion interaction ceased to adequately describe inverse β-scattering. More specifically, it was found that this interaction must be modified to include the exchange of a new spin-1 particle. β-decay was actually the result of a new force, mediated by the newly discovered $W^\pm$ boson as shown in Fig. 1.1. As expected, with the of inclusion this new particle exchange into the theory, the probability of *inverse* β-scattering changes its behavior at high energies in a way that does not violate unitarity.

The reason that the $W^\pm$ bosons can only be resolved at extremely small length scales is because they can only exist and propagate for a *very* short time before they decay into other particles. This is because the $W^\pm$ particles are *massive* gauge bosons, a fact that immediately gives rise to another problem with the theory. In a manner similar to the case of inverse β-scattering, the longitudinally polarized components of any *massive* gauge boson have a probability of scattering that also grows with the square of the collision energy

$$\mathcal{P}(W_L^+ W_L^- \to W_L^+ W_L^-) \propto \alpha^2 s \tag{1.4}$$

Thus the same problem exists that any theory of massive gauge bosons will violate unitarity, predicting interaction probabilities that exceed unity at very high scattering energies. Shortly after this became apparent, Steven Weinberg famously realized that if there existed a single spin-0 scalar particle h that interacts with the massive

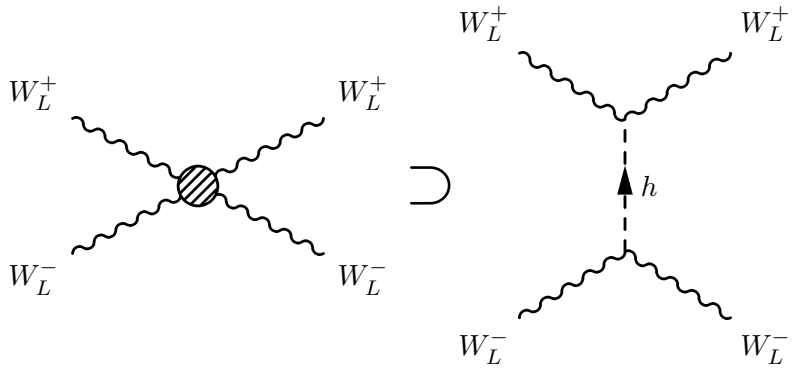

Figure 1.2: Contribution of a Higgs exchange diagram to the scattering of longitudinally polarized $W^{\pm}$ bosons.

gauge bosons, the contribution of h to the scattering process would come with exactly the correct properties to cancel off this unitarity violating behavior. This is shown diagrammatically in Fig. 1.2. This spin-0 scalar h is the famed Higgs boson.

1.2 Symmetries and Scalars

The concept of *symmetry* has proven to be an extremely powerful organizing principle with which to think about QFT's in general. So powerful in fact, that a specification of the symmetries of a theory along with a specification of the representations with which the constituent fields transform under these symmetries, is practically sufficient for the complete construction of any QFT. Once these symmetries and representations have been identified, every possible operator up to dimension four $\mathcal{O}_{d=4}$ that can be built from combinations of fields that are invariant with respect to the symmetries, will be found in the (renormalizable) Lagrangian of the theory $\mathcal{L}_{d=4}$, with appropriate coefficients a_i

$$\mathcal{L}_{d=4} \supset \sum_i a_i \mathcal{O}_{d=4,i} \tag{1.5}$$

In other words, any process that is not forbidden by the symmetries of the theory will be generated by *quantum corrections*. One of the salient features of the EFT perspective is that the effects of unknown physics above the scale Λ are generically parameterizable by the coefficients of higher dimensional operators (HDO) of the form

$$\mathcal{L}_{HDO} = \sum_{d>4} \sum_{i} \frac{b_{d,i}}{\Lambda^{d-4}} \mathcal{O}_{d,i} \tag{1.6}$$

The goal of the particle physics research program can then be viewed as a quest to ascertain the physics of the full theory with the Lagrangian description

$$\mathcal{L}_{full} = \mathcal{L}_{d=4} + \mathcal{L}_{HDO} \tag{1.7}$$

Or in other words, to measure any coefficients a_i or $b_{d,i}$ that may be accessible to experiment.

Scalar degrees of freedom, generically labeled ϕ, are (by definition) already invariant with respect to the symmetries under which they may be called *scalars*. This means that there are no non-trivial symmetry transformations that could possibly restrict the form of the quantum corrections to the propagator of a scalar field. The fully quantum corrected mass of any scalar field m_ϕ will therefore contain terms proportional to the squared masses of every particle with which it interacts.

$$m_\phi^2 \supset \sum_{i}^{\text{all}} c_i M_i^2 \tag{1.8}$$

This might seem benign for an EFT with a limited energy range of validity, but every time a cut-off energy has been explored experimentally, heavy new particle states have been discovered with masses of order the cut-off scale. We therefore expect that, in the absence of some new dynamics at the scale Λ or some delicate cancellataions between terms in the sum of m_ϕ^2, that the mass of any scalar degree of freedom should be on the order of the cut-off energy $m_\phi^2 \sim \Lambda^2$. This general principle has proven valid for every scalar that had been found prior to 2012. Notably, the scalar mesons (bound states of quarks and antiquarks) all have masses of order Λ_{QCD}, the scale at which their description as fundamental particles breaks down and their composite nature becomes apparent. Indeed there exist many effective theories in nature with scalar degrees of freedom in the form of composite particles. Their masses may always be computed in the effective theory to be dependent on the masses squared of every particle up to the cut-off energy, which is the energy scale at which their contituents supercede them as

the relevant degrees of freedom.

1.3 Hierarchies and the Higgs

The Standard Model of particle physics with a fundamental scalar Higgs boson has no known cut-off energy. It can be extrapolated as a consistent description of nature all the way up to $\Lambda \sim M_{Pl}$, where the strength of gravity implies the existence of new degrees of freedom. On one hand, the mass of the Higgs boson m_h is responsible for setting the scale of electroweak symmetry breaking at $M_{EW} \sim \mathcal{O}(10^2 \text{ GeV})$. On the other hand, it must contain the sum of squared masses of every particle that it interacts with up to its cut-off, which could be as large as $M_{Pl} \sim \mathcal{O}(10^{20}\text{GeV})$.

$$m_h^2 \sim M_{EW}^2 \sim \sum_i^{\text{all}} c_i \Lambda^2 \quad , \quad \Lambda^2 < M_{Pl}^2 \tag{1.9}$$

If $\Lambda \sim M_{EW}$, then this is totally sensible, and we should expect to discover some new phenomena upon the systematic probing of energies close to M_{EW}. However, if the SM holds to a scale $\Lambda >> M_{EW}$ (worst case $\Lambda \sim M_{Pl}$), then there must apparently be extremely delicate and unnatural cancellations between the terms in the sum of Eq. 1.9, and we have no explanation for why $M_{EW} << M_{Pl}$. This is *the hierarchy problem* concerning the unnatural value of m_h^2. Many theoretical physicists have taken the position that the very existence of a scalar degree of freedom in the SM stands as a strong indication that it must be an EFT with a cut-off energy on the order of M_{EW}. It is a position that history has vindicated with numerous post-dictions and the observation that no fundamental scalar has ever been known to exist in nature. It also comes with the completely generic expectation that some new degrees of freedom should become apparent upon the systematic experimental exploration of energies (or distances) at that scale.

On July 4^{th} of 2012, upon careful analysis of $\sim 10\,\text{fb}^{-1}$ of particle collisions at 7 and 8 TeV center-of-mass energy, experimentalists at the Large Hadron Collider officially announced the discovery of the Higgs boson with $m_h \sim 125\,\text{GeV} \sim M_{EW}$ as expected. Since then, all of its measured properties have been found to be consistent

with the fundamental scalar degree of freedom expected from a minimal SM Higgs boson. To date, there has been no indication of the existence of any other new degrees of freedom around M_{EW}. Thus for the first time in history, the field of theoretical particle physics finds itself with no indication from nature on how to proceed with the march to understand the universe at smaller distances and higher energies. In every analagous instance through history, nature has pointed towards some distance or energy scale where some paradoxical theoretical conundrum required a resolution through the introduction of new ideas. For the first time, we find ourselves in the position of having to explain the *absence* of such a conundrum.

From a practical standpoint, this has immediate implications for how we should approach our experiments from this point on. The purpose of this dissertation is then to describe a more modern approach to new physics searches in high energy experiments. One that is more adaptive to this newfound climate of relative theoretical uncertainty. The first part of this thesis will thus be dedicated to a description of broad and relatively model-independent searches strategies for heavy new particle states. The value of model independence has certainly risen from the new danger that a positive signal in the data might go unnoticed because we didn't know where to look. The second part will be dedicated to the use of powerful experimental techniques to probe the Higgs sector in ways that are both complementary and orthogonal to the avenues currently being explored. Despite lacking a concrete characterization of what new phenomena (if anything) to expect when Run II at the LHC commences, there is at least some sound theoretical motivation to expect that it would involve the Higgs sector, if nothing else. Finally, the last section of this thesis is dedicated to post-discovery analyses, and techniques to extract theoretical paramters from data. The existence of potentially very subtle new physics effects have presented the challenge of devising equally subtle methods for extracting information from experimental observables of ever-increasing complexity. The impotance of comprehensiveness in this modern climate of high energy particle physics suggests such a multi-pronged approach for exploring new laws of physics at the Large Hadron Collider, at multiple stages of the discovery process.

Part I

The First Prong: Model Independent Searches for Heavy New States

Chapter 2

Simplified Models

A new physics model may be defined by an effective Lagrangian describing the particle content and interactions of the theory at the TeV scale. So called "simplified models" are specifically designed to involve only a few new particles and interactions and may be viewed as the limit of more general new physics scenarios where all but a few particles have been integrated out. Such models can alternatively be described by a small number of collider physics observables corresponding to specific experimental signatures, for example particle masses, production cross-sections, and branching fractions.

Although simplified models are model dependent, they do enjoy some benefits of model independence. In particular, the sensitivity of new-physics searches to models with only a small number of parameters can be studied and presented simply as a function of these parameters and in particular, over the full range of new particle masses. Though defined within a simplified model, these topology-based limits also apply to more general models giving rise to the same topologies.

The purpose of simplified models are three-fold

- To identify the boundaries of search sensitivity: Any critical assessment of LHC searches needs to include a clear identification of the boundaries of sensitivity - for example, the dependence of reconstruction and selection efficiencies on the mass differences between a parent particle and its decay products. One- and two-dimensional slices within a simplified model can illustrate these boundaries very clearly. Only with this information can experimentalists and theorists identify kinematic ranges (or entire topologies!) for which existing search strategies are not efficient, and devise appropriate generalizations to these strategies. For the same reasons, limits on simplified models also serve as a valuable reference for

theorists who wish to estimate a searchs sensitivity to alternative new-physics models in their own Monte Carlo.

- To characterize new physics signals: If new physics is observed, it will be important to fully characterize the range of particle quantum numbers, masses, and decay topologies that it may involve. As has been discussed in [1], simplified models can offer a natural starting point for quantifying the consistency of a signal with different kinds of physics reactions. Similar strategies have been discussed in [2, 3].

- To derive limits on more general models: Constraints on a wide variety of models can be deduced from limits on simplified models. Within each final state, simplified model limits can be formulated as an upper limit on the number of events in a signal region, and a parametrized efficiency for each simplified-model topology to populate the signal region. Limits on other models giving rise to the same topologies can be inferred by summing the effective cross-section for each topology (a product of cross-sections and branching ratios), weighted by their experimental efficiencies, and comparing the result to the upper bound. This procedure can be extended to multiple signal regions if a combined likelihood is reported as a function of the number of signal events in each signal region. These procedures are discussed in several talks at the workshop and, for example, in [4]. We also give an example in Section II 3. It should be emphasized that this procedure yields weaker limits than the direct study of experimental efficiencies for a given specific model, as the procedure uses only topologies populated by both the specific and simplified models. This procedure should therefore be regarded as an initial check only, which can be followed by a dedicated study or RECAST-style analysis [5] if higher precision is needed. Finally, we note that simplified models can be simulated either as modules from widely used model frameworks (like the MSSM) in Pythia [97] or MadGraph [93], as new models in MadGraph, or as OSETs using Marmoset [3] or recent versions of Pythia.

Experiments at the LHC could enhance the applicability of new-physics searches

by considering their sensitivity to these "simplified models". Simplified models should be defined in such a way that their topologies are representative of the wide variety of new-physics possibilities that could be seen at the LHC. These pre-defined simplified models should then be used in the design of new-physics searches and characterization of their results. The hope is that the simplified models listed here will provide a foundation for assessing the impact of existing searches, and how they can be extended or better optimized. In addition, we expect that the simplified models here will be a useful starting point for characterizing any evidence for new physics, in a systematic and unbiased manner. Simplified models may be organized according to classes of signatures. For example those involving jets, heavy-flavor (b or τ), leptons, photons, and exotic objects such as new displaced vertices, non-standard timing, or novel jet-like structures.

This section, adapted from [4], outlines the important elements that go into any simplified model analysis. As an illustrative example, it focuses on gluino production and decay as a model for hadronic jets plus missing energy signals. We will discuss how limits can be set in a multidimensional parameter space and how the limits from multiple topologies can be combined. The procedure outlined here is a general one and can be applied to any of the simplified models listed in this review.

2.1 Effective Lagrangians

Consider a direct three-body gluino decay into an electroweak gaugino and two light-flavored quarks,

$$\tilde{g} \to q\bar{q}\chi^0 \tag{2.1}$$

This decay mode occurs in supersymmetric models where the squarks are significantly heavier than the gluino; it proceeds through the dimension-six operator

$$\mathcal{L}_{int} = \frac{\lambda_i^2}{M_i^2}\tilde{g}q_i\bar{q}_i\chi^0 + h.c. \tag{2.2}$$

where i runs over the different quark flavors, λ_i is the Yukawa coupling for the quark-squark-χ^0 vertex, and M_i is the effective scale of the interaction. The flavor structure of the final state is determined by the mass spectrum of the corresponding squarks, with decays through lighter mass squarks occurring more rapidly. In this example, only light-flavor decay modes are considered.

Direct three-body decays arise in models where the squarks are decoupled, such as in split-supersymmetry [8], or where the soft masses of the squarks are at the TeV-scale, but are still somewhat larger than the gluino mass. These decays dominate when

- $\chi^0 = B$ and the right-handed squarks are lightest, or the W is kinematically inaccessible
- $\chi^0 = W$ and the left-handed squarks are lightest, or all squark masses are comparable
- $\chi^0 = H$ and the heavy-flavor squarks are kinematically accessible in gluino decays, or the $\widetilde{B}$ and $\widetilde{W}$ are kinematically inaccessible

In mSUGRA [9–13] and GMSB-like [14–23, 42] models, the LSP is usually bino-like and there is no strong splitting between the left and right-handed squarks; therefore, the direct decays usually do not dominate. In contrast, AMSB scenarios [25–28] have a wino-like LSP and a large wino gauge-Yukawa coupling, leading to a large branching ratio for three-body gluino decays.

A complementary simplified model corresponds to the case where the gluino goes through a three-body decay to a chargino that subsequently decays to a gauge boson and the LSP,

$$\tilde{g} \to q\overline{q}'\chi^{\pm} \to q\overline{q}'(W^{\pm}\chi^0) \quad \text{or} \quad \tilde{g} \to q\overline{q}\chi'^0 \to q\overline{q}(Z^0\chi^0) \tag{2.3}$$

The decay chain "gluino $\to$ heavy electroweakino $\to$ lightest electroweakino is preferred in many supersymmetric scenarios [29], including mSUGRA. A similar chain KK-gluon $\to$ KK-gauge boson $\to$ KK-graviton is also present in Extra Dimensions [30–32]. When the intermediate particle is a chargino, all events have two $W^{\pm}$ bosons in the

final state. Alternative simplified models exist in which the intermediate state is neutral and decays to a Z^0 boson or higgs instead of a $W^{\pm}$. When exchanging a $W^{\pm}$ for a Z^0, the mass difference is a small effect at the LHC. However, the difference between their leptonic decay modes is quite significant. In hadronic searches, the difference between modes is manifested in two ways: the fraction of events that are truly hadronic, and the presence in the W mode of leptonic W's that are not vetoed in the searches (e.g., if the lepton is non-isolated or out of acceptance). These effects are unlikely to affect the optimization of search regions, but do introduce complications in translating limits from one simplified model to another. Answering this question requires understanding the differences in the acceptances/efficiencies for events with Z^0 final states versus $W^{\pm}$ final states.

2.2 Simplified Model Parametrization

A simplified model is described by a minimal set of parameters that often include the particle masses and the production cross sections. For example, the three-body direct decay model is parametrized in terms of $m_{\tilde{g}}$, m_{χ^0} , and $\sigma(pp \to \tilde{g}\tilde{g} + X)$. The one-step cascade decay introduces two new parameters: the mass of the intermediate particle $m_{\chi^{\pm}}$ and the branching ratio of g decaying into $\chi^{\pm}$. However, it is much easier to consider each simplified model with branching ratios set to 100%. Models with multiple decay modes can be studied by taking linear combinations of results for single decay modes, as discussed in the following section. When the efficiencies of a search for two decay modes are very different, studies of mixed topologies may also be desirable. Assuming a 100% branching ratio reduces the number of parameters in the one-step cascade model to four. The choice of $m_{\chi^{\pm}}$ alters the kinematics of the theory and must be included, despite the challenges of presenting limits in a four-dimensional space. It is instructive to consider lower-dimensional mass slices in $m_{\chi^{\pm}}$, which illustrate the distinctive features of the one-step cascade and capture all the relevant corners of phase space. An example of a useful family of chargino mass slices is

$$m_{\chi^{\pm}} = m_{\chi^0} + r(m_{\tilde{g}} - m_{\chi^0}) \tag{2.4}$$

The case of $r = 0$ is identical to the direct three-body decay. The case of $r = 1$ closely resembles a direct two-body gluino decay, provided the $W^{\pm}$ is boosted so that its decay products merge together. A few intermediate values of r (e.g. 0.25, 0.5, and 0.75) cover a variety of kinematics. In hadronic searches, the limit of small r approaches the direct three-body decay, but the precise $\chi^{\pm} - \chi^0$ mass difference significantly affects the sensitivity of leptonic searches. For these, a mass slice with mg fixed near the limit of detectability, and m_{χ^0} and $m_{\chi^{\pm}}$ varied independently, is also relevant. To explore the effect of on-shell decays near threshold, the alternative mass slice

$$m_{\chi^{\pm}} \sim m_{\chi^0} + m_{W^{\pm}} \tag{2.5}$$

is useful. Threshold effects are fairly modest because the mass scales accessible at the LHC are sufficiently above $m_{W^{\pm}}$, though they do become important for lighter gluino masses. In [33], this can be seen as a sharp drop in the cross section sensitivity along the line in Eq. 2.5.

2.3 Combining Topologies

The above discussion has focused on topologies corresponding to particle-antiparticle pair production, with the two produced particles decaying through identical channels. More generally, associated production topologies and 'mixed' decay modes, where, for instance, one gluino decays directly to the LSP (mode A) while the other decays through a cascade (mode B). It is useful to consider what one may infer about these models given only a search's sensitivity to the two 'symmetric' decay modes. We consider this question in the context of an idealized search result with two components: an upper limit N_{max} on the expected number of signal events in a signal region of interest, and the efficiency for each process to populate this signal region. If all efficiencies were known, one could infer a cross-section limit σ_{max} for models with branching ratios B_A, B_B by

$$\sigma_{max} = \frac{N_{max}}{B_A^2 \epsilon_{AA} + 2 B_A B_B \epsilon_{AB} + B_B^2 \epsilon_{BB}} \tag{2.6}$$

(the cross-section upper limits for the two symmetric decays are simply $\sigma_{max,AA} = N_{max}/\epsilon_{AA}$ and similarly for the mode BB). However, we wish to consider what can be gleaned about σ_{max} if the efficiency ϵ_{AB} is unknown. Upper and lower bounds on σ_{max} can be obtained simply by using the fact that $0 \leq \epsilon_{AB} \leq 1$. The lower bound corresponding to $\epsilon_{AB} \to 0$ amounts to "throwing out" the mixed events. The resulting limit is conservative (it always under-estimates the true strength of a search result), but can be a considerable underestimate of the actual search sensitivity, particularly when both branching ratios are comparable or the dominant decay mode has low efficiency. In many cases where the decay modes A and B produce similar final states, the mixed decay modes have an efficiency comparable to those of the two symmetric modes, and typically intermediate:

$$\min(\epsilon_{AA}, \epsilon_{BB}) \leq \epsilon_{AB} \leq \max(\epsilon_{AA}, \epsilon_{BB}) \tag{2.7}$$

If the ϵ_{AA} and ϵ_{BB} are comparable, then inserting these bounding values into Eq. 2.6 allows a fairly precise determination of σ_{max}, even when branching ratios are nearly evenly split between the two decay modes.

It is important to emphasize that Eq. 2.7 is by no means guaranteed. When expected violations of Eq. 2.7 are large, the mixed topologies warrant careful dedicated study. As an extreme example, if mode A is fully hadronic and mode B typically produces a lepton, then for a one-lepton search one expects $\epsilon_{AB} \gg \epsilon_{AA}, \epsilon_{BB}$. These correspond to cases where it is clearly important to parametrize a search's sensitivity to the mixed decay modes directly. However, in the case of hadronic searches and the gluino decays, Eq. 2.7 is typically true at least to a good approximation. A reasonable assessment of whether Eq. 2.7 is likely to hold can be obtained by studying the step-by-step efficiencies of a search for the two symmetric decay modes. If mode AA passes each individual cut with comparable or greater efficiency than BB (or vice versa), then Eq. 2.7 is likely to hold. Even when this is not the case, the lower bound is robust in many examples. Thus, in most cases one may draw powerful conclusions from the symmetric decay modes alone.

2.4 Supersymmetry to Simplified Models

Despite tension with experiment, supersymmetry remains a well motivated framework for thinking about new physics at the LHC. Although its application to particle physics at the TeV scale was originally motivated by considerations of naturalness and the hierarchy problem, the enormous size of its parameter space alone has proven it to be extremely useful on a pragmatic level, for motivating searches that transitively cover the space of possible experimental signatures. It can thus be viewed as an extremely efficient "signature generator" within the context of simplified models discussed above.

The minimal supersymmetric extension of the Standard Model (MSSM) introduces 119 new parameters that can give rise to nearly any type of final state. Indeed even within the MSSM framework, two entirely different models can give rise to very similar final state signatures. The huge volume of the signature space and the abundance of such degeneracies suggests the need for a more streamlined approach towards experimental searches. From this perspective, it is useful to consider the experimental signature space of the LHC as a high-dimensional Cartesian space $\mathbb{R}^n$, of which a three-dimensional projection is shown in Fig. 2.1. In this picture, one can assign any quantifiable physical observable to an axis in this space. For illustrative purposes, on this slice we have chosen H_T: defined as the scalar sum of the p_T's of all the hadronically interacting objects in an event, $\not{E}_T$: defined as the norm of the vector sum of all the non-interacting objects in an event, and lepton-number $\ell_{\#}$: defined as the number of light leptons (e or μ) produced in the hard process of an event.

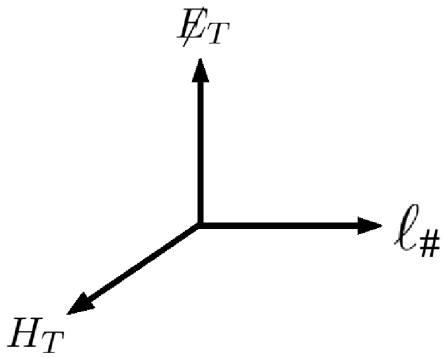

Figure 2.1: A three-dimensional slice of the experimental signature space.

With this definition, one event corresponds to a point in this space, and a sample of events associated with a given trigger corresponds to a density along a subspace. The Standard Model is known to produce events that fill this space with a density peaked near the origin, while models for physics beyond the Standard Model (BSM) such as supersymmetry can easily produce models that occupy the extremities of this space. Given the relatively simple structure of possible final state signatures from this perspective, it would be vastly more efficient to scan over this experimental signature space than, for example the space of couplings in supersymmetric theories. Points on the experimental signature space can be organized into simplified models, determined by their decay topology, thus forming a bridge between potentially large classes of BSM models and the various searches being carried out at the LHC.

2.5 Phenomenological Structure of Gauge Mediation

One class of supersymmetric models that is particularly appealing from a predictive phenomenological perspective, is gauge mediated supersymmetry breaking (GMSB). The salient feature of theories with gauge mediation, is that the SUSY breaking scale is low, which provides useful control of aspects of the phenomenology in such models. If the supersymmetry breaking scale is relatively low, gauge interactions are likely to play a role in transmitting supersymmetry breaking to the visible Standard Model superpartners [41]. If gauge interactions represent the dominant couplings of squarks, sleptons, and gauginos to the SUSY breaking sector, then it is natural to expect a gauge-ordered spectrum for the superpartners in which the right-handed sleptons and the bino with $U(1)_Y$ interactions are lightest, left-handed sleptons and the wino with $SU(2)_L$ interactions are heavier, and squarks and the gluino with $SU(3)_c$ interactions are heaviest.

A significant conceptual advancement in the simplified parameterization of BSM physics has been the generalization of the GMSB scenario to a framework known as General Gauge Mediation (GGM). In GGM, there is no assumed gauge ordered mass hierarchy. The MSSM soft masses are assumed to be free at the messenger scale and are subject only to the following conditions: (1) A gravitino LSP (2) Vanishing A-terms at

the scale of SUSY breaking (3) Sfermion mass sum rules (4) Flavor universality. In particular, there is not necessarily a hierarchy between colored states (squarks, gluinos) and uncolored states (wino, bino, higgsinos, sleptons). With no real theoretical constraint on how light the color charged particles can be, GGM leaves room for the possibility of large production cross sections from compressed spectra, resulting in high discovery potential at early LHC runs. This is in stark contrast to the more restrictive Minimal Gauge Mediation (MGM) scenario, where colored states are always heavier than the uncolored states and are thus out of reach for the early LHC runs.

The MGM restriction to a single source of SUSY breaking is not generally realized except in the simplest models. One specific scenario that fits within the classification of GGM is Gauge Mediation with Split Messengers (GMSM) [38, 39] in which the strong and weak messenger fields feel independent sources of SUSY breaking, and also allow for additional requisite SUSY breaking in the Higgs sector. In this simple generalization of MGM, the superpartner mass spectra are grouped roughly into strongly and weakly interacting sets. Over much of the parameter space the masses of both these groups can be comparable, yielding relatively compressed spectra with colored states not much heavier than weakly interacting states.

The simplest version of gauge mediation with split messengers (GMSM) is defined by the six parameters

$$N_5 \quad \Lambda_L \quad \Lambda_d \quad M \quad \tan\beta \quad \mu \tag{2.8}$$

where Λ_L and Λ_d are the SUSY breaking scales for the weak and strong messenger chiral multiplet fields $L \oplus \overline{L}$ and $d \oplus \overline{d}$, transforming as $(1,2,-1) \oplus (1,2,+1)$ and $(\overline{3},1,+\frac{2}{3}) \oplus (3,1,-\frac{2}{3})$ respectively under $SU(3)_c \times SU(2)_L \times U(1)_Y$. Here the electric charge generator is normalized as $Q = T_3 + \frac{1}{2}Y$. The gaugino masses in this version of GMSM are given by

$$m_{\lambda_i} = \frac{\alpha_i}{4\pi}\Lambda_{\lambda_i} \tag{2.9}$$

where $i = 1, 2, 3$ for bino, wino, and gluino, $\alpha_i = g_i^2/4\pi$ where g_i are in GUT normalization $g_1^2 = (5/3)g'^2$,

$$\begin{aligned} \Lambda_{\lambda_1} &= N_5\left(\frac{3}{5}\Lambda_L + \frac{2}{5}\Lambda_d\right) \\ \Lambda_{\lambda_2} &= N_5\Lambda_L \\ \Lambda_{\lambda_3} &= N_5\Lambda_d \end{aligned} \tag{2.10}$$

and all quantities are understood to be evaluated at the messenger scale. The squark and slepton masses squared are given by

$$m_\phi^2 = 2\sum_{i=1}^{3} C_i\left(\frac{\alpha_i}{4\pi}\right)^2 |\Lambda_{\phi,i}|^2 \tag{2.11}$$

where $C_1 = \frac{3}{5}\left(\frac{Y}{2}\right)^2$, $C_2 = \frac{3}{4}(0)$ for $SU(2)_L$ doublets(singlets), and $C_3 = \frac{4}{3}(0)$ for $SU(3)_c$ triples(singlets), and

$$\begin{aligned} |\Lambda_{\phi,1}|^2 &= N_5\left(\frac{3}{5}|\Lambda_L|^2 + \frac{2}{5}|\Lambda_d|^2\right) \\ |\Lambda_{\phi,2}|^2 &= N_5|\Lambda_L|^2 \\ |\Lambda_{\phi,3}|^2 &= N_5|\Lambda_d|^2 \end{aligned} \tag{2.12}$$

where again all quantities are understood to be defined at the messenger scale. The superpartner SUSY breaking masses at the electroweak scale are determined by renormalization group evolution from the messenger scale. The masses squared for the Higgs fields at the messenger scale are determined by consistent renormalization group evolution up to the conditions implied by electroweak symmetry breaking, which are determined by $\tan\beta$ and μ at the electroweak scale. This allows for a parameterization of requisite SUSY breaking contributions to the Higgs masses at the messenger scale in addition to the gauge mediated contributions.

An important feature of gauge mediation which is captured by GMSM, is that while superpartner spectra are generally gauge ordered (defined above) the masses need not be directly proportional to gauge couplings squared. This allows for the possibility of

gauge ordered but compressed superpartner spectra in which the squarks and gluinos are only somewhat heavier than the the sleptons, bino, and wino. The existence within the GMSM parameterization of a variable level of compression for the superpartner spectrum, in particular squarks and gluinos that are lighter than what is implied by the MGM restriction, has important implications for the total production cross section and therefore the discovery potential. Much of the phenomenology of simplified models is determined by the next-to-lightest stable particle (NLSP) in the spectrum.

Chapter 3

Topologies with a Neutralino NLSP

One broad class of GMSM scenarios is that in which the NLSP is a neutralino [36, 37]. The GMSM parameterization of the space of these models can be interpreted in the context of a simplified model, which can then be used to apply a very general analysis to the final state signatures that arise here. In this scenario, the lightest neutralino will generically decay to a gravitino plus its superpartner, which can be either a photon, a Z boson, or a Higgs boson, depending on whether the lightest neutralino is bino-like, wino-like, or Higgsino-like.

$$\chi_1^0 \rightarrow (\ \gamma \ , \ Z \ , \ h \ ) + \widetilde{G} \tag{3.1}$$

This results in a large number of interesting signatures, typically involving high p_T leptons, jets, photons and missing energy. One example of such a signature is shown in Fig. 3.1

The GMSM framework is advantageous for early LHC searches due to the fact that there is no restriction to gauge ordered superpartner mass spectra, as is required in the minimal case. As such there are large portions of parameter space where the masses of strongly and weakly interacting sets are comparable, thus accomodating light colored states and compressed spectra. Tevatron constraints on neutralino NLSP can be found in [143]. As discussed there, the phenomenology of general neutralino NLSPs is best understood by going to simplifying gauge eigenstate limits. The discrete possibilities are then: bino-like, wino-like, and Higgsino-like NLSPs. Higgsino NLSPs in turn can be classified by their decay modes, which can be dominated by Z's (the "Z-rich" scenario), Higgses (h-rich), or a roughly equal mix of Z and Higgs. For a wino-like NLSP, the mass splitting between the charged and neutral states is generically small. Therefore

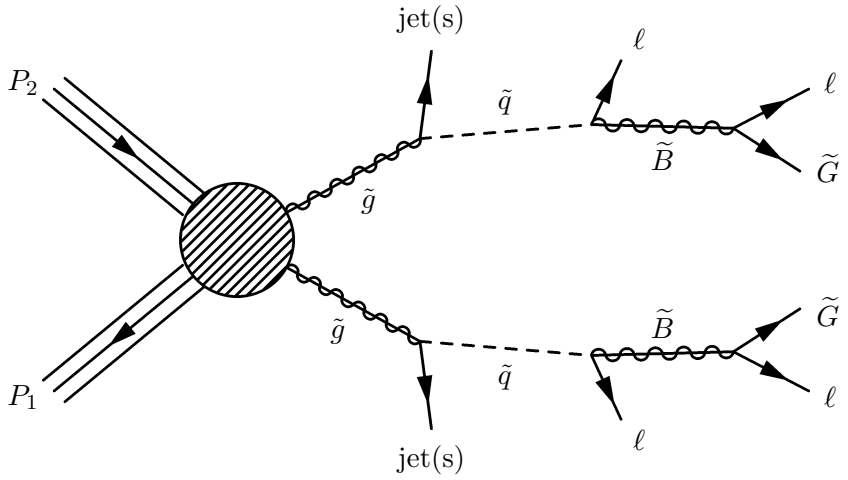

Figure 3.1: One example process with a bino-like NLSP produced via cascade from colored production. Here, two gluinos are pair produced, and each one decays through an on (or off) shell squark to two jets and the bino. In this example, each bino decays to a photon and a gravitino, resulting in a $\gamma\gamma + \not{E}_T$ signature.

large swaths of the GGM parameter space fall into the category called "wino-coNLSP", where three-body decays to a neutral wino are kinematically disfavored or disallowed, and the charged wino decays to a $W^{\pm} + \widetilde{G}$. Such signatures include W's as well as Z's and γ's in the final state. This is in contrast to the situation with a Higgsino-like NLSP, where the mass splitting between charged and neutral Higgsinos is generically larger and only the lightest neutralino can decay directly to the $\widetilde{G}$.

In general, a neutralino NLSP can decay to $X + \widetilde{G}$ where $X = \gamma, Z, h$ and the different gauge eigenstates may be characterized by their branching fractions to the different possible X's. A bino-like NLSP will decay dominantly to photons as $\mathrm{Br}(\widetilde{B} \to \gamma + \widetilde{G}) \sim \cos^2\theta_W$, with a subdominant component to Z's $\mathrm{Br}(\widetilde{B} \to Z + \widetilde{G}) \sim \sin^2\theta_W$. Conversely, a neutral wino-like NLSP will decay mostly to Z's and the situation is flipped. A Higgsino-like NLSP will decay dominantly to Z or h with a branching fraction that depends on $\tan\beta$ and $\mathrm{sgn}\mu$. The Z-rich scenario occurs for low values of $\tan\beta$ and $\mathrm{sgn}\mu = +$, the h-rich scenario occurs for low values of $\tan\beta$ and $\mathrm{sgn}\mu = -$, and the mixed Z/h case occurs for moderate to large values of $\tan\beta$. Although this behavior is generic over the entire GGM parameter space, pathological situations such as multiple SUSY-breaking sectors with Goldstini can lead to different NLSP branching

ratios.

Given a choice of neutralino NLSP, there is still a high-dimensional parameter space the characterizes the remaining superpartner spectrum so additional simplifying assumptions are required to define a tractable parameter space. We choose here a framework for benchmark spectra motivated by early LHC discovery potential. We thus focus on compressed spectra with large production cross sections from strongly interacting superpartners.

3.1 Bino NLSP

For bino NLSPs, since the bino has a small direct production cross-section, the dominant production for the minimal benchmark is gluino pair production (with cross-section determined by the gluino mass). GMSM inspired benchmarks are additionally dominated by gluino-squark and squark-squark production, as well as wino pair production for the final benchmark described above with weak production. The produced states always cascade decay down to the bino NLSP, which then decays to either $\gamma + \widetilde{G}$ or $Z + \widetilde{G}$. For $m_{\widetilde{B}} \gg m_Z$, this happens in a $0.77 : 0.23$ ratio. The final states which contain either one photon or two leptons are: $\gamma + X + \not{E}_T$, $Z(\ell\ell) + X + \not{E}_T$, $\gamma\gamma + \not{E}_T$, $\gamma Z(\ell\ell) + \not{E}_T$, $Z(\ell\ell)Z(\ell\ell) + \not{E}_T$. The last has too small of a branching fraction to be useful, so we will ignore it (however, the Higgsino NLSP will populate this final state, see below). We also lump the hadronic and invisible decays of the Z into the inclusive "X" category.

The most recent relevant CMS published result analyzes diphoton events, due to the enhanced $\mathrm{Br}(\widetilde{B} \to \gamma + \widetilde{G})$, from the first $4.93\,\mathrm{fb}^{-1}$ of data at 7 TeV. The bino-like NLSP is assumed to be pair produced via cascade decays from Squark/gluino strong production modes. The lightest chargino is assumed to be heavy and decoupled. Fig. 3.2 shows the resulting upper limits on the GGM production cross section, at 95 % CL, as well as exclusion contours for the gluino versus squark mass plane from 400 to 2000 GeV in squark and gluino mass, with the neutralino mass fixed at 375 GeV. This mass value is chosen to represent a reasonably light NLSP, but high enough to be outside current exclusion limits. For the bino-like scenario, the diphoton cross section limit is of

order 0.003 - 0.01 pb at 95 % CL with a typical acceptance of 30 % for $\not\!\!E_T > 100\,\text{GeV}$, excluding squark and gluino masses up to about 1 TeV. Fig. 3.3 shows the exclusion contours in the plane of gluino versus neutralino mass, and we find that the diphoton search excludes gluino production for a bino-like neutralino for gluino masses up to about 1 TeV rather independent of the neutralino mass.

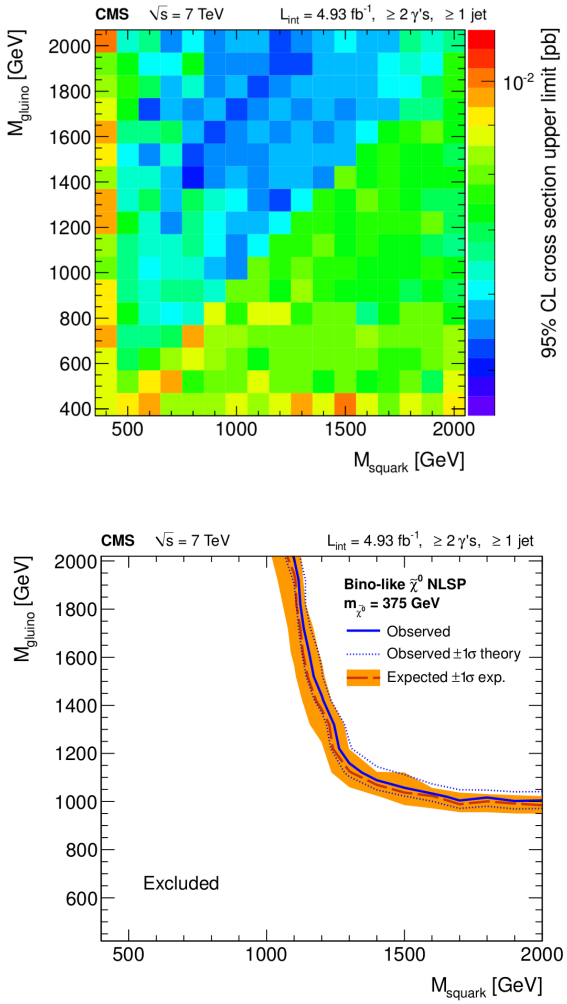

Figure 3.2: Observed upper limits at 95 % CL on the signal cross section (left) and corresponding exclusion contours (right) in gluino-squark mass space for the diphoton analysis for a bino-like neutralino. The shaded uncertainty bands around the expected exclusion contours correspond to experimental uncertainties, while the NLO renormalization and PDF uncertainties of the signal cross section are indicated by dotted lines around the observed limit contour.

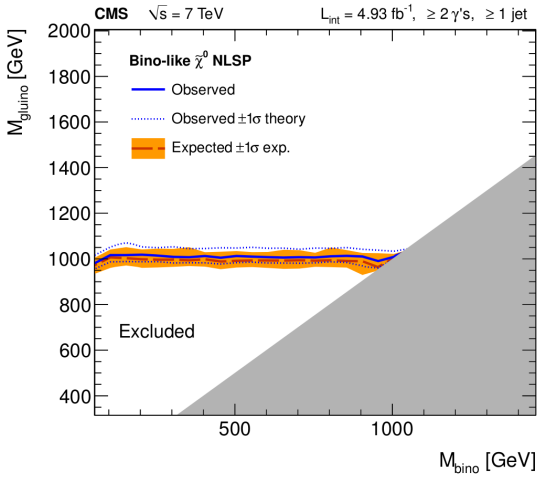

Figure 3.3: Exclusion contours at 95 % CL in the plane of gluino versus neutralino mass for the diphoton analysis for a bino-like neutralino.

3.2 Wino NLSP

Here production arises from both colored states that decay to the wino and directly from wino pair production, so the production cross-section is controlled by both the gluino mass and the wino mass. The wino chargino and neutralino are nearly mass degenerate and form coNLSPs, so we have to keep track of which "-ino" the colored states decay into. When the squarks are heavier than the gluino, as in the minimal benchmark, each gluino decays to a charged wino with branching fraction $\sim 60\%$ and a neutral wino the remaining $\sim 40\%$. The CC case leads to $W^+(\ell\nu)W^-(\ell\nu) + \not{E}_T$. The CN case leads to $\gamma + X + \not{E}_T$, $W^+(\ell\nu)\gamma + \not{E}_T$, $Z(\ell\ell) + X + \not{E}_T$, or $W(\ell\nu)Z(\ell\ell) + \not{E}_T$. The NN case leads to the same final states as bino NLSP, except now with the reversed ratio of $\gamma + \widetilde{G}$ to $Z + \widetilde{G}$.

The most recent relevant CMS published result analyzes single photon events, due to the reduced $\mathrm{Br}(\widetilde{W} \to \gamma + \widetilde{G})$, from the first $4.93\,\mathrm{fb}^{-1}$ of data at 7 TeV. Contributions from strong production squark/gluino cascades as well as the direct weak production of chargino-neutralino pairs are considered. Fig. 3.4 shows the resulting upper limits on the GGM production cross section, at 95 % CL, as well as exclusion contours for the gluino versus squark mass plane from 400 to 2000 GeV in squark and gluino mass, with the neutralino mass fixed at 375 GeV. This mass value is chosen to represent a

reasonably light NLSP, but high enough to be outside current exclusion limits. The single-photon cross section upper limit is of order 0.003-0.1 pb at 95 % CL with a typical acceptance of 7 %, excluding squark and gluino masses up to about 800 GeV. Fig. 3.5 shows the exclusion contours in the plane of gluino versus neutralino mass

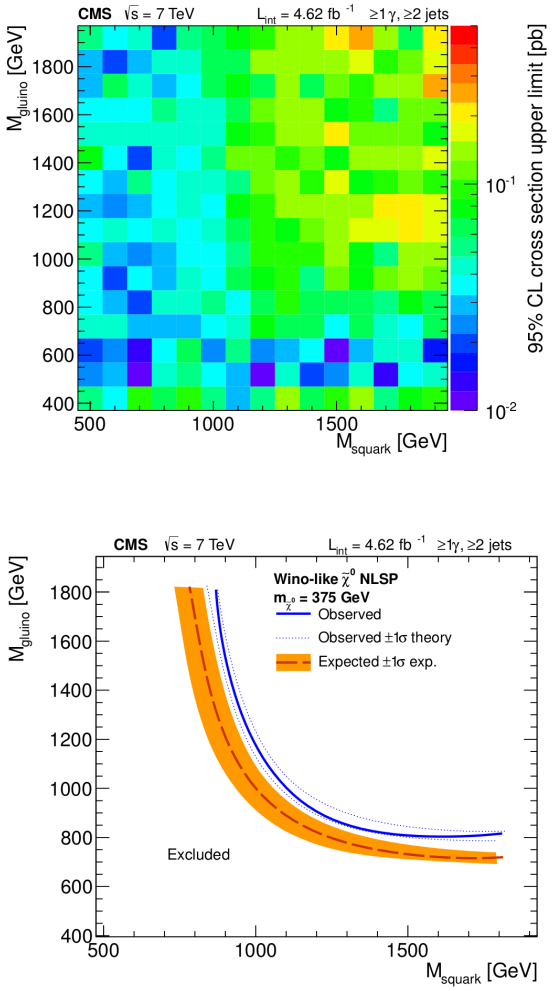

Figure 3.4: Observed upper limits at 95 % CL on the signal cross section (left) and corresponding exclusion contours (right) in gluino-squark mass space for the single-photon search in the wino-like scenario. The shaded uncertainty bands around the expected exclusion contours correspond to experimental uncertainties, while the NLO renormalization and PDF uncertainties of the signal cross section are indicated by dotted lines around the observed limit contour.

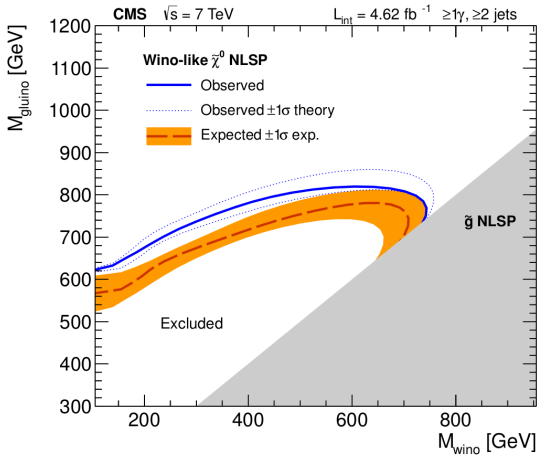

Figure 3.5: Exclusion contours at 95 % CL in the plane of gluino versus neutralino mass for the single-photon search in the wino-like scenario.

3.3 Z-rich Higgsino NLSP

Here as for the winos, the Higgsinos can be directly produced, or produced in decays of colored states, so the overall cross-section is controlled by both the gluino and Higgsino masses. For all the benchmarks defined here we choose parameters such that the heavier Higgsino states always decay down to the lightest Higgsino neutralino. That is, there is no coNLSP and just a single Higgsino NLSP. In particular, we choose to change the gravitino mass with the Higgsino mass such that the Higgsino decay length is fixed $\sim$ 0.1 mm. For this decay length, the charged Higgsino always decays first to the neutral Higgsino. The NLSP in turn can decay either to photon, Z or Higgs. For the Z-rich case (low $\tan\beta$, $\mu > 0$), the branching ratio to Higgs is negligible, and the branching ratio to photon is negligible except when the NLSP is very light and the Z decay mode is squeezed. Thus for Z-rich Higgsino NLSPs, the available final states are $Z(\ell\ell) + X + \not{E}_T$ and $Z(\ell\ell)Z(\ell\ell) + \not{E}_T$.

The most recent relevant CMS published result analyzes 19.5 fb^{-1} of data at 8 TeV in the context of the "natural Higgsino NLSP" scenario. This scenario is characterized by light stop squarks, which provide the dominant production mechanism for the Higgsino NLSP through the enhanced third generation Yukawa coupling. The Higgsinos then decay to $Z\widetilde{G}$ or $h\widetilde{G}$, yielding a final state with hZ, ZZ, or ZZ plus $\not{E}_T$. In addition

to top-squark pair production, the natural Higgsino NLSP scenario also encompasses direct electroweak Higgsino pair production leading the same final state of except with less jet activity. Fig. 3.6 shows the excluded regions in the $m_{\widetilde{H}}$ vs. $m_{\tilde{t}}$ plane for the various scenarios described above (Z-rich, h-rich, and mixed Z/h scenarios).

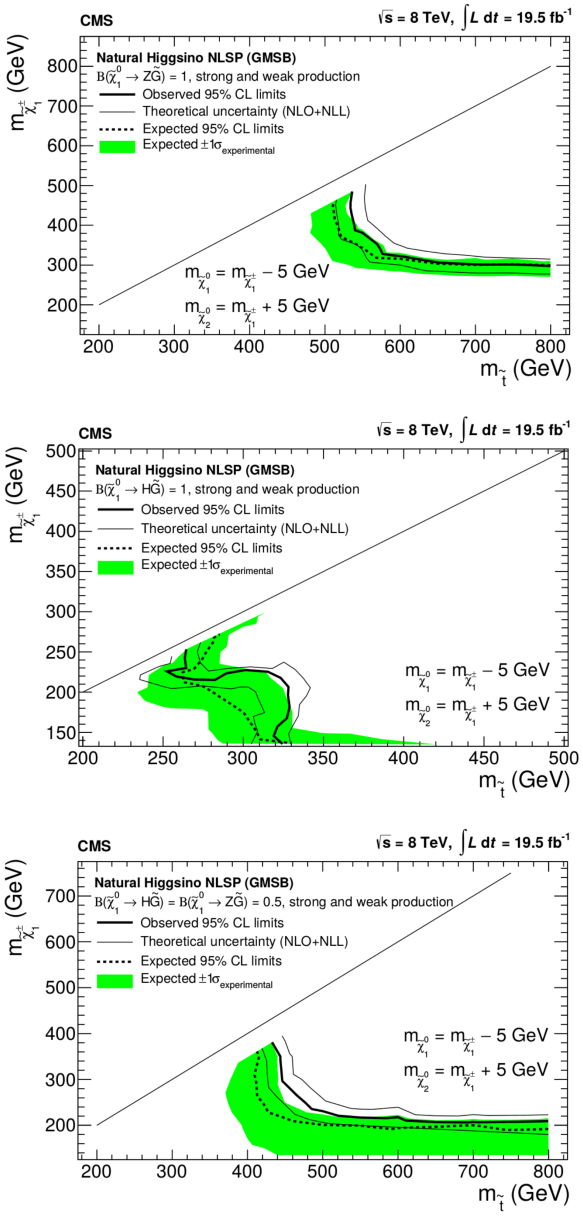

Figure 3.6: The 95 % confidence level upper limits in the top squark versus chargino mass plane, for the natural Higgsino NLSP scenario with $\mathrm{Br}(\widetilde{H} \to Z\widetilde{G}) = 1.0$ (top left), $\mathrm{Br}(\widetilde{H} \to h\widetilde{G}) = 1.0$ (top right), and $\mathrm{Br}(\widetilde{H} \to h\widetilde{G}) = \mathrm{Br}(\widetilde{H} \to Z\widetilde{G}) = 0.5$ (bottom). Both strong and electroweak production mechanisms are considered. The region to the left and below the contours is excluded. The region above the diagonal straight line is unphysical.

Chapter 4

Topologies with a Slepton NLSP

Another general class of MSSM scenarios, is that in which a slepton is the next-to-lightest superpartner (NLSP) [36, 41, 37]. In such scenarios, the slepton NLSP decays to its partner leptons plus a gravitino

$$\tilde{\ell} \to \ell + \widetilde{G} \tag{4.1}$$

Low scale gauge-mediated supersymmetry breaking naturally gives rise to superpartner spectra with nearly degenerate right-handed sleptons playing the role of the coNLSP, with a bino-like neutralino as the next to next to lightest superpartner (NNLSP) [34, 38, 39, 143, 44]. If the NLSP slepton is right-handed, then the only unsuppressed cascade decays to the NLSP must proceed through the bino component of a neutralino.

$$\widetilde{B} \to \widetilde{\ell}_R^{\pm} + \ell^{\mp} \tag{4.2}$$

Cascade decays from heavier superpartners will then always pass sequentially through the bino, then to one of the co-NLSP sleptons emitting a lepton, and finally to the un-observed Goldstino, emitting another lepton. Therefore, pair-production of heavier superpartners gives rise to inclusive signatures that include four hard leptons and missing transverse energy,

$$pp \to X + \ell^{\pm}\ell^{\mp}\ell^{\pm}\ell^{\mp} + \not{E}_T \tag{4.3}$$

where $\ell = e, \mu, \tau$, and X represents whatever Standard Model particles are emitted in cascade decays to $\widetilde{B}$. An example of such a process is shown in Fig. 4.1.

If the superpartner pair production is through strong interactions, then conservation of $SU(3)_c$ color implies that at least one jet must be emitted in each cascade decay

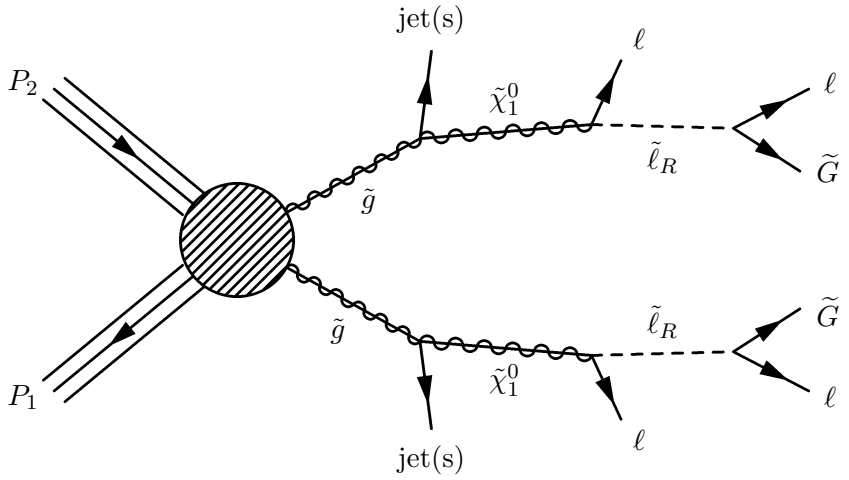

Figure 4.1: One example process with a slepton-coNLSP produced via cascade from colored production. Here, two gluinos are pair produced, and each one decays through an NNLSP bino to a right handed slepton emitting one jet and one lepton. Each slepton then decays to a lepton and a gravitino, resulting in a $2j + 4\ell + \not{E}_T$ signature.

to the neutralino, giving an inclusive SUSY signature of at least $2j + 4\ell + \not{E}_T$. A right-handed selectron NLSP with a heavier bino-like neutralino is generic in gauge ordered SUSY spectra that arise in many scenarios for supersymmetry breaking. So the inclusive 4 leptons + missing energy SUSY signature covers a fairly wide range of possibilities for how SUSY might be realized at the electroweak scale. This signature is best covered by an exclusive hierarchical search for quad-leptons, tri-leptons, and same-sign dileptons, including $\not{E}_T$ in the latter two cases as necessitated by backgrounds. The principal strong production channels that are relevant for early LHC searches are pairs of gluinos and/or squarks, while weak production of charginos, neutralinos, and direct production of sleptons should become relevant in future searches. A reach or upper limit on $\sigma \times$ BR for $pp \rightarrow$ multi-leptons + $\not{E}_T$ as a function of the gluino and the chargino masses provides a unified summary of the sensitivity to this topology for both strong and weak production of superpartners. These scenarios can be used to explore the discovery potential of searches for multiple leptons in early LHC running.

Given that final states with multiple high-p_T leptons are generally clean discovery modes for new physics, it is of special interest to investigate the possibilities for producing such signatures within the context of GGM and GMSM. Multi-lepton final states

arise most naturally in the subset of GGM and GMSM parameter spaces where the right-handed sleptons are flavor-degenerate and at the bottom of the MSSM spectrum. These 'slepton coNLSPs' decay 100% of the time to $\ell + \widetilde{G}$, and so all events with MSSM production contain at least two high-p_T leptons. Depending on the details of the heavier states in the spectrum, these leptons can be same sign or opposite sign, and there can be additional energetic leptons in the event [41, 37]. In the case that a bino-like neutralino is the next heavier superpatner above the slepton coNLSPs at least 4 leptons arise in each event [41, 37].

For the slepton NLSP scenario there is an huge multi-dimensional parameter space characterizing the remainder of the superpartner spectrum. Defining useable benchmarks within tractable parameter spaces therefore requires additional simplifying assumptions. The main motivation and focus here for early LHC searches is on compressed spectra with significant production cross section from strongly interacting superpartners. In the following sections, we will describe various interesting benchmark scenarios of this type.

4.1 GMSM Inspired Benchmark Spectra

For early LHC searches it is useful to utilize simple parameter spaces that reproduce the important features of superpartner spectra that arise from simple underlying models. Here we formulate a benchmark of this type inspired by GMSM.

The GMSM inspired scenario described here is defined to be right handed slepton coNLSP, a gluino and (nearly) degenerate squarks, the bino, wino, and left handed sleptons. The wino and gluino masses given by M_2 and M_3 respectively may be taken to be independent masses for a two parameter parameterization of this benchmark. The squark soft masses are taken to be degenerate with value $m_{\tilde{q}}$ related to the gluino mass by

$$m_{\tilde{q}} = 0.8\ M_3 \tag{4.4}$$

The left-handed slepton masses, bino, and right-handed slepton coNLSP masses are

related to the wino mass by

$$m_{\tilde{\ell}_L} = 0.8\ M_2$$

$$M_1 = 0.5\ M_2$$

$$m_{\tilde{\ell}_R} = 0.3\ M_2 \tag{4.5}$$

All these ratios are close to those of GMSM with $N = 5$ messenger generations. The squark and slepton mixings are defined to vanish. This approximates the small mixing that is obtained in most theories of low scale gauge mediation. All other soft parameters may be set to some large value such as 1.5 TeV. With both squarks and gluinos in the spectrum, the dominant strong production modes at the LHC are $pp \to \tilde{q}\tilde{q}, \tilde{q}\tilde{g}$ with a smaller fraction of $\tilde{g}\tilde{g}$. The inclusion of all these states with the relations given above gives a two-parameter space benchmark that interpolates between weak and strong production - this feature allows a comparison between existing Tevatron bounds (which are based on weak production) and early reach at the LHC from strong production.

4.2 Slepton-coNLSP

In the slepton NLSP scenario for SUSY, the splitting among the sleptons plays a central role in determining the associated accelerator signatures. Low scale gauge-mediated supersymmetry breaking with significant left-right sparticle mixing arising at large values of $\tan\beta$ can naturally give rise to a stau slepton as the next to lightest superpartner (NLSP) [41]. The approximate flavor universality of gauge-mediation ensures that the a selectron and smuon are slightly heavier, and decay through both charge- preserving and charge-changing reactions to the stau through the emission of soft lepton pairs.

$$\tilde{e}_R \to \tilde{\tau}_1^{\mp}\tau^{\pm}e \quad \text{and} \quad \tilde{\mu}_R \to \tilde{\tau}_1^{\mp}\tau^{\pm}\mu \tag{4.6}$$

However if the mass splittings among the selectron, smuon, and lightest stau are less than the tau mass, then the three-body decays are kinematically blocked. In this case the decays in Eq. 4.1 of the selectron, smuon, and lightest stau to the partner lepton

and the Goldstino can dominate if the SUSY breaking scale is not too high, and all three sleptons act effectively as the NLSP. The unsuppressed cascade decays (Eq. 4.2) that pass through the light sleptons in this case are then of the form

$$\begin{aligned} \widetilde{B} &\to \widetilde{\ell}_i^{\pm} \ell_i^{\mp} \\ &\quad \hookrightarrow \ell_i^{\pm} \widetilde{G} \end{aligned} \tag{4.7}$$

where here $i = e, \mu, \tau$. So starting from superpartner pair production, the specific flavor and charge structure of the inclusive 4 lepton + missing energy signature that arises in the slepton coNLSP scenario is

$$pp \to \ell_i^+ \ell_i^- \ell_j^+ \ell_j^- + X + \not{E}_T \tag{4.8}$$

where $i, j = e, \mu, \tau$ with approximately equal weight. The slepton coNLSP scenario is generally obtained for low to moderate values of $\tan\beta$ for which stau renormalization group evolution and left-right mixing effects proportional to the tau Yukawa coupling are small.

This signature can arise either from strong production of squarks and gluinos via cascade decays, or through direct weak production of chargino-neutralino or right handed slepton pairs. Both scenarios give rise to decay patterns that eventually lead to a bino-like neutralino, which decays as we've described leading to a final state of multileptons plus $\not{E}_T$. The relative importance of strong-weak production mechanisms depends on the values of the superpartner masses. Fig. 4.2 shows the result of the most recent CMS multi-lepton analysis, with $19.5\,\text{fb}^{-1}$ of data at 8 TeV, interpreted in the context of the slepton coNLSP scenario. Using the benchmark mass spectrum we proposed earlier, in addition to the requirements of no L-R fermion mixing, The 95 % CL exclusion limit is presented in the gluino-chargino mass plane. In the region dominated by strong superpartner production, the exclusion curve asymptotically approaches a horizontal plateau, while it tends towards a vertical line in the region dominated by weak superpartner production.

Besides the stau-NLSP scenario, we also consider the stau-NNLSP scenario in which

mass-degenerate right-handed selectrons and smuons are coNLSPs, while the right-handed stau is the next-to-next-to-lightest SUSY particle (NNLSP). The process proceeds via electroweak pair production of staus. The staus decay to the NLSP and a τ lepton. The NLSPs decay to a τ lepton and gravitino. The search channels most sensitive to the stau-(N)NLSP scenarios contain τ_h leptons, no tagged b jets, off-Z OSSF pairs, and large $\not{E}_T$. The 95 % CL exclusion limits for the stau-(N)NLSP scenario are shown in Fig. 4.2. When the mass difference between the stau and the other sleptons is small, the leptons are soft. This results in low signal efficiency, which causes the exclusion contour to become nearly parallel to the diagonal for points near the diagonal. The difference between the expected and observed limits in the region below the diagonal is driven by the excesses observed between the data and SM estimates in the four-or-more lepton, OSSF1, off-Z, τ_h channels without b jets.

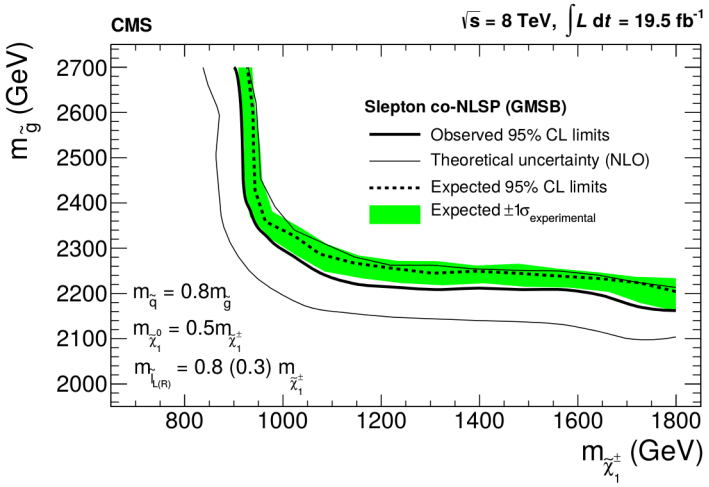

Figure 4.2: The 95 % confidence level upper limits for the slepton coNLSP model in the gluino versus chargino mass plane. The region to the left and below the contours is excluded.

4.3 Stau-(N)NLSP

On the other hand, if the splitting between the selectron and stau, and the smuon and stau, are larger than the tau mass, then the three-body decays in Eq. 4.6 are kinematically allowed, and generally dominate over the decays in Eq. 4.1 to the Goldstino. With

this type of superpartner spectra, nearly all cascade decays pass through the metastable stau slepton, which decays to the un-observed Goldstino and tau [35]. The lightest stau thus acts as the NLSP. The unsuppressed cascade cascade decays in Eq. 4.2 that pass through the light sleptons in this case are then of a charge preserving form

$$\begin{aligned} \widetilde{B} &\to \widetilde{\ell}_i^{\pm} \ell_i^{\mp} \\ &\quad \hookrightarrow \widetilde{\tau}_1^{\pm} (\tau^{\mp} \ell^{\pm}) \\ &\quad\quad \hookrightarrow \tau^{\pm} \widetilde{G} \end{aligned} \tag{4.9}$$

or a charge changing form

$$\begin{aligned} \widetilde{B} &\to \widetilde{\ell}_i^{\pm} \ell_i^{\mp} \\ &\quad \hookrightarrow \widetilde{\tau}_1^{\mp} (\tau^{\pm} \ell^{\pm}) \\ &\quad\quad \hookrightarrow \tau^{\mp} \widetilde{G} \end{aligned} \tag{4.10}$$

The lepton and tau emitted in intermediate three-body decays in Eq. 4.9 or Eq. 4.10 are generally very soft, as indicated by the parentheses, and likely to have rather low acceptance and efficiency in the detector. So neglecting these soft leptons, starting from superpartner pair production, the stau NLSP scenario gives rise to the inclusive signature of 2 leptons + 2 taus + missing energy. The specific flavor and charge structures of the hard leptons and taus are

$$\begin{aligned} pp \to \ell_i^{\pm} \ell_j^{\mp} \tau^{\pm} \tau^{\mp} + X + \not{E}_T \\ \ell_i^{\pm} \ell_j^{\pm} \tau^{\pm} \tau^{\mp} + X + \not{E}_T \\ \ell_i^{\pm} \ell_j^{\mp} \tau^{\pm} \tau^{\pm} + X + \not{E}_T \\ \ell_i^{\pm} \ell_j^{\pm} \tau^{\pm} \tau^{\pm} + X + \not{E}_T \end{aligned} \tag{4.11}$$

where here $i, j = e, \mu$ with equal weight. The stau NLSP scenario is generally obtained for moderate to high values of $\tan\beta$ for which stau renormalization group evolution and left-right mixing effects proportional to the tau Yukawa coupling are significant.

On the other hand, if the stau NLSP is mostly right-handed, then the only unsuppressed cascades come directly from the bino component of heaver neutralinos.

$$\begin{aligned} \widetilde{B} &\to \tilde{\tau}_R^{\pm}\tau^{\mp} \\ &\quad \hookrightarrow \tau^{\pm}\widetilde{G} \end{aligned} \tag{4.12}$$

Pair production of any superpartners with cascade decays that pass through these neutralinos then give rise to the inclusive signature of four hard taus with missing energy,

$$pp \to \tau^{\pm}\tau^{\mp}\tau^{\pm}\tau^{\mp} + \not{E}_T \tag{4.13}$$

It is important to note that since all the relevant cascade decays have the possibility to flip the superpartner charges, these signatures arise in all charge and lepton flavor combinations. This signature is best covered by a di-lepton plus one or two identified taus plus $\not{E}_T$ search in all flavor and charge channels. The principal strong production channels that are relevant for early LHC are pairs of gluinos and/or squarks.

Direct weak production of charginos, neutralinos, and sleptons will become relevant in future searches. A reach or upper limit on $\sigma \times \mathrm{BR}$ for $pp \to \tau\tau + \not{E}_T$ as a function of the gluino and the chargino provides a unified summary of the sensitivity to this topology for both strong and weak production of superpartners. Sensitivity to the remaining soft leptons emitted in the cascades between the selectron or smuon and NLSP stau may be illustrated in the above parameter plane for different fixed values of the mass splitting between these states.

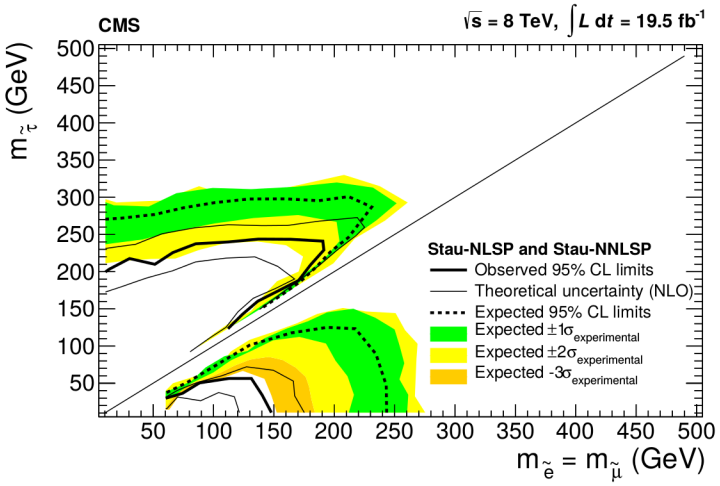

Figure 4.3: The 95 % confidence level upper limits for stau-(N)NLSP scenarios in the stau versus degenerate-smuon and -selectron mass plane (right). The region to the left and below the contours is excluded.

Part II

The Second Prong: Exploring the Higgs Sector with Multi-Leptons

Chapter 5

The Minimal Standard Model Higgs at the LHC

The combined data sets at 7 and 8 TeV from Run I at the LHC, have established beyond reasonable doubt, the existence of a Standard-Model-like Higgs boson. The discovery and characterization of the Higgs has inarguably been among the central aims of the physics program at the Large Hadron Collider (LHC). Its well-defined production and decay modes have allowed for mass-dependent searches tailored to a variety of specific channels (for a review, see [45] and references therein). Although the bulk of the sensitivity for this discovery came from dedicated searches in the $h \to \gamma\gamma$ and $h \to ZZ^* \to \ell^+\ell^-\ell'^+\ell'^-$ resonant decay channels, the results of searches in all of the known decay modes have been found to be consistent with a minimal Standard Model Higgs.

The dominant production channel of the SM Higgs at hadron colliders is through gluon-fusion ($gg \to h$) and existing LHC Higgs searches are typically tailored towards this channel due to both the large cross section and the resulting Higgs resonance. However, there are also a variety of ancillary channels in which the Higgs is produced in association with other quarks or vector bosons. These are, in order of decreasing production rate: weak vector boson fusion (VBF), $qq \to qqh$; Wh and Zh associated production (or Higgs-strahlung), $qq \to Wh, Zh$; and $t\bar{t}h$ associated production, $qq, gg \to t\bar{t}h$. Loosely speaking, the cross sections for weak VBF and Wh, Zh associated production are an order of magnitude smaller than that of gluon-fusion, while $t\bar{t}h$ associated production is smaller by a further order of magnitude. Di-Higgs production through gluon-gluon fusion, $gg \to hh$, is smaller by roughly a further order of magnitude. Nonetheless, they may provide interesting alternative routes to the discovery of the Higgs.

Whatever the mechanism of Higgs production, current search strategies are principally governed by the decay products of the Higgs. The primary decay modes for a light Higgs include $h \to b\bar{b}$, $\tau^+\tau^-$, $c\bar{c}$, gg, WW, ZZ, $\gamma\gamma$, and $Z\gamma$. Branching ratios to these final states are a sensitive function of the Higgs mass, with $b\bar{b}, \tau^+\tau^-$, and gg dominating at low masses ($m_h \sim 135$ GeV) and WW^*, ZZ^* dominating at higher masses. The colored final states $b\bar{b}$, $c\bar{c}$, and gg are inauspicious search modes at the LHC due to large QCD backgrounds; more promising are the diphoton channel and the leptonic final states of the WW, ZZ, and $\tau^+\tau^-$ channels.

The production and decay modes of the Higgs lead to a variety of possible search strategies at hadron colliders. At the LHC, the three main search methods with the greatest discovery potential are $h \to \gamma\gamma$, $h \to ZZ \to 4\ell$, and $h \to WW \to \ell\nu\ell\nu$. Although the branching ratio for $\gamma\gamma$ is small, the distinctive final state topology makes it a crucial search channel for lighter masses. At higher masses the increased branching fraction to WW and ZZ, combined with the cleanliness of 2ℓ and 4ℓ final states, make $h \to \ell\nu\ell\nu$ and $h \to 4\ell$ particularly attractive. Significantly, both $h \to ZZ \to 4\ell$ and $h \to \gamma\gamma$ (the so-called gold- and silver-plated channels) are resonant search modes, in that the invariant mass of the final state reconstructs the Higgs mass. This allows the direct determination of the Higgs mass, but at the expense of sensitivity to, e.g., non-resonant 4ℓ final states. This is in contrast to the $h \to WW \to \ell\nu\ell\nu$ channel, in which the missing energy from the neutrinos makes reconstructing the Higgs mass more challenging. Individually and in combination, these search channels are growing ever closer to constraining the production of a Standard Model Higgs boson in the light mass window, although backgrounds for these channels are large and potentially quite subtle.

Despite the focus of existing searches on the gluon-fusion production channel, the LHC has demonstrated considerable sensitivity to final states populated predominantly by associated production channels of the Higgs boson. Although these have weaker prospects for the determination of the Higgs mass based on kinematics, they often lead to final states with particularly low Standard Model backgrounds. In particular, the multitude of 3- and 4-lepton final states available from Higgs production in association

with W and Z bosons or a $t\bar{t}$ pair provides a key handle on picking the Higgs signal out of Standard Model backgrounds. Although searches in some specific alternate production and decay channels have been proposed previously [48], recent advances in multi-lepton searches at the LHC [91] have brought the possibility of a dedicated multi-lepton Higgs search across multiple channels into sharp focus.

Such a multi-lepton search enjoys several advantages. Standard Model backgrounds to multi-lepton processes are quite low, particularly in the absence of an on-shell Z boson. Further discrimination may be obtained by looking in regions of high missing energy or hadronic activity, away from typical Standard Model processes. Ultimately, perhaps the greatest advantage lies in the plethora of possible multi-lepton channels; more sensitivity to Higgs searches may be added by combining various 3ℓ and 4ℓ channels (as well as same-sign 2ℓ channels), particularly those that do not reconstruct an on-shell Z or the Higgs resonance itself.

In this chapter we pursue a simple goal: applying the existing CMS multi-lepton search strategy to the Higgs boson in order to determine how effective a new low-background, multi-channel analysis may be in the hunt for the Higgs. To this end, we focus on the Higgs production and decay channels most likely to produce 3ℓ and 4ℓ final states. These are dominated by Wh, Zh and $t\bar{t}h$ associated production with $h \to WW, ZZ$. At low masses, significant contributions may also arise from $h \to \tau^+\tau^-$ with both τs decaying leptonically. Additional contributions to $h \to 3\ell$ and nonresonant $h \to 4\ell$ arise from the dominant gluon and vector boson fusion production modes, where $h \to ZZ \to \ell\ell\tau\tau$ and the τs decay leptonically. Finally, a surprisingly significant contribution to resonant multi-lepton final states not covered by current resonant searches arises at low mass (particularly $m_h < 130$ GeV) when the Higgs decays to two off-shell Z bosons, $h \to ZZ \to 4\ell$. Taken together, the signal of these multi-lepton modes exceeds that of the gold-plated resonant 4ℓ mode. Exploring the sensitivity of existing multi-lepton searches to these production channels may allow the development of a search tailored channel-by-channel toward the discovery and characterization of the Higgs.

We will start by describing a prescription for interpreting current CMS multi-lepton searches for exotica, in terms of limits for the various hypotheses of the Higgs boson

mass. We will then show the results of this analysis using $5\,\mathrm{fb}^{-1}$ of data. Finally we will conclude with suggestions for refinements that could be performed to further increase the sensitivty of such an analysis.

5.1 Multi-Lepton Higgs Searches

Multi-lepton searches have been employed to good effect in the context of simplified models since early in Run I [91], and provide a necessary complementary search strategy for the Higgs. The total multi-lepton Higgs signal exceeds the four lepton gold-plated resonant mode, but is spread over many channels with same-sign di-lepton, tri-lepton, and four lepton final states. So while any individual channel alone is not significant, the exclusive combination across multiple channels was shown to provide a sensitivity competitive with other discovery level searches for the Higgs boson. While simply applying the existing multi- lepton search strategy to a Higgs signal is not optimal out of the box, it illustrated the considerable power of combining several low-background channels in the same search. The sensitivity of each individual channel to Higgs production may subsequently be improved by tailoring cuts to the corresponding dominant production mode for that channel. Thus our analysis was, in part, intended as an exercise to determine how these individual channels might best be optimized for a dedicated Higgs search.

5.1.1 Multi-Lepton Signal Channels

The prompt irreducible Standard Model backgrounds to multi-lepton searches are small and arise predominantly through leptonic decays of W and Z bosons. Such backgrounds may therefore be reduced by demanding significant hadronic activity and/or missing energy in the events. Hadronic activity can be quantified by the variable H_T , defined as the scalar sum of the transverse energies of all jets passing the preselection cuts. The missing transverse energy (MET) is the magnitude of the vector sum of the momenta of all particles in the event. Both H_T and MET are sensitive discriminating observables for new physics, including the Higgs.

The background reduction ability of H_T and MET may be exploited in the following manner: Events with $H_T > 200$ ($\not{E}_T > 50$) GeV may be categorized as having "high" H_T (MET), while those with $H_T < 200$ ($\not{E}_T < 50$) GeV may be categorized as having low H_T (MET). The high H_T and high MET requirements (individually or in combination) lead to a significant reduction in Standard Model backgrounds. Backgrounds may also be reduced using the variable S_T, which is defined to be the scalar sum of MET, H_T, and leptonic p_T, but for simplicity and because of its omission in existing multi-lepton searches [91], we will not discuss the implications of cutting on this variable here.

Further background reduction may be accomplished with a "Z veto", in which the invariant mass of opposite-sign same-flavor (OSSF) lepton pairs is required to lie outside a 75 - 105 GeV window around the Z mass; we simply denote events passing the Z veto as "no Z". In the case of 3ℓ events, it is also useful to differentiate between events with no OSSF pairs (which we label "DY0", i.e., no possible Drell-Yan pairs) and one OSSF pair (DY1). Although the current CMS multi-lepton analysis also includes channels with one or more hadronic τ's, in this analysis we will focus our attention on $\ell = e^{\pm}, \mu^{\pm}$ only. We include leptonic τ's in our analysis, classifying them according to their leptonic final state.

Production	Decay
$gg \to h$	$h \to 4\ell$
VBF $\to h$	$h \to 4\ell$
$q\bar{q} \to Wh$	$Wh \to WWW, WZZ, W\tau\tau$
$q\bar{q} \to Zh$	$Zh \to ZWW, ZZZ, Z\tau\tau$
$t\bar{t}h$	$t\bar{t}h \to t\bar{t}WW, t\bar{t}ZZ, t\bar{t}\tau\tau$

Table 5.1: The 11 independent production and decay topologies simulated for the Standard Model Higgs Boson with $m_h = 125$ GeV. The Higgs boson branching ratios are factored out of each topology. All top-quark, τ-lepton, and W- and Z bosons branching ratios are Standard Model.

The possible decay modes of the SM Higgs leading to multi-lepton final states is given in Table 5.1. Dividing the multi-lepton signals into 3ℓ or 4ℓ events, there are 20 possible combinations of H_T high/low; MET high/low; Z/no Z; and DY0/DY1; these may be aggregated to form the 11 channels used in [91], with the addition of one further channel for SS dileptons. The collected channels are presented in Table 1. For each of

the 3ℓ and 4ℓ categories, channels are presented in approximately descending order of sensitivity, with the last such channel dominated by SM backgrounds.

5.1.2 Simulation Details

The production rates and branching ratios of the Standard Model Higgs are fixed by SM gauge couplings and fermion masses. The cross sections for each SM Higgs boson production channel and branching ratios for Higgs decays at each mass point were taken from the LHC Higgs Cross Section Group [96]. The gg-fusion cross section is computed to $\mathrm{NNLO_{QCD}} + \mathrm{NNLL_{QCD}} + \mathrm{NLO_{EWK}}$ precision; the weak VBF and associated Wh, Zh cross sections are computed to $\mathrm{NNLO_{QCD}} + \mathrm{NLO_{EWK}}$ precision; and $t\bar{t}h$ is computed to $\mathrm{NLO_{QCD}}$ precision.

For simulating signal processes, we have used MadGraph v4 [92, 93] and rescaled the cross sections to match the NLO results described above. For the production channels of Wh, Zh, qqh and $t\bar{t}h$, the Higgs boson was decayed in the WW^*, ZZ^*, $\tau^+\tau^-$ modes using BRIDGE [95]. For the $gg \to h$ channel, the parton-level generation was done entirely within MadGraph with four charged leptons in the final state, thus including the effects of both Zs going off-shell, as well as the contribution from two on-shell Zs with the Higgs boson being off-shell. For the gluon fusion channel, the Higgs width was taken in accordance with [96]. Subsequent showering and hadronization effects were simulated using Pythia [97]. Detector effects were simulated using PGS with the isolation algorithm for muons and taus modified to more accurately reflect the procedure used by the CMS collaboration. In particular, we introduce a new output variable called trkiso for each muon or tau. The variable trkiso is defined to be the sum p_T of all tracks, ECAL, and HCAL deposits within an annulus of inner radius 0.03 and outer radius 0.3 in ΔR surrounding a given muon or tau. Isolation requires that for each muon or tau, trkiso/p_T of the muon or tau be less than 0.15. The efficiencies of PGS detector effects were normalized by simulating the mSUGRA benchmark studied in [91] and comparing the signal in 3ℓ and 4ℓ channels. To match efficiencies with the CMS study we applied an efficiency correction of 0.87 per lepton to our signal events. As discussed earlier, we applied preselection and analysis cuts in accordance with those

in [91].

5.2 Multi-Lepton Signals of the Higgs

The results of the analysis at $5\,\mathrm{fb}^{-1}$ are presented in Tables 5.2 and 5.3. Table 5.2 contains the observed and expected Standard Model background and expected signal events for the Standard Model $m_h = 125\,\mathrm{GeV}$ Higgs boson at $5\,\mathrm{fb}^{-1}$, broken down into the channels discussed earlier. The channels that provide the most stringent limits on Standard Model Higgs production are marked with a (†). Which channels provide the best limits is a sensitive balance of both signal and background.

In the 4ℓ final states, the strongest constraints on a Standard Model Higgs arise from the [MET high, H_T low] channel and from the two [MET low, H_T low] channels, both with Z and without Z. That these latter two channels provide a constraint on Higgs production is not surprising; here the signal is dominated by $h \to ZZ^* \to 4\ell$ (where the h is produced via ggF or VBF) and the same channels are used in the conventional gold-plated resonant $h \to 4\ell$ Higgs search. However, it bears emphasizing that this existing search is sensitive only to resonant production of the four-lepton final state, while in fact these two channels are populated both by resonant and non-resonant signal events. Here "resonant" is taken to mean that $m_{4\ell}$ is within ± 5 GeV of the Higgs mass. In contrast, non-resonant events receive significant contributions from, e.g., $h \to ZZ^* \to 2\ell 2\tau$.

The remaining sensitive 4ℓ channel, [MET high, H_T low], is dominated by an entirely different process, Zh associated production with $h \to WW^*$. At low masses the branching fraction $h \to WW^*$ drops off, but is largely compensated for by a rise in $h \to \tau^+\tau^-$ with both τs decaying leptonically. Additional contributions to the Higgs signal in this channel come from $t\bar{t}h$ associated production with $h \to WW^*$; these events tend to have high H_T , but a significant fraction fall below the H_T cut.

In the 3ℓ final states, the most stringent limits come from [MET all, H_T low, DY0]; [MET all, H_T high, DY0]; and [MET high, H_T low, DY1 no Z]. For both low-H_T channels the primary contribution to signal comes from associated Wh production

				Observed	Expected	SM Higgs Signal
4 Leptons						
†MET HIGH	HT HIGH	No Z		0	0.018 ± 0.005	0.03
†MET HIGH	HT HIGH	Z		0	0.22 ± 0.05	0.01
†MET HIGH	HT LOW	No Z		1	0.20 ± 0.07	0.06
†MET HIGH	HT LOW	Z		1	0.79 ± 0.21	0.22
†MET LOW	HT HIGH	No Z		0	0.006 ± 0.001	0.01
†MET LOW	HT HIGH	Z		1	0.83 ± 0.33	0.01
†MET LOW	HT LOW	No Z		1	2.6 ± 1.1	0.36
†MET LOW	HT LOW	Z		33	37 ± 15	1.2
3 Leptons						
†MET HIGH	HT HIGH	DY0		2	1.5 ± 0.5	0.15
†MET HIGH	HT LOW	DY0		7	6.6 ± 2.3	0.67
†MET LOW	HT HIGH	DY0		1	1.2 ± 0.7	0.04
†MET LOW	HT LOW	DY0		14	11.7 ± 3.6	0.63
†MET HIGH	HT HIGH	DY1	No Z	8	5.0 ± 1.3	0.38
†MET HIGH	HT HIGH	DY1	Z	20	18.9 ± 6.4	0.19
†MET HIGH	HT LOW	DY1	No Z	30	27.0 ± 7.6	1.8
MET HIGH	HT LOW	DY1	Z	141	134 ± 50	1.6
†MET LOW	HT HIGH	DY1	No Z	11	4.5 ± 1.5	0.13
†MET LOW	HT HIGH	DY1	Z	15	19.2 ± 4.8	0.09
MET LOW	HT LOW	DY1	No Z	123	144 ± 36	1.8
MET LOW	HT LOW	DY1	Z	657	764 ± 183	4.3

Table 5.2: Observed and expected number of events in various exclusive multi-lepton channels from the CMS multi-lepton search with 5 fb^{-1} of 7 TeV proton-proton collisions [67], along with expected number of Standard Model Higgs boson signal events for $m_h = 125$ GeV after acceptance and efficiency. HIGH and LOW for MET and HT indicate $\not{E}_T \gtrless 50$ GeV and $H_T \gtrless 200$ GeV respectively. DY0 $\equiv \ell'^{\pm}\ell^{\mp}\ell^{\mp}$, DY1 $\equiv \ell^{\pm}\ell^{+}\ell^{-}, \ell'^{\pm}\ell^{+}\ell^{-}$, for $\ell = e, \mu$. No Z and Z indicate $|m_{\ell\ell} - m_Z| \gtrless 15$ GeV for any opposite sign same flavor pair. The channels with moderate to good sensitivity to multi-lepton Higgs boson signals are indicated with daggers.

with $h \to WW^*$. However, as with the 4ℓ events, an additional contribution arises from associated $t\bar{t}h$ production with $h \to WW^*$ that falls below the H_T cut. Likewise, the [MET all, H_T high, DY0] channel is dominated by $t\bar{t}h$ with $h \to WW^*$. In all cases, the decrease in $h \to WW^*$ at low masses is compensated by a rise in $h \to \tau^+\tau^-$.

Although limits may be placed on Higgs production due to any individual channel in the multi-lepton search, the greatest sensitivity comes from combining all channels. Table 5.3 contains the observed and expected 95% CL limits from the CMS multi-lepton search with $5\,\text{fb}^{-1}$ of 7 TeV proton-proton collisions on the Higgs boson production cross section times branching ratio in multiples of that for Standard Model Higgs multi-lepton production and decay topologies listed in Table 5.1 with Standard Model branching ratios. We differentiate between the limits set by all contributions (including the resonant $h \to 4\ell$ final states present in the existing golden channel search) and those set by purely non-resonant contributions unique to the multi-lepton search. Notably, the current search strategy may already limit cross sections on the order of a few times the Standard Model value.

m_h	120 GeV	125 GeV	130 GeV
Observed	5.4	4.9	3.5
Expected	4.2	3.8	2.8

Table 5.3: Observed and expected 95% CL limits from the CMS multi-lepton search with 5 fb^{-1} of 7 TeV proton-proton collisions [67] on the Higgs boson production cross section times branching ratio in multiples of that for Standard Model Higgs multi-lepton production and decay topologies listed in Table 5.1with Standard Model branching ratios. Limits are obtained from an exclusive combination of the observed and expected number of events in all the multi-lepton channels presented in Table 5.2.

We emphasize that although the multi-lepton search may not appear to be as sensitive to the Standard Model Higgs boson as some of the current search strategies being pursued at ATLAS and CMS, the sensitivity shown in Table 5.3 corresponds to the current multi-lepton search strategy without any further optimization for a Higgs search. Sensitivity may readily be improved by further tailoring cuts, as we will discuss next.

5.3 Towards a Dedicated Multi-Lepton Higgs Search

We have seen that the existing CMS multi-lepton search strategy has considerable sensitivity to the Standard Model Higgs and its variants, with the potential to exclude production cross sections of a few times the Standard Model value in the light mass window without specific tailoring to the Higgs signal. However, significant improvements in sensitivity may be achieved by refining the search strategy for a dedicated Higgs multi-lepton combination.

Among the 4ℓ channels with highest sensitivity to the Higgs, the [MET low, H_T low, Z / no Z] channels are already fairly optimized for the Higgs; they receive principal contributions from the $h \to ZZ^* \to 4\ell$ golden mode as well as the $h \to Z^*Z^* \to 4\ell$ mode. The same is true of the [MET high, H_T low] channel dominated by Zh associated production with $h \to WW^*$. We emphasize, though, that the sensitivity of these channels to nonresonant 4ℓ production may give an appreciable advantage over the conventional golden mode search.

However, it is also important to emphasize the role of $t\bar{t}h$ associated production in potential 4ℓ signals. In particular, $t\bar{t}h$ associated production with $h \to WW^*$ contributes significantly to the 4ℓ [MET high, H_T low] channel without the presence of a Z boson. Dividing the 4ℓ [MET high, H_T low] channel into two channels, with and without Z, would help to reduce backgrounds for this signal. Furthermore, these final states include two b quarks from the decays of the tops. Since the primary background in this channel is from di-Z production where one Z is off-shell for which there are no b quarks in the final state further discrimination may be obtained by requiring one or two b-tags in the final state. Requiring b-tags should also increase the sensitivity of other channels that receive a significant contribution from $t\bar{t}h$, particularly [MET all, H_T high]. While this channel is not the most sensitive of the 4ℓ channels, further reduction of the Standard Model background expectation perhaps by b-tags and the addition of a Z veto may render it more useful. It should be emphasized, of course, that requiring b-tags in channels sensitive to $t\bar{t}h$ will not completely erase the Standard Model background expectation. In addition to di-Z contributions to these channels,

there may be considerable backgrounds from $t\bar{t}\gamma^*$ that are not accounted for in the current CMS search. These backgrounds would survive b-tag requirements, and should be carefully accounted for in a dedicated search.

Similar improvement may be attained by requiring one or two b-tags in the 3ℓ [MET all, H_T high, DY0] and [MET all, H_T high, DY1] channels, which are likewise dominated by $t\bar{t}h$. The remaining sensitive 3ℓ channels receive signals primarily from associated Wh production with $h \to WW^*$, for which the existing cuts are adequately optimized.

Finally, we note that many of the sensitive search channels in both 3ℓ and 4ℓ final states receive significant contributions from Wh, Zh, and $t\bar{t}h$ associated production with $h \to \tau^+\tau^-$, particularly for low Higgs masses ($m_h \sim 130\,\text{GeV}$). These decays contribute directly to existing search channels when one or both of the τ's decay leptonically. However, some sensitivity is lost since the τ leptonic branching fraction is only 35%. Since it is possible to tag hadronically-decaying τ's with some degree of accuracy, sensitivity to associated production may be improved by adding channels for exclusive final states with, e.g., two leptons and one or two hadronic τ's.

5.4 Going Forward

In this chapter we have evaluated the possibility of augmenting existing LHC searches for the Higgs via the combination of channels with multiple non-resonant leptons. The total multi-lepton Higgs signal in these channels exceeds the gold-plated 4ℓ resonant mode, though it is spread over various 3ℓ and 4ℓ final states. The exclusive combination of these channels using the existing CMS multi-lepton search strategy yields a sensitivity competitive with other discovery-level searches for the Higgs boson, both for the Standard Model Higgs and for variants with enhanced branching ratios to leptons and gauge bosons. Refinements focused specifically on the Higgs boson signal, such as b-tags in channels involving $t\bar{t}h$ associated production, would provide even more sensitivity. The extensive study of Standard Model backgrounds in current multi-lepton searches suggest that an effective multi-lepton search for the Higgs could be implemented fairly quickly.

Although we have focused in this paper on the sensitivity of a multi-lepton search for a single Higgs doublet, we emphasize that there may be even greater discovery potential for an extended Higgs sector with an enhanced total multi-lepton cross section, which study in the next chapter. The advantage of a multi-lepton search lies in its exclusive combination of multiple leptonic final states, both resonant and nonresonant alike. As such, it is sensitive to simultaneous contributions from more than one new state with appreciable leptonic decays. For example, in a two-Higgs doublet model the multi-lepton signals of the lightest neutral Higgs h are augmented by new production and decay channels from the heavier neutral Higgs H, the pseudoscalar A, and the charged Higgses $H^{\pm}$. Processes such as $gg \to H \to hh \to WW^*WW^*$ and $gg \to A \to Zh \to ZWW^*$ contribute significantly to both 3ℓ and 4ℓ final states. Moreover, in such models the cross section for specific resonant final states such as $h \to \gamma\gamma$ and $h \to ZZ^* \to 4\ell$ may be suppressed relative to the Standard Model expectation, reducing the effectiveness of existing resonant searches. Should the Higgs sector prove to be extended beyond a single electroweak doublet, a dedicated multi-lepton Higgs search may provide the most promising avenue for discovery.

Chapter 6

Extended Higgs Sectors at the LHC

Beyond the search for the Standard Model Higgs [59, 60], the LHC has a more general primary objective of probing the mechanism of electroweak symmetry breaking (EWSB) in detail. The goal, therefore extends much more broadly to include the search for additional Higgs states that could be a window into the underlying physics of EWSB.

Two Higgs doublet models (2HDMs) offer a canonical framework for extended electroweak symmetry breaking. Indeed, in many extensions of the minimal Standard Model (SM), supersymmetric or otherwise, the Higgs sector is extended to two scalar doublets [61]. It is therefore worthwhile to study the generic features of the 2HDM scenario independent of the specific underlying model, purely as an effective theory for extended EWSB. The phenomenology of 2HDMs is rich, as five physical Higgs sector particles remain after EWSB: two neutral CP-even scalars, h, H; one neutral CP-odd pseudoscalar, A; and two charged scalars, H^+ and H^-. All of these states could have masses at or below the TeV scale, in a regime accessible to the LHC. The parameter space of the 2HDM scenario is large enough to accommodate a wide diversity of modifications to the production and decay modes of the lightest Higgs boson, as well as to provide non-negligible production mechanisms for the heavier Higgs states that may decay directly to SM final states, or through cascades that yield multiple Higgs states.

Much of the study of 2HDM phenomenology to date has been devoted to the specific setup that arises in minimal supersymmetric models [62], which occupies a restricted subset of possible 2HDM signals. Even more general 2HDM studies [63–65] have largely focused on the direct production and decays of scalars in SM-like channels, or on specific cascade decays between scalars. In this work, we wish to pursue a more inclusive objective: the sensitivity of the LHC to the sum total of production and decay modes

available in a given 2HDM, including both direct decays of scalars and all kinematically available scalar cascades. Such an approach exploits the large multiplicity of signals arising from production and decay of the various states in an extended EWSB sector.

Searches for final states involving three or more leptons are well matched to this objective, since both direct scalar decays and scalar cascades populate multi-lepton final states with low Standard Model backgrounds. The CMS multi-lepton search strategy [66, 67] is particularly well-suited in this respect, since its power lies in the combination of numerous exclusive channels. While the sensitivity to new physics in any individual channel alone is not necessarily significant, the exclusive combination across multiple channels can provide considerable sensitivity. This is particularly effective in the search for extended EWSB sectors such as 2HDMs, where multi-lepton final states may arise from many different production and decay processes that would evade detection by searches narrowly focused on kinematics or resonantly-produced final states of specific topologies. With a potentially sizable multiplicity of rare multi-lepton signatures, an extended Higgs sector therefore provides an excellent case study for the sort of new physics that could first be discovered in an exclusive multi-channel multi-lepton search at the LHC.

Multi-lepton searches are already sensitive to Standard Model Higgs production [68], as well as the production of a SM-like Higgs in rare decay modes of states with large production cross sections [69]. This suggests that these studies may be particularly amenable to searching for evidence of extended Higgs sectors. Theories with two Higgs doublets enjoy all of the multi-lepton final states available to the Standard Model Higgs, albeit with modified cross sections, as well as the multi-lepton final states of additional scalars and cascade decays between scalars that often feature on-shell W and Z bosons in the final state. These additional particles give rise to numerous new production mechanisms for multi-lepton final states.

The goal of this paper is to perform a detailed survey of the multi-lepton signals that arise in some representative 2HDM parameter spaces. In particular, we will consider four different CP- and flavor-conserving 2HDM benchmark mass spectra that have qualitatively distinct production and decay channels. For each mass spectrum, we will

consider each of the four discrete types of 2HDM tree-level Yukawa couplings between the Higgs doublets and the SM fermions that are guaranteed to be free of tree-level flavor changing neutral currents (FCNCs). A study of the sensitivity to the myriad rare production and decay processes over a grid of points in the parameter spaces defining these sixteen representative 2HDMs using standard simulation techniques, while in principle straightforward, is computationally prohibitive.

So instead we employ a factorized mapping procedure to go between model parameters and signatures [70]. In this procedure the acceptance times efficiency for each individual production and decay topology is independently determined from monte carlo simulation, assuming unit values for all branching ratios in the decay topology. The production cross section and branching ratios are then calculated externally as functions of model parameters. The total cross section times branching ratio into any given final state at any point in parameter space is then given by a sum over the production cross section times acceptance and efficiency for each topology times a product of the branching ratios at that parameter space point. For the study here, we simulate the acceptance times efficiency in 20 exclusive multi-lepton channels for 222 independent production and decay topologies that arise in the four benchmark 2HDM spectra. For each benchmark spectrum we combine the 20 exclusive multi-lepton channels to obtain an overall sensitivity as a function of two-dimensional mixing angle parameter spaces that characterize each of the four discrete types of flavor conserving 2HDMs. With this, we identify regions of 2HDM parameter space that are excluded by the existing CMS multi-lepton search [67], as well as those regions where future multi-lepton searches at the LHC will have sensitivity.

Beyond requiring CP-conservation and no direct tree-level flavor violation in the Higgs sector, we will not address constraints imposed by low energy precision flavor measurements on the parameter space of 2HDMs (see [64] and references therein, and [71] for a very recent analysis). In general, contributions to loop-induced flavor changing processes, such as $B \to X_s\gamma$, may be reduced by destructive interference among different loops, so that new physics outside of our low-energy effective theory can relax flavor bounds on the 2HDM sector. Additionally, with the assumptions employed

here, flavor constraints are driven by the mass of the charged Higgs, which typically does not play a significant role in the production of multi-lepton final states. For the benchmark spectra we consider, the charged Higgs may generally be decoupled in mass without substantially altering the phenomenology. More generally, we emphasize that our benchmark spectra are intended to qualitatively illustrate the relevant topologies for producing multi-lepton final states. Various scalar masses may be raised to accommodate flavor physics without changing the qualitative multi-lepton signatures, though of course particular numeric limits will be altered.

The outline of this chapter is as follows: In Section 6.1, we will briefly review the relevant aspects of 2HDMs and define the parameter space within which we will conduct our survey. In Section 6.2, we will give an overview of the most interesting production and decay channels for 2HDM collider phenomenology which result in multi-lepton final states. Additionally, we select benchmark spectra in Section 6.3 that have a representative set of multi-lepton production and decay topologies. Section 6.4 is devoted to summarizing the multi-lepton search strategy and the simulation methods we use. The results of our study are displayed in Section 6.5 where we identify the regions of parameter space that are excluded on the basis of the existing CMS multi-lepton search with 5 fb^{-1} of 7 TeV proton-proton collisions [67] as well as those regions to which future searches will have sensitivity. In Section 6.6 we suggest some refinements to future multi-lepton searches that could enhance the sensitivity to extended Higgs sectors.

6.1 Parameterizing the Space of Two-Higgs Doublet Models

The physically relevant parameter space specifying the most general 2HDM is large (for a review of general 2HDMs see, for example, [63] and [64]). The goal here is not to consider the most general theory, but rather to define a manageable parameter space in which to characterize multi-lepton signals. The couplings of physical Higgs states that are relevant to the production and decay topologies considered below include those of a single Higgs boson to two fermions or two gauge bosons, couplings of two Higgs bosons to a single gauge boson, and couplings of three Higgs bosons. Other higher multiplicity

couplings do not appear in the simplest topologies.

For simplicity we consider CP-conserving 2HDMs that are automatically free of tree-level flavor changing neutral currents. With these assumptions, the renormalizable couplings of a single physical Higgs boson to pairs of fermions or gauge bosons, and of two Higgs bosons to a gauge boson, are completely specified in terms of two mixing angles, as detailed below. With a mild restriction to renormalizable potentials of a certain class described below, couplings involving three Higgs bosons are specified in terms of Higgs masses and these same mixing angles.

The absence of tree-level flavor changing neutral currents in multi-Higgs theories is guaranteed by the Glashow-Weinberg condition [72] which postulates that all fermions of a given gauge representation receive mass through renormalizable Yukawa couplings to a single Higgs doublet. With this condition, tree-level couplings of neutral Higgs bosons are diagonal in the mass basis. In the case of two Higgs doublets with Yukawa couplings

$$-V_{\text{yukawa}} = \sum_{i=1,2} \left(q\tilde{h}_i y_i^u \bar{u} + q h_i y_i^d \bar{d} + \ell h_i y_i^e \bar{e} + \text{ h.c. } \right) \tag{6.1}$$

where $y_i^{u,d,e}$ are 3×3 flavor matrices and $\tilde{h}_i \equiv i\sigma_2 h_i$ and our conventions are such that the two $SU(2)_L$ doublets H_1 and H_2 both have positive hypercharge. The Glashow-Weinberg condition is satisfied by precisely four discrete types of 2HDMs distinguished by the possible assignments of fermion couplings with either $y_1^F = 0$ or $y_2^F = 0$ for each of $F = u, d, e$. This requirement can be imposed through a $\mathbf{Z}_2$ symmetry under which one of the Higgs doublets is odd, and the quarks and leptons are assigned charges to ensure that the desired terms in Eq. 6.1 survive. Under this restriction, we can always denote the Higgs doublet that couples to the up-type quarks as H_u. Having fixed this, we have two binary choices for whether the down-type quarks and the leptons in (6.1) couple to H_u or H_d. Of these four possibilities, "Type I" is commonly referred to as the fermi-phobic Higgs model in the limit of zero mixing, as all fermions couple to one doublet and the scalar modes of the second doublet couple to vector bosons only. "Type II" is MSSM-like, since this is the only choice of charge assignments consistent

with a holomorphic superpotential. "Type III" is often referred to as "lepton-specific," since it assigns one Higgs doublet solely to leptons. Finally, "Type IV" is also known as "flipped," since the leptons have a "flipped" coupling relative to Type II. These possible couplings are illustrated in Table 6.1. We will restrict ourselves to these four choices as they exhaust all possibilities where tree-level FCNCs are automatically forbidden.

	2HDM I	2HDM II	2HDM III	2HDM IV
u	H_u	H_u	H_u	H_u
d	H_u	H_d	H_u	H_d
e	H_u	H_d	H_d	H_u

Table 6.1: The four discrete types of 2HDM H_u and H_d Yukawa couplings to right-handed quarks and leptons that satisfy the Glashow-Weinberg condition. By convention H_u is taken to couple to right handed up-type quarks, and the assignments of the remaining couplings are indicated.

For any of the CP-conserving 2HDMs satisfying the Glashow-Weinberg condition, the coefficient of the couplings of a single physical Higgs boson to fermion pairs through the Yukawa couplings in Eq. 6.1 depend on the fermion mass, the ratio of the Higgs expectation values, conventionally defined as $\tan\beta \equiv \langle H_u\rangle/\langle H_d\rangle$, and the mixing angle α that diagonalizes the 2×2 neutral scalar $h-H$ mass squared matrix. The parametric dependences of these couplings on α and β relative to coupling of the Standard Model Higgs boson with a single Higgs doublet are given in Table 6.2. The parametric dependence of the couplings of the charged scalar, $H^{\pm}$, are the same as those of the pseudo-scalar, A.

The renormalizable couplings of a single physical Higgs boson to two gauge bosons are fixed by gauge invariance in terms of the mixing angles in any CP-conserving 2HDM as

$$g_{hVV} = \sin(\beta-\alpha)g_V \qquad g_{HVV} = \cos(\beta-\alpha)g_V$$
$$g_{AVV} = 0 \qquad g_{H^{\pm}W^{\mp}Z} = 0 \tag{6.2}$$

where for $V = W, Z$ the Standard Model Higgs couplings are $g_W = g$ and $g_Z = g/\cos\theta_W$, where g is the $SU(2)_L$ gauge coupling and θ_W the weak mixing angle. The

renormalizable couplings of two physical Higgs bosons to a single gauge boson are likewise fixed in any CP-conserving 2HDM as

$$g_{hZA} = \frac{1}{2} g_Z \cos(\beta - \alpha) \qquad g_{HZA} = -\frac{1}{2} g_Z \sin(\beta - \alpha)$$

$$g_{hW^\mp H^\pm} = \mp \frac{i}{2} g \cos(\beta - \alpha) \qquad g_{HW^\mp H^\pm} = \pm \frac{i}{2} g \sin(\beta - \alpha)$$

$$g_{AW^\mp H^\pm} = \frac{1}{2} g \tag{6.3}$$

None of these couplings involve additional assumptions about the form of the full non-renormalizable scalar potential, beyond CP conservation.

This is in contrast with (CP and flavor conserving) multi-Higgs theories for which the tree-level couplings to Standard Model fermions and massive gauge bosons are in general all independent. Thus the general tree-level couplings of CP-conserving 2HDMs satisfying the Glashow-Weinberg condition are restricted to particular two-dimensional sub-spaces of the general four-dimensional space of Higgs couplings to the Standard Model fermions and massive gauge bosons. This is also to be contrasted with the single Higgs theory with general non-renormalizable couplings, in which the coupling to every Standard Model state is independent and deviations from renormalizable couplings are parameterized by non-renormalizable operators.

The couplings between three physical Higgs bosons depends on details of the Higgs scalar potential. Specifying these therefore requires additional assumptions to completely specify the branching ratios that appear in some of the decay topologies discussed below. The main goal here is to present multi-lepton sensitivities to 2HDMs in relatively simple, manageable parameter spaces. A straightforward condition that fulfills this requirement is to consider 2HDM Higgs potentials that, in additional to being CP-conserving, are renormalizable and restricted by a (discrete) Peccei-Quinn symmetry that forbids terms with an odd number of H_u or H_d fields. The most general potential of this type is given by

$$\begin{aligned} V_{\text{scalar}} \;=\; & m_u^2 H_u^\dagger H_u + m_d^2 H_d^\dagger H_d + \frac{1}{2}\lambda_1 (H_u^\dagger H_u)^2 + \frac{1}{2}\lambda_2 (H_d^\dagger H_d)^2 + \lambda_3 (H_u^\dagger H_u)(H_d^\dagger H_d) \\ & + \lambda_4 (H_u^\dagger H_d)(H_d^\dagger H_u) + \left[\frac{1}{2}\lambda_5 (H_u^\dagger H_d)^2 + \text{ h.c.} \right] \end{aligned} \tag{6.4}$$

$y_{\rm 2HDM}/y_{\rm SM}$	2HDM I	2HDM II	2HDM III	2HDM IV
hVV	$\sin(\beta-\alpha)$	$\sin(\beta-\alpha)$	$\sin(\beta-\alpha)$	$\sin(\beta-\alpha)$
hQu	$\cos\alpha/\sin\beta$	$\cos\alpha/\sin\beta$	$\cos\alpha/\sin\beta$	$\cos\alpha/\sin\beta$
hQd	$\cos\alpha/\sin\beta$	$-\sin\alpha/\cos\beta$	$\cos\alpha/\sin\beta$	$-\sin\alpha/\cos\beta$
hLe	$\cos\alpha/\sin\beta$	$-\sin\alpha/\cos\beta$	$-\sin\alpha/\cos\beta$	$\cos\alpha/\sin\beta$
HVV	$\cos(\beta-\alpha)$	$\cos(\beta-\alpha)$	$\cos(\beta-\alpha)$	$\cos(\beta-\alpha)$
HQu	$\sin\alpha/\sin\beta$	$\sin\alpha/\sin\beta$	$\sin\alpha/\sin\beta$	$\sin\alpha/\sin\beta$
HQd	$\sin\alpha/\sin\beta$	$\cos\alpha/\cos\beta$	$\sin\alpha/\sin\beta$	$\cos\alpha/\cos\beta$
HLe	$\sin\alpha/\sin\beta$	$\cos\alpha/\cos\beta$	$\cos\alpha/\cos\beta$	$\sin\alpha/\sin\beta$
AVV	0	0	0	0
AQu	$\cot\beta$	$\cot\beta$	$\cot\beta$	$\cot\beta$
AQd	$-\cot\beta$	$\tan\beta$	$-\cot\beta$	$\tan\beta$
ALe	$-\cot\beta$	$\tan\beta$	$\tan\beta$	$-\cot\beta$

Table 6.2: Tree-level couplings of the neutral Higgs bosons to up- and down-type quarks, leptons, and massive gauge bosons in the four types of 2HDM models relative to the SM Higgs boson couplings as functions of α and β. The coefficients of the couplings of the charged scalar $H^{\pm}$, are the same as those of the pseudo-scalar, A

This potential has seven free parameters, which may be exchanged for the overall Higgs expectation value, the four physical masses m_h, m_H, m_A, and $m_{H^{\pm}}$, and the two mixing angles, α and β. So all the Higgs boson couplings in a renormalizable 2HDM with the potential in Eq. 6.4 are, for a given mass spectrum, specified entirely in terms of the mixing angles α and β. The couplings of three physical Higgs bosons from the potential in Eq. 6.4 that are relevant to the production and decay topologies studied below are

$$\begin{aligned} g_{HH^+H^-} &= \frac{1}{v}\left(m_H^2\left(\cos\beta\cot\beta\sin\alpha+\sin\beta\tan\beta\cos\alpha\right)+2m_{H^{\pm}}^2\cos(\beta-\alpha)\right) \\ g_{HAA} &= \frac{1}{v}\left(m_H^2\left(\cos\beta\cot\beta\sin\alpha+\sin\beta\tan\beta\cos\alpha\right)+2m_A^2\cos(\beta-\alpha)\right) \\ g_{Hhh} &= \frac{1}{v}(m_H^2+2m_h^2)\cos(\beta-\alpha)(\sin 2\alpha/\sin 2\beta) \end{aligned} \tag{6.5}$$

We emphasize that the choice of the potential given by Eq. 6.4 is illustrative to allow a simple presentation in terms of a two-dimensional parameter space of mixing angles for a given physical spectrum. Although there is additional parametric freedom available in the most general CP-conserving 2HDM potential, the phenomenology is qualitatively similar. The only important generalization in the production and decay topologies studied below for the most general CP- and flavor-conserving 2HDMs as compared

with the assumptions outlined here is that the partial decay widths of the CP-even heavy Higgs boson, H, to pairs of lighter Higgs bosons become free parameters, rather than being specified in terms of α and β through the couplings in Eq. 6.5.

6.2 Multi-lepton Signals of Two Higgs Doublet Models

The wide range of possibilities for Higgs boson mass spectrum hierarchies and branching ratios in 2HDMs yields a diversity of production and decay channels that are relevant for multi-lepton signatures at the LHC. Multi-lepton final states become especially important when the decay of one Higgs scalar to a pair of Higgs scalars or a Higgs scalar and a vector boson is possible. Of course, the availability of these inter-scalar decays comes at a price, as the decaying Higgs must be sufficiently heavy for the decay modes to be kinematically open, so that the production cross section is reduced. Performing a full multi-dimensional scan of the mass spectra of 2HDMs is not only computationally untenable, but also unnecessary for our purposes; most of the salient features may be illustrated by exploring a few benchmark scenarios in which all the relevant types of cascade decays are realized. We will focus on four such mass spectra with various orderings of the scalar mass spectrum, fixing the lightest CP-even Higgs mass at 125 GeV in each case.

The various 2HDM production and decay topologies that give rise to multi-lepton signatures fall into two broad categories: those resulting from the direct production and decay of an individual scalar, and those resulting from cascades involving more than one scalar. The first category includes the resonant four-lepton signals of the Standard Model-like Higgs h, from gluon fusion and vector boson fusion production followed by $h \to ZZ^*$ with $Z^{(*)} \to \ell\ell$. Other resonant and non-resonant multi-lepton signals arise from quark–anti-quark fusion production of Wh, Zh, along with tth associated production with $t \to Wb$, all followed by $h \to WW^*, ZZ^*, \tau\tau$ with leptonic decays of (some of the) $W \to \ell\nu$, $Z^{(*)} \to \ell\ell$ and $\tau \to \ell\nu\nu$. These modes were studied in depth in [68] to obtain multi-lepton limits on the Standard Model Higgs and simple variations. The same modes of production and decay are available to the heavy CP-even scalar, H, albeit with reduced production cross sections due to its larger mass and mixing

suppression of some of its couplings.

While the branching fractions of these modes depend on the parameters of the theory, their existence is robust and common to all benchmark spectra we consider. In contrast, the sole multi-lepton mode involving direct production of the pseudoscalar, A, without cascade decays through other scalars is ttA associated production followed by $t \to Wb$ and $A \to \tau\tau$ with leptonic decays of (some of the) $W \to \ell\nu$ and $\tau \to \ell\nu\nu$. And there are no multi-lepton signals resulting from direct production of the charged Higgs, $H^{\pm}$, without cascade decays through other scalars.

Scalar cascades add a variety of new multi-lepton processes, including production and decay modes that contribute to some of the same final states that arise from a Standard Model Higgs boson. Processes of this type include gluon fusion production of A with $A \to Zh$, ZH followed by $h, H \to WW^*$, ZZ^*, $\tau\tau$ with (some of the) $W \to \ell\nu$, $Z^{(*)} \to \ell\ell$, and $\tau \to \ell\nu\nu$. Another example of this type is gluon fusion and vector boson fusion production of H with $H \to AA$, hh followed by $A \to \tau\tau$ or $h \to bb$, WW^*, ZZ^*, $\tau\tau$ with (some of the) $W \to \ell\nu$, $Z^{(*)} \to \ell\ell$ and $\tau \to \ell\nu\nu$. With only a single Higgs doublet, direct Standard Model di-Higgs production is a very rare process, but resonant heavy Higgs production and decay into these final states can be up to two orders of magnitude larger in 2HDMs.

Scalar cascade decays of the heavy Higgs scalar, H, can also contribute to entirely new multi-lepton final states that do not arise with a single Higgs doublet. These include gluon fusion and vector boson fusion production of H with $H \to AA$, H^+H^-, ZA, $WH^{\pm}$ with $A \to bb, Zh, \tau\tau$, and $H^{\pm} \to tb$, $\tau\nu$, Wh with $t \to Wb$ followed by $h \to bb$, WW^*, ZZ^*, $\tau\tau$ with (some of the) $W \to \ell\nu$, $Z^{(*)} \to \ell\ell$ and $\tau \to \ell\nu\nu$. These processes can give final states with up to six W and/or Z bosons. Similar processes in this same category include gluon fusion production of A with $A \to ZH$ followed by $H \to hh$ with $h \to bb, WW^*, ZZ^*, \tau\tau$ with (some of the) $W \to \ell\nu$, $Z^{(*)} \to \ell\ell$ and $\tau \to \ell\nu\nu$. These processes can give final states with up to five W and/or Z bosons.

Direct di-Higgs production of non-Standard Model-like Higgs bosons either with or without scalar cascade decay processes can also give rise to multi-lepton final states that do not arise with a single Higgs doublet. These include quark–anti-quark fusion

production of $Ah, AH, H^{\pm}A$ followed by $H \to WW^*$, ZZ^*, $\tau\tau$, AA, and $H^{\pm} \to tb$, $\tau\nu$, Wh, WA with $t \to Wb$, and $A \to bb$, $\tau\tau$, all with $h, H \to WW^*$, ZZ^*, $\tau\tau$ with (some of the) $W \to \ell\nu$, $Z^{(*)} \to \ell\ell$ and $\tau \to \ell\nu\nu$. The existence of some of these processes is sensitive to mass hierarchies in the Higgs spectrum; other production and decay processes of this type can arise depending on mass orderings.

Additional multi-lepton final states not associated with a single Higgs doublet can arise from production of non-Standard Model-like Higgs bosons in association with top quarks. These include ttH, ttA, and $tbH^{\pm}$ associated production with $t \to Wb$ followed by $H \to AA$, and $H^{\pm} \to Wh$, WA, and $A \to Zh$, bb, $\tau\tau$, all with $h, H \to WW^*$, ZZ^*, $\tau\tau$ with (some of the) $W \to \ell\nu$, $Z^{(*)} \to \ell\ell$ and $\tau \to \ell\nu\nu$. While the production and decay processes listed here and above do not completely exhaust all possibilities for contributions to multi-lepton signatures in every conceivable 2HDM mass spectrum, they do include the leading topologies for a very wide range of mass hierarchies.

6.3 Benchmark Spectra

All of the production and decay processes outlined above are represented in one or more of the benchmark Higgs mass spectra described below. The value of the scalar masses chosen for each benchmark spectrum are shown in Table 6.3. In the benchmark spectra 1-3, for simplicity the pseudoscalar and the charged Higgs are taken to form an isotriplet with degenerate masses. In spectrum 4, this simplifying assumption is relaxed, with the pseudoscalar Higgs taken to be the lightest scalar. For all four 2HDM spectra, the light, CP-even scalar, h, has no available decay modes beyond those of a Standard Model Higgs boson, although the branching fractions may significantly differ from the SM values.

The simplest benchmark spectrum is that with all the heavy non-Standard Model like Higgs bosons decoupled. In this case the remaining Standard Model Higgs boson can be produced in gluon fusion, vector boson fusion, and in assocation with vector bosons and top quarks, and it can decay to $h \to WW^*, ZZ^*, \tau\tau$. The leading topologies that contribute to multi-lepton signatures from these production and decay channels are

	SM (GeV)	Spectrum 1 (GeV)	Spectrum 2 (GeV)	Spectrum 3 (GeV)	Spectrum 4 (GeV)
h	125	125	125	125	125
H	–	300	140	500	200
A	–	500	250	230	80
$H^{\pm}$	–	500	250	230	250

Table 6.3: Higgs boson masses in the SM Benchmark and our four 2HDM Benchmark Spectra.

given in Table 6.4. These topologies are associated to the Standard Model-like Higgs boson in all 2HDMs. The important additional production and decay channels that contribute to multi-lepton signatures (beyond those of the Standard Model-like Higgs boson) in each of our four 2HDM benchmark spectra are as follows:

Benchmark spectrum 1: The heavy neutral Higgs, H, is produced mainly through gluon fusion and vector boson fusion, and can decay through the same channels as a heavy Standard Model Higgs, plus the new kinematically allowed decay $H \to hh$. The pseudoscalar, A, is produced mainly through gluon fusion and can decay by $A \to Zh, ZH$. The charged Higgs, $H^{\pm}$, does not play an important role in this spectrum. The complete list of topologies that contribute to multi-lepton signatures from these production and decay channels, along with those from the Standard Model-like Higgs boson, are given in Table 6.5.

Benchmark spectrum 2: This spectrum is qualitatively similar to the first, but with $H \to hh$ no longer kinematically allowed. Production of the Heavy Higgs, H, can proceed through gluon fusion, vector boson fusion, and in association with vector bosons and top quarks, with decays to Standard Model channels. Production of the pseudoscalar, A, through gluon fusion production and in association with top quarks with $A \to Zh$, ZH, $\tau\tau$ is much greater than in spectrum 1 due to the lower A mass. The charged Higgs, $H^{\pm}$, can also be produced in association with a top quark, and can decay by $H^{\pm} \to Wh$. The complete list of topologies that contribute to multi-lepton signatures from these production and decay channels, along with those from the Standard Model-like Higgs boson, are given in Table 6.6.

Benchmark spectrum 3: This spectrum is the most rich in the multiplicity of multi-lepton final states, as the decay channels $H \to hh$, AA, H^+H^-, AZ are all kinematically open, in addition to the Standard Model decay channels. The heavy Higgs, H, can be produced in gluon fusion and vector boson fusion. The pseudoscalar, A, is produced in gluon fusion, as well as from decays f the H, with decays $A \to Zh$, $\tau\tau$. The charged Higgs, $H^\pm$, can be produced in association with a top quark, or from decay of H with decays $H^\pm \to \tau\nu$, Wh. This spectrum includes topologies with sequential cascade decays through up to three Higgs scalars. The complete list of topologies that contribute to multi-lepton signatures from all these production and decay channels, along with those from the Standard Model-like Higgs boson, are given in Table 6.7.

Benchmark spectrum 4: This spectrum breaks the degeneracy between the pseudoscalar, A, and the charged Higgs, $H^\pm$, in order to highlight the role of a light pseudoscalar. Quark–anti-quark fusion production of A with the scalar Higgses, H, h or charged Higgs, $H^\pm$, is significant, with decays $A \to bb$, $\tau\tau$ and $H^\pm \to \tau\nu$, Wh, WA as well as $H \to AA$, in addition to the Standard Model decay channels. The later decay yields a topology with three pseudoscalar Higgses in the final state. The pseudoscalar, A, as well as H and $H^\pm$, can also be produced in association with top quarks. The heavy Higgs, H, can also be produced in gluon fusion and vector boson fusion. The very small partial width for the decay $h \to AA^*$ in this spectrum will be ignored. The complete list of topologies that contribute to multi-lepton signatures from all these production and decay channels, along with those from the Standard Model-like Higgs boson, are given in Table 6.8.

All 233 production and decay topologies listed in Tables 6.4 - 6.8 were individually simulated in our studies of multi-lepton signatures of the Standard Model Higgs and our four 2HDM spectra benchmarks. Certain channels for the 2HDM benchmarks were omitted for the sake of conciseness. In general, channels were omitted if the production cross section times fixed Standard Model branching ratios to multi-lepton final states was much less than 1 fb even in the most promising regions of parameter space. For nominal simplicity, for the 2HDM benchmarks, we omitted associated production channels for h with $h \to ZZ^*$, having found in [68] that with the integrated luminosity

considered here, these channels did not contribute significantly to even low-background search channels. However, with significantly more integrated luminosity these channels would begin to contribute to the sensitivity.

Production	Decay
$gg \to h$	$h \to 4\ell$
VBF $\to h$	$h \to 4\ell$
$q\bar{q} \to Wh$	$Wh \to WWW, WZZ, W\tau\tau$
$q\bar{q} \to Zh$	$Zh \to ZWW, ZZZ, Z\tau\tau$
$t\bar{t}h$	$t\bar{t}h \to t\bar{t}WW, t\bar{t}ZZ, t\bar{t}\tau\tau$

Table 6.4: The 11 independent production and decay topologies simulated for the Standard Model Higgs Boson with $m_h = 125$ GeV. The Higgs boson branching ratios are factored out of each topology. All top-quark, τ-lepton, and W- and Z bosons branching ratios are Standard Model.

Production	Decay
$gg \to h$	$h \to 4\ell$
VBF $\to h$	$h \to 4\ell$
$gg \to H$	$H \to 4\ell$
	$H \to hh \to 4W, WW\tau\tau, 4\tau, ZZb\bar{b}, ZZWW, 4Z, ZZ\tau\tau$
VBF $\to H$	$H \to 4\ell$
	$H \to hh \to 4W, WW\tau\tau, 4\tau, ZZb\bar{b}, ZZWW, 4Z, ZZ\tau\tau$
$gg \to A$	$A \to Zh \to ZWW, Z\tau\tau, ZZZ$
	$A \to ZH \to ZWW, Z\tau\tau, ZZZ$
	$A \to ZH \to Zhh \to ZWWWW, ZWW\tau\tau, Z\tau\tau\tau\tau, ZZZb\bar{b}, ZZZWW, 5Z, ZZZ\tau\tau$
$q\bar{q} \to Wh$	$Wh \to WWW, W\tau\tau$
$q\bar{q} \to Zh$	$Zh \to ZWW, Z\tau\tau$
$t\bar{t}h$	$t\bar{t}h \to t\bar{t}WW, t\bar{t}\tau\tau$

Table 6.5: The 37 independent production and decay topologies simulated for the 2HDM Benchmark Spectrum 1 with $m_h = 125$ GeV, $m_H = 300$ GeV, $m_A = m_{H^\pm} = 500$ GeV. All Higgs boson branching ratios are factored out of each topology. All top-quark, b-quark, τ-lepton, and W- and Z-boson branching ratios are Standard Model.

6.4 Search Strategy and Simulation Tools

In principle, it might be possible to design a multi-lepton search with sensitivity specifically tailored to certain features of the signatures that arise from some of the production and decay topologies of 2HDMs. However, designing such a dedicated search would require a detailed understanding of backgrounds in many channels that is well beyond the

Production	Decay
$gg \to h$	$h \to 4\ell$
VBF $\to h$	$h \to 4\ell$
$gg \to H$	$H \to 4\ell$
VBF $\to H$	$H \to 4\ell$
$gg \to A$	$A \to Zh \to ZWW, Z\tau\tau, ZZZ$
	$A \to ZH \to ZWW, Z\tau\tau, ZZZ$
$q\bar{q} \to Wh$	$Wh \to WWW, W\tau\tau$
$q\bar{q} \to Zh$	$Zh \to ZWW, Z\tau\tau$
$q\bar{q} \to WH$	$WH \to WWW, W\tau\tau$
$q\bar{q} \to ZH$	$ZH \to ZWW, Z\tau\tau$
$t\bar{t}h$	$t\bar{t}h \to t\bar{t}WW, t\bar{t}\tau\tau$
$t\bar{t}H$	$t\bar{t}H \to t\bar{t}WW, t\bar{t}\tau\tau$
$t\bar{t}A$	$t\bar{t}A \to t\bar{t}\tau\tau$
	$t\bar{t}A \to t\bar{t}Zh \to t\bar{t}ZWW, t\bar{t}Z\tau\tau, t\bar{t}Zb\bar{b}, t\bar{t}ZZZ$
	$t\bar{t}A \to t\bar{t}ZH \to t\bar{t}ZWW, t\bar{t}Z\tau\tau, t\bar{t}Zb\bar{b}, t\bar{t}ZZZ$
$tbH^{\pm}$	$tbH^{\pm} \to tbWh \to tbWWW, tbW\tau\tau, tbWZZ$

Table 6.6: The 34 independent production and decay topologies simulated for the 2HDM Benchmark Spectrum 2 with $m_h = 125$ GeV, $m_H = 140$ GeV, $m_A = m_{H^{\pm}} = 250$ GeV. All Higgs boson branching ratios are factored out of each topology. All top-quark, b-quark, τ-lepton, and W- and Z-boson branching ratios are Standard Model.

scope of a theory-level study. Instead, as done previously in a study of the multi-lepton signatures of the Standard Model Higgs boson [68], we will adopt the selection cuts and background estimates of an existing CMS multi-lepton analysis [66, 67] to demonstrate the efficacy of a 2HDM multi-lepton search. In the conclusions, we will comment briefly on how a focussed search could be further optimized to maximize sensitivity to multi-lepton final states arising from an extended scalar sector.

Although the CMS analysis includes hadronically decaying τ-leptons, for simplicity of simulation, we will consider only strictly leptonic $\ell = e, \mu$ final states (of course, still including leptonic τ decays). Additionally, we treat all hadronic taus as having failed selection criteria, thus being identified as jets. Because of this, some events (mainly those involving 4τ final states) will be categorized differently than in the CMS analysis. For instance, an event with three e/μ and one hadronic τ that the CMS analysis would have included in a 4ℓ (with 1τ) bin, will instead be included in a 3ℓ bin in our analysis, potentially with higher H_T due to the additional energy of the hadronic τ-lepton. While this is a deviation from the exact procedure of the CMS analysis, it goes in the conservative direction, as the 4ℓ with 1τ bins have significantly smaller

Production	Decay
$gg \to h$	$h \to 4\ell$
VBF $\to h$	$h \to 4\ell$
$gg \to H$	$H \to 4\ell$
	$H \to hh \to 4W, WW\tau\tau, 4\tau, ZZb\bar{b}, ZZWW, 4Z, ZZ\tau\tau$
	$H \to AA \to 4\tau$
	$H \to AA \to \tau\tau Zh \to \tau\tau ZWW, \tau\tau Z\tau\tau, \tau\tau Zb\bar{b}, \tau\tau ZZZ$
	$H \to AA \to ZhZh \to ZZWWWW, ZZWW\tau\tau, ZZWWb\bar{b}, ZZ\tau\tau b\bar{b}, ZZ\tau\tau\tau\tau$
	$H \to AA \to ZhZh \to ZZb\bar{b}b\bar{b}, ZZZZb\bar{b}, ZZZZ\tau\tau, ZZZZWW, 6Z$
	$H \to H^+H^- \to WhWh \to WWWWWW, WWWW\tau\tau, WWWWb\bar{b}, WW\tau\tau\tau$
	$H \to H^+H^- \to WhWh \to WW\tau\tau b\bar{b}, WWZZb\bar{b}, WWWWZZ, WWZZZZ, WWZZ\tau\tau$
	$H \to H^+H^- \to \tau\nu Wh \to \tau\nu WWW, \tau\nu W\tau\tau, \tau\nu WZZ$
	$H \to H^+H^- \to tbWh \to tbWWW, tbW\tau\tau, tbWZZ$
	$H \to ZA \to Z\tau\tau$
	$H \to ZA \to ZZh \to ZZ\tau\tau, ZZWW, ZZb\bar{b}, ZZZZ$
	$H \to WH^\pm \to WWh \to WW\tau\tau, WWWW, WWZZ$
VBF $\to H$	$H \to 4\ell$
	$H \to hh \to 4W, WW\tau\tau, 4\tau, ZZb\bar{b}, ZZWW, 4Z, ZZ\tau\tau$
	$H \to AA \to 4\tau$
	$H \to AA \to \tau\tau Zh \to \tau\tau ZWW, \tau\tau Z\tau\tau, \tau\tau Zb\bar{b}, \tau\tau ZZZ$
	$H \to AA \to ZhZh \to ZZWWWW, ZZWW\tau\tau, ZZWWb\bar{b}, ZZ\tau\tau b\bar{b}, ZZ\tau\tau\tau\tau$
	$H \to AA \to ZhZh \to ZZb\bar{b}b\bar{b}, ZZZZb\bar{b}, ZZZZ\tau\tau, ZZZZWW, 6Z$
	$H \to H^+H^- \to WhWh \to WWWWWW, WWWW\tau\tau, WWWWb\bar{b}, WW\tau\tau\tau$
	$H \to H^+H^- \to WhWh \to WW\tau\tau b\bar{b}, WWZZb\bar{b}, WWWWZZ, WWZZZZ, WWZZ\tau\tau$
	$H \to H^+H^- \to \tau\nu Wh \to \tau\nu WWW, \tau\nu W\tau\tau, \tau\nu WZZ$
	$H \to H^+H^- \to tbWh \to tbWWW, tbW\tau\tau, tbWZZ$
	$H \to ZA \to Z\tau\tau$
	$H \to ZA \to ZZh \to ZZ\tau\tau, ZZWW, ZZb\bar{b}, ZZZZ$
	$H \to WH^\pm \to WWh \to WW\tau\tau, WWWW, WWZZ$
$gg \to A$	$A \to Zh \to ZWW, Z\tau\tau, ZZZ$
$q\bar{q} \to Wh$	$Wh \to WWW, W\tau\tau$
$q\bar{q} \to Zh$	$Zh \to ZWW, Z\tau\tau$
$t\bar{t}h$	$t\bar{t}h \to t\bar{t}WW, t\bar{t}\tau\tau$
$t\bar{t}A$	$t\bar{t}A \to t\bar{t}\tau\tau$
	$t\bar{t}A \to t\bar{t}Zh \to t\bar{t}ZWW, t\bar{t}Z\tau\tau, t\bar{t}Zb\bar{b}, t\bar{t}ZZZ$
$tbH^\pm$	$tbH \to tbWh \to tbWWW, tbW\tau\tau, tbWZZ$

Table 6.7: The 111 independent production and decay topologies simulated for the 2HDM Benchmark Spectrum 3 with $m_h = 125$ GeV, $m_H = 500$ GeV, $m_A = m_{H^\pm} = 230$ GeV. All Higgs boson branching ratios are factored out of each topology. All top-quark, b-quark, τ-lepton, and W- and Z-boson branching ratios are Standard Model.

Production	Decay
$gg \to h$	$h \to 4\ell$
VBF $\to h$	$h \to 4\ell$
$gg \to H$	$H \to 4\ell$
	$H \to AA \to 4\tau$
VBF $\to H$	$H \to 4\ell$
	$H \to AA \to 4\tau$
$q\bar{q} \to Wh$	$Wh \to WWW, W\tau\tau$
$q\bar{q} \to Zh$	$Zh \to ZWW, Z\tau\tau$
$t\bar{t}h$	$t\bar{t}h \to t\bar{t}WW, t\bar{t}\tau\tau$
$t\bar{t}H$	$t\bar{t}H \to t\bar{t}WW, t\bar{t}\tau\tau$
	$t\bar{t}H \to t\bar{t}AA \to t\bar{t}\tau\tau\tau\tau, t\bar{t}\tau\tau bb$
$t\bar{t}A$	$t\bar{t}A \to t\bar{t}\tau\tau$
$tbH^{\pm}$	$tbH^{\pm} \to tbWh \to tbWWW, tbW\tau\tau, tbWZZ$
	$tbH^{\pm} \to tbWA \to tbW\tau\tau$
$q\bar{q} \to H^{\pm}A$	$H^{\pm}A \to Whb\bar{b} \to WWWb\bar{b}, W\tau\tau b\bar{b}, WZZb\bar{b}$
	$H^{\pm}A \to Wh\tau\tau \to WWW\tau\tau, W\tau\tau\tau\tau, Wb\bar{b}\tau\tau, WZZ\tau\tau$
	$H^{\pm}A \to \tau\nu\tau\tau, t\bar{b}\tau\tau$
	$H^{\pm}A \to WAA \to W\tau\tau\tau\tau, W\tau\tau b\bar{b}$
$q\bar{q} \to Ah$	$Ah \to \tau\tau WW, \tau\tau\tau\tau, \tau\tau ZZ$
$q\bar{q} \to AH$	$AH \to \tau\tau WW, \tau\tau\tau\tau, \tau\tau ZZ$
	$AH \to AAA \to 6\tau, \tau\tau\tau b\bar{b}$

Table 6.8: The 40 independent production and decay topologies simulated for the 2HDM Benchmark Spectrum 4 with $m_h = 125$ GeV, $m_H = 200$ GeV, $m_A = 80$ GeV, $m_{H^{\pm}} = 250$ GeV.All Higgs boson branching ratios are factored out of each topology. All top-quark, b-quark, τ-lepton, and W- and Z-boson branching ratios are Standard Model.

backgrounds than the 3ℓ with 0τ bins. Thus, if we could implement a satisfactory modeling of hadronic τ identification in our study, we would expect our bounds to become stronger in regions of parameter space where 4τ final states are driving the limits. For other final states such as $H \to hh \to 4W$, the impact of this effect on our signal is at the few percent level or less.

6.4.1 Signal Channels

The prompt irreducible Standard Model backgrounds to multi-lepton searches are small and arise predominantly through leptonic decays of W and Z bosons. Such backgrounds may therefore be reduced by demanding significant hadronic activity and/or missing energy in the events. Hadronic activity can be quantified by the variable H_T , defined as the scalar sum of the transverse energies of all jets passing the preselection cuts. The missing transverse energy (MET) is the magnitude of the vector sum of the momenta of all particles in the event. In order to make use of H_T and MET, the CMS analysis of [8, 9] divides events with $H_T > 200$ (MET > 50) GeV into a high H_T (MET) category, and those with $H_T < 200$ (MET < 50) GeV into a low H_T (MET) category. The high H_T and high MET requirements (individually or in combination) lead to a significant reduction in Standard Model backgrounds.

Another useful observable in reducing backgrounds is the presence of Z candidates, specifically the existence of an opposite-sign same-flavor (OSSF) lepton pair with an invariant mass between $75-105$ GeV. Events are thus further subdivided, and assigned a No Z channel if no such pair exists. It is also useful to characterize events according to whether they may contain off-shell γ/Z^* candidates, given by the number of OSSF lepton pairs. Thus, for instance, three-lepton events are assigned to the DY0 (no possible Drell-Yan pairs) or DY1 category (one OSSF pair). The full combination of 3 and 4 lepton events results in 20 possible categories of H_T high/low; MET high/low; Z/no Z; and DY0/DY1.

The 20 channels were presented already in Table 5.2. For each of the 3ℓ and 4ℓ categories, channels are listed from top to bottom in approximately descending order of backgrounds, or equivalently ascending order of sensitivity, with the last such channel

at the bottom dominated by Standard Model backgrounds. Events are entered in the table exclusive-hierarchically from the top to the bottom. This ensures that each event appears only once in the table, and in the lowest possible background channel consistent with its characteristics. Although the backgrounds in the individual channels vary over a wide range, all 20 channels are used to compute sensitivity limits.

6.4.2 Simulation

For simulating signal processes, we have used MadGraph v4 [92, 93]. In order to simulate a general 2HDM in MadGraph, we treat the 2HDM as a simplified model using a modified version of the `2HDM4TC` model file [75]. Cascade decays were performed in BRIDGE [95]. Subsequent showering and hadronization effects were simulated using Pythia [97]. Detector effects and object reconstruction was simulated using PGS [78] with the isolation algorithm for muons and taus modified to more accurately reflect the procedure used by the CMS collaboration. In particular, we introduce a new output variable called `trkiso` for each muon [98]. The variable `trkiso` is defined to be the sum p_T of all tracks, ECAL, and HCAL deposits within an annulus of inner radius 0.03 and outer radius 0.3 in ΔR surrounding a given muon. Isolation requires that for each muon, I=`trkiso`$/p_T$ of the muon be less than 0.15. The efficiencies of PGS detector effects were normalized by simulating the mSUGRA benchmark studied in [66] and comparing the signal in 3ℓ and 4ℓ channels. To match efficiencies with the CMS study, we applied a lepton ID efficiency correction of 0.87 per lepton to our signal events. As discussed earlier, we applied preselection and analysis cuts in accordance with those in [66].

In order to assess the multi-lepton signatures of the 2HDMs studied here we employ a factorized mapping procedure [70] to go between model parameters and signatures. In this procedure the acceptance times efficiency is independently determined in each of the 20 exclusive multi-lepton channels by monte carlo simulation of each individual production and decay topology in each of the four 2HDM mass spectra as well as for the individual topologies of the Standard Model Higgs boson. The cross section times branching ratio times acceptance and efficiency in any of the 20 exclusive channels at

any point in parameter space in a given mass spectrum is then given by a sum over the production cross section times acceptance and efficiency for each topology of that spectrum, times a product of the branching ratios that appear in each topology

$$\sigma \cdot \mathrm{Br} \cdot \mathcal{A}(pp \to f) = \sum_t \sigma(pp \to t)\mathcal{A}(pp \to t \to f) \prod_a \mathrm{Br}_a(t \to f) \tag{6.6}$$

where f is a given exclusive final state channel, t labels the topology, and a the branching ratios of the decays in the t-th topology. Dependence on the parameter space characterized by α and β enters only through the production cross sections and decay branching ratios. The factorized terms in Eq. 6.6 are determined as follows:

- **Acceptance times Efficiency:** For each individual production and decay topology listed in Tables 6.4 - 6.8, the acceptance times detector efficiency into each of the 20 exclusive multi-lepton channels listed in Table 5.2 was simulated with the monte carlo tools described above. The acceptance times efficiency of each topology was calculated assuming unit branching ratios for all Higgs boson decays but with Standard Model values for decays of W and Z bosons, and top quarks and τ-leptons. A total of 50,000 events were simulated for each topology to ensure good statistical coverage of all the exclusive multi-lepton channels.

- **Cross Sections:** For the case of the Standard Model Higgs boson, the NLO production cross sections for gluon fusion, vector boson fusion, and production in association with a vector boson or top quarks are taken from the LHC Higgs Cross Section Group [80]. For the 2HDM spectra the ratio of LO production partial widths in each production channel for h and H relative to a Standard Model Higgs boson of the same mass are calculated analytically from the couplings presented in Section 6.1 as functions of the mixing parameters α and β. The NLO Standard Model Higgs production cross sections in each production channel are then rescaled by these factors to obtain an estimate for the NLO cross sections; for instance the α, β dependent cross section for gluon fusion production of H is taken to be

$$\sigma_{\mathrm{NLO}}(gg \to H)|_{\alpha,\beta} = \sigma_{\mathrm{NLO}}(gg \to h_{\mathrm{SM}}) \, \frac{\Gamma_{\mathrm{LO}}(H \to gg)\big|_{\alpha,\beta}}{\Gamma_{\mathrm{LO}}(h_{\mathrm{SM}} \to gg)} \tag{6.7}$$

The same procedure of normalizing to Standard Model Higgs boson NLO cross sections through the α and β dependent ratios of LO production partial widths is used for production of A by gluon fusion or in association with top quarks. This is expected to be a good approximation since the fractional size of NLO corrections in these cases should not be strongly dependent on the parity of the Higgs scalar. For the modes that involve production of two Higgs bosons, or of the charged Higgs in association with a top quark, the LO cross sections are calculated using Madgraph v4 with a conservative K-factor of $K = 1.2$ applied. These cross sections are calculated for a single canonical value of α and β and then rescaled analytically using the couplings in Section 6.1 to obtain the cross sections at general values.

- **Higgs Bosons Branching Ratios:** For the case of the Standard Model Higgs boson, the NLO partial decay widths and branching ratios are taken from the LHC Higgs Cross Section Group [80]. For the 2HDM spectra the ratio of LO partial decay widths for h relative to a Standard Model Higgs boson of the same mass are calculated analytically as functions of the mixing parameters α and β using the couplings presented in Section 6.1. The NLO Standard Model Higgs boson partial decay widths are then rescaled by these factors to obtain estimates for the NLO partial widths; for instance the α, β dependent partial width for the light scalar h to $b\bar{b}$ is taken to be

$$\Gamma_{\mathrm{NLO}}(h \to b\bar{b})|_{\alpha,\beta} = \Gamma_{\mathrm{NLO}}(h_{\mathrm{SM}} \to b\bar{b}) \, \frac{\Gamma_{\mathrm{LO}}(h \to b\bar{b})\big|_{\alpha,\beta}}{\Gamma_{\mathrm{LO}}(h_{\mathrm{SM}} \to b\bar{b})} \tag{6.8}$$

The same procedure of normalizing to Standard Model Higgs boson NLO partial decay widths through the ratio of LO decay widths is used for the H and A decay modes listed in Table 6.9that are in common with the h decay modes. This estimate is used since, just as for a production cross section, the fractional size of NLO corrections to decay widths in these cases should not be strongly dependent

on the parity of the Higgs scalar. For the remainder of the H and A decay modes listed in Table 6.9 that are kinematically open in a given spectrum, as well as the $H^{\pm}$ decay modes given in the Table that are open, the LO decay widths are calculated analytically [81] as a function of α and β using the couplings in Section 6.1. Except for the charged Higgs decays to quarks, none of thesedecay modes involve strongly interacting particles, so LO widths should be a good approximation in this case. The partial widths for all the open decay modes of each Higgs scalar in Table 6.9 are then used to calculate the α and β dependent total widths and branching ratios in each mass spectrum.

Higgs Boson	Decay Modes
h	$bb, cc, \tau\tau, WW^*, ZZ^*, gg, \gamma\gamma, Z\gamma$
H	$tt, bb, cc, \tau\tau, WW^{(*)}, ZZ^{(*)}, hh, AA, H^+H^-, ZA, WH^{\pm}, gg, \gamma\gamma, Z\gamma$
A	$tt, bb, cc, \tau\tau, Zh, ZH, gg, \gamma\gamma, Z\gamma$
$H^{\pm}$	$tb, ts, cs, \tau\nu, WA, Wh, WH$

Table 6.9: Decay modes of the Higgs boson scalars used in branching ratio calculations. Partial widths of the kinematically open decay modes are calculated in each benchmark spectrum as a function of the mixing parameters α and β to determine the total width and individual branching ratios.

Using this factorized mapping procedure, each of the 20 exclusive multi-lepton channels for a given benchmark spectrum over the entire α, β plane in all four 2HDM types is covered by a single set of monte carlo samples for the production and decay topologies.

In some cases, particularly in Spectrum 3, the total widths of some scalars (particularly H) increase drastically in certain regions of parameter space, typically due to enhanced scalar couplings. Our simulation and normalization techniques, however, treat all particles in the narrow width approximation and assume the validity of perturbation theory in the scalar couplings. In the regions of parameter space where scalar widths grow large, one expects higher-order effects to modify the limits; in this respect the limits we find in high-width regions should be viewed as rough estimates subject to potentially large corrections beyond the scope of our approach.

6.5 Results

In this section, we present the results of the analysis outlined above using the CMS multi-lepton search based on 5 fb^{-1} of 7 TeV proton-proton collisions at the LHC [67]. We first consider the sensitivity of the CMS multi-lepton search to a Standard Model Higgs boson near 125 GeV before presenting limits in the full 2HDM parameter space for our four benchmark spectra.

For each benchmark, we briefly discuss the major processes that contribute to multi-lepton final states, including direct production and decay of individual scalars as well as cascades among scalars. We also illustrate many of the partial widths and $\sigma \cdot \text{Br}$'s for key scalar cascades, which helps to capture the qualitative shape of the multi-lepton limits in the space of $(\sin\alpha, \tan\beta)$. In many cases, the signals of Type I and Type III 2HDM (and separately Type II and Type IV 2HDM) are often similar, up to final states involving τ-leptons. These similarities arise because in each case the quark couplings are identical for the pairs of 2HDM types, so in particular the scaling of the $h \to b\bar{b}$ partial widths that often govern the total width (as well as the $ht\bar{t}$ couplings that governs the gluon fusion production rate) are identical. The only substantial distinction arises in standard channels with τ final states, since the lepton couplings differ among these pairs of 2HDM types.

In each case, we show the regions of parameter space excluded by the 5 fb^{-1} CMS multi-lepton search. In regions not yet excluded, we show the 95% CL limits on the production cross section times branching ratio in multiples of the theory cross section times branching ratio for the benchmark spectrum and 2HDM type. To compute our 95% CL limits, we used a Bayesian likelihood function assuming poisson distributions for each of the 20 channels with a flat prior for the signal. We treated the magnitude of the backgrounds in each exclusive channel as nuisance parameters with distributions given by a truncated positive definite Gaussian distribution with width equal to the background uncertainty. The number of signal events in each exclusive channel for a given α and β was obtained from the cross section times branching times acceptance and efficiency in each channel times the integrated luminosity. For simplicity, we assumed

there was no error on the signal. To generate the expected limits, a large number of background-only pseudo-experiments were used in place of data.

For comparison, we also show regions where the heavy, CP-even scalar, H, is currently excluded by standard Higgs searches at 7 TeV [59] at roughly the same luminosity of the multi-lepton search. For Spectra 1, 3, and 4 we use the combined CMS Higgs limit at 5 fb^{-1} of 7 TeV collisions, which is driven by ZZ and WW final states. For Spectrum 2, where $m_H = 140$ GeV, we use the $WW \to 2\ell 2\nu$ CMS Higgs limit at 5 fb^{-1} of 7 TeV collisions, which dominates the exclusion limit at this mass. We also consider direct limits on the pseudoscalar A and the charged Higgses $H^{\pm}$, but these do not impact the parameter space explored here. For the pseudoscalar, the best current CMS limits come from MSSM Higgs searches for $b\bar{b}A$ associated production with $A \to \tau\tau$ [82]. For a Type II 2HDM, the current exclusion is relevant only for $\tan\beta > 10$, and in all other 2HDM types the $\sigma \cdot \mathrm{Br}$ for $b\bar{b}A$ associated production with $A \to \tau\tau$ is smaller than in the Type II case. Searches for di-tau resonances [83] do not lead to meaningful limits. Finally, searches for charged Higgses such as [84] are sensitive only to $H^{\pm}$ production in decays of the top quark, which are not relevant for the benchmark spectra considered here.

6.5.1 Spectrum 1

Now let us turn to the multi-lepton signals and limits of our 2HDM benchmark spectra. The multi-lepton limits on the first benchmark spectrum for all four types of 2HDM are shown in Figure 6.1. Limits in this and the following figures were obtained from an exclusive combination of the observed and expected number of events in all the multi-lepton channels presented in Table 5.2 on an evenly-spaced grid in $-1 \leq \sin\alpha \leq 0$ and $1 \leq \tan\beta \leq 10$ with spacing $\Delta(\sin\alpha) = 0.1$ and $\Delta(\tan\beta) = 1$; contours were determined by numerical interpolation between these points.

In addition to the Standard Model-like production and decays of scalars to SM final states, the first benchmark spectrum also features the inter-scalar decays $H \to hh$, $A \to Zh$, and $A \to ZH$. The partial widths for these three inter-scalar decays (which are independent of the 2HDM type) and the $\sigma \cdot \mathrm{Br}$ for the dominant processes $gg \to$

$H \to hh$, $gg \to A \to Zh$, and $gg \to A \to ZH$ (which depend weakly on the 2HDM type; here, we display those of a Type I 2HDM) are shown in Figure 6.2; their parametric behavior as a function of $\sin\alpha$ and $\tan\beta$ helps to explain many of the detailed features of the exclusion limits in Figure 6.1.

The partial width, $\Gamma(H \to hh)$, has a complicated dependence on α, β, but is greatest when $\tan\beta$ is large and $\sin\alpha \simeq -0.85$. This process only contributes significantly to multi-lepton limits in 2HDM types for which the multi-lepton decays of h are unsuppressed in the same region where $\mathrm{Br}(H \to hh)$ is large. The partial width, $\Gamma(A \to Zh) \propto \cos^2(\beta - \alpha)$, is largest away from the alignment limit, while the partial width, $\Gamma(A \to ZH) \propto \sin^2(\beta - \alpha)$, is largest in the alignment limit. In both cases, the multi-lepton limits are strongest for 2HDM types where the multi-lepton decays of h and H are significant when $\mathrm{Br}(A \to Zh)$ and $\mathrm{Br}(A \to ZH)$ are respectively large.

On the production side, the dominant production cross section for H, $\sigma(gg \to H)$, is largest at small $\tan\beta$ and $\sin\alpha \to -1$, while the dominant cross section for A, $\sigma(gg \to A)$, is independent of $\sin\alpha$ (since the pseudoscalar couplings to fermions, and hence gluons, depend only on $\tan\beta$) and increases as $\tan\beta \to 0$. These production cross sections and scalar partial widths are largely independent of the 2HDM type; the gluon fusion rates for Type II and Type IV 2HDM increase slightly at large $\tan\beta$ due to the sizable bottom quark coupling.

The threefold combination of production rates, inter-scalar decay widths, and multi-lepton widths of scalars determines the shape of limits in the plane of $\sin\alpha$ and $\tan\beta$. These vary among different 2HDM types, though similarities between Type I & III and between Type II & IV make it worthwhile to discuss these two sets together.

Types I & III

In the Type I 2HDM, the multi-lepton signals of the SM-like Higgs, h, generally decrease as we move away from the alignment limit (in large part because the coupling to vectors is suppressed, reducing both the Vh associated production rate and the branching ratios, $\mathrm{Br}(h \to VV^*)$; for an extended discussion, see [85]), but are not a strong function of $\sin\alpha$ and $\tan\beta$; only near $\sin\alpha \to -1$ are the $\sigma \cdot \mathrm{Br}$ for the conventional multi-lepton

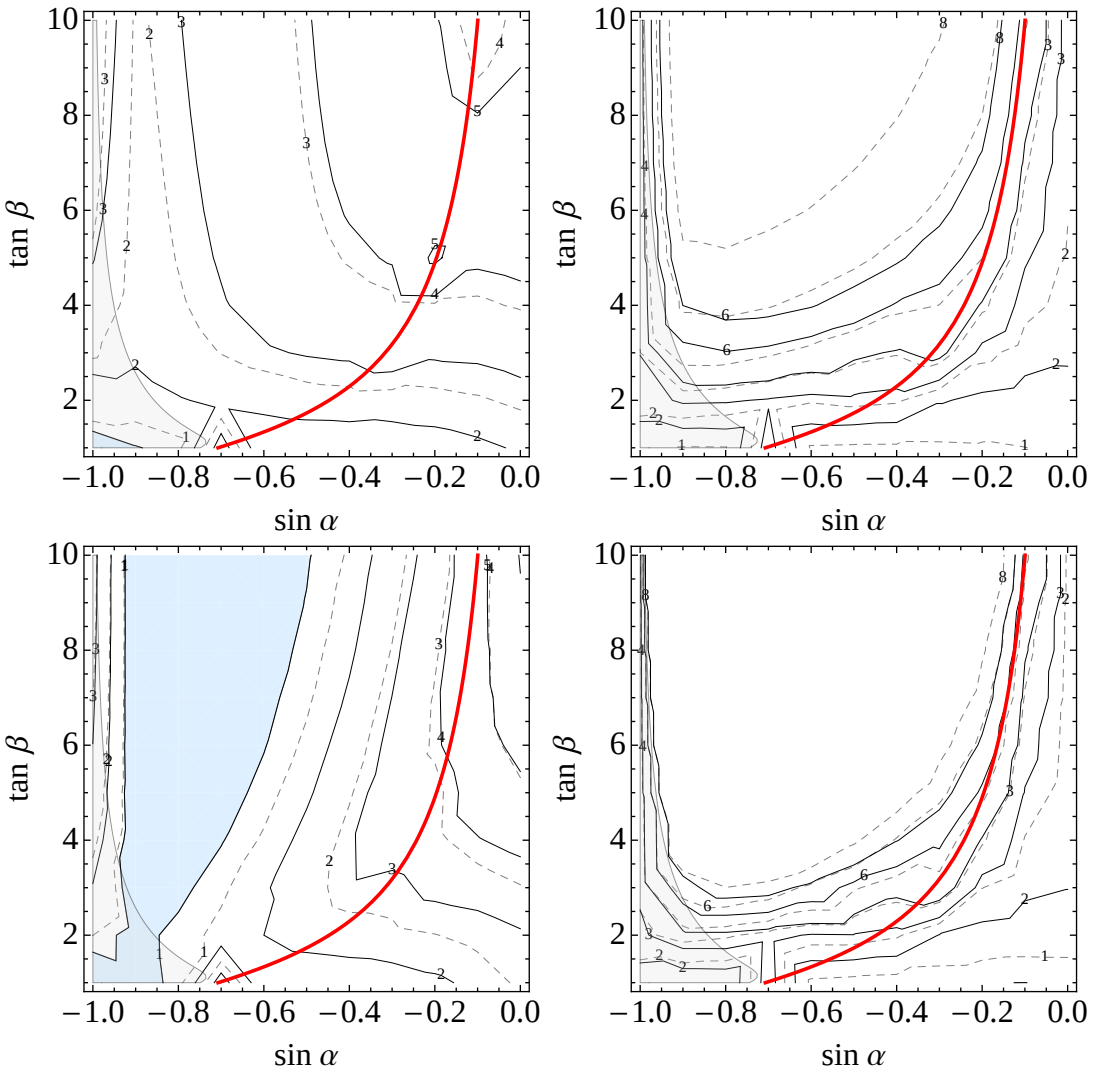

Figure 6.1: Multi-lepton limits from the CMS multi-lepton search with 5 fb^{-1} of 7 TeV proton-proton collisions [67] for the production and decay topologies of Benchmark Spectrum 1 given in Table 6.5, for Type I (top left), Type II (top right), Type III (bottom left), and Type IV (bottom right) couplings as a function of $\sin\alpha$ and $\tan\beta$. Limits were obtained from an exclusive combination of the observed and expected number of events in all the multi-lepton channels presented in Table 5.2. The solid and dashed lines correspond to the observed and expected 95% CL limits on the production cross section times branching ratio in multiples of the theory cross section times branching ratio for the benchmark spectrum and 2HDM type. The blue shaded regions denote excluded parameter space. The solid red line denotes the alignment limit $\sin(\beta-\alpha)=1$. he gray shaded region corresponds to areas of parameter space where vector decays of the heavy CP-even Higgs, $H\to VV$, are excluded at 95% CL by the SM Higgs searches at 7 TeV [59].

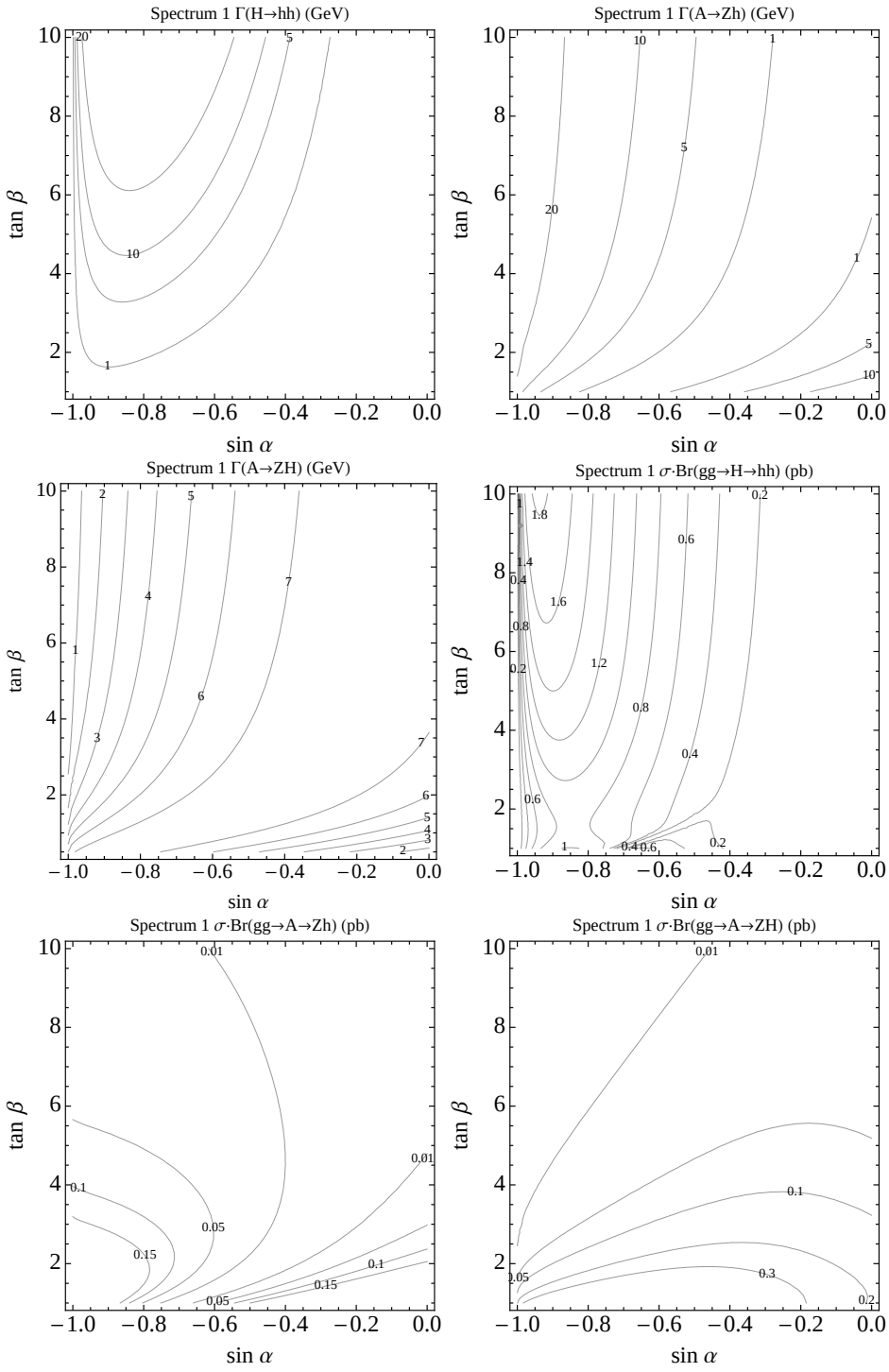

Figure 6.2: 2HDM Benchmark Spectrum 1 partial widths $\Gamma(H \to hh)$, $\Gamma(A \to Zh)$, and $\Gamma(A \to ZH)$ in units of GeV, and cross section times branching ratios $\sigma \cdot \mathrm{Br}(gg \to H \to hh)$, $\sigma \cdot \mathrm{Br}(gg \to A \to Zh)$, and $\sigma \cdot \mathrm{Br}(gg \to A \to ZH)$ in units of pb, all for Type I couplings. These partial widths and $\sigma \cdot$Brs are qualitatively similar for the other types of 2HDM couplings; the production cross sections $\sigma(gg \to H, A)$ are moderately enhanced at large $\tan\beta$ for Type II and Type IV 2HDM due to the contribution from bottom loops.

channels of h significantly diminished. However, the SM-like multi-lepton signals of h are typically never enhanced as we move away from the alignment limit (the exception being a mild enhancement of VBF and Vh associated production with $h \to VV^*$ at small $\tan\beta$ and $\sin\alpha \to -1$; see [85] for more detail). In the region where the multi-lepton signals of h are diminished, the conventional multi-lepton signals of H are correspondingly enhanced since the HVV coupling is complementary to the hVV coupling. While for $m_H = 300$ GeV, the production cross section for H is somewhat smaller than that of h, it nonetheless contributes significantly to multi-lepton limits near $\sin\alpha \to -1$ through primarily SM-like production and decay modes. Note that the direct decays of the pseudoscalar A never result in more than two leptons, so the pseudoscalar contributes to the multi-lepton signal only through scalar cascades and $t\bar{t}A$ associated production.

In addition to the conventional SM-like production and decay modes of h and H, we must also consider the various production channels involving inter-scalar decays. The $\sigma \cdot \mathrm{Br}(gg \to H \to hh)$ is largest at large $\tan\beta$ and $\sin\alpha \sim -0.8$ where g_{Hhh} is largest. The parametric behavior of this $\sigma \cdot \mathrm{Br}$, along with the fact that the multi-lepton final states of h in a Type I 2HDM are only mildly suppressed when $\sigma \cdot \mathrm{Br}(gg \to H \to hh)$ is significant, largely explains the strengthening of the multi-lepton limit around $\sin\alpha \sim -0.85$.

For the pseudoscalar, $\sigma \cdot \mathrm{Br}(gg \to A \to Zh)$ is large away from the alignment limit, but decreases at large $\tan\beta$ due to the falling gluon fusion rate for A. Similarly, $\sigma \cdot \mathrm{Br}(gg \to A \to ZH)$ is large only at low $\tan\beta$, since the branching ratio for $A \to ZH$ is large along the alignment line but the gluon fusion rate for A again decreases at large $\tan\beta$. Thus, both $\sigma \cdot \mathrm{Br}(gg \to A \to Zh)$ and $\sigma \cdot \mathrm{Br}(gg \to A \to ZH)$ contribute to limit-setting at small $\tan\beta$, essentially independent of $\sin\alpha$, while $\sigma \cdot \mathrm{Br}(gg \to A \to Zh)$ also contributes at larger $\tan\beta$ for $\sin\alpha \lesssim -0.5$.

All three scalar decays contribute to setting the strongest limits at small $\tan\beta$ (relatively insensitive to $\sin\alpha$), while $\sigma \cdot \mathrm{Br}(gg \to H \to hh)$ predominantly explains the limits at large $\tan\beta$ around $\sin\alpha \sim -0.85$. The additional contributions from scalar cascades are exemplified in Figure 6.3, which illustrates the H_T and MET distributions

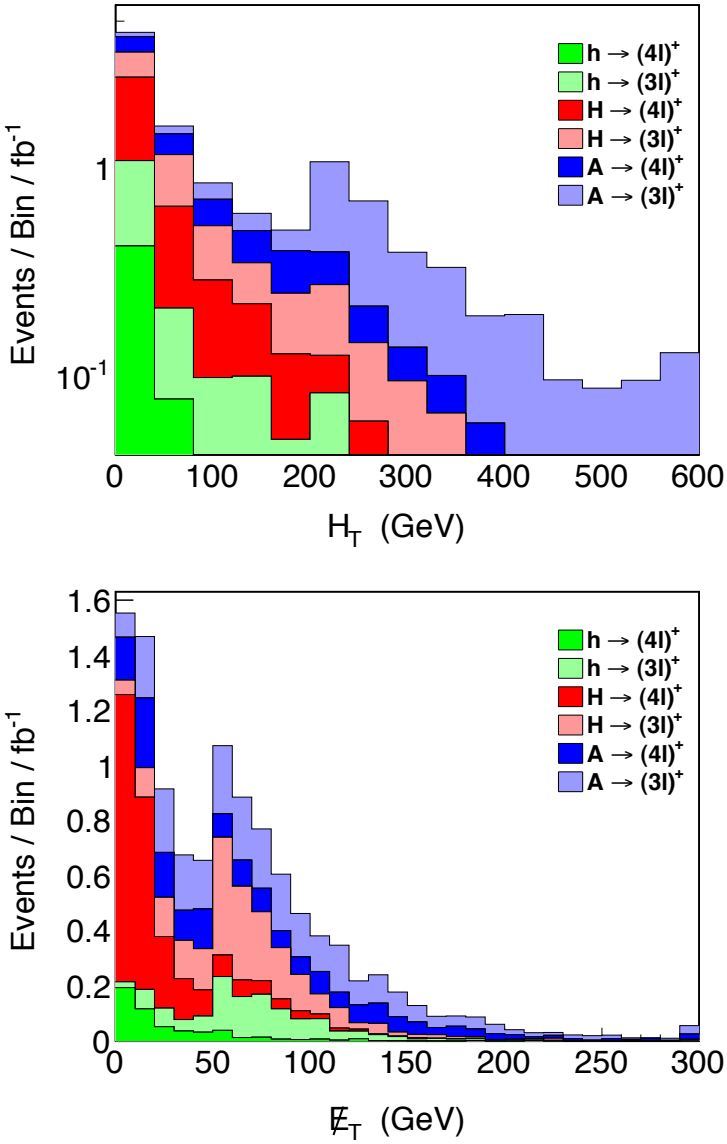

Figure 6.3: The 2HDM signal transverse hadronic energy distribution (left) and missing transverse energy distribution (right) after acceptance and efficiency for 7 TeV proton-proton collisions arising from the production and decay topologies of Benchmark Spectrum 1 given in Table 6.5 with $m_h = 125$ GeV, $m_H = 300$ GeV, $m_{H^\pm} = m_A = 500$ GeV, for Type I 2HDM couplings with $\sin\alpha = -0.9$ and $\tan\beta = 1.0$. Signal events correspond to those falling in the exclusive three- or four-lepton channels labelled with a dagger in Table 5.2 that have moderate to good sensitivity. The colors indicate the initial type of Higgs boson produced. For each color, the lighter shade corresponds to three-lepton channels, while the darker shade corresponds to four-lepton channels. The bin size is 40 GeV for H_T and 10 GeV for $\not{E}_T$, and in both cases the highest bin includes overflow.

for the sum of multi-lepton events at the point ($\sin\alpha = -0.9, \tan\beta = 1.0$), distinguished by the initial scalar produced in each multi-lepton event.

The multi-lepton signals in the Type III, or "lepton-specific," model are similar to those of the Type I model, since the couplings of the Higgs scalars to quarks and vectors are identical for these 2HDM types. The exception is a significant improvement in the limits around $-0.9 \lesssim \sin\alpha \lesssim -0.6$ relative to the Type I 2HDM. Here, the branching ratio, $\mathrm{Br}(h \to \tau\tau)$, is substantially increased over the SM rate and contributes both through SM-like associated production of h and production of $H \to hh$ with one or both h decaying to $\tau\tau$. Indeed, processes such as Vh associated production with $h \to \tau\tau$ are as much as ten times larger than the SM rate, with $\sigma \cdot \mathrm{Br}(Wh \to W\tau\tau)$ as large as several hundred fb. Scalar cascades involving τs are even more important, with $\sigma \cdot \mathrm{Br}(gg \to H \to hh \to 4\tau)$ as large as several pb. The enhancement of $\Gamma(h \to \tau\tau)$ renders this the 2HDM type most amenable to detection by the multi-lepton search, and, in fact, a large region of parameter space is already excluded by the CMS multi-lepton search with 5 fb^{-1}. While some of this region is already excluded by conventional searches for $h \to \tau\tau$, there exist regions not constrained by current searches where the dominant multi-lepton limit comes from scalar cascades.

Types II & IV

A very important difference in the phenomenology of the Type II & IV 2HDM compared to the preceding description of the Type I & III phenomenology is that the down-type quarks now couple to H_d rather than H_u, thus the partial width of $h \to b\bar{b}$ has an entirely different parametric dependence. Since this decay mode dominates in the SM-like alignment limit, its variation sharply affects the Br's of all other decay modes as well. For instance, the multi-lepton signals of the SM-like Higgs h change rapidly as we move away from the alignment limit, decreasing sharply with increasing $\tan\beta$ above the $\sin(\beta-\alpha) = 1$ line due to the rapidly increasing partial width, $\Gamma(h \to b\bar{b})$, and rising rapidly below $\sin(\beta-\alpha) = 1$ as $\Gamma(h \to b\bar{b})$ drops. Thus at large $\tan\beta$ above the alignment line, the multi-lepton signals of h diminish rapidly, weakening the limit both from SM-like production of h and from new associated production,

such as $H \to hh$. The only exception are multi-lepton signals involving $h \to \tau\tau$, since $\Gamma(h \to \tau\tau)/\Gamma(h \to b\bar{b})$ is fixed in a Type II 2HDM. On the other hand, below the alignment line there is an overall enhancement of multi-lepton decays involving $h \to VV^*$ since the partial width $\Gamma(h \to b\bar{b})$ drops, leading to an increase in the purely SM-like multi-lepton production and decay modes of h. As $\sin\alpha \to -1$, the direct multi-lepton decays of H somewhat compensate for the loss of h signals, but there is a wide region of large $\tan\beta$ and moderate $\sin\alpha$ where neither h nor H decays significantly to multi-lepton final states; this is clearly displayed by the weak limits in the range $-0.9 \lesssim \sin\alpha \lesssim -0.2$.

Scalar cascade decays do not significantly help to constrain a Type II 2HDM. While the $\sigma \cdot \mathrm{Br}(gg \to H \to hh)$ is parametrically similar to the Type I 2HDM, in a Type II 2HDM the SM-like Higgs h decays predominantly to $b\bar{b}$ in this region, so this channel does not contribute substantially to multi-lepton limits (except for the rare $hh \to 4\tau$). Likewise, the contributions from $\sigma \cdot \mathrm{Br}(gg \to A \to Zh)$ at large $\tan\beta$ lead to multi-lepton signals only through $h \to \tau\tau$.

At low $\tan\beta$, the direct multi-lepton decays of h are still significant, as are the added contributions from $H \to hh, A \to Zh$, and $A \to ZH$. The multi-lepton limits on the first benchmark spectrum for a Type II 2HDM are strongest at low $\tan\beta$, where h decays and inter-scalar decays to multi-lepton final states are enhanced; limits at $\sin\alpha \to -1$ come predominantly from direct decays of H, while those at $\sin\alpha \to 0$ come from direct decays of h. The contributions of the pseudoscalar in this limit are exemplified by Figure 6.4, which illustrates the H_T and MET distributions for the sum of multi-lepton events at the point $(\sin\alpha = -0.3, \tan\beta = 1.0)$, for which there is a large contribution from $A \to Zh, ZH$.

The multi-lepton signals in the Type IV, or "flipped," model are similar to that of the Type II model, since the couplings of the Higgs scalars to quarks and vectors are identical for these 2HDM types. The notable exception are the reduced limits in the region of moderate $\sin\alpha$ and large $\tan\beta$. This reduction in sensitivity is due to the fact that in a Type IV 2HDM the partial width, $\Gamma(h \to \tau\tau)$, no longer scales with $\Gamma(h \to b\bar{b})$, and so in the region where $\Gamma(h \to b\bar{b})$ is particularly large there are no longer meaningful

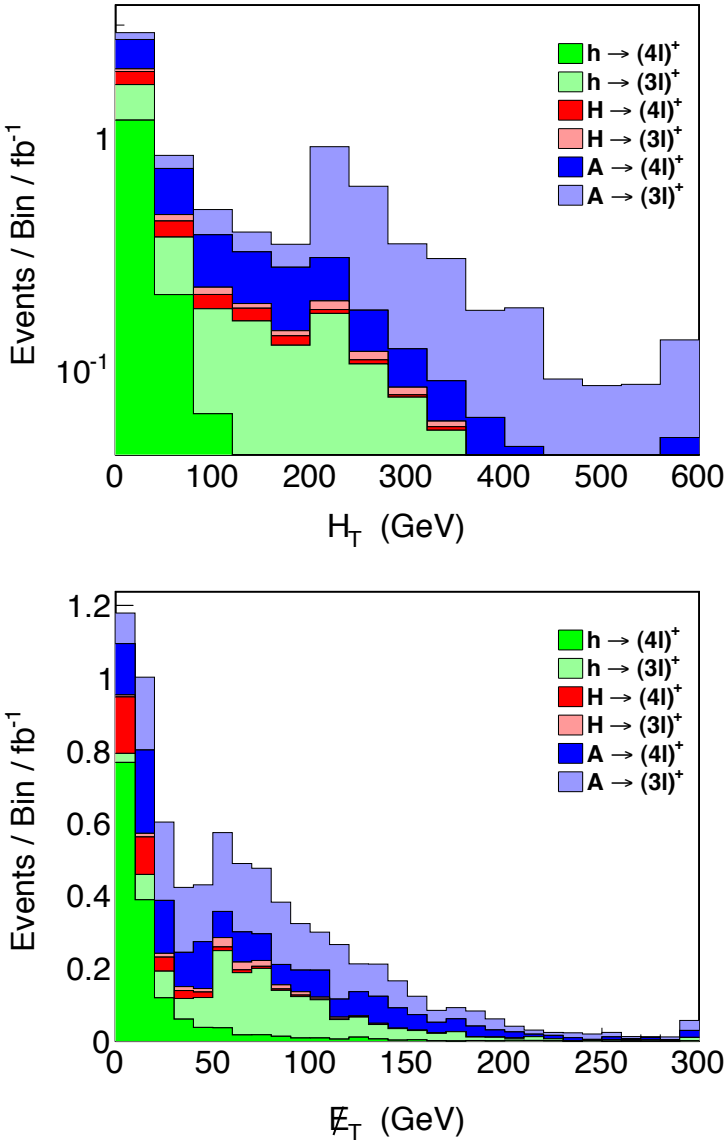

Figure 6.4: The 2HDM signal transverse hadronic energy distribution (left) and missing transverse energy distribution (right) after acceptance and efficiency for 7 TeV proton-proton collisions arising from the production and decay topologies of Benchmark Spectrum 1 given in Table 6.5 with $m_h = 125$ GeV, $m_H = 300$ GeV, $m_{H^\pm} = m_A = 500$ GeV, for Type II 2HDM couplings with $\sin\alpha = -0.3$ and $\tan\beta = 1.0$. Signal events correspond to those falling in the exclusive three- or four-lepton channels labelled with a dagger in Table 5.2 that have moderate to good sensitivity. The colors indicate the initial type of Higgs boson produced. For each color, the lighter shade corresponds to three-lepton channels, while the darker shade corresponds to four-lepton channels. The bin size is 40 GeV for H_T and 10 GeV for $\not\!\!E_T$, and in both cases the highest bin includes overflow.

contributions to multi-lepton limits from $h \to \tau\tau$ with leptonically decaying τ-leptons. In particular, this removes possible multi-lepton signals from associated production of h in this region, both through SM associated production and scalar cascades.

6.5.2 Spectrum 2

The multi-lepton limits on the second benchmark spectrum are shown in Figure 6.5. Much like the first benchmark spectrum, this spectrum includes the scalar decays $A \to Zh$ and $A \to ZH$, albeit with greater cross sections since $m_A = 250$ GeV in this spectrum. However, the decay $H \to hh$ is now kinematically forbidden. Since the parametric behavior of the relevant partial widths and $\sigma \cdot \text{Br}$'s is the same as in the first benchmark up to overall rescalings, we do not show them explicitly, but emphasize that the cross sections for production of A and H are substantially larger compared to the first benchmark since both A and H are lighter in this case.

Types I & III

The multi-lepton limits for Type I 2HDM are similar to those of the Type I model for Spectrum 1, albeit without the contributions from $H \to hh$. Particularly, the stronger limits around $\sin\alpha \sim -0.85$ in Spectrum 1 are absent here, but otherwise the parametric contributions are similar. The limits for this spectrum are stronger at small $\tan\beta$ because the now lighter A has a larger production cross section, $\sigma(gg \to A)$, than in Spectrum 1. Similarly, the limits are stronger as $\sin\alpha \to -1$ since here the direct production and multi-lepton decays of H dominate the limit, and the production cross section for H is effectively SM-like in this region since $m_H = 140$ GeV.

Likewise, the multi-lepton limits for Type III 2HDM are similar to those of the Type III model for Spectrum 1, although they again lack the contributions from $H \to hh$, meaning that there is no significant 4τ contribution with this spectrum.

Types II & IV

Unsurprisingly, the limits for Type II & Type IV 2HDM are similar to the analogous limits in Spectrum 1, although somewhat stronger due to the enhanced production

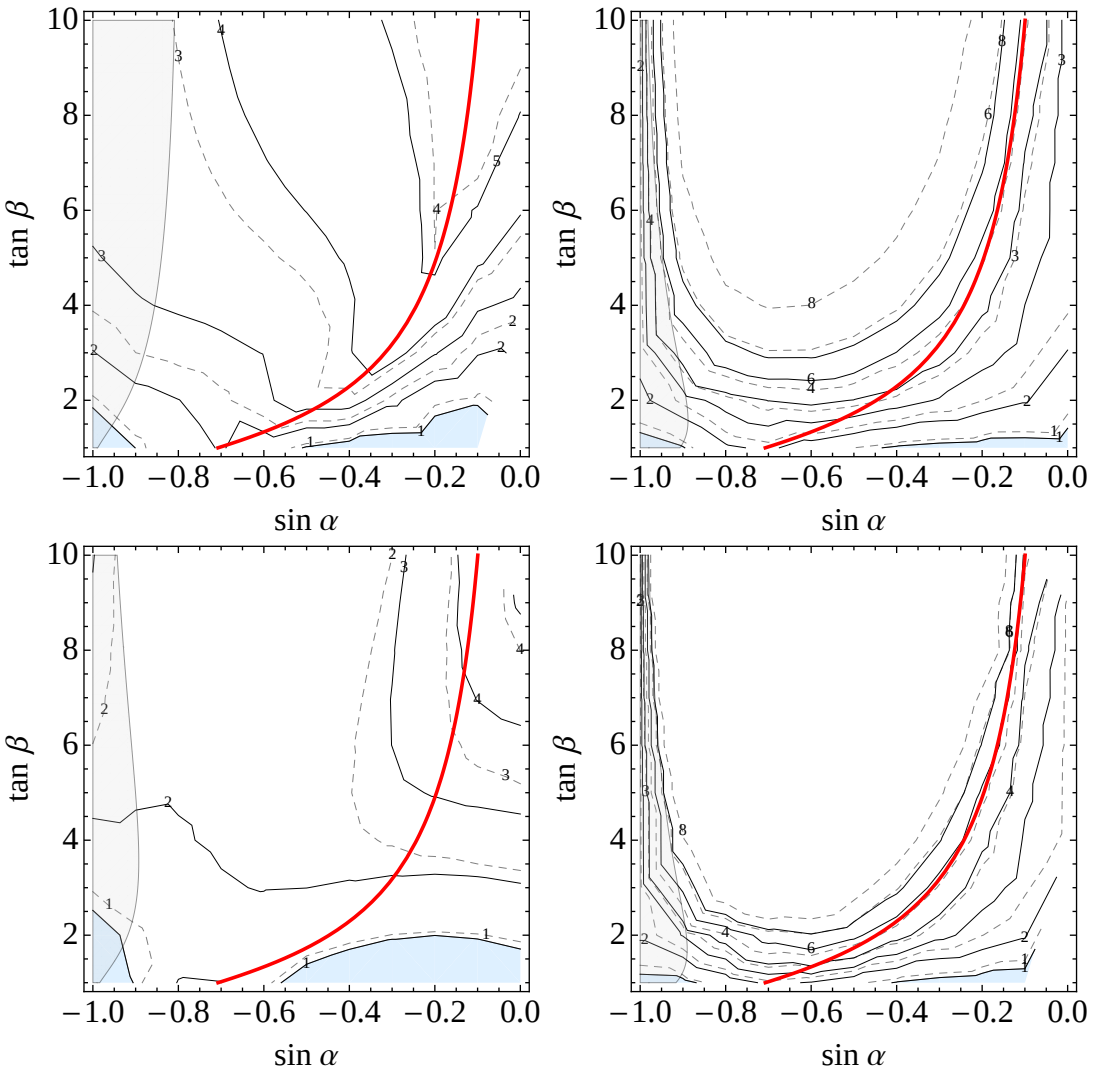

Figure 6.5: Multi-lepton limits from the CMS multi-lepton search with 5 fb^{-1} of 7 TeV proton-proton collisions [67] for the production and decay topologies of Benchmark Spectrum 2 given in Table 6.5, for Type I (top left), Type II (top right), Type III (bottom left), and Type IV (bottom right) couplings as a function of $\sin\alpha$ and $\tan\beta$. Limits were obtained from an exclusive combination of the observed and expected number of events in all the multi-lepton channels presented in Table 5.2. The solid and dashed lines correspond to the observed and expected 95% CL limits on the production cross section times branching ratio in multiples of the theory cross section times branching ratio for the benchmark spectrum and 2HDM type. The blue shaded regions denote excluded parameter space. The solid red line denotes the alignment limit $\sin(\beta-\alpha)=1$. The gray shaded region corresponds to areas of parameter space where vector decays of the heavy CP-even Higgs, $H \to WW^*$, are excluded at 95% CL by the SM Higgs searches at 7 TeV [59].

cross sections for A and H. Note that there is no significant weakening of the limit at large $\tan\beta$ and moderate $\sin\alpha$ compared to Spectrum 1, despite the disappearance of the decay $H \to hh$. This exemplifies the fact that in Type II and Type IV 2HDM, the multi-lepton decays of h are suppressed in this range, so the presence or absence of $H \to hh$ does not significantly alter the limit.

6.5.3 Spectrum 3

The multi-lepton limits on the third benchmark spectrum for all four types of 2HDM are shown in Figure 6.6. The third benchmark spectrum enjoys a plethora of inter-scalar cascade decays. In particular, the important inter-scalar decays include $H \to hh$, $H \to AA$, $H \to H^+H^-$, $H \to ZA$, $H^\pm \to W^\pm h$, and $A \to Zh$. The fact that $H \to H^+H^-, AA, ZA$ and both $H^\pm \to W^\pm h$ and $A \to Zh$ are open allows for the possibility of multi-step cascades involving three Higgs scalars. Also note that the range of possible decays of H means that the overlap of large $\Gamma(H \to hh)$ with multi-lepton decays of h is not as important to limit-setting as it was in Spectrum 1, since, e.g., $H \to AA, ZA$ with $A \to \tau\tau$ may be important even when the multi-lepton decays of h are small. However, since H is relatively heavy in this benchmark ($m_H = 500$ GeV), the direct multi-lepton decays of H are less important to limit-setting relative to other benchmarks due to the lower production cross section. The partial widths and $\sigma \cdot \mathrm{Br}$ for those processes unique to Spectrum 3 are shown in Figure 6.7 (the parametric dependence of $H \to hh$ and $A \to Zh$ were already shown in Figure 6.2 and the dependence of $H^\pm \to W^\pm h$ will be shown in Figure 6.11 when we discuss Spectrum 4).

The partial widths $\Gamma(H \to AA)$ and $\Gamma(H \to H^+H^-)$ are complicated functions of α and β, but grow as $\tan\beta$ increases and $\sin\alpha$ goes to zero. The partial widths, $\Gamma(H \to ZA)$ and $\Gamma(H \to H^\pm W^\mp)$, scale simply as $\sin^2(\beta - \alpha)$, and so is largest in the alignment limit, while the partial widths, $\Gamma(A \to hZ)$ and $\Gamma(H^\pm \to W^\pm h)$, scale as $\cos^2(\beta - \alpha)$ and is largest away from the alignment limit. Note in Figure 6.7 the partial widths, $\Gamma(H \to AA)$ and $\Gamma(H \to H^+H^-)$, grow quite large with increasing $\tan\beta$, such that the total width of H exceeds its mass for $\tan\beta \gtrsim 5$ and $\sin\alpha \gtrsim -0.8$.

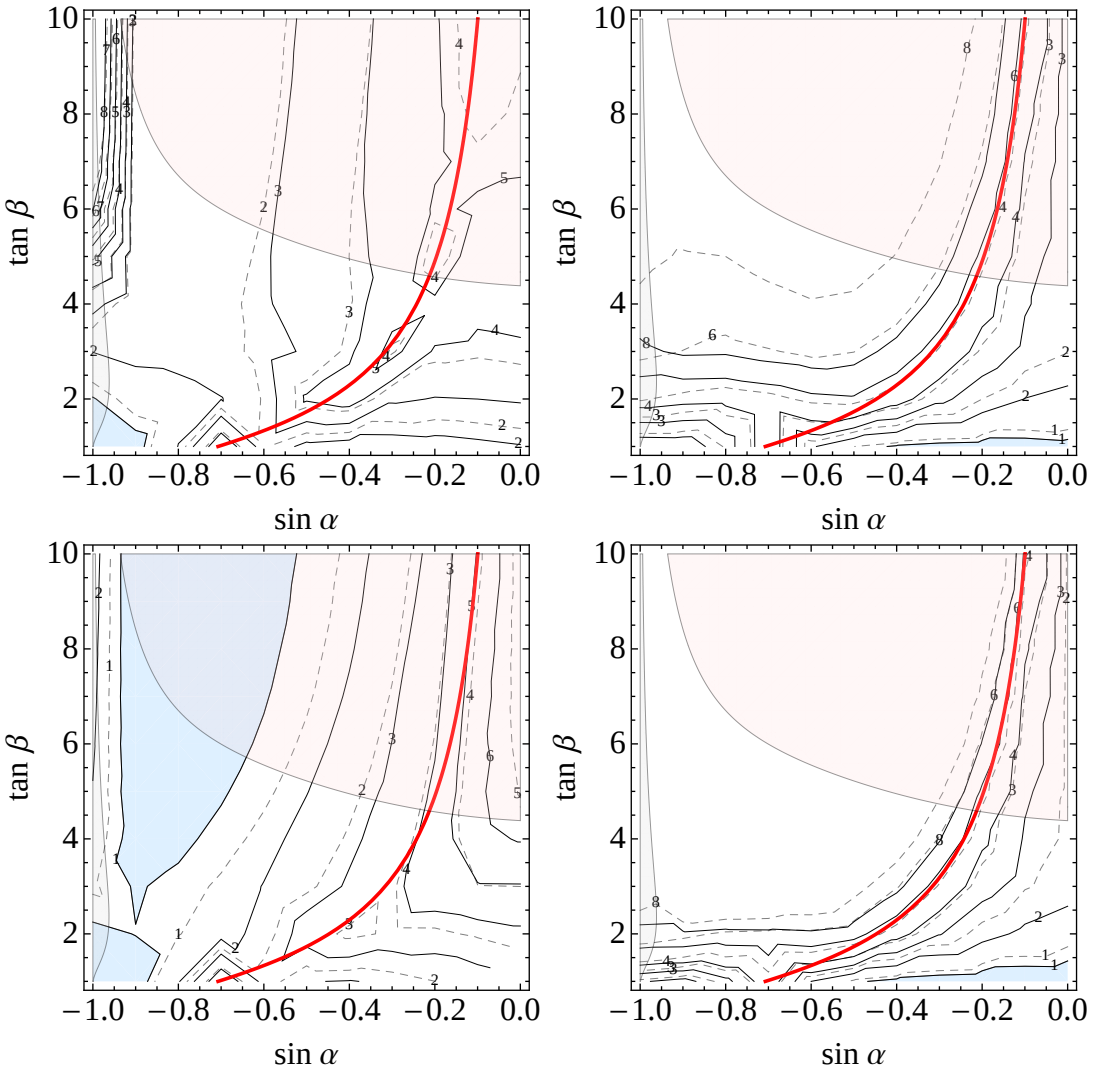

Figure 6.6: Multi-lepton limits from the CMS multi-lepton search with 5 fb^{-1} of 7 TeV proton-proton collisions [67] for the production and decay topologies of Benchmark Spectrum 3 given in Table 6.5, for Type I (top left), Type II (top right), Type III (bottom left), and Type IV (bottom right) couplings as a function of $\sin\alpha$ and $\tan\beta$. Limits were obtained from an exclusive combination of the observed and expected number of events in all the multi-lepton channels presented in Table 5.2. The solid and dashed lines correspond to the observed and expected 95% CL limits on the production cross section times branching ratio in multiples of the theory cross section times branching ratio for the benchmark spectrum and 2HDM type. The blue shaded regions denote excluded parameter space. The solid red line denotes the alignment limit $\sin(\beta-\alpha)=1$. The gray shaded region corresponds to areas of parameter space where vector decays of the heavy CP-even Higgs, $H \to VV^*$, are excluded at 95% CL by the SM Higgs searches at 7 TeV [59].In all cases, for $\tan\beta \gtrsim 5$ and $\sin\alpha \gtrsim -0.8$ the total width of H grows comparable to its mass and the precise exclusion limit in this region is subject to large theoretical uncertainties, these regions are highlighted in light red.

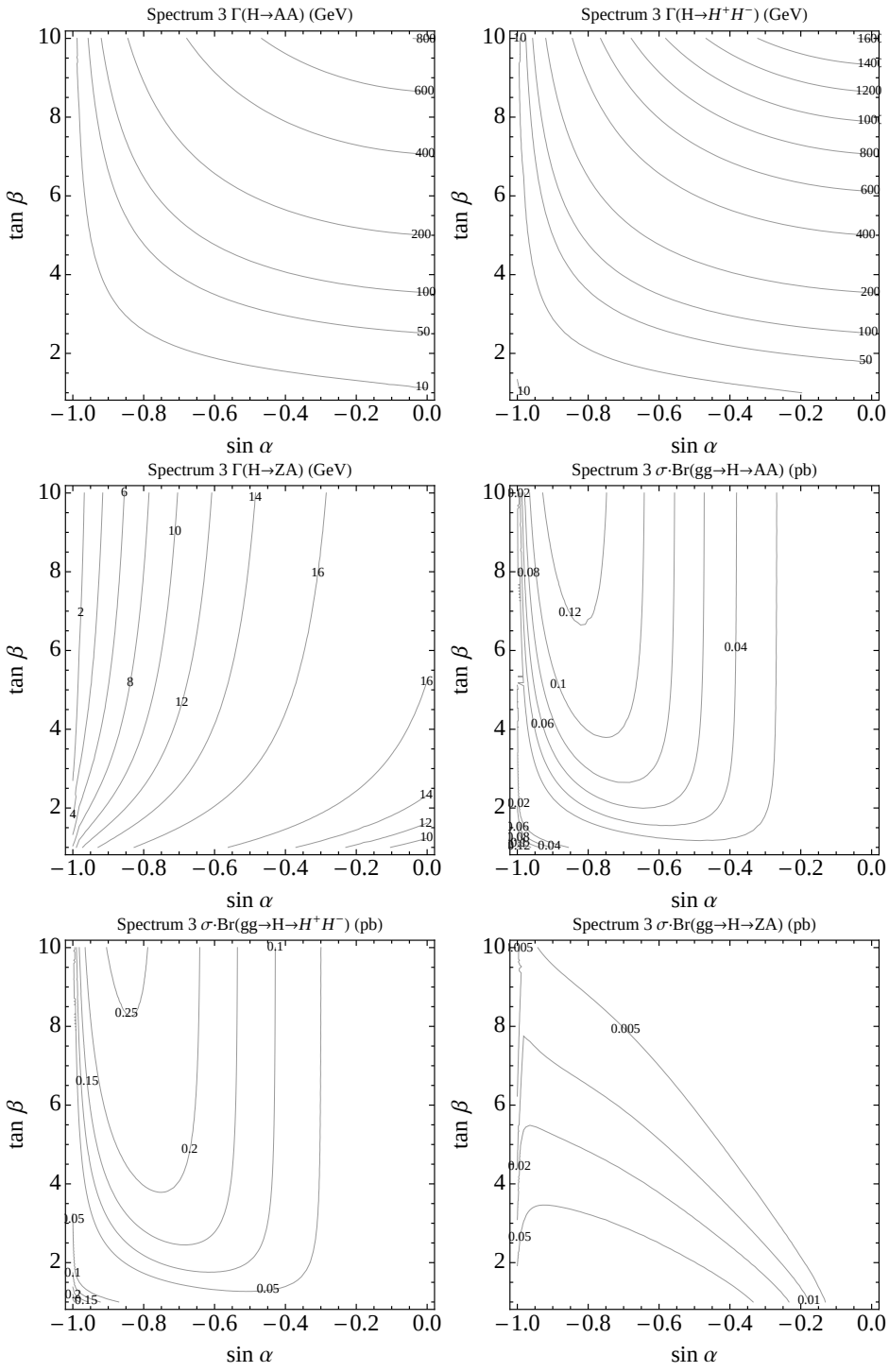

Figure 6.7: 2HDM Benchmark Spectrum 3 partial widths $\Gamma(H \to AA)$, $\Gamma(H \to H^+H^-)$, and $\Gamma(H \to ZA)$ in units of GeV, and cross section times branching ratios $\sigma \cdot \mathrm{Br}(gg \to H \to AA)$, $\sigma \cdot \mathrm{Br}(gg \to H \to H^+H^-)$, and $\sigma \cdot \mathrm{Br}(gg \to H \to ZA)$ in units of pb, all for Type I couplings. These partial widths and $\sigma \cdot \mathrm{Brs}$ are qualitatively similar for the other types of 2HDM; the production cross section $\sigma(gg \to H)$ is moderately enhanced at large $\tan\beta$ for Type II and Type IV 2HDM due to the contribution from bottom loops.

In this regime, both the perturbative expansion in scalar couplings and the narrow width approximation break down, and the precise exclusion limit should be treated with caution.

On the production end, as noted earlier the dominant production mode for H, $\sigma(gg \to H)$, is largest at small $\tan\beta$ and $\sin\alpha \to -1$. The combination of this dependence and the partial widths implies that $\sigma \cdot \mathrm{Br}(gg \to H \to AA)$ and $\sigma \cdot \mathrm{Br}(gg \to H \to H^+H^-)$ are largest at moderate $\sin\alpha$, peaking around $\sin\alpha \sim -0.8$ and increasing mildly with $\tan\beta$; both contribute over a somewhat wider range than $gg \to H \to hh$. In contrast, $\sigma \cdot \mathrm{Br}(gg \to H \to ZA)$ is largest at low $\tan\beta$ and $\sin\alpha \to -1$.

Types I & III

The signals of the Type I 2HDM for the third benchmark spectrum are similar to those of the first benchmark spectrum, to the extent that they are largely governed by the multi-lepton final states of h combined with the scalar decays of H and A. However, in contrast to Spectrum 1, here the direct multi-lepton decays of H are less significant in limit-setting since the production cross section for $m_H = 500$ GeV is considerably smaller. Thus, the limits at large $\tan\beta$ and $\sin\alpha \to -1$ coming from direct multi-lepton decays of H are noticeably weaker in this case. On the other hand, scalar decays of H contribute meaningfully over a wide range in $\sin\alpha$ since $\sigma \cdot \mathrm{Br}(gg \to H \to AA)$ and $\sigma \cdot \mathrm{Br}(gg \to H \to H^+H^-)$ change slowly as a function of $\sin\alpha$ compared to $\sigma \cdot \mathrm{Br}(gg \to H \to hh)$.

In the case of processes involving $H \to AA$, the multi-lepton limits are dominated by the decays $A \to Zh$ rather than $A \to \tau\tau$. This is because in a Type I model the $A\tau\tau$ coupling decreases with increasing $\tan\beta$, so that the branching ratio $\mathrm{Br}(A \to \tau\tau)$ is not large in the same region as $\sigma \cdot \mathrm{Br}(gg \to H \to AA)$. In contrast, the branching ratio $\mathrm{Br}(A \to Zh)$ is large precisely when $\mathrm{Br}(H \to AA)$ is large, hence $H \to AA \to ZhZh$ contributes substantially to the limit at large $\tan\beta$ and $-0.9 \lesssim \sin\alpha \lesssim -0.4$, with $\sigma \cdot \mathrm{Br}(gg \to H \to AA \to ZhZh)$ growing as large as ~ 120 fb in the region of study.

For processes involving $H \to H^+H^-$, the multi-lepton limits always require at least one charged Higgs to decay via $H^\pm \to W^\pm h$, since the other decay modes such as e.g.

$H^+ \to t\bar{b}, \tau^+\nu$ give at most one lepton. In a Type I model, $\mathrm{Br}(H^\pm \to W^\pm h)$ is sizable when $\mathrm{Br}(H \to H^+H^-)$ is large, so $H \to H^+H^- \to W^+hW^-h$ is important at large $\tan\beta$ in the range $-0.9 \lesssim \sin\alpha \lesssim -0.5$. Processes involving $H \to H^+H^-$ with one decay to $t\bar{b}$ and $\tau\nu$ are also important at moderate $\tan\beta$.

As in previous cases, $gg \to A \to Zh$ is important at small $\tan\beta$, as is $gg \to H \to ZA$ with both $A \to \tau\tau$ and $A \to Zh$. Various exemplary features of the third benchmark spectrum with Type I 2HDM couplings are shown in Figure 6.8, which illustrates the H_T and MET distributions for the sum of multi-lepton events at the point ($\sin\alpha = -0.9, \tan\beta = 1.0$), distinguished by the initial scalar produced in each multi-lepton event.

The Type III 2HDM shares many of the qualitative features of the Type I 2HDM, albeit with additional contributions to multi-lepton signals coming from the fact that the partial widths $\Gamma(h \to \tau\tau)$ and $\Gamma(A \to \tau\tau)$ grow with $\tan\beta$. So, in addition to the significant signals discussed earlier, both $H \to hh \to 4\tau$ and $H \to AA \to 4\tau$ are important in the Type III 2HDM, particularly at moderate $\sin\alpha$ and large $\tan\beta$ where $\mathrm{Br}(H \to hh, AA)$ are large and so too are $\mathrm{Br}(h, A \to \tau\tau)$. Taken together, these contributions are still not as great as in Spectrum 1 due to the reduced production cross section for H, but nonetheless lead to large regions already excluded using the 5 fb^{-1} data.

Types II & IV

As in previous cases, the multi-lepton final states of h decrease rapidly above the alignment limit, with the sole exception of $h \to \tau\tau$. Here, the reduced contribution from direct multi-lepton decays of H is particularly noticeable, with a substantial weakening of the limit as $\sin\alpha \to -1$.

Much as in Spectrum 1 Type II, processes involving $H \to hh$ contribute little to the limit, since h has suppressed multi-lepton final states when $\mathrm{Br}(H \to hh)$ is large. The decay, $H \to AA$, is somewhat more important, but, as with the Type III model, the contribution to multi-leptons comes primarily from $A \to \tau\tau$ as opposed to $A \to Zh$, especially at large $\tan\beta$. The $A\tau\tau$ coupling grows with $\tan\beta$ in a Type II 2HDM, but,

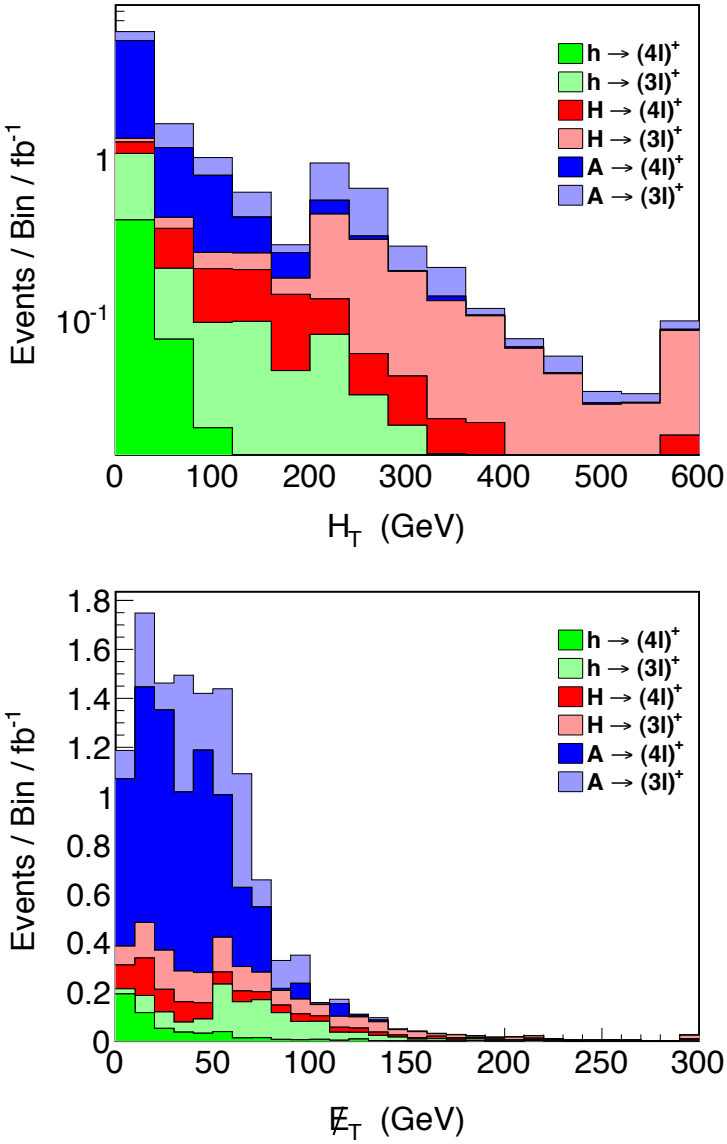

Figure 6.8: The 2HDM signal transverse hadronic energy distribution (left) and missing transverse energy distribution (right) after acceptance and efficiency for 7 TeV proton-proton collisions arising from the production and decay topologies of Benchmark Spectrum 3 given in Table 6.7 with $m_h = 125$ GeV, $m_H = 500$ GeV, $m_{H^\pm} = m_A = 230$ GeV,for Type I 2HDM couplings with $\sin\alpha = -0.9$ and $\tan\beta = 1.0$. Signal events correspond to those falling in the exclusive three- or four-lepton channels labelled with a dagger in Table 5.2 that have moderate to good sensitivity. The colors indicate the initial type of Higgs boson produced. For each color, the lighter shade corresponds to three-lepton channels, while the darker shade corresponds to four-lepton channels. The bin size is 40 GeV for H_T and 10 GeV for $\not{E}_T$, and in both cases the highest bin includes overflow.

as before, $A \to b\bar{b}$, with the same parametric scaling, still dominates the total width of A. Similarly, $H^\pm$ decays primarily to tb and $\tau\nu$ at large $\tan\beta$, so $H^\pm \to W^\pm h$ is suppressed in this range and processes involving $H \to H^+H^-$ do not contribute much to the multi-lepton limits.

The processes $gg \to A \to Zh$ and $gg \to H \to Z(A \to Zh)$ are important at small $\tan\beta$; here the multi-lepton decays of h are enhanced below the alignment line, so that these processes contribute significantly to the limit through the direct multi-lepton decays of h. The contributions of the pseudoscalar are exemplified by Figure 6.9, which illustrates the H_T and MET distributions for the sum of multi-lepton events at the point $(\sin\alpha = -0.2, \tan\beta = 1.0)$, for which there is a large contribution from $A \to Zh$.

The Type IV 2HDM recapitulates many of the features of the Type II 2HDM, albeit without significant contributions from $h \to \tau\tau$ or $A \to \tau\tau$ at large $\tan\beta$. This eliminates contributions from, e.g., $H \to hh \to 4\tau$ and $H \to AA \to 4\tau$, so that the multi-lepton limits are particularly weak at moderate $\sin\alpha$ and large $\tan\beta$. As before, the multi-lepton decays of h are important below the alignment line, and accumulate extra contributions from $gg \to A \to Zh$ and $gg \to H \to Z(A \to Zh)$ at low $\tan\beta$.

6.5.4 Spectrum 4

The multi-lepton limits on the first benchmark spectrum for all four types of 2HDM are shown in Figure 6.10. The fourth benchmark spectrum highlights the signals of a light pseudoscalar, both through decays of other scalars and through direct production in association with those scalars. Kinematically available inter-scalar decays include $H \to AA$, $H^\pm \to W^\pm h$, and $H^\pm \to W^\pm A$, while interesting associated production processes unique to this benchmark include $q\bar{q} \to H^\pm A$, $q\bar{q} \to Ah$, and $q\bar{q} \to AH$ through off-shell W and Z bosons. The partial widths and $\sigma \cdot \mathrm{Brs}$ for several of these processes are shown in Figure 6.11.

The partial width $\Gamma(H^\pm \to W^\pm h)$ scales as $\cos^2(\beta-\alpha)$ and hence grows away from the alignment limit. In contrast, $\Gamma(H^\pm \to W^\pm A)$ is entirely independent of the angles α, β. On the production side, $\sigma(q\bar{q} \to Ah) \propto \cos^2(\beta-\alpha)$ grows away from the alignment limit, while $\sigma(q\bar{q} \to AH) \propto \sin^2(\beta-\alpha)$ grows as we approach the alignment limit. The

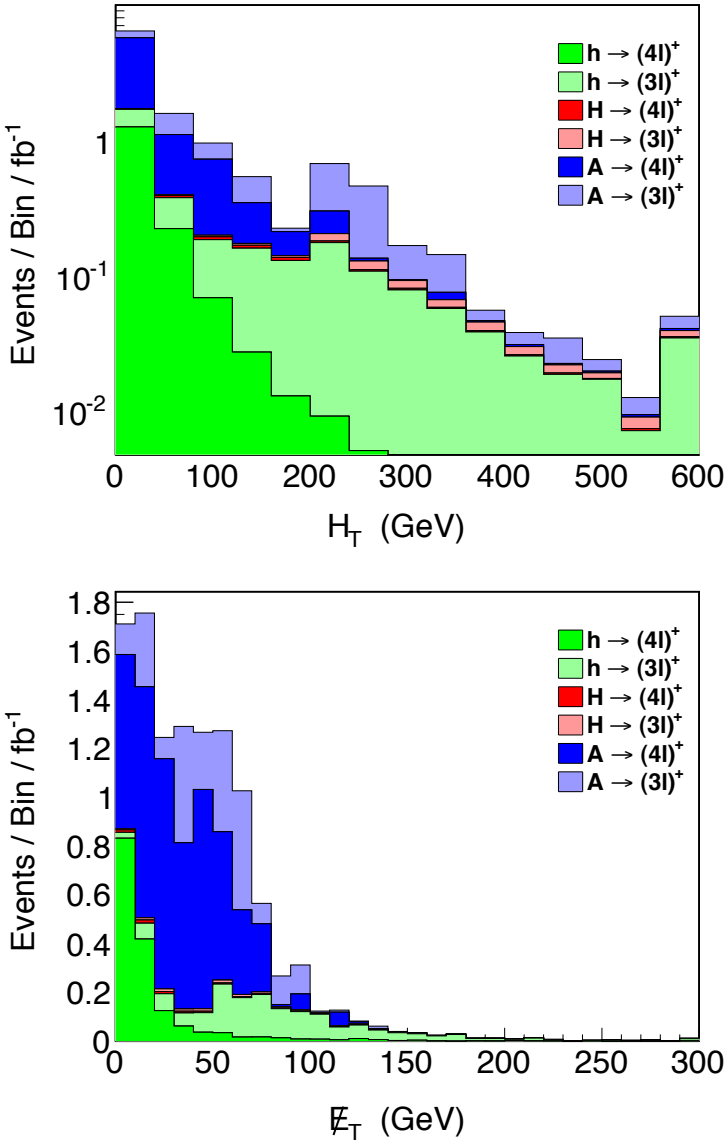

Figure 6.9: The 2HDM signal transverse hadronic energy distribution (left) and missing transverse energy distribution (right) after acceptance and efficiency for 7 TeV proton-proton collisions arising from the production and decay topologies of Benchmark Spectrum 3 given in Table 6.7 with $m_h = 125$ GeV, $m_H = 500$ GeV, $m_{H^\pm} = m_A = 230$ GeV, for Type II 2HDM couplings with $\sin\alpha = -0.2$ and $\tan\beta = 1.0$. Signal events correspond to those falling in the exclusive three- or four-lepton channels labelled with a dagger in Table 5.2 that have moderate to good sensitivity. The colors indicate the initial type of Higgs boson produced. For each color, the lighter shade corresponds to three-lepton channels, while the darker shade corresponds to four-lepton channels. The bin size is 40 GeV for H_T and 10 GeV for $\not{E}_T$, and in both cases the highest bin includes overflow.

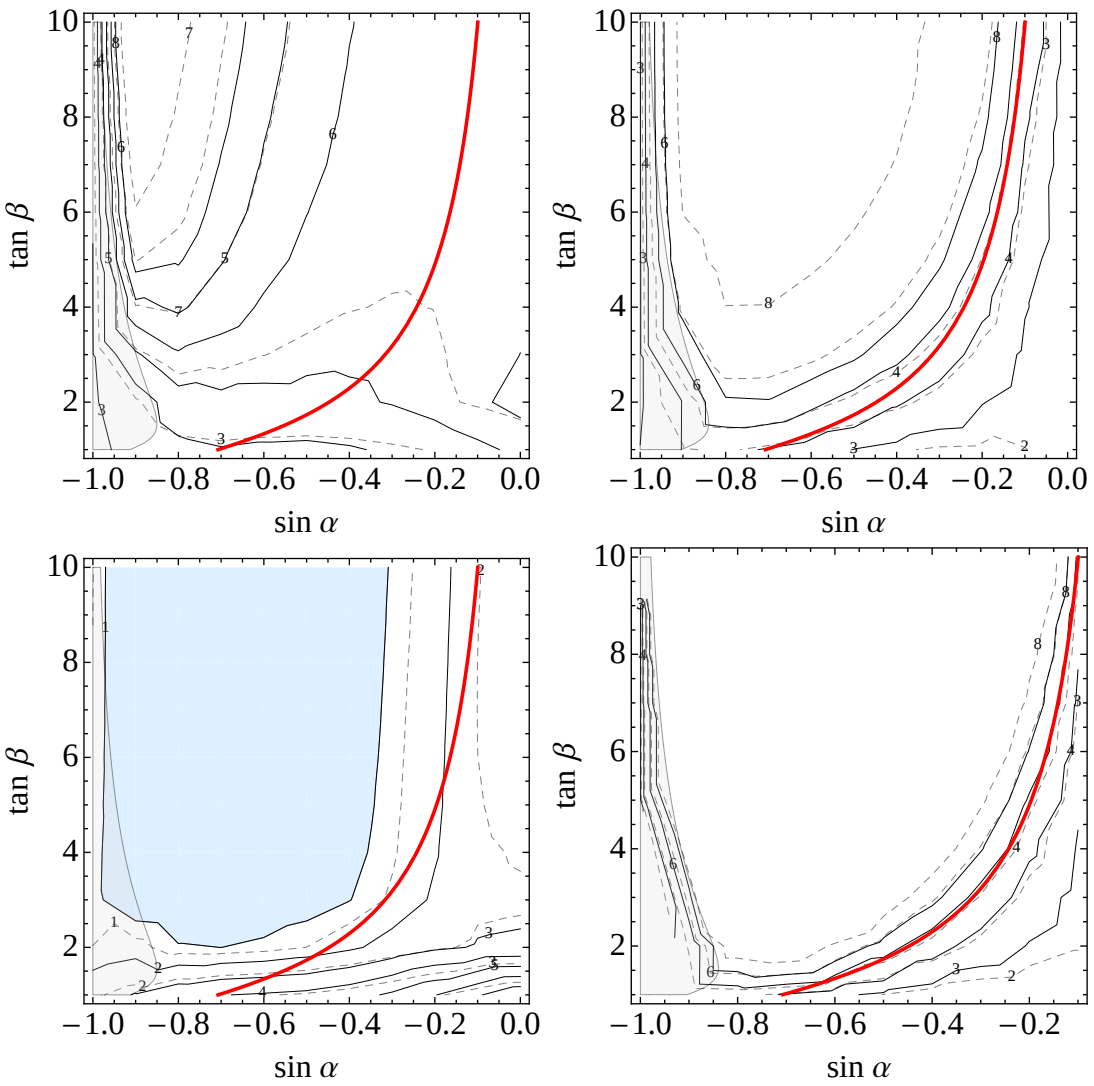

Figure 6.10: Multi-lepton limits from the CMS multi-lepton search with 5 fb^{-1} of 7 TeV proton-proton collisions [67] for the production and decay topologies of Benchmark Spectrum 4 given in Table 6.5, for Type I (top left), Type II (top right), Type III (bottom left), and Type IV (bottom right) couplings as a function of $\sin\alpha$ and $\tan\beta$. Limits were obtained from an exclusive combination of the observed and expected number of events in all the multi-lepton channels presented in Table 5.2. The solid and dashed lines correspond to the observed and expected 95% CL limits on the production cross section times branching ratio in multiples of the theory cross section times branching ratio for the benchmark spectrum and 2HDM type. The blue shaded regions denote excluded parameter space. The solid red line denotes the alignment limit $\sin(\beta-\alpha)=1$. The gray shaded region corresponds to areas of parameter space where vector decays of the heavy CP-even Higgs, $H\to VV^*$, are excluded at 95% CL by the SM Higgs searches at 7 TeV [59].

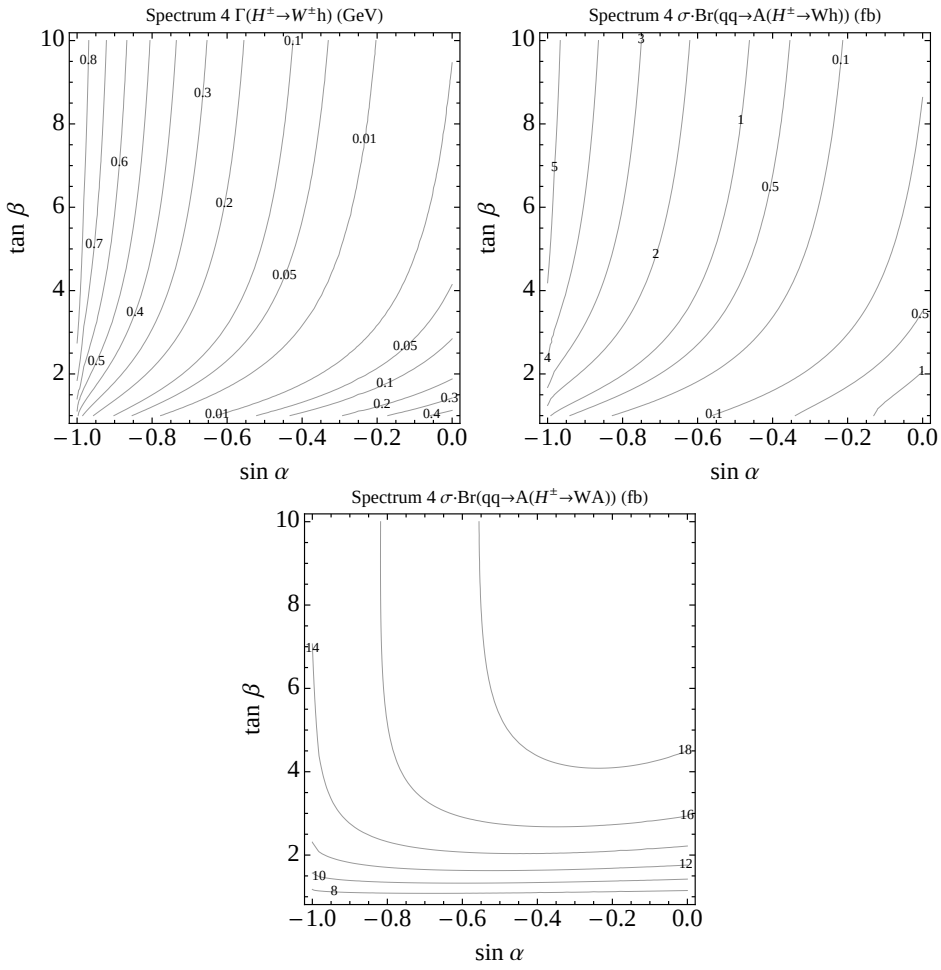

Figure 6.11: 2HDM Benchmark Spectrum 4 partial width $\Gamma(H^{\pm} \to W^{\pm}h)$ in units of GeV, and cross section times branching ratios $\sigma \cdot \mathrm{Br}(q\bar{q} \to A(H^{\pm} \to Wh))$ and $\sigma \cdot \mathrm{Br}(q\bar{q} \to A(H^{\pm} \to WA))$ in units of pb for Type I couplings. he partial width $\Gamma(H^{\pm} \to W^{\pm}A)$ is independent of α and β and is not shown explicitly.

production cross section $\sigma(q\bar{q} \to H^{\pm}A)$ is likewise independent of α, β since it scales as the square of the $H^{\pm}W^{\mp}A$ coupling. However, the partial widths of $H^{\pm}$ decays to SM states do depend on α and β, so the $\sigma \cdot \mathrm{Br}(q\bar{q} \to A(H^{\pm} \to W^{\pm}A))$ ultimately varies with $\sin\alpha$ and $\tan\beta$ due to the changing total width. As is apparent in Figure 6.11, the cross section for these processes is quite low, on the order of a few tens of femtobarns before further branching fractions are applied, so their inclusion is essentially for the sake of completeness; they contribute very little to the total multi-lepton limit.

Consequently, most qualitative features of this benchmark spectrum may be understood simply by the combination of the direct multi-lepton decays of H and h as well as the cascade decay $H \to AA$ with $A \to \tau\tau$, which in this spectrum is the only source of multi-lepton signals from processes involving the pseudoscalar.

Types I & III

In a Type I 2HDM, the limit is largely governed by the direct multi-lepton decays of h and H. In particular, the multi-lepton decays of h are SM-like around the alignment limit and decrease slowly away from this limit. As $\sin\alpha \to -1$, the multi-lepton signals of H become important and somewhat compensate for the vanishing signals of h. The branching ratio $H \to AA$ is large at moderate $\sin\alpha$ and large $\tan\beta$, but $\mathrm{Br}(A \to \tau\tau)$ does not grow exceptionally large in this regime, so the contribution to multi-lepton limits from $H \to AA$ is not great.

In the Type III 2HDM, the multi-lepton signals are much as in the Type I 2HDM with the exception of those involving $h \to \tau\tau$ and $A \to \tau\tau$. Thus, the process $gg \to H \to AA \to 4\tau$ contributes significantly in this 2HDM type. Unsurprisingly, in the region excluded by 5 fb^{-1} data, $\sigma \cdot \mathrm{Br}(gg \to H \to AA \to 4\tau)$ is large, $\gtrsim 500$ fb, with the current exclusion contour tracking the contours of $\Gamma(H \to AA)$.

Types II & IV

In Type II, the multi-lepton signals of h from decays to vectors decrease rapidly above the alignment limit and increase rapidly below it, again supplemented by the multi-lepton signals of H as $\sin\alpha \to -1$. The multi-lepton signals of associated production

with $h \to \tau\tau$ are somewhat important at large $\tan\beta$, but are not significantly enhanced over the SM rate since $h \to b\bar{b}$ grows equally quickly and controls the total width. Similarly, although the $A\tau\tau$ coupling grows with $\tan\beta$, so too does the coupling $Ab\bar{b}$, so $H \to AA \to 4\tau$ is not particularly important here.

For Type IV 2HDM the limits are much as in the Type II 2HDM, albeit with the loss of multi-lepton signals coming from $h \to \tau\tau$ and $A \to \tau\tau$ at large $\tan\beta$, leading to the weakest overall limits among 2HDM types.

6.6 Towards a Dedicated Multi-Lepton 2HDM Search

In the wake of the discovery of a Standard Model-like Higgs, exploring and bounding extensions of the EWSB sector takes on paramount importance. Models with two Higgs doublets are among the simplest and best motivated such extensions to the Higgs sector. In this work, we have examined the reach of multi-lepton searches for probing the collective leptonic signatures resulting from the additional Higgs bosons in 2HDMs. In a study of 20 exclusive multi-lepton channels in four benchmark spectra with four discrete types of fermion couplings across 222 production and decay topologies, using a factorized mapping procedure [70] we determined regions of 2HDM parameter space probed by data from a recent CMS multi-lepton search [67] with 5 fb^{-1} of 7 TeV proton-proton collisions. These results provide new limits in some regions of 2HDM parameter space that have not been covered by other types of direct experimental investigations. Increased luminosity and production rates with 8 TeV proton-proton collisions and beyond will extend the 2HDM limits and discovery potential of multi-lepton searches.

Although the CMS multi-lepton searches [66, 67] in their current incarnation are extremely powerful tools for probing new physics, with appropriate modifications the searches could be tailored in order to enhance sensitivity to 2HDM signals. Subdividing all exclusive multi-lepton channels by zero, one, or two or more b-tagged jets in an event should significantly increase sensitivity to 2HDM final states with bottom quarks. Although many of 3- and 4- lepton events coming from production and

decays of scalars in 2HDM populate the exclusive channels with relatively high backgrounds, most of the irreducible prompt background does not contain additional b-jets. For those backgrounds that do, very rarely, b-jets will provide isolated leptons, so two b-tags will substantially reduce major backgrounds (with the notable exception of $t\bar{t}$ plus a prompt fake lepton and $t\bar{t}V$), while leaving many 2HDM signal processes, such as $H \to hh \to ZZbb$, $t\bar{t}A \to t\bar{t}Zh$, $t\bar{t}A \to t\bar{t}\tau\tau$, $H \to A(A \to Zh) \to \tau\tau Zbb$, $H \to H^+H^- \to tbWh$, $H \to ZA \to ZZh \to ZZb\bar{b}$, and, of course, $t\bar{t}h$, relatively unaffected.

Final states with multiple τ-leptons are among the most promising for discovery or exclusion of various 2HDM. In our study, we have focused solely on leptonically-decaying τs, since final states with hadronic τs will often have larger backgrounds. However, ignoring hadronic τs reduces sensitivity to, in particular, four-τ final states with low $\sigma \cdot \mathrm{Br}$. A further partitioning of the 4ℓ, 2τ bins in a study optimized for four-τ signals may yield lower backgrounds in DY0 bins, e.g. $\tau_h^+\tau_h^+e^-\mu^-$, allowing for improved limits. As much of the energy in these events are going into leptons, defining signal regions either with harder p_T cuts on leptons or with a cut on $\sum p_{T,\ell}$ could serve to significantly deplete the high SM backgrounds in some bins while leaving the signal largely unfazed. We have also restricted our focus to three- and four-lepton final states. Some additional sensitivity may be gained by adding exclusive channels with same-sign di-leptons subdivided by various combinations of $\not{E}_T$ and H_T. These channels would capture other decay modes of some of the production and decay topologies studied here, as well as bring in additional topologies that do not yield three or more leptons. Multiple Higgs bosons can also give rise to rare five- or more lepton signatures; adding channels to separate out these signatures would also increase sensitivity, particularly at high luminosity.

Finally, with a known Higgs mass, one can capitalize on partial or full kinematic constraints of its decays to help to isolate Higgs particles arising via new sources of associated production. Such kinematic tagging can serve to further reduce SM backgrounds. One example of this would be forward jet tagging to highlight VBF signals. Another would be channel specific lepton kinematics focussed at specific decay topologies. One

of the simplest and most effective ways to utilize kinematic tagging to enhance sensitivity to certain multi-lepton signatures that include a SM-like Higgs boson would be to subdivide the DY2 four- or more lepton channels into an On Higgs category in which the invariant mass of the four leptons fall within a small window centered on the Higgs boson mass. Signals that include at least one SM-like Higgs boson that decays directly to four leptons fall in this sub-channel. The backgrounds in this special On Higgs sub-channel are very limited, thereby increasing sensitivity to such Higgs boson signals. Utilizing partial (rather than full) kinematic tagging could also increase sensitivity to other decay topologies that fall in other channels.

While we have focused on 2HDMs, other extensions of the Higgs sector can lead to the production of new heavy, Higgs-like scalar resonances with decay topologies similar to those studied in this work. Such new, Higgs-like particles generally lead to intermediate states composed of the heaviest SM particles, including t, h, Z, W, b and τ, whose final states contain multi-lepton signatures. If there exists an extended Higgs sector, multi-lepton searches optimized for the leptonic final states of Higgs scalars may prove an effective route for discovering new physics beyond the Standard Model.

Chapter 7

Rare Flavor Processes involving Higgs

The existence of a Standard Model-like Higgs boson has been firmly established at the Large Hadron Collider (LHC) with an experimentally fortuitous value of mass at 125 GeV. This mass is fortuitous because of fact that at 125 GeV, an unusually large the number of channels for the Higgs decay are allowed by the kinematics and the couplings.

One opportunity that automatically presents itself upon the discovery of any new particle, is the opportunity to explore deviations in flavor observables coming from processes involving this new particle. The Higgs is no exception to this. In fact we've already seen that multi-lepton signatures originating from Standard Model production and decay of the Higgs boson itself provide considerable sensitivity [86] to searches for new physics, and in conjunction with additional leptons they could provide powerful probes of non-Standard Model processes that include a Higgs.

One class of non-Standard Model processes of interest are those in which the Higgs boson appears only rarely in association with other particles. In this case, observation of a new physics process requires a large production cross section, making it fruitful to consider Standard Model processes with large production cross section. The production of top-anti-top quark pairs is particularly attractive in this respect, with a cross section of 100's of pb at the LHC. This suggests looking for Higgs bosons in the decay products of the top quark, such as would arise through the rare neutral flavor-changing transition to a charm quark, $t \to ch$. Although this decay is not forbidden by any symmetry, the Standard Model contribution to the branching ratio suffers from GIM suppression and second-third generation mixing, suppressing it to the order of $\mathrm{Br}(t \to ch) = 10^{-13} - 10^{-15}$ [87–89]. Thus a positive observation of the process $t \to ch$ well above the Standard Model rate would be a convincing indication of new physics beyond the

Standard Model.

Pair production of top-anti-top followed by the rare decay $t \to ch$ gives rise to multi-lepton final states with up to five leptons. The leading processes involve leptonic charged- current decay of one of the top quarks, $t \to Wb$ with $W \to \ell\nu$, and flavor-changing decay of the other top quark, $\bar{t} \to \bar{c}h$ with leptonic final state decay modes of the Higgs boson. These include $h \to WW \to \ell\nu\ell\nu$, and $h \to \tau\tau$ with leptonic decay of the tau-leptons, $\tau \to \ell X$, as well as $h \to ZZ^* \to jj\ell\ell, \nu\nu\ell\ell, \ell\ell\ell\ell$. Hadronic decay of one of the top quarks, $t \to Wb$ with $W \to jj$, and flavor-changing decay of the other top quark, $\bar{t} \to \bar{c}h$ with $h \to ZZ \to \ell\ell\ell\ell$ also contributes. Such multi-lepton final states have relatively low Standard Model backgrounds, making them promising targets for a multi-lepton search. To investigate the utility of searching for $t \to ch$ in this way, we make use of the results of a multi-lepton search conducted by the CMS collaboration with $5\,\mathrm{fb}^{-1}$ of data collected from 7 TeV pp collisions [90] to estimate a limit on the branching ratio $\mathrm{Br}(t \to ch)$. The power of this search lies in the combination of numerous exclusive channels. While any individual channel alone is not necessarily significant, the exclusive combination across multiple channels is found to provide an interesting sensitivity to $\mathrm{Br}(t \to ch)$ at the percent- level. To our knowledge this is the first use of the Higgs boson as a probe for new physics in existing data.

The neutral flavor-changing decay of a top quark to the Higgs boson and charm quark, $t \to ch$, is of interest because it provides a direct probe of flavor violating couplings to the Higgs sector for the quark that is most strongly coupled to that sector. Previous probes of flavor violating couplings to the Higgs sector for the lighter quarks have been only indirect. It is also of general interest because up-type quark flavor violation is less well constrained than that for down-type quarks. Given that this process has not been investigated experimentally at any level previously, the percent-level bound on $\mathrm{Br}(t \to ch)$ obtained here begins to open up an interesting new window into flavor violating physics. First we present an effective operator analysis of the rare decay $t \to ch$ and give the relation between the branching ratio and new physics scale of the leading operator that contributes to this process. Then we review multi-channel multi-lepton searches and compare the results of a CMS search with our simulation of

top quark pair production and decay, including $t \to ch$, to obtain the first limits on $\mathrm{Br}(t \to ch)$ for a Standard Model-like Higgs boson. We also suggest improvements that could increase the intrinsic sensitivity of future dedicated multi-lepton searches for $t \to ch$. We then conclude by discussing the wider applicability of this result couched in terms of a cross section times branching limit on new physics that yields final states with a W -boson in association with a Higgs boson. It should be noted that, although throughout we refer to the flavor-violating decay of the top quark to a Higgs boson as $t \to ch$, since the identity of the charm quark is not integral to the analysis, the discussion and results apply more generally to the decay $t \to Xh$ with inclusive X final states.

7.1 Effective Operator Description of $t \to ch$

New physics contributions to the flavor-violating top quark decay $t \to ch$ may be encoded in an effective field theory description of the operators that can contribute to this process. For the field content of the minimal Standard Model, the leading coupling of the Higgs boson to up-type quarks is through the renormalizable dimension-four Yukawa coupling

$$\lambda_{ij} Q_i H \overline{u}_j + h.c. \tag{7.1}$$

where the quark fields are two component complex Weyl Fermions. The most relevant sub-leading interactions coupling the Higgs to up-type quarks come from dimension-six operators. Up to operator relations at this order, these may written in terms of a single non-renormalizable operator

$$\frac{\xi_{ij}}{M^2} H^\dagger H Q_i H \overline{u}_j + h.c. \tag{7.2}$$

At this order in an effective field theory expansion, both the Yukawa coupling in Eq. 7.1 and dimension-six operator in Eq. 7.2 contribute to the up-quark mass matrix and effective coupling to the physical Higgs boson

$$m_{ij}u_i\overline{u}_j + \lambda^h_{ij}u_i\overline{u}_j + h.c. \tag{7.3}$$

where the up-quark mass matrix is given by

$$m_{ij} = \frac{v}{\sqrt{2}}\left[\lambda_{ij} + \frac{v}{2M^2}\xi_{ij}\right] \equiv \frac{v}{\sqrt{2}}\lambda^m_{ij} \tag{7.4}$$

and where $H^0 = \frac{1}{\sqrt{2}}(v+h)$ and λ^m_{ij} is the mass effective Yukawa coupling. The Higgs effective Yukawa coupling, λ_h , of the physical Higgs boson to up-quarks is given at this order in the effective field theory description by the derivative of the mass matrix with respect to the Higgs expectation value

$$\lambda^h_{ij} = \frac{\partial m_{ij}}{\partial v} = \frac{1}{\sqrt{2}}\left[\lambda^m_{ij} + \frac{v^2}{M^2}\xi_{ij}\right] \tag{7.5}$$

Since the mass effective Yukawa is by definition diagonal in the mass basis, flavor-violating interactions come only from the second term in parentheses in Eq. 7.5. Misalignment between the mass and Higgs effective Yukawa couplings, λ^m_{ij} and λ^h_{ij} , vanishes in the $M \to \infty$ limit.

The partial decay width of the top quark to a Higgs boson and massless charm quark from the effective Higgs interaction in Eq. 7.3 with flavor violating couplings in Eq. 7.5 is given by

$$\Gamma(t \to ch) = \frac{(|\xi_{tc}|^2|\xi^2_{ct}|)m_t}{128\pi G_F^2 M^4}\left(1 - \frac{m_h^2}{m_t^2}\right)^2 \tag{7.6}$$

where $G_F^{-1} = \sqrt{2}v^2$. For comparison, the partial decay width of the top quark to the W -boson and massless b-quark through the minimal charged current interaction is

$$\Gamma(t \to Wb)\frac{G_F^2 m_t^3 |V_{tb}|^2}{8\pi\sqrt{2}}\left(1 - \frac{m_W^2}{m_t^2}\right)^2\left(1 + \frac{2m_W^2}{m_t^2}\right) \tag{7.7}$$

Assuming $\mathrm{Br}(t \to Wb)$ is close to unity, the leading order branching ratio for $t \to ch$ is then given by

$$\mathrm{Br}(t \to ch) \simeq \frac{|\xi_{tc}|^2 + |\xi_{ct}|^2}{8\sqrt{2}G_F^3 m_t^2 M^4 |V_{tb}|^2}\frac{(1 - m_h^2/m_t^2)^2}{(1 - m_W^2/m_t^2)^2(1 + 2m_W^2/m_t^2)} \tag{7.8}$$

For Higgs boson and top quark masses of $m_h = 125\,\text{GeV}$ and $m_t = 173.5\,\text{GeV}$ respectively, the numerical value of the branching ratio in terms of the dimension-six operator scale and flavor-violating Higgs effective Yukawa coupling are

$$\text{Br}(t \to ch) \simeq 150^4\ \text{GeV}^4 \frac{|\xi_{tc}|^2 + |\xi_{ct}|^2}{M^4} \simeq 0.29(|\lambda^h_{tc}|^2 + |\lambda^h_{ct}|^2) \tag{7.9}$$

7.2 A Multi-Lepton Search for $t \to ch$

Multilepton searches at hadron colliders provide great sensitivity to new physics processes. In this work we follow and use the results of the multi-lepton search strategies adopted by the CMS collaboration [90, 91]. The sensitivity to new physics arises from dividing three-or more lepton final states into a large number of exclusive search channels based on lepton flavor and charge combinations, hadronic activity, missing transverse energy, and the kinematic properties of the leptons in an event. We first review the details of this search strategy before applying it to obtain a bound on $\text{Br}(t \to ch)$.

7.2.1 Multi-Lepton Signal Channels

Standard Model backgrounds to multi-lepton searches for new physics are small and may be further reduced by imposing cuts on hadronic activity or missing energy. In this case hadronic activity is characterized by the variable H_T , the scalar sum of the transverse jet energies for all jets passing the preselection cuts. The missing transverse energy, MET, is given by the magnitude of the vector sum of the momenta of all reconstructed objects. Both H_T and MET are sensitive discriminating observables for new physics in a given lepton flavor and charge channel.

The CMS multilepton search [90] exploits the background discrimination of H_T and MET in the following way: Events with $H_T > 200$ (MET > 50) GeV are assigned HIGH H_T (MET), while those with $H_T < 200$ (MET < 50) GeV are assigned LOW H_T (MET). The high H_T and high MET requirements (individually or in combination) lead to a significant reduction in Standard Model backgrounds.

Further background reduction may be accomplished with a Z-boson veto, in which

the invariant mass of opposite-sign same-flavor (OSSF) lepton pairs is required to lie outside a 75 - 105 GeV window around the Z mass; we simply denote events passing the Z veto as No Z. In the case of 3ℓ events, it is also useful to differentiate between events with no OSSF pairs, which we denote DY0 to indicate no possible Drell-Yan pairs, and one OSSF pair which we denote DY1. Although the CMS multi-lepton analysis [90, 91] also includes channels with one or more objects consistent with hadronically decaying τ-leptons, in this analysis we will focus our attention on $\ell = e, \mu$ only. We do implicitly include leptonically decaying τ-leptons in our analysis, which for all practical purposes in the detector are simply e- or μ-leptons.

The 3ℓ or 4ℓ channels may be divided into 20 possible combinations of H_T HIGH/LOW; MET HIGH/LOW; Z/No Z; and DY0/DY1. Again the 20 channels have already been presented in Table 5.2. For each of the 3ℓ and 4ℓ categories, channels are listed from top to bottom in approximately descending order of backgrounds, or equivalently ascending order of sensitivity, with the last such channel at the bottom dominated by Standard Model backgrounds. However, all channels contribute to the limit.

7.2.2 Simulation Details

We closely follow the CMS multilepton analysis [90], applying the same cuts to our signal sample and making use of the CMS background estimates and observations with $5\,\text{fb}^{-1}$ of 7 TeV pp collision data. For our signal, we simulate tt production events with one side decaying through conventional charged current interaction via $t \to Wb$ and the other side decaying via $t \to ch$. For definiteness we take $m_h = 125\,\text{GeV}$ with Standard Model branching ratios. For simulating signal processes, we have used MadGraph v4 [92, 93] and rescaled the tt production cross section to the NLO value $\sigma(pp \to tt) = 165$ pb at 7 TeV [94]. The Higgs boson was decayed inclusively using BRIDGE [95]. The branching ratios and total width for Higgs decay in BRIDGE were taken from the LHC Higgs Cross Section Group [96]. Subsequent showering and hadronization effects were simulated using Pythia [97]. Detector effects were simulated using PGS [98] with the isolation algorithm for muons modified to more accurately reflect the procedure used by the CMS collaboration. In particular, we introduce a trkiso variable for each muon

[99]. The variable trkiso is defined to be the sum pT of all tracks, ECAL, and HCAL deposits within an annulus of inner radius 0.03 and outer radius 0.3 in R surrounding a given muon. Isolation requires that for each muon, trkiso/pT μ is less than 0.15. The efficiencies of PGS detector effects were normalized by simulating the TeV3 mSUGRA benchmark studied in [91] and comparing the signal in 3ℓ and 4ℓ channels. To match efficiencies with the CMS study we applied an efficiency correction of 0.87 per lepton to our signal events [86]. We applied preselection and analysis cuts in accordance with those used in the CMS analysis [90]. A total of 500,000 events were simulated to give good statistical coverage of all the relevant multi-lepton channels.

7.2.3 Results

The multi-lepton final states coming from $t \to ch$ in $t\bar{t}$ pair production arise mainly from charged current decay of one top quark, $t \to Wb$ with $W \to \ell\nu$, and flavor-violating decay of the other top quark, $t \to ch$, with h decaying to final states with two or more leptons. The most relevant Higgs final states are those with two leptons that arise from $h \to WW^* \to \ell\nu\ell\nu$ and $h \to \tau\tau$ with leptonic decays of the τ-leptons, $\tau \to \ell X$, as well as $h \to ZZ^* \to jjll, \nu\nu\ell\ell$. All of these decay modes give three-lepton final states. Although the total branching ratio of the Higgs to two leptons is comparable for $h \to WW^*$ and $h \to ZZ^*$, leptons coming from Z and/or Z^* decays are less significant because they fall into higher-background DY1 channels with either Z or No Z. In contrast, pairs of leptons coming from WW^* decay are uncorrelated in flavor and fall into lower-background DY0 channels, in addition to the higher-background DY1 channels. There are additionally four- and five-lepton final states from charged current decay of one top quark, $t \to Wb$ with $W \to jj$ or $\ell\nu$ respectively, and flavor-violating decay of the other top quark, $t \to ch$, with $h \to ZZ \to \ell\ell\ell\ell$. The small total branching ratio for these final states makes them less significant than the three-lepton final states in obtaining a bound from the $5\,\mathrm{fb}^{-1}$ of integrated luminosity in the CMS search [90]. However, in the future with more integrated luminosity, these channels should contribute more significantly to the sensitivity for $t \to ch$. The signal contributions to each of the exclusive multi-lepton channels are shown in Table 1. Events

are entered in the table exclusive-hierarchically from the top to the bottom. In this way each event appears only once in the table, and in the lowest possible background channel consistent with its characteristics. The strongest limit-setting channels for $t \to ch$ are those with three leptons. The best limits come from [MET HIGH, H_T LOW, DY1 No Z], which alone constrains $\mathrm{Br}(t \to ch) < 3.7\%$, and [MET HIGH, H_T LOW, DY0], which constrains $\mathrm{Br}(t \to ch) < 4.2\%$. In each case the lack of a reconstructed Z or OSSF lepton pair reflects the contributions from $h \to WW^*$ and $h \to \tau\tau$, while the MET comes predominantly from neutrinos emitted in the W and τ -lepton decays. Significant limits also come from the channel [MET HIGH, H_T HIGH, DY1 No Z], which constrains $\mathrm{Br}(t \to ch) < 6.5\%$; and [MET LOW, H_T LOW, DY0], which constrains $\mathrm{Br}(t \to ch) < 7.9\%$; these likewise reflect dominant contributions from the Higgs decays $h \to WW^*$ and $h \to \tau\tau$. All other channels give constraints on the branching ratio that are weaker than 10% in an individual channel.

Although limits may be placed on the signal from any individual channel in the multi- lepton search, the greatest sensitivity comes from combining all exclusive channels. Com- bining all multilepton channels, we find that the $5\,\mathrm{fb}^{-1}$ multi-lepton CMS results [90] yield an observed limit of $\mathrm{Br}(t \to ch) < 2.7\%$, with an expected limit $\mathrm{Br}(t \to ch) < 1.7\%$. This corresponds to a bound on the scale of the dimension-six effective operator (Eq. 7.2) of $M^2/\sqrt{|\xi_{tc}|^2 + |\xi_{ct}|^2} > (370\,\mathrm{GeV})^2$ or equivalently on the flavor-violating Higgs Yukawa couplings (Eq. 7.5) of $|\lambda^h_{tc}|^2 + |\lambda^h_{tc}|^2 < 0.31$. This limit represents a combined Bayesian 95% CL limit computed using the observed event counts, background estimates, and systematic errors listed in Table 7.1.

An upper limit on the branching ratio $\mathrm{Br}(t \to ch)$ can also be expressed in terms of a limit on the cross section times branching ratio $\sigma\ \mathrm{Br}(pp \to t\bar{t} \to Wbhc)$. This is related to the cross section and branching ratio individually by $\sigma\ \mathrm{Br}(pp \to t\bar{t} \to Wbhc) = \sigma(pp \to t\bar{t} \cdot 2\ \mathrm{Br}(t \to hc)$ where the factor of two accounts for combinatorics of the top quark decay. With this, our estimate for the observed upper limit of $\mathrm{Br}(t \to ch) < 2.7\%$ corresponds to $\sigma\ \mathrm{Br}(pp \to t\bar{t} \to Wbhc) < 8.9\,\mathrm{pb}$ for 7 TeV pp collisions. While this limit is specific to the acceptance and efficiency associated to top-anti-top production and decay, it does give a rough indication of the cross section times branching limit

that would be obtained from the results of the CMS multi-lepton search [90] for other new physics processes $pp \to WhX$ with similar kinematics.

The sensitivity of future dedicated multi-lepton searches for flavor-changing top quark decay $t \to ch$ could be improved in a number of ways. The most straightforward improve- ment would be to include the CMS exclusive multi-lepton channels that contain τ -leptons. For simplicity these were neglected in this study. These channels have higher backgrounds, but would contribute a bit to the overall sensitivity. Another improvement would be to sub-divide the exclusive multi-lepton channels according to whether there are tagged b- quarks in an event. The $t \to ch$ signal has both a b- and c-quark in the final state, and so would fall primarily in the b-tagged channels. Although there is background from $t\bar{t}$ production with fully-leptonic decay and a fake lepton in these channels, other Standard Model backgrounds from, e.g. W Z production with fully leptonic decay, would be reduced in these channels. Yet another possibility would be to incorporate exclusive same-sign di- lepton channels, again with b-quark tagging sub-division [99]. Although the backgrounds in these channels are by definition larger than those of three- or more-lepton channels, this would bring in other relevant final states of the $t\bar{t}$ signal such as charged current decay of one top quark, $t \to Wb$ with $W \to \ell\nu$, and flavor-violating decay of the other top quark, $t \to ch$ with $h \to WW^* \to \ell\nu jj$. Since the Higgs boson is neutral, the charges of the two leptons from these decays are uncorrelated and same-sign half the time. Finally, further signal specific sub-divisions of channels could be utilized based on partial kinematic tagging information of the top quark and/or Higgs boson to isolate regions of phase space that are populated only by the signal.

We emphasize that in respect to possible improvements focused at the $t \to ch$ signal, the current work represents a proof of principle illustrating the power of the CMS exclusive channel multi-lepton search strategy [90, 91] that may be extended for certain new physics signals by a targeted refinement of the search channels.

			Observed	Expected	Signal
4 Leptons					
MET HIGH	HT HIGH	No Z	0	0.018 ± 0.005	0.02
MET HIGH	HT HIGH	Z	0	0.22 ± 0.05	0.0
MET HIGH	HT LOW	No Z	1	0.20 ± 0.07	0.11
MET HIGH	HT LOW	Z	1	0.79 ± 0.21	0.04
MET LOW	HT HIGH	No Z	0	0.006 ± 0.001	0.0
MET LOW	HT HIGH	Z	1	0.83 ± 0.33	0.04
MET LOW	HT LOW	No Z	1	2.6 ± 1.1	0.08
MET LOW	HT LOW	Z	33	37 ± 15	0.15
3 Leptons					
MET HIGH	HT HIGH	DY0	2	1.5 ± 0.5	0.48
MET HIGH	HT LOW	DY0	7	6.6 ± 2.3	2.1
MET LOW	HT HIGH	DY0	1	1.2 ± 0.7	0.26
MET LOW	HT LOW	DY0	14	11.7 ± 3.6	1.68
MET HIGH	HT HIGH	DY1 No Z	8	5.0 ± 1.3	1.54
MET HIGH	HT HIGH	DY1 Z	20	18.9 ± 6.4	0.41
MET HIGH	HT LOW	DY1 No Z	30	27.0 ± 7.6	5.8
MET HIGH	HT LOW	DY1 Z	141	134 ± 50	2.0
MET LOW	HT HIGH	DY1 No Z	11	4.5 ± 1.5	0.80
MET LOW	HT HIGH	DY1 Z	15	19.2 ± 4.8	0.72
MET LOW	HT LOW	DY1 No Z	123	144 ± 36	3.1
MET LOW	HT LOW	DY1 Z	657	764 ± 183	2.4

Table 7.1: Observed number of events, expected number of background events, and expected number of $t \to ch$ signal events with $\mathrm{Br}(t \to ch) = 1$ % in various CMS multi-lepton channels after acceptance and efficiency for $5\,\mathrm{fb}^{-1}$ of 7 TeV proton-proton collisions. HIGH and LOW for MET and HT indicate $\not\!\!E_T \gtrless 50\,\mathrm{GeV}$ and $HT \gtrless 200\,\mathrm{GeV}$ respectively. DY0 $\equiv \ell'^{\pm}\ell^{\mp}\ell^{\mp}$, DY1 $\equiv \ell^{\pm}\ell^{+}\ell^{-}, \ell'^{\pm}\ell^{+}\ell^{-}$, for $\ell = e, \mu$. No Z and Z indicate $|m_{\ell\ell} - m_Z| \gtrless 15\,\mathrm{GeV}$ for any opposite sign same flavor pair.

7.3 Going Forward

The discovery of a Standard Model-like Higgs opens the door to a plethora of new searches that employ Higgs decay products to probe new physics processes that involve Higgs boson associated production or decay. In this paper we have studied one of the simplest such processes, the rare flavor-violating top quark decay to a Higgs boson and charm quark, $t \to ch$. Using the results of the CMS multi-lepton search with $5\,\mathrm{fb}^{-1}$ of 7 TeV pp collision data [90], we obtain the estimated upper bounds of $\mathrm{Br}(t \to ch) < 2.7\%$ and $\sigma\ \mathrm{Br}(pp \to t\bar{t} \to Wbhc) < 8.9\,\mathrm{pb}$ for a 125 GeV Standard Model Higgs boson with Standard Model branching ratios. Future multi-lepton searches at the LHC optimized for this signal, including τ -lepton channels, exclusive same-sign di-lepton channels, subdivision of channels based on b-quark tagging, and with increasing integrated luminosity, should be able improve the sensitivity to $t \to ch$ considerably.

The results presented here should be more widely applicable to a range of new physics processes that yield final states with a W -boson in association with a Higgs boson. For processes with kinematics that are similar to top-anti-top production and decay, our estimated bound from the CMS multi-lepton search [90] corresponds very roughly to $\sigma\ \mathrm{Br}(pp \to WhX) \lesssim 9\,\mathrm{pb}$. Just one example of many such new physics processes that are of interest is production of supersymmetric wino- or Higgsino like chargino and neutralino, either directly or from cascade decays, with decay of the chargino to a W -boson and lighter neutralino or the Goldstino, and decay of the neutralino to a Higgs boson and a lighter neutralino or the Goldstino, $pp \to X \to \chi^{\pm}\chi_i^0 Y \to W^{\pm}h\chi_j^0\chi_j^0 Y$. In many scenarios the branching ratios $\mathrm{Br}(\chi^{\pm} \to W^{\pm}\chi_j^0)$ and $\mathrm{Br}(\chi_i^0 \to h\chi_j^0)$can approach unity [100]. While the upper limit on the cross section times branching ratio obtained above does not quite bound direct electroweak chargino-neutralino production with these decays, it would provide bounds on certain scenarios with strong superpartner production where the chargino and neutralino are emitted in cascade decays. The future improvements to exclusive channel multi-lepton searches mentioned above would improve the sensitivity also to these supersymmetric

processes with associated Higgs bosons. In particular, direct chargino-neutralino production would yield final states without b-quarks, and so would appear as signal in the b-quark anti-tagged subdivision of exclusive same sign di-lepton and multi-lepton channels. The Higgs boson will provide a new calibration for experimental physics at high energy colliders. Higgs boson leptonic decay modes are but one of many possible applications of Higgs decays to the search for new physics.

The results of a multi-lepton search conducted by the CMS collaboration with $5\,\mathrm{fb}^{-1}$ of data collected from 7 TeV pp collisions are used to place the first bound on the rare flavor-changing decay of the top quark to a Higgs boson and charm quark. Combining results from a number of exclusive three- and four-lepton search channels yields an estimated upper limit of $\mathrm{Br}(t \to ch) < 2.7\%$ for a Higgs boson mass of 125 GeV. The sensitivity of future dedicated searches for $t \to ch$ could be improved by adding exclusive same sign di-lepton channels, as well as by sub-dividing channels based on b-quark tagging and partial kinematic top quark and Higgs boson tagging. This bound may be interpreted more widely within a range of new physics processes that yield final states with a W -boson in association with a Higgs boson. For such processes with kinematics that are similar to topanti-top production and decay, the estimated limit on cross section times branching ratio corresponds to roughly $\sigma\ \mathrm{Br}(pp \to WhX) < 9\,\mathrm{pb}$.

Part III

The Third Prong: Post-Discovery

Chapter 8

Particle Masses from Cascade Decays

Much of the new physics program at the Large Hadron Collider (LHC) involves the search for new heavy particles states through their decay signatures involving known Standard Model particles. Identification of these new particles necessarily involves measuring their properties such as their masses, spins, and quantum numbers. Particle masses for example, can be directly measured via the construction of kinematic observables such as a mass peak resonance if all of the decay products are observable through the detector. However, reconstructing particle masses is much more challenging in channels that include missing transverse energy (MET), which can arise if one of more of the decay products is neutral under the electromagnetic and strong nuclear forces, and hence unobservable through the detector. In this case there is not enough kinematic data to compute the invariant mass or infer the center of mass frame of the new produced particle.

One interesting class of decay topologies that arises in a wide range of models for physics beyond the Standard Model is the sequential on-shell cascade decay. This topology involves the production of some heavy new particle state, followed by a sequence of two-body on-shell decays of one new particle state to one lighter new particle and one visible Standard Model particle. This sequence can terminate after n such two-body decays when a stable new particle is produced that may be unobserved and appear as MET. Sequential decays of this type are generic in extensions of the Standard Model, such as supersymmetry or same spin partner theories, that involve a sector of new particle states which carry a conserved quantum number for a symmetry under which the Standard Model particles are invariant.

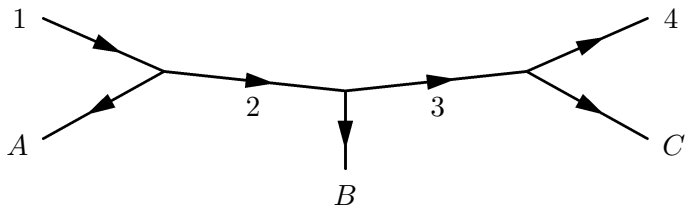

Figure 8.1: A sequential on-shell cascade decay with visible Standard Model particles A, B, and C. Particle 4 is assumed to be non-interacting.

The sequential on-shell cascade decay can be characterized by the number of two-body decays n that exist as subprocesses. In this chapter, we demonstrate that for $n = 3$ (Fig. 8.1), the invariant mass correlations from observable Standard Model particles A, B, and C alone are enough to extract the masses of all the new particle states (we defer the generalization of $n > 3$ to later work). This is possible despite the loss of kinematic data because of the dependence of the invariant decay distribution in phase space on the new particle masses m_1, m_2, m_3, and m_4. In fact, this phase space distribution reveals a sharp kinematic boundary when mapped into a generalized three-dimensional Dalitz space spanned by invariants for the nearest and next-to-nearest branches $m^2_{AB}, m^2_{BC}, m^2_{AC}$. Furthermore, the density of the decay distribution generically becomes singular everywhere on the boundary because of the Jacobian for this mapping. We thus propose a next to nearest on-shell mass extraction technique (NNOMET) in which the new particle masses m_1, m_2, m_3, m_4 are measured through a fit of entire decay distribution in Eq. 8.6 in the three-dimensional Dalitz space to an analytic likelihood function computed from the kinematic structure of this topology.

Of course there currently exist numerous methods in the literature for extracting particle masses from missing energy signatures. Many such methods are based on the construction of clever variables such as m_{T_2} [116] and other quantities related to transverse mass [102, 118, 104]. Other techniques rely on kinematic features of invariant mass distributions in one [115, 124, 107, 108] or two [109, 110] dimensions, or on the total shapes of invariant mass distributions [111–113]. All techniques have their own relative advantages and weaknesses, and NNOMET is no exception to this rule. The

main drawback of the NNOMET procedure described here is that it requires at least three sequential on-shell decays to observable Standard Model particles, and is not applicable to cascade decays with only one or two observable branches. In addition, in the limit that any two of the new particle states along the decay chain become degenerate, the three-dimensional decay distribution Eq. 8.6 effectively becomes one-dimensional. In this case only a single function of the four paraticle masses can generically be determined. Despite this, the advantages of NNOMET are numerous:

- No measurement of the MET vector is required. MET is by definition the least well measured of all reconstructed objects and will become increasingly less reliable in the high pile-up environment of the LHC Run II
- Since this technique relies only on the measurement of invariants, to leading order it is insensitive to initial state radiation
- The NNOMET procedure is easily adapted to handle combinatoric confusion coming from the possible misidentification of identical particles on different branches.
- It makes use of all correlations between invariants in the full three-dimensional phase space. This is in contrast to existing methods that rely on kinematic features in lower dimensional projections that wash out the strongest correlations, and effectively use only a small fraction of the data over a limited region of the available phase space

The remainder of this chapter will be organized as follows. In Section 8.1, we give a general discussion of the phase space for sequential on-shell cascade decays with $n = 3$, focusing attention on the Dalitz parameterization in three dimensions. The dominant kinematic features of the phase space distribution are described in Section 8.2, with attention focused on the dependence of these kinematic features on particle masses. Section 8.3 describes the map between the Dalitz parameters and the physical particle masses as well as a discussion on how to handle the issue of combinatoric ambiguity. In Section 8.4, we describe the NNOMET procedure for extracting particle masses from the invariant correlations in the Dalitz space distribution of these decay toplogies. A

simple example from an early CMS supersymmetry benchmark is presented in Section 8.5 as a proof of concept with background estimates. We then conclude with general remarks.

8.1 The Phase Space of Sequential On-Shell Cascade Decays

The phase space configuration of the on-shell cascade decay consisting of three sequential two-body decays, as shown in Fig. 8.1, is completely fixed by the specification of three decay angles $(\theta^{(2)}_{AB}, \theta^{(2)}_{BC}, \phi^{(3)}_{AB,BC})$. Here $\theta^{(2)}_{AB}$ is the angle between $\vec{p}_A$ and $\vec{p}_B$ in the rest frame of particle 2, $\theta^{(3)}_{BC}$ is the angle between $\vec{p}_B$ and $\vec{p}_C$ in the rest frame of particle 3, and $\phi^{(3)}_{AB,BC}$ is the angle between the decay plane spanned by particles $(\vec{p}_A, \vec{p}_B)$ and the decay plane spanned by particles $(\vec{p}_B, \vec{p}_C)$ in the rest frame of particle 3. The ranges for the polar and azimuthal angles are $-1 \leq \cos\theta \leq 1$ and $0 \leq \cos\phi < 2\pi$.

A more experimentally favorable Lorentz invariant basis for this decay topology is the set of independent invariant mass squared pairings formed from the four-momenta of the visible Standard Model final state particles $(m^2_{AB}, m^2_{BC}, m^2_{AC})$ where for example $m^2_{AB} \equiv (p_A + p_B)^2$. The techniques developed below for extracting particle masses thus rely on correlations among these invariants, which span a generalized Dalitz space. In this paper we will restrict our analysis to situations in which $m_A = m_B = m_C = 0$. This not only simplifies the equations tremendously, but is also a practical assumption since most of the stable Standard Model particles that could conceivably be labeled by A, B and C are leptons or quarks that may be treated as effectively massless in the relativistic regime. It should be noted however, that all techniques to be described here may easily be generalized to account for the finite masses of these particles.

In the case of three visible final state particles, there are three independent pairings of invariant masses squared so the decay distribution covers a three-dimensional generalized Dalitz space. In the limit of massless final state particles A, B, and C, they can be calculated in terms of the three independent angles that characterize the kinematics of this decay topology

$$m^2_{AB} = \frac{m^{2\,\max}_{AB}}{2}\left(1 - \cos\theta^{(2)}_{AB}\right) \tag{8.1}$$

$$m^2_{BC} = \frac{m^{2\,\max}_{BC}}{2}\left(1-\cos\theta^{(3)}_{BC}\right) \tag{8.2}$$

$$m^2_{AC} = \frac{1}{4}\Bigg[m^{2\,\max}_{AC}\left(1+\cos\theta^{(2)}_{AB}\right)\left(1-\cos\theta^{(3)}_{BC}\right)+m^{2\,\max}_{AC_0}\left(1-\cos\theta^{(2)}_{AB}\right)\left(1+\cos\theta^{(3)}_{BC}\right)$$
$$-2\cos\phi^{(3)}_{AB,BC}\sqrt{m^{2\,\max}_{AC}m^{2\,\max}_{AC_0}\left(1-\cos^2\theta^{(2)}_{AB}\right)\left(1-\cos^2\theta^{(3)}_{BC}\right)}\Bigg] \tag{8.3}$$

The extrema of the Dalitz variables are calculable in terms of the new particle state masses

$$m^{2\,\max}_{AB} = \frac{(m_1^2-m_2^2)(m_2^2-m_3^2)}{m_2^2}$$
$$m^{2\,\max}_{BC} = \frac{(m_2^2-m_3^2)(m_3^2-m_4^2)}{m_3^2}$$
$$m^{2\,\max}_{AC} = \frac{(m_1^2-m_2^2)(m_3^2-m_4^2)}{m_3^2}$$
$$m^{2\,\max}_{AC_0} \equiv m^{2\,\max}_{AC}|_{m_{BC}=0} = \frac{(m_1^2-m_2^2)(m_3^2-m_4^2)}{m_2^2} \tag{8.4}$$

where $m^{2\,\max}_{AC_0}$ is the maximum value for m^2_{AC} in the limit where $m_{BC}=0$. Notice that a measurement of just these four extrema would alone be enough to fully reconstruct the full set of new particle masses. A fit to the full three-dimensional decay distribution based on invariant mass correlations is essentially a fit to these four parameters. However some of them ($m^{2\,\max}_{AC_0}$ in particular) occupy very sparse and narrow regions of phase space and are often difficult or impossible to practically extract from lower dimensional projections, which tend to obscure the kinematic features that characterize them. Utilizing the full three-dimensional correlations is thus crucial for extracting the new particle state masses.

The invariant decay distribution in this three-dimensional generalized Dalitz space is determined by the matrix element squared for the four-body decay of particle 1, in addition to the Jacobian factors that arise when moving from the angular basis to the generalized Dalitz space. These Jacobian factors are:

$$J_{AB} = \frac{m^{2\,\max}_{AB}}{2}\left|\frac{\partial\ \cos\theta^{(2)}_{AB}}{\partial\ m^2_{AB}}\right| = 1$$

$$J_{BC} = \frac{m^{2\,\max}_{BC}}{2}\left|\frac{\partial\ \cos\theta^{(3)}_{BC}}{\partial\ m^2_{BC}}\right| = 1$$

$$J_{AC}(m^2_{AB}, m^2_{BC}, m^2_{AC}) = \frac{m^{2\ \max}_{AC}}{2\pi} \left| \frac{\partial\ \phi^{(3)}_{AB,BC}}{\partial\ m^2_{AC}} \right|$$

$$= \frac{i}{2\pi} \lambda^{-\frac{1}{2}} \left[\frac{m^2_{AC}}{m^{2\ \max}_{AC}}, \frac{m^2_{BC}}{m^{2\ \max}_{BC}} \left(1 - \frac{m^2_{AB}}{m^{2\ \max}_{AB}} \right), \frac{m^2_3}{m^2_2} \frac{m^2_{AB}}{m^{2\ \max}_{AB}} \left(1 - \frac{m^2_{BC}}{m^{2\ \max}_{BC}} \right) \right] \tag{8.5}$$

where in the equation for $J_{AC}(m^2_{AB}, m^2_{BC}, m^2_{AC})$ we have made use of the Källen (triangle) function $\lambda(a,b,c) \equiv a^2 + b^2 + c^2 - 2ab - 2bc - 2ac$. Therefore, without specifying the matrix element for this process, we can express the invariant decay distribution in the three-dimensional generalized Dalitz space in terms of the angular decay distribution

$$\frac{d^3\Gamma_{1\to A\ B\ C\ 4}}{dm^2_{AB}\ dm^2_{BC}\ dm^2_{AC}} = \frac{8\pi\ J_{AC}(m^2_{AB}, m^2_{BC}, m^2_{AC})}{m^{2\ \max}_{AB}\ m^{2\ \max}_{BC}\ m^{2\ \max}_{AC}} \frac{d^3\Gamma_{1\to A\ B\ C\ 4}}{d\cos\theta^{(2)}_{AB}\ d\cos\theta^{(3)}_{BC}\ d\phi^{(3)}_{AB,BC}} \tag{8.6}$$

where $J_{AC}(m^2_{AB}, m^2_{BC}, m^2_{AC})$ is defined in Eq. 8.5. The dependence of this distribution on the Dalitz invariants and hence on the masses of the new particle states is what allows these masses to be measured. In important examples such as supersymmetry, the angular decay distribution is even flat $d^3\Gamma_{1\to A\ B\ C\ 4}/d\cos\theta^{(2)}_{AB}\ d\cos\theta^{(3)}_{BC}\ d\phi^{(3)}_{AB,BC} = 1$. Therefore the invariant decay distribution is given entirely by Eq. 8.6 and all particle masses can be extracted from a fit to just one Jacobian factor.

8.2 Kinematic Features of Cascade Decays in Dalitz Space

The phase space distribution of cascade decays in the three-dimensional generalized Dalitz space reveals several striking kinematic features, owing to kinematic correlations between invariants, that facilitate the extraction of particle masses. These correlations take a contribution from the matrix element squared for the process and from the mapping between the angular basis and the Dalitz basis. The latter contribution is summarized in Eqs. 8.1 - 8.3, which taken together give the relation:

$$m^2_{AC} = m^{2\ \max}_{AC} \frac{m^2_{BC}}{m^{2\ \max}_{BC}} \left(1 - \frac{m^2_{AB}}{m^{2\ \max}_{AB}} \right) + m^{2\ \max}_{AC_0} \frac{m^2_{AB}}{m^{2\ \max}_{AB}} \left(1 - \frac{m^2_{BC}}{m^{2\ \max}_{BC}} \right)$$

$$-2\cos\phi^{(3)}_{AB,BC} \sqrt{m^{2\ \max}_{AC} m^{2\ \max}_{AC_0} \frac{m^2_{AB}}{m^{2\ \max}_{AB}} \frac{m^2_{BC}}{m^{2\ \max}_{BC}} \left(1 - \frac{m^2_{AB}}{m^{2\ \max}_{AB}} \right) \left(1 - \frac{m^2_{BC}}{m^{2\ \max}_{BC}} \right)} \tag{8.7}$$

For a discussion of these kinematic features, it will prove convenient both notationally and conceptually, to define dimensionless invariant mass quantities

$$x = \frac{m_{AB}^2}{m_{AB}^{2\ \max}} \quad ; \quad y = \frac{m_{BC}^2}{m_{BC}^{2\ \max}} \quad ; \quad z = \frac{m_{AC}^2}{m_{AC}^{2\ \max}}$$

$$R = \frac{m_3^2}{m_2^2} \tag{8.8}$$

Non-dimensionalizing Eq. 8.7 we have

$$z = y(1-x) + Rx(1-y) - 2\cos\phi\sqrt{Rxy(1-x)(1-y)} \tag{8.9}$$

where we have dropped the labels on the azimuthal angle ϕ whose definition is unambiguous. The invariant decay distribution for sequential three-branch cascade decays in our dimensionless Dalitz space is completely determined by Eq. 8.9. The most salient feature of this distribution is the existence of a kinematic boundary in Dalitz space corresponding to the maximum and minimum values of $\cos\phi$ respectively

$$0 \le x \le 1$$

$$0 \le y \le 1$$

$$z_- \le z \le z_+ \tag{8.10}$$

with $z_\pm$ being the obvious function of the four new particle masses

$$z_\pm = y(1-x) + Rx(1-y) \pm 2\sqrt{Rxy(1-x)(1-y)} \tag{8.11}$$

Such a structure implies that in the dimensionless Dalitz space (x, y, z) , all of the events are restricted to lie within the interior of some closed region. The shape of the boundary of this region is determined by the analytic Eq. 8.11 and closely resembles a pillow, as illustrated in Fig. 8.2

Recall that ϕ was defined to be the angle between the $A - B$ and $B - C$ decay planes in rest frame of particle 3. Thus the two-dimensional boundary of the allowed kinematic region corresponding to $\cos\phi = \pm 1$ corresponds to the condition that the three-momenta of all three branch particles $\vec{p}_A$, $\vec{p}_B$, and $\vec{p}_C$, are co-planar in the 3 rest frame. Also implicit in these equations are additional boundary conditions, which

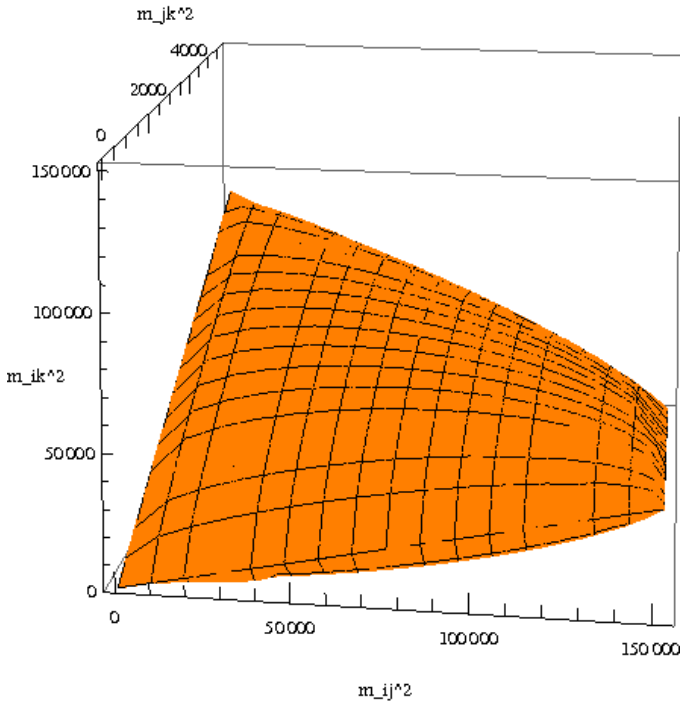

Figure 8.2: The surface of the "pillow" shaped region, which is the kinematic boundary for sequential, on-shell, cascade decays in three dimensional Dalitz space.

reduce Eq. 8.11 to one-dimensional relations at certain kinematic limits of the variables x and y giving us the four edges of the pillow. In the rest frame of 2, when $\vec{p}_A$ is parallel to $\vec{p}_B$, Eq. 8.11 reduces to $z_\pm = y$ corresponding to the boundary at $x = 0$. When $\vec{p}_A$ becomes anti-parallel to $\vec{p}_B$, Eq. 8.11 reduces to $z_\pm = R(1 - y)$ corresponding to the boundary at $x = 1$. Similar kinematic limits can be found in the rest frame of 3. Here when $\vec{p}_B$ is parallel to $\vec{p}_C$, Eq. 8.11 reduces to $z_\pm = Rx$ corresponding to the boundary at $y = 0$. Finally when $\vec{p}_B$ becomes anti-parallel to $\vec{p}_C$, Eq. 8.11 reduces to $z_\pm = 1 - x$ corresponding to the boundary at $y = 1$.

In addition to the strict boundaries of the pillow, there are other distinctive features about this space that correspond to specific and special kinematic configurations of the branch particles. For example, the point $x = z = y = 0$ is a generic solution to the distribution Eq. 8.9 and corresponds to the configuration where all of the branch particles A, B and C are all parallel and pointing in the same direction. Since by assumption, these particles are all massless, this condition is frame-independent. The point $x = y = 1$, $z = 0$ is another generic solution and corresponds to the configuration

where particles A and C are parallel (pointing in the same direction) while particle B is anti-parallel (pointing in the opposite direction) to particles A and C. The "highest point" on the pillow is given by the solution $x = 0$, $y = 1$, $z = 1$. This corresponds to the configuration where particles A and B are parallel while particle C is anti-parallel to particles A and B. Finally there is the intermediate point whose solution is $x = 1$, $y = 0$, $z = R$. This corresponds to the configuration where particles B and C are parallel while particle A is anti-parallel to particles B and C. Note that all of these kinematic features are derived from Eq. 8.9 and hence depend on masses only. In particular, these are all independent of the matrix elements of any specific processes.

The second important feature of the distribution equation are the singularities of the invariant decay distribution at the boundaries of the pillow. In terms of dimensionless quantities, the Dalitz space decay distribution is simply

$$\frac{d^3\Gamma_{1\to A\ B\ C\ 4}}{dx\ dy\ dz} = \frac{4i}{\lambda^{1/2}[z, y(1-x), x(1-y)]}\ \frac{d^3\Gamma_{1\to A\ B\ C\ 4}}{d\cos\theta^{(2)}_{AB}\ d\cos\theta^{(3)}_{BC}\ d\phi^{(3)}_{AB,BC}} \tag{8.12}$$

These singularities are a direct consequence of the form of Eq. 8.9, and arise from the Jacobian associated with the map from angular parameters to Dalitz parameters. In particular, the Jacobian associated with the map $\phi \to z$, which goes like the inverse square root of the Källen function. For fixed values of x and y, the singularity is thus of $\mathcal{O}(z - z_\pm)^{-\frac{1}{2}}$ as illustrated in Fig. 8.3.

The Jacobian peak is only apparent in the full three-dimensional Dalitz space, and is not visible in simple one- or two-dimensional projections considered previously [115, 124, 107–113]. What this means practically is that a distribution of events plotted in this three-dimensional Dalitz space will not only be restricted to the interior of the pillow region, but will pile up along the boundaries of the pillow in a singular fashion unless the matrix element squared $|\mathcal{M}(1 \to A\ B\ C\ 4)|^2 \sim \mathcal{O}(z - z_\pm)^n$ with $n \geq 1$. The pile-up of events at the pillow boundary is well illustrated by the following scatter plot of a finite width two-dimensional cross section of the pillow in Fig. 8.4.

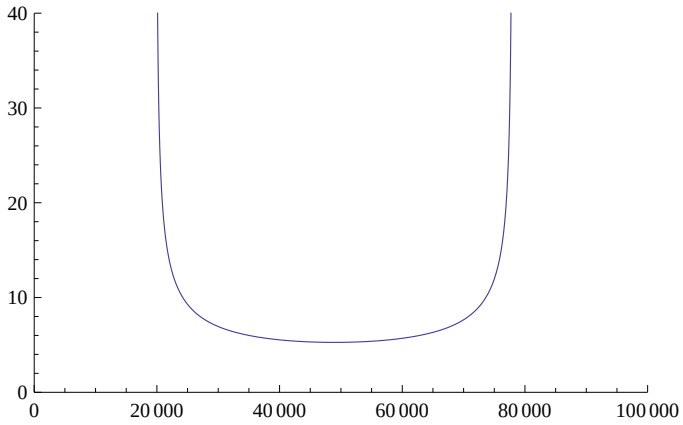

Figure 8.3: Fixing one point in the (m_{AB}, m_{BC}), the Jacobian for the invariant decay distribution from the angle basis to the Dalitz basis is singular near the kinematic boundary.

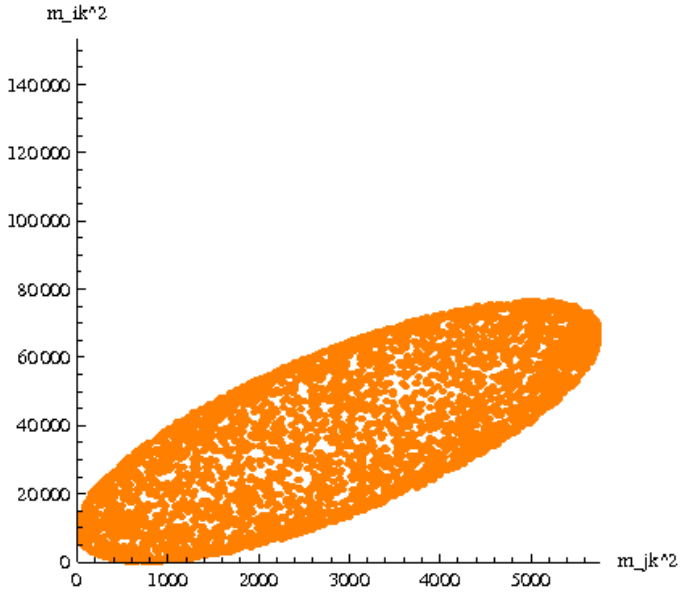

Figure 8.4: A cross section of the signal event distribution in the (m_{BC}, m_{AC}) plane. The singular nature of the Jacobian from the angle basis to the Dalitz basis clearly results in a divergence in the density of eventsnear the kinematic boundary.

8.3 From Three Dimensional Dalitz Parameters to Particle Masses

The interpretation of the mass measurement from a fit to the space of Dalitz parameters essentially amounts to a mapping from Dalitz space to the space of particle masses. The metric on these two spaces is related as

$$dm_i = \frac{\partial m_i}{\partial m_{IJ}^{2\,\max}} dm_{IJ}^{2\,\max} \tag{8.13}$$

where $i \in \{1,2,3,4\}$ and $(IJ) \in \{(AB),(BC),(AC),(AC_0)\}$. The Jacobian for the transformation $\partial m_i / \partial m_{IJ}^{2\,\max}$ is thus in general a 4×4 matrix. For simplicity we restrict attention to the two-dimensional subspace

$$\frac{\partial m_i}{\partial m_{IJ}^{2\,\max}} = \begin{pmatrix} \partial m_2/\partial m_{AC}^{2\,\max} & \partial m_2/\partial m_{AC_0}^{2\,\max} \\ \partial m_3/\partial m_{AC}^{2\,\max} & \partial m_3/\partial m_{AC_0}^{2\,\max} \end{pmatrix} \tag{8.14}$$

which describes the map from $(m_{AC}^{2\,\max}, m_{AC_0}^{2\,\max}) \to (m_2, m_3)$. This Jacobian can be computed easily from the inversion of the equations for the maxima of the Dalitz parameters:

$$\begin{aligned} m_1^2 &= \frac{m_{AC}^{2\,\max} m_{AB}^{2\,\max} m_{BC}^{2\,\max}}{(m_{AC}^{2\,\max} - m_{AC_0}^{2\,\max})^2} + \frac{m_{AC}^{2\,\max} m_{AB}^{2\,\max}}{m_{AC}^{2\,\max} - m_{AC_0}^{2\,\max}} \\ m_2^2 &= \frac{m_{AC}^{2\,\max} m_{AB}^{2\,\max} m_{BC}^{2\,\max}}{(m_{AC}^{2\,\max} - m_{AC_0}^{2\,\max})^2} \\ m_3^2 &= \frac{m_{AC_0}^{2\,\max} m_{AB}^{2\,\max} m_{BC}^{2\,\max}}{(m_{AC}^{2\,\max} - m_{AC_0}^{2\,\max})^2} \\ m_4^2 &= \frac{m_{AC_0}^{2\,\max} m_{AB}^{2\,\max} m_{BC}^{2\,\max}}{(m_{AC}^{2\,\max} - m_{AC_0}^{2\,\max})^2} - \frac{m_{AC_0}^{2\,\max} m_{BC}^{2\,\max}}{m_{AC}^{2\,\max} - m_{AC_0}^{2\,\max}} \end{aligned} \tag{8.15}$$

We thus have a natural interpretation of the likelihood contours in Dalitz space to the likelihood contours for the particle masses.

The Jacobian may be diagonalized by a bi-orthogonal transformation, and so may always be brought to the form

$$\frac{\partial m_i}{\partial m_{IJ}^{2\,\max}} = O(\vartheta) \begin{pmatrix} \xi_1 & 0 \\ 0 & \xi_2 \end{pmatrix} O^{-1}(\varphi) \tag{8.16}$$

where O is an orthogonal rotation matrix and $|\xi_1| > |\xi_2|$. Written in this form, the action of the Jacobian in transforming on a small closed region around some point in the

$(m^{2\,\max}_{AC}, m^{2\,\max}_{AC_0})$ space to the (m_2, m_3) space is first a rotation, followed by a squashing, followed by another rotation. So for example in the limit that the likelihood contours form circular regions in the $(m^{2\,\max}_{AC}, m^{2\,\max}_{AC_0})$ plane, the rotation $O^{-1}(\varphi)$ has no effect, and the remaining squashing and rotation gives a rotated ellipse in the (m_2, m_3) plane. Here ϑ is the rotation angle of the ellipse in the (m_2, m_3) plane with respect to the m_3 direction in the counter clockwise direction, and is given in terms of $R \equiv m_3^2/m_2^2$ as:

$$\vartheta = \frac{1}{2}\tan^{-1}\left(\frac{4\sqrt{R}(1+R)^2}{(R-1)^3}\right) \tag{8.17}$$

The degree of squashing of the Jacobian transformation Eq. 8.16 may be parameterized by an eccentricity parameter

$$\varepsilon = \frac{\xi_1}{\xi_2} = \frac{\sqrt{R}\,(1+R)\tan\vartheta - 2R}{(1+R)\tan\vartheta + 2\sqrt{R}} \tag{8.18}$$

where $|\varepsilon| \geq 1$. Although the expression in Eq. 8.17 for the eccentricity looks rather innocuous, it is a very rapidly rising function of R. For $R \to 0$, the rotation vanishes as $\vartheta \sim R^{1/2}$ and the eccentricity diverges as $\varepsilon \sim R^{-1/2}$. For $R \to 1$, the rotation approaches $\vartheta \to \pi/4$ and the eccentricity again diverges, this time as $\varepsilon \sim (1-R)^{-2}$. The eccentricity achieves a minimum value of approximately $\varepsilon \gtrsim 6.507$ at $R \simeq 0.0672$. This extreme behavior for ϑ and ε has strong implications for the accuracy with which particle masses may be inferred from invariant correlations in principle. The large eccentricity ε that exists in large parts of parameter space means that only a particular linear combination of m_2 and m_3 can be measured with very high accuracy and the particular value of the rotation angle ϑ determines which linear combination.

8.3.1 Combinatoric ~~Confusion~~ Clarity

Combinatoric confusion is a problem that arises when two or more of the final state particles in a given signature are experimentally indistinguishable on an event by event basis. If one is searching for features in the distribution of events containing such a signature, then it is impossible to tell a priori whether or not an unambiguously correct choice has been made for particle identification. Combinatoric confusion is thus an irreducible source of background that one must understand and account for when

searching for specific kinematic signals. This is particularly simple within the framework of the NNOMET procedure because the invariant differential decay distribution for any misidentified pair of particles is easily calculable. For example, if the Standard Model particles B and C are indistinguishable on an event-by event basis, the correlation for the incorrect assignment may be given simply by Eq. 8.9 with an exchange of $m^2_{AB} \leftrightarrow m^2_{AC}$. In terms of dimensionless coordinates this amounts to the replacements $x \to (m^{2\,\max}_{AC}/m^{2\,\max}_{AB})\ z$ and $z \to (m^{2\,\max}_{AB}/m^{2\,\max}_{AC})\ x$

$$x = \frac{m^{2\,\max}_{AC}}{m^{2\,\max}_{AB}} y\left(1 - \frac{m^{2\,\max}_{AC}}{m^{2\,\max}_{AB}} z\right) + \frac{m^{2\,\max}_{AC} m^{2\,\max}_{AC_0}}{m^{4\,\max}_{AB}} z(1-y)$$
$$+\ 2\cos\phi \sqrt{\frac{m^{4\,\max}_{AC} m^{2\,\max}_{AC_0}}{m^{6\,\max}_{AB}} yz\left(1 - \frac{m^{2\,\max}_{AC}}{m^{2\,\max}_{AB}} z\right)(1-y)} \qquad (8.19)$$

The distribution of events in Dalitz space with the incorrect particle assignment has the same kinematic features for the distribution with the correct assignment since it is literally just a reflection across the B/C axis in momentum space. Thus the combinatoric confusion which typically obscures the signal as a background in most analyses, can be anticipated and treated as though it were part of the signal using these techniques. The complete structure under consideration is thus given by the superposition of the signal and combinatoric pillows and is illustrated in Dalitz space in Fig. 8.5.

8.4 Extracting Masses from the Dalitz Distribution

Because of the dependence of the functional form of the kinematic boundary in Eq. 8.11 in the three-dimensional Dalitz space on the new particle invariant masses m_1, m_2, m_3, m_4, a fit to the boundary alone could in principle yield all four masses. However, in order make maximal use of all possible invariant mass correlations within the cascade decay (Fig. 8.1) we suggest here a next to nearest on-shell mass extraction technique (NNOMET) in which the entire decay distribution in Eq. 8.6 in the three-dimensional Dalitz space is fit to a given hypothesis for the new particle spins, with a likelihood function used to extract the four new particle masses. This amounts essentially to a simple invariant matrix element technique for the process in Fig. 8.1 where the matrix element or decay probability distribution Eq. 8.6 depends only on masses.

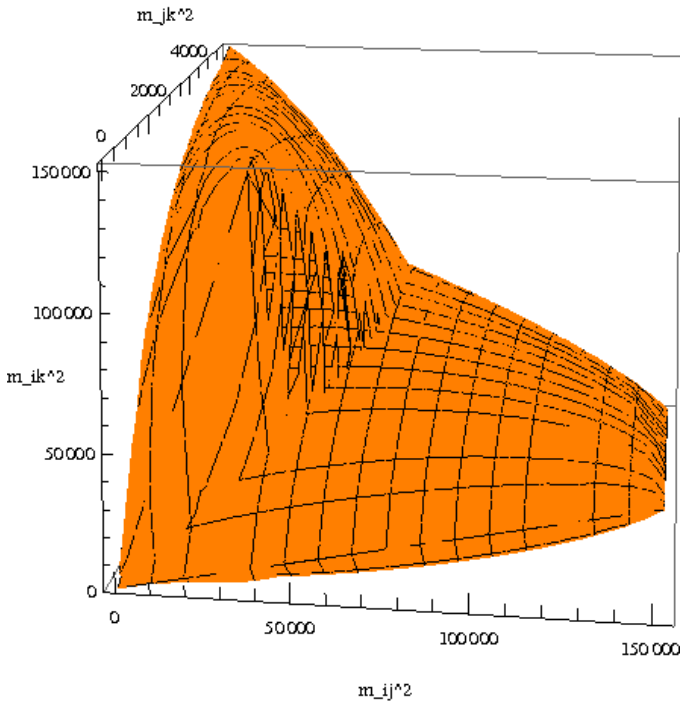

Figure 8.5: The kinematic boundary for signal events in the three dimensional Dalitz space, overlaid with the kinematic boundary given the combinatoric confusion from the incorrect identification of particles B and C. The kinematic distribution of both the correct and incorrect assignments are predictable in the NNOMET framework.

For simplicity, we will restrict our attention forward to the isotropic case where the functional dependence on particle masses is determined completely by the Jacobian, however the generalization is straightforward. Isotopic decays of the type are generic in supersymmetric theories, where the decays of new particle states alternate between spin 0 and spin 1/2, summing over spin states results in isotropic decays at each step of the decay. Thus the angular distributions of $\theta^{(2)}_{AB}$ and $\theta^{(3)}_{BC}$ are flat in their respective rest frames and the correlations between the invariant masses are encoded entirely in the Jacobian functions. Restricting our attention to this limit, the functional dependence of the invariant decay distribution on the masses of the new particle states is given entirely by the maximum values of the Dalitz parameters, of which there are four Eq. 8.4. We emphasize here that this technique makes full use of the correlations in three-dimensional Dalitz space and thus implicitly subsumes any method that utilizes the kinematic features of one or two-dimensional projections without the discrete ambiquities associated with projections. This fact is compounded by the strong Jacobian peak in three-dimensions that is completely obscured in lower-dimensional projections and is robust enough to survive the degradation due to experimental resolution.

In the isotropic limit, we thus define the normalized probability distribution function for the signal

$$P_s\ (m^2_{AB}, m^2_{BC}, m^2_{AC} | m^{2\ \max}_{AB}, m^{2\ \max}_{BC}, m^{2\ \max}_{AC}, m^{2\ \max}_{AC_0}) = \frac{J_{AC}(m^2_{AB}, m^2_{BC}, m^2_{AC})}{\int dm^2_{AB}\ dm^2_{BC}\ dm^2_{AC}\ J_{AC}(m^2_{AB}, m^2_{BC}, m^2_{AC})}$$

with $J_{AC}(m^2_{AB}, m^2_{BC}, m^2_{AC})$ again given by Eq. 8.5. We may similarly define the normalized probability distribution function for the combinatoric confusion

$$P_c\ (m^2_{AB}, m^2_{BC}, m^2_{AC} | m^{2\ \max}_{AB}, m^{2\ \max}_{BC}, m^{2\ \max}_{AC}, m^{2\ \max}_{AC_0}) = P_s(m^2_{AB} \leftrightarrow m^2_{AC}) \qquad (8.20)$$

In practice, accounting for the background in the signal region of the Dalitz space requires a parameterized model from which the functional form for the background probability distribution function $P_b\ (m^2_{AB}, m^2_{BC}, m^2_{AC})$ in terms of Dalitz parameters

may be extracted. For a signal to background ratio given by ϵ, we may thus write the total probability distribution function with which to fit to data as

$$\begin{aligned} & P_{tot}\ (m^2_{AB}, m^2_{BC}, m^2_{AC} | m^{2\ \max}_{AB}, m^{2\ \max}_{BC}, m^{2\ \max}_{AC}, m^{2\ \max}_{AC_0}) \\ & = \epsilon P_s\ (m^2_{AB}, m^2_{BC}, m^2_{AC} | m^{2\ \max}_{AB}, m^{2\ \max}_{BC}, m^{2\ \max}_{AC}, m^{2\ \max}_{AC_0}) \\ & + \epsilon P_c\ (m^2_{AB}, m^2_{BC}, m^2_{AC} | m^{2\ \max}_{AB}, m^{2\ \max}_{BC}, m^{2\ \max}_{AC}, m^{2\ \max}_{AC_0}) \\ & + (1 - 2\ \epsilon) P_b\ (m^2_{AB}, m^2_{BC}, m^2_{AC}) \end{aligned} \tag{8.21}$$

Once the maxima of the Dalitz parameters are extracted from this fit, the Jacobian function defined in Eq. 8.16 may be used to measure the particle masses.

8.5 NNOMET Masses: A Supersymmetric Example

For a proof of principle, we use a mass spectrum and cross section roughly corresponding to the CMS collaboration early supersymmetry benchmark LM1 [114], which contains the process

$$\begin{aligned} \widetilde{q} &\to \widetilde{\chi}^0_2 + q \\ &\quad \hookrightarrow \widetilde{\ell} + \ell_1 \\ &\quad\quad \hookrightarrow \widetilde{\chi}^0_1 + \ell_2 \end{aligned} \tag{8.22}$$

and a mass spectrum given in Table 8.1. In this toy analysis, we employ our own event generator called COSET Monte Carlo in order to simulate the kinematics of two-body sequential on-shell cascade decays. COSET MC is a barebones simulator that generates four-vectors with two-body on-shell kinematics. The decay angles at each step of the decay are determined via random number generator determined by the functional form of the angular distributions that are characteristic of a particle with the appropriate spin. Each pair of four-vectors are then Lorentz boosted back to the lab frame along the directions of their progenitors. For particles identified as quarks, the entire four-vector is multiplied by a random number generated by a Gaussian centered at unity with a variance of 0.1 to simulate jet resolution effects. Approximately 20,000 LM1-like signal events are generated corresponding to about 1 fb^{-1} of data, with jet resolution

	$\widetilde{q}$	$\widetilde{\chi}_2^0$	$\widetilde{\ell}$	$\widetilde{\chi}_1^0$	$m_{q\ \ell_1}^{2\ \max}$	$m_{q\ \ell_2}^{2\ \max}$	$m_{q\ \ell_2\ 0}^{2\ \max}$	$m_{\ell_1\ \ell_2}^{2\ \max}$
Mass (GeV)	552	178	118	97	391^2	298^2	197^2	76^2

Table 8.1: LM1 benchmark sparticle masses and mass parameters determining the three-dimensional Dalitz distribution of the $\widetilde{q} \to \widetilde{\chi}_2^0 \to \widetilde{\ell} \to \widetilde{\chi}_1^0$ cascade transition.

applied to the first branch of the decay chain representing the quark that has decayed from the squark. The Dalitz triplet values for $(m_{q\ \ell_1}^{2\ \max}, m_{\ell_1\ell_2}^{2\ \max}, m_{q\ \ell_2}^{2\ \max})$ are the output. The Standard Model background for this process is dominated by $t\bar{t}$ production. Using $t\bar{t}$ samples produced in Pythia6 at 14 TeV, we fit the distribution of the $t\bar{t}$ events in the same three-dimensional Dalitz space to a falling exponential. We then generate a generic background sample to this fit using a random number algorithm to output the same Dalitz triplet data for the background. The LM1 signal and $t\bar{t}$ background event distribution in dimensionful Dalitz space is shown in Fig. 8.6

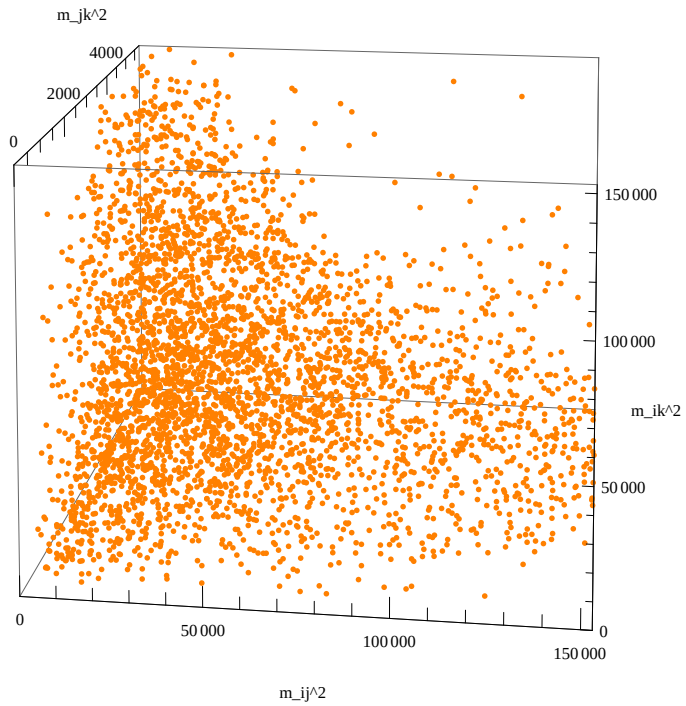

Figure 8.6: A scatter plot of signal events with the combinatoric confusion in three dimensional Dalitz space. Signal events were generated using COSET Monte Carlo with a mass spectrum following the CMS SUSY LM1 benchmark.

To illustrate the proof of principle for the NNOMET technique, we will also restrict attention here to the two dimensional subspace of the $\partial m_i/\partial m_{IJ}^{2\,\max}$ detailed in Section (2.2). This two dimensional fit to the $(m_{AC}^{2\,\max}, m_{AC_0}^{2\,\max})$ is not only conceptually simpler, but also reflects the practical fact that the equations for the nearest branch invariant Jacobians $m_{AB}^{2\,\max}$ and $m_{BC}^{2\,\max}$ project onto one-dimensional distributions with distinct kinematic "edges" that can easily be read off from invariant mass distributions. Indeed measurements of the parameters $m_{AB}^{2\,\max}$ and $m_{BC}^{2\,\max}$ are discussed extensively in the existing literature [115, 124, 107–110]. In contrast, the extrema $m_{AC}^{2\,\max}$ and $m_{AC_0}^{2\,\max}$ of the next-to-nearest branch Dalitz parameters contain no such sharp kinematic features in their lower dimensional projections and are significantly more difficult to discern as a result. Determining $m_{AC_0}^{2\,\max}$ is particularly difficult without the NNOMET methods as it is by definition the end point of some distribution restricted to a narrow kinematic regime in which statistics are low. It is on the extraction of these parameters that the NNOMET procedure has its unique advantage. Thus since the nearest branch Dalitz invariants $m_{q\,\ell_1}^{2\,\max}$, $m_{\ell_1\ell_2}^{2\,\max}$ may be easily determined in this example, we input the correct values for these. We then scan over the next-to-nearest branch Dalitz invariants $m_{q\,\ell_2}^{2\,\max}$, $m_{q\,\ell_{2_0}}^{2\,\max}$, each from 0.9 to 1.1 times their correct values in steps of 0.02 times the correct values using the probability distribution function Eq. 8.21. The likelihood contours in dimensionful $(m_{q\,\ell_2}^{2\,\max}, m_{q\,\ell_{2_0}}^{2\,\max})$ are shown in Fig. 8.7.

At the benchmark point we consider, $R \simeq 0.44$. Even though this is not a particularly degenerate spectrum, the rotation angle for $R = 0.44$ is very close to its limiting value $\vartheta \simeq 0.994(\pi/4)$ and the eccentricity is large $\varepsilon \simeq 26.5$. The 1σ contour in the $(m_{\chi_2^0}, m_{\tilde{\ell}})$ mass plane is shown in Fig. 8.8 and we can see the rotation angle and large eccentricity reflected in the precise measurement of only a specific linear combination of masses $m_{\chi_2^0}$ and $m_{\tilde{\ell}}$.

The sensitivity here is obviously optimistic given the lack of realistic cuts and proper simulation of detector effects and uncertainties. This over-simplified study is meant only to demonstrate a proof of concept for the techniques described and a more detailed study must be done to make quantitative statements about the sensitivity to mass measurement in the much more unforgiving environment that will be present during

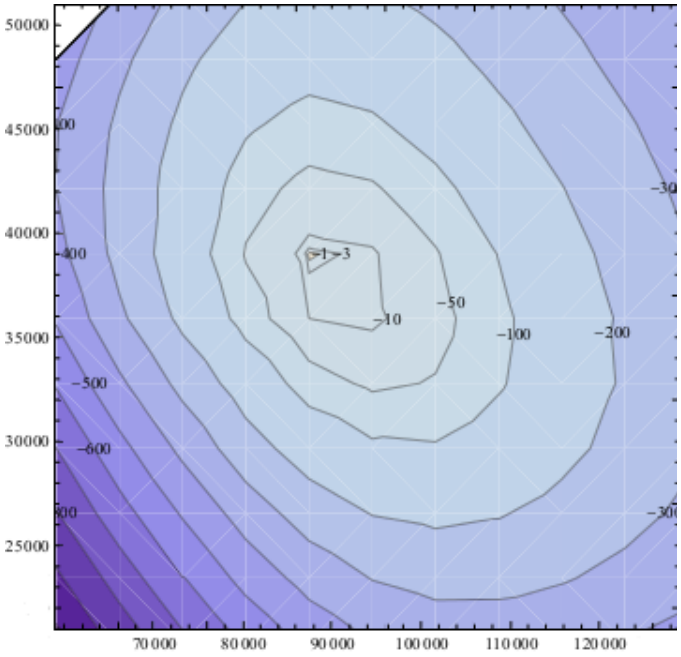

Figure 8.7: Likelihood contours of the NNOMET fit in the ($m^{2\,\max}_{AC}$, $m^{2\,\max}_{AC_0}$) plane.

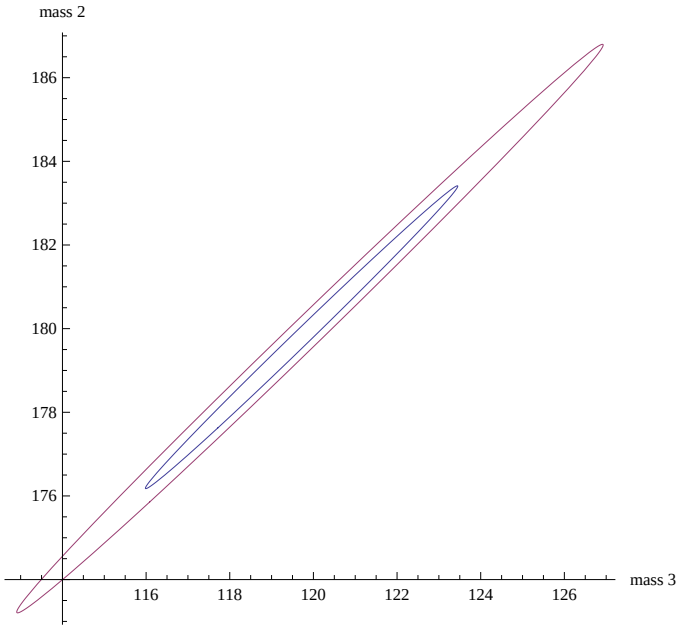

Figure 8.8: The 1σ likelihood contour was estimated from the likelihood fit in Fig. 8.7 and mapped onto the (m_2, m_3) plane. The rotation angle $\vartheta \approx 0.78$ and eccentricity $\epsilon \approx 26.5$ restricts a percent level mass measurement to a specific linear combinations of masses given by ϑ.

Run II of LHC operation.

8.6 Going Forward

Despite a lack of any conclusive excess in events with large amounts of missing energy in Run I of LHC operation, the sequential on-shell cascade decay with missing energy remains a generic signature topology of new physics to look for in Run II. The NNOMET procedure outlined in this analysis seems to be a powerful tool for identifying such signatures and extracting important theoretical parameters for new physics in the event that such signatures are observed in LHC data. The lack of a reliance on measurements of missing energy, which are notoriously subject to error especially in the large pile-up environment expected in Run II, is one of the many virtues of this analysis. Importantly the NNOMET procedure conceptually subsumes many of the techniques currently used to infer particle masses from LHC kinematic observables. In particular, techniques that make use of features in one or two dimensional distributions of invariant masses, where we have shown that many of the strongest correlations between invariants are completely obscured in such lower dimensional projections.

Although we have made the assumption of massless final particle states in this analysis, the generalization to massive particle final states is straightforward. In particular, obvious improvements can be made by taking finite masses of jets into account within the framework of the NNOMET procedure. With jet mass corrections, and matrix element and phase space improvements for finite width and final state radiation effects, the NNOMET procedure for extracting particle masses would approach, but not exceed, the level of sophistication and complexity of matrix element techniques currently employed to extract the top quark mass at the Tevatron in the semi-leptonic channel. And since NNOMET employs an invariant sub-process matrix element and phase space, it would be much less computationally demanding than current top quark matrix element techniques that require marginalization over the entire phase space of initial parton distribution functions, initial state radiation, and individual neutrino four-vectors.

The wide range of independent techniques that have been suggested to measure

particle masses at the LHC provides a well founded hope that no matter what new particles are discovered, their masses will ultimately be measured. It only remains to see precisely how well.

Chapter 9

Particle Masses from Displaced Tracks

Much of the research program at the Large Hadron Collider (LHC) is currently being dedicated to the search for specific proposed extensions of the Standard Model (SM) beyond the weak scale. Although a model independent approach to new physics searches should primarily involve searching for deviations from SM predictions of any kind, a specific discovery cannot be claimed without more detailed information about the processes that occur subsequent to the initial particle collisions. Therefore obtaining precise measurements of theoretical parameters, such as the mass spectrum of new particle states, is an endeavor of particular importance.

In this paper, we propose techniques for measuring particle masses from several different signatures containing missing transverse momentum. We assume that some heavy new particle states are pair produced and then participate in sequential two-body cascade decays that produce visible SM particles, until some effectively stable and non-interacting new particle is reached at the bottom of the decay chain. This is the canonical and well-studied dual cascade decay chain signature, well known for being the canonical signature of R-parity conserving supersymmetry (SUSY) models. None of the kinematic techniques discussed in this paper will rely on the fact that the cascade decay chains be supersymmetric in nature, thus all of these techniques may be applied generally to any BSM model that contains this topology as a signature. However, due to the familiarity with supersymmetric terminology, we will generically refer to the Lightest meta-Stable Particle as the LSP and the Next-to-Lightest meta-Stable Particle as the NLSP. Our analysis will focus on a subset of these scenarios in which the last step of the cascade decay involves some long-lived new particle state that travels a finite distance before decaying in flight This will result in a signature of

displaced vertices or displaced tracks in the detector.

The techniques to be described here are model independent which is fortunate since missing transverse momentum is a fairly generic feature of models for physics beyond the SM. This is because general phenomenological considerations often motivate new discrete symmetries, resulting in the presence of effectively non-interacting stable particle states. In the case of SUSY for example, R-parity is often invoked to exclude dangerous operators that can result in phenomenologically inconsistent effects like proton decay. In the case of extra dimensional models, it is the conservation of momentum along the extra dimension that will result in the pair production of Kaluza-Klein (KK) states and subsequently guarantee the stability of the lightest KK mode. One can even invoke cosmological arguments like the WIMP Miracle calculations to argue that missing energy signatures might be a generic phenomenologically desirable feature of models for new physics at the weak scale. The presence of metastable new particle states is also fairly common and can arise in supersymmetric models with low scale SUSY breaking or scenarios where R-parity conservation is only approximate. In this paper, we address the question of whether or not it is possible, under any circumstances, to recover all of the kinematic information lost through missing energy on an event-by-event basis.

If all of the final state particles from a given collision are visible through the detector, then the measurement of on-shell particle masses can easily be performed through the straightforward reconstruction of a mass resonance peak. However, if one or more of the final state particles are effectively stable and non-interacting, then the situation is much more challenging. In particular, particle masses cannot be calculated directly on a mass peak resonance since crucial kinematic quantities cannot be measured. In response to this issue, many general techniques have been developed for performing indirect measurements of particle masses through cleverly constructed kinematic variables [115–120]. In particular, the author in [123] introduces a very generic method for constructing such variables via phase space singularity structures. Many studies have also been performed based on kinematics specific to the canonical cascade decay chain [124–128, 130–139]. In general, novel kinematic structures that characterize an event can often be used to reconstruct lost information. For example, [121, 122] also discuss a long-lived

NLSP, and the use of timing information to perform such reconstructions. For different topologies of the decay chain, [139] provides a comprehensive review. The drawback to most of these methods is the fact that most of the kinematic variables that can be constructed to provide an indirect mass measurement, require a very large number of events for telling features to become practically visible in statistical distributions. These methods would therefore be difficult to utilize during early discovery level searches.

First, using our assumptions we will show that one can write down an expression for the 3-momenta of each LSP as a function of the direction of the 3-momenta of each NLSP. This unit vector can then be written in terms of the locations of the secondary vertices. We will then follow with a description of some novel methods for reconstructing particle masses using this information. Examples of explicit mass reconstruction will be performed using Monte Carlo parton-level data, highlighting the effectiveness of these methods in some of the diverse topologies that can occur within the cascade. Finally we will conclude with a discussion of how this relates to current SUSY searches being performed at the LHC. We argue then, that the optimal strategy for searching under the lamp post during these early uns will be to search for signatures with two displaced vertices (or two displaced tracks in situations where the exact location of the secondary vertices can not be measured).

9.1 Kinematics of Displaced Vertices

9.1.1 Counting the Unknowns

Let us denote the stable LSP particles by X_1 and Y_1, their mother NLSP particles as X_2 and Y_2 and the final visible SM particles as a_1 and b_1. Fig. 9.1 shows a diagram of a typical event. Since we assume that the 4-momenta of the two LSPs are not measurable, each event yields 8 unknown quantities. The transverse missing momentum is given by the vector sum of the LSP 3-momenta projected onto the transv erse plane. Since this plane is 2-dimensional, a missing transverse momentum measurement eliminates 2 degrees of freedom bringing the number of unknowns down to 6. In order to construct constraint equations with which to solve for these unknowns, we follow the work of

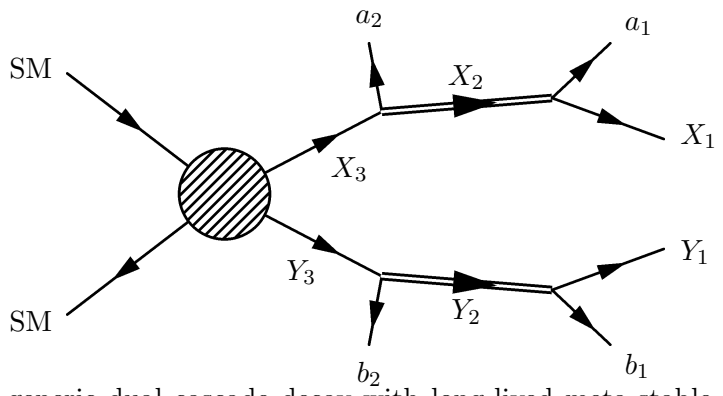

Figure 9.1: A generic dual cascade decay with long-lived meta-stable NLSP's. Long-lived particles are denoted by a double line.

[140–142] and assume some symmetry between the two sides of the decay chains. For example, if we assume that $m_{X_2} = m_{Y_2}$ then we can use the fact that $(p^\mu_{X_1} + p^\mu_{a_1})^2 = (p^\mu_{Y_1} + p^\mu_{b_1})^2$ as a constraint with which to eliminate one of the unknown momentum components.

Let k denote the number of such equations we can construct. Since all of the unknown quantities involve components of the LSP 4-momenta, k can be viewed as the number of masses starting from the bottom of one decay chain but excluding the LSP, that we assume to be equal to the masses on the opposite side of the decay chain. Utilizing these constraints, the number of unknowns can be reduced to $6 - k$. It is important to keep in mind however, that such an exact relationship between the masses of these particles only holds in the very narrow width limit. In general, the true kinematically reconstructed masses will lie on the distribution of some mass peak resonance and the equality of the asses will only be approximately true. This will affect both the accuracy of the mass measurement as well as potentially the existence of solutions to the constraint equations. We will return to a more detailed discussion of this in the body of the paper.

If we assume that we have access to m events with the same topology then we can use the equality of masses across events to further constrain the problem as done in [140–142]. For the first event we counted $6 - k$ unknowns. Each additional event contributes another $6 - k$ unknowns but if we enforce the equality of masses across different events then we should subtract off another factor of k. Thus each additional event contributes $6 - 2k$. For m events, the total number of unknowns is $6 - k + (m - 1)(6 - 2k) =$

$6m - 2km + k$. The condition which must be satisfied in order to properly constrain the problem is thus clearly $6m - 2km + k \leq 0$.

Given our assumptions that the NLSP is the only particle in the spectrum with a finite and measurable decay length, an accurate measurement of the locations of the displaced vertices can be used to provide additional constraints. Here we assume that all of the decays occur on a microscopic length scale before the NLSPs travel a finite macroscopic distance and decay to a pair of invisible LSPs and a pair of visible SM particles. This implies that the direction of the NLSP 3-momentum is equal to the unit vector pointing in the direction of the secondary vertex. The NLSP unit 3-momentum contains two degrees of freedom, thus an accurate measurement of two displaced vertices will allow us to subtract off another $4m$ nknowns. In some situations, it will not be possible to measure the locations of the displaced vertices and only the trajectories of the displaced tracks will be visible. In these situations, the locations of the secondary vertices can be constrained to lie on the trajectories of the displaced tracks and can be parameterized by one number thus removing $2m$ unknown quantities.

9.1.2 Parameterizing the Unknowns

In this section we propose a parameterization of the unknown quantities that makes the utility of displaced vertices and displaced tracks maximally transparent. More specifically, we will show that it will be possible to write down an expression for the 3-momenta of each LSP that depends only the location of the displaced vertices. Throughout this analysis let us assume that the 4-momenta of the visible Standard Model particles a_1 and b_1 can be measured accurately. Let us restrict our attention to one side of the decay chain and denote the 4-momenta for particle X_1, X_2 and a_1 as in Eq. 9.1

$$p_{X_1} = \begin{pmatrix} E_{X_1} \\ |\vec{p}_{X_1}|\hat{p}_{X_1} \end{pmatrix} \quad ; \quad p_{X_2} = \begin{pmatrix} E_{X_2} \\ |\vec{p}_{X_2}|\hat{p}_{X_2} \end{pmatrix} \quad ; \quad p_{a_i} = \begin{pmatrix} E_{a_i} \\ |\vec{p}_{a_i}|\hat{p}_{a_i} \end{pmatrix} \tag{9.1}$$

To isolate the unknown quantities, it is useful to decompose the 3-momenta of particles a_1 and X_1 in terms of their components parallel and orthogonal to the momentum of particle X_2 as in Fig. 9.2. For notational convenience, let us define the projection

symbol as in Eq. 9.2

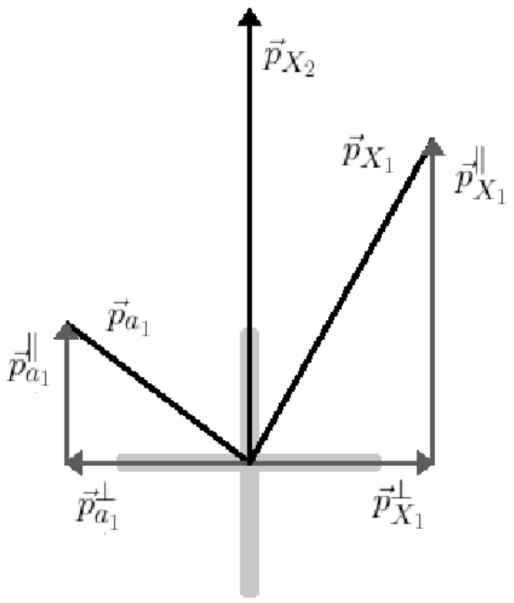

Figure 9.2: A decomposition of the final decay products into their components parallel and orthogonal to particle X_2. Note that the component of $\vec{p}_{X_1}$ orthogonal to the direction of the NLSP, is equal in magnitude and opposite in direction to the component of $\vec{p}_{a_1}$ orthogonal to the direction of the NLSP.

$$\mathbb{P}^i_j \equiv \vec{p}_i \cdot \hat{p}_j \tag{9.2}$$

This denotes the projection of the 3-momentum of particle i along the direction of the 3-momentum of a different particle j. In this basis and with this notation we can decompose $\vec{p}_{a_1}$ into its component parallel $\vec{p}^{\,\parallel}_{a_1} = \mathbb{P}^{a_1}_{X_2}\hat{p}_{X_2}$ and orthogonal $\vec{p}^{\,\perp}_{a_1} = \vec{p}_{a_1} - \mathbb{P}^{a_1}_{X_2}\hat{p}_{X_2}$ to particle X_2. Conservation of momentum allows us to immediately write down the orthogonal component of the 3-momentum of particle X_1 as $\vec{p}^{\,\perp}_{X_1} = -\vec{p}^{\,\perp}_{a_1} = \mathbb{P}^{a_1}_{X_2}\hat{p}_{X_2} - \vec{p}_{a_1}$. The magnitude of the component of the 3-momentum of particle X_1 along the direction of X_2 remains unknown. In this paper we will denote it as $c_1 \equiv \mathbb{P}^{X_1}_{X_2}$ so the parallel component can be expressed as $\vec{p}^{\,\parallel}_{X_1} = c_1\hat{p}_{X_2}$. Since the other side of the decay chain is subject to identical kinematic considerations, the 3-vector of each LSP is given by

$$\vec{p}_{X_1} = (\mathbb{P}^{a_1}_{X_2} + c_1)\hat{p}_{X_2} - \vec{p}_{a_1} \quad \text{and} \quad \vec{p}_{Y_1} = (\mathbb{P}^{b_1}_{Y_2} + c_2)\hat{p}_{Y_2} - \vec{p}_{b_1} \tag{9.3}$$

Let $\alpha = 1, 2$ be indices parameterizing a basis in the two-dimensional transverse plane. The experimentally measured missing transverse momentum $\vec{\not{p}}^T_\alpha$ contains two degrees of freedom and is restricted to the transverse plane. Since by assumption, the missing transverse momentum in this scenario is taken from the vector sum of the 3-momenta of the two LSPs, it can be calculated as the sum of contributions from each LSP as in Eq. 9.4

$$\vec{\not{p}}^T_\alpha = \vec{p}^{X_1}_\alpha + \vec{p}^{Y_1}_\alpha = (\mathbb{P}^{a_1}_{X_2} + c_1)\hat{p}^{X_2}_\alpha + (\mathbb{P}^{b_1}_{Y_2} + c_2)\hat{p}^{Y_2}_\alpha - \vec{p}^{a_1}_\alpha - \vec{p}^{b_1}_\alpha \tag{9.4}$$

These two equations can then be used to solve for c_1 and c_2 as in Eq. 9.5

$$\begin{aligned} c_1 &= \frac{(p^{a_1}_\alpha + p^{b_1}_\alpha + \not{p}_\alpha)p^{Y_2}_\beta \epsilon^{\alpha\beta}}{p^{X_2}_\alpha p^{Y_2}_\beta \epsilon^{\alpha\beta}} - \mathbb{P}^{a_1}_{X_2} \\ c_2 &= \frac{(p^{a_1}_\alpha + p^{b_1}_\alpha + \not{p}_\alpha)p^{X_2}_\beta \epsilon^{\alpha\beta}}{p^{Y_2}_\alpha p^{X_2}_\beta \epsilon^{\alpha\beta}} - \mathbb{P}^{b_1}_{Y_2} \end{aligned} \tag{9.5}$$

Here $\epsilon^{\alpha\beta}$ is the totally antisymmetric 2×2 tensor. The key result here is that an accurate measurement of the missing transverse momentum will allow us to write down the 3-momentum of each LSP as a function of the direction of the NLSP 3-momenta by plugging Eq. 9.5 into Eq. 9.3. The result is summarized by Eq. 9.6

$$\begin{aligned} \vec{p}_{X_1} &\to \vec{p}_{X_1}(\hat{p}_{X_2}, \hat{p}_{Y_2}) \\ \vec{p}_{Y_1} &\to \vec{p}_{Y_1}(\hat{p}_{X_2}, \hat{p}_{Y_2}) \end{aligned} \tag{9.6}$$

Let us denote the location of the two secondary vertices by 3-vectors in the Cartesian coordinates of the lab frame $\vec{r}_X$ and $\vec{r}_Y$. Here the subscripts X and Y correspond to the location of the decays of particles X_2 and Y_2. Note that given our assumptions $|\vec{r}_X| = d_X$ simply the distance traveled by particle X_2 before decaying while $|\vec{r}_Y| = d_Y$ is the distance traveled by particle Y_2 before decaying, assuming all other decays are prompt. Now recall our initial assumption that the decay length of particles X_2 and Y_2

are the only decay lengths that are measurably large. Then subsequent to the initial collision, a cascade will occur on some microscopic length scale before the NLSPs travel a finite macroscopic distance and decay to a pair of invisible LSPs and a pair of visible SM particles. This implies that the direction of the NLSP 3-momentum is equal to the unit vector pointing in the direction of the secondary vertex. The exact relationship is $\hat{p}_{X_2} = \vec{r}_X/|\vec{r}_X|$. Therefore in actuality we have derived an expression for the LSP 3-momenta that depends only on the location of the secondary vertices as in Eq. 9.7

$$\begin{aligned} \vec{p}_{X_1} &\to \vec{p}_{X_1}(\vec{r}_X, \vec{r}_Y) \\ \vec{p}_{Y_1} &\to \vec{p}_{Y_1}(\vec{r}_X, \vec{r}_Y) \end{aligned} \tag{9.7}$$

In some situations, the displaced vertices may not be directly measurable and only the trajectories of the displaced tracks may be extracted. However, it may be inferred that the displaced vertices must lie somewhere along the path of the displaced tracks. We may thus parameterize the location of the displaced vertices according to their location along the beam axis. Let z_X and z_Y denote the location along the z-axis of $\vec{r}_X$ and $\vec{r}_Y$ respectively and let us set the location of the primary vertex to be $z = 0$. Indeed if we denote the location of particle a_1's collision with the tracker by $\vec{r}_0 = (x_0, y_0, z_0)$, then an exact functional form for $\vec{r}_X(z_X)$ is given by Eq. 9.8.

$$\vec{r}_X(z_X) = \begin{pmatrix} x_0 + (\mathbb{P}^{a_2}_{\hat{x}}/\mathbb{P}^{a_1}_{\hat{z}})(z_X - z_0) \\ y_0 + (\mathbb{P}^{a_2}_{\hat{y}}/\mathbb{P}^{a_1}_{\hat{z}})(z_X - z_0) \\ z_X \end{pmatrix} \tag{9.8}$$

This will allow us to derive an expression for the LSP 3-momenta that depends only on the location of the secondary vertices along the beam axis as in Eq. 9.9

$$\begin{aligned} \vec{p}_{X_1} &\to \vec{p}_{X_1}(z_X, z_Y) \\ \vec{p}_{Y_1} &\to \vec{p}_{Y_1}(z_X, z_Y) \end{aligned} \tag{9.9}$$

From this parameterization we can explicitly see the dependence of the 3-momentum of each missing particle on the locations of the displaced vertices or the trajectories of

the displaced tracks. Now that it is clear how such measurements can be used to reduce the number of unknowns and further constrain the kinematics of this decay topology, we move on to some practical examples.

9.2 Monte Carlo Simulations for Displaced Tracks

Here we give some details about how to prepare the MC information and how we derive the weighting factor. We first took the lhe file from a fixed SUSY spectrum, where the 4-momenta of gravitino, slepton and lepton are accessible. The information of the beginning and ending points of displaced tracks are missing. We take the proper decay length of slepton to be half of detector radius and impose the location of 2nd vertex according to the exponential decay distribution. With all those information, we can calculate the beginning and ending points of displaced tracks for each event. Since displaced tracks are assumed to be measurable in experiments, but 4-momenta of gravitino and slepton are not, we would use the track information and forget the momenta information for the later analysis. Also, the transverse missing energy is assumed to be only coming from two gravitinos, thus it can be calculatedwhen we prepare the MC information. One needs to be very careful on what information is accessible and what is not. We summarize the accessible information as following: the location of primary vertex, the beginning and ending points of the two displaced tracks for each event, the 4-momenta of each displaced track, and transverse missing energy. Except for those, all other information will be treated as inaccessible.

After we finish the preparation of MC information, we proceed to scan in the possible locations of 2nd vertex along one of the displaced tracks. The scanning we do is taking a constant step along the track. The calculation of weighting factor for each scanning point is a little tricky, because part of the information of exponential decay has already been included in the distribution of displaced tracks. Thus the uniform step of scanning along each tracks in many events is not giving us a uniform distribution of points in space. To gain the correct weighting factor, one has to first include a weighting factor of each displaced track. This factor is described more precisely in the following Appendix, then an exponential decay factor can be applied. Thus the weighting factor for each

point takes the form in Eq. 9.10

9.2.1 Weight Functions

Here we give a detailed discussion on how to extract a rough estimate of the decay length from the observation of a few displaced tracks. This can be done by looking at the distribution of perpendicular distances from the primary vertex to the point of closest approach for all displaced tracks $d_\perp$. Suppose X_2 travels a distance l before decaying, as in Fig. 9.3. Let θ be the angle between PS and CS. Then we have

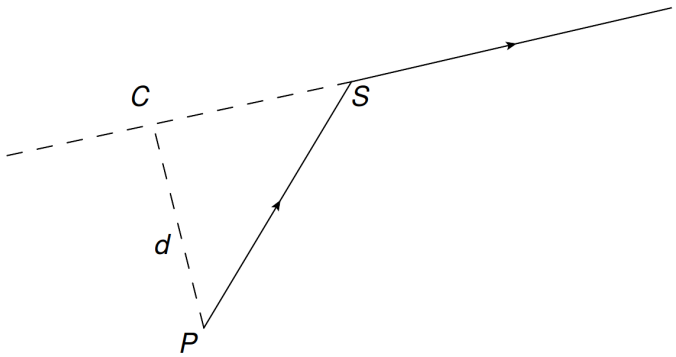

Figure 9.3: The kinematics of a displaced track. Here d is distance of closest approach between the primary vertex and the displaced track, C is the point of closest approach, l is the distance between the primary vertex and the hypothetical point of decay on the displaced track and l_0 is the characteristic decay length of the NLSP.

$$d_\perp = l \sin\theta$$

Let l_0 be the characteristic decay length of particle X_2. Since the measured decay distance for an event l must an exponentially decaying distribution, the properly normalized probability distribution is:

$$\frac{\partial P(l,\theta,\phi)}{\partial l}|_{\theta,\phi} = \frac{1}{l_0} e^{-l/l_0} f(\theta,\phi)$$

Also, we know that the decay of particle X_2 is isotropic in its rest frame. Since the mass of X_2 is $\mathcal{O}(100\,\mathrm{GeV})$, the boost from lab frame to the rest frame of X_2 is not large. We can thus approximate the anglular distribution in lab frame to be isotropic:

$$\frac{\partial^2 P(l,\theta,\phi)}{\partial(\cos\theta)\partial\phi}|_l = \frac{1}{4\pi}g(l)$$

Since we l, θ and ϕ are independent variables, we have:

$$\frac{\partial^3 P(l,\theta,\phi)}{\partial l\partial(\cos\theta)\partial\phi} = \frac{1}{4\pi l_0}e^{-l/l_0}$$

From the relation between $d_\perp$ and (l,θ), we have

$$\frac{\partial d_\perp}{\partial(\cos\theta)}|_l = -l^2\sqrt{1-\frac{d_\perp^2}{l^2}}$$

Finally, we get

$$\frac{dP}{d(d_\perp)} = \int_{d_\perp}^{\infty}\frac{dl}{2l_0}\frac{e^{-l/l_0}}{l\sqrt{l^2-d_\perp^2}} \tag{9.10}$$

Though this integral is not easy to solve, one can cut the integral at very large values and get the distribution numerically. Thus, with just a couple of displaced tracks from a few events, one can extract the rough value of the decay length of X_2.

9.3 Examples with a Massless LSP

From the counting arguments given in the introduction, we found that for m events and k constraint equations, the total number of unknown quantities was equal to $6-2km+k$. In principle, the problem is simply a matter of solving for enough constraint equations to obtain a unique solution for all unknown quantities. In practice however, the contraint equations are highly nonlinear and generically contain multiple solutions. As a result, a confident mass measurement should really involve the analysis of a number of events greater than the minimum required to properly constrain the problem. We will now explore a few specific examples. For concreteness, we will start with an analysis of selected benchmark points for multi-lepton searches inspired by scenarios with general gauge mediated SUSY breaking (GMSB). In such scenarios, where the scale of SUSY breaking is sufficiently low, the LSP is an effectively massless gravitino. With the mass

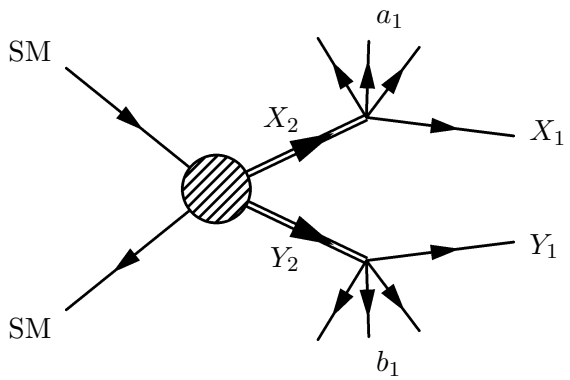

Figure 9.4: The special case of a dual cascade decay where the Standard Model particles a_1 and b_1 decay promptly. In this situation, the decay products of particles a_1 and b_1 can be traced back to their displaced secondary vertices.

of the LSP set to zero, $2m$ unknowns are removed from the problem resulting in a total number given by Eq. 9.11

$$\text{Number of Unknowns for Massless LSP Scenario} = 4m - 2km + k \tag{9.11}$$

9.3.1 Measurable Displaced Vertices

If a_1 and b_1 each decay promptly to two or more visible particles, it will be possible to experimentally trace back the track of each decay product and reconstruct the position of the secondary vertex. The momenta p_{a_1} and p_{b_1} can then be computed through the sum of 4-momenta of their respective decay products, assuming none of them contribute to the missing transverse momentum. The situation is depicted in Fig. 9.4. In this case we can directly measure the quantities $\hat{p}_{X_2} = \vec{r}_X/|\vec{r}_X|$ and $\hat{p}_{Y_2} = \vec{r}_Y/|\vec{r}_Y|$ and thus completely solve for the 3-momenta of particles X_1 and Y_1. Since these particles are massless by assumption, a measurement of the 3-momenta is equivalent to a measurement of the full 4-momenta. Therefore in situations where the LSP is massless, a simple measurement of the locations of the displaced vertices already recovers all of the information lost through missing energy. In terms of the unknowns we see that substituting one event $m = 1$ into Eq. 9.11 gives us $4 - k$. A measurement of the displaced vertices removes exactly 4 unknowns, which means that the condition for total kinematic recovery is already met for $k = 0$. This example is thus trivial and will not be discussed further.

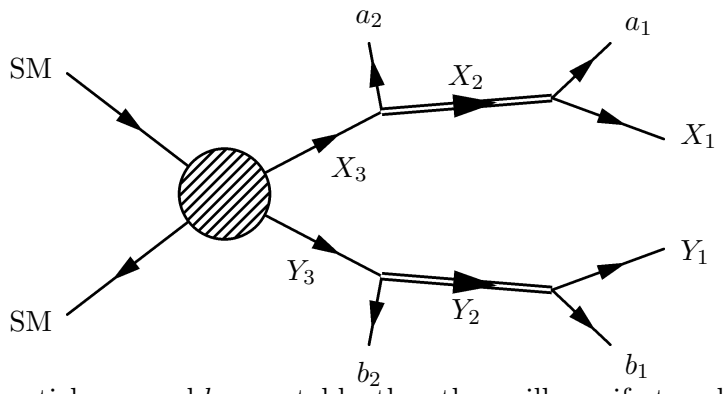

Figure 9.5: If particles a_1 and b_1 are stable, then they will manifest as displaced tracks. In this situation, at least two on-shell decays are required on each leg in order to fully reconstruct the masses of all the particles.

9.3.2 Measurable Displaced Tracks

If a_1 and b_1 are stable and hit the detector, then p_{a_1} and p_{b_1} can be directly measured. In this scenario, the exact location of the secondary vertex cannot be measured but one can constrain their location to a point along the displaced tracks of particles a_1 and b_1. Parameterizing the 3-momentum $\vec{p}_{X_1}$ by z_X and $\vec{p}_{Y_1}$ by z_Y removes $2m$ unknown quantities from Eq. 9.11 bringing the requirement for total kinematic recovery down to $2m - 2km + k \leq 0$. Acheiving this with $m = 1$ event requires that $k \geq 2$ so we will use the fact that $m_{X_3} = m_{Y_3}$ and $m_{X_2} = m_{Y_2}$ in order to measure the particle masses. Our canonical example for this scenario, depicted in Fig. 9.5, comes from GMSB. Here we consider the case where two partons collide resulting in the pair production of two right-handed squarks. Each squark decays to Bino-like neutralinos X_3 and Y_3, emitting jets in the process. Each neutralino then decays to right-handed sleptons X_2 and Y_2, emitting leptons a_2 and b_2 in the process. Finally the right-handed sleptons decay to the LSP gravitinos X_1 and Y_1, emitting additional leptons a_1 and b_1 in the process. The relevant part of the spectrum is summarized in the following table:

Particle	Symbol	Mass
Bino	$\tilde{B}$	199.30 GeV
Right-handed Slepton	$\tilde{l}_R$	107.44 GeV
Gravitino	$\tilde{G}$	0 GeV

Another point to keep in mind is that the further up we go in the decay chain, the higher the chance for combinatoric confusion among the visible particles, labeled in

this example by a_1, a_2, b_1, and b_2. In general it may not always be possible to identify the correct particle with its correct position within a given decay chain. If this is the case then all possibilities should be considered which will result in a larger multiplicty of solutions. A slightly larger data sample may then be required in order to make a definitive mass measurement by finding a common value for the masses. Since the visible SM particles are leptons, we will treat them as effectively massless. The relevant formulae are then given in Eq. 9.12 with the expressions for c_1 and c_2 given by Eq. 9.5.

$$
\begin{aligned}
m_{X_3}^2 &= 2(E_{a_1}+E_{a_2})\sqrt{c_1^2-(\mathbb{P}_{X_2}^{a_1})^2+\vec{p}_{a_1}^{\,2}} - 2(c_1+\mathbb{P}_{X_2}^{a_1})(\mathbb{P}_{X_2}^{a_1}+\mathbb{P}_{X_2}^{a_2}) + 2\vec{p}_{a_1}^{\,2} + 2E_{a_1}E_{a_2} \\
m_{Y_3}^2 &= 2(E_{b_1}+E_{b_2})\sqrt{c_2^2-(\mathbb{P}_{Y_2}^{b_1})^2+\vec{p}_{b_1}^{\,2}} - 2(c_2+\mathbb{P}_{Y_2}^{b_1})(\mathbb{P}_{Y_2}^{b_1}+\mathbb{P}_{Y_2}^{b_2}) + 2\vec{p}_{b_1}^{\,2} + 2E_{b_1}E_{b_2} \\
m_{X_2}^2 &= 2E_{a_1}\sqrt{c_1^2+\vec{p}_{a_1}^{\,2}-(\mathbb{P}_{X_2}^{a_1})^2} - 2(\mathbb{P}_{X_2}^{a_1}+c_1)\mathbb{P}_{X_2}^{a_1} + 2\vec{p}_{a_1}^{\,2} \\
m_{Y_2}^2 &= 2E_{b_1}\sqrt{c_2^2+\vec{p}_{b_1}^{\,2}-(\mathbb{P}_{Y_2}^{b_1})^2} - 2(\mathbb{P}_{Y_2}^{b_1}+c_2)\mathbb{P}_{Y_2}^{b_1} + 2\vec{p}_{b_1}^{\,2}
\end{aligned}
\tag{9.12}
$$

In practice, we are using two equations to solve for two unknowns $m_{X_2}(z_X, z_Y) = m_{Y_2}(z_X, z_Y)$ and $m_{X_3}(z_X, z_Y) = m_{Y_3}(z_X, z_Y)$. The calculation of unknown particle masses m_{X_2} and m_{X_3} in this scenario is presented here in the table with incorrect and correct solutions separated by columns:

Event	correct (Higgino,Slepton)	wrong (Gravitino,Slepton)
1	(201.77, 108.221)	(467.428, 289.917)
2	(199.207, 107.231)	(191.439, 92.8328)
3	(204.876, 110.958)	Null
4	(200.149, 109.002)	(405.112, 346.093)
5	(199.768, 107.928)	(209., 122.639),(490.134, 254.298)

Using $\mathcal{O}$(few) events we see that the correct solutions can be separated from the incorrect solutions by their sheer multiplicity.

9.3.3 Can We Do Better?

It may be argued that the equality of masses following from the condition $k = 2$ is too specific. Indeed if there was a way to measure the particle mass spectrum without

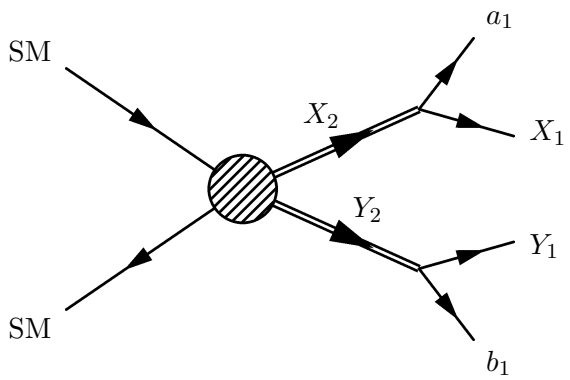

Figure 9.6: With only one on-shell decay on each leg, and no measurable displaced vertices, it is still possible to reconstruct all particle masses with $\mathcal{O}$(few) events.

demanding $m_{X_3} = m_{Y_3}$, these techniques would gain a lot in generality and become useful in a far wider range of possible new physics scenarios. Thus a natural next step would be to see if it would be possible, under any circumstances, to measure particle masses under the condition $k = 1$ as depicted in Fig. 9.6. As demonstrated in the previous section, in scenarios with a massless LSP where the trajectories of the displaced tracks are known, the requirement for total kinematic recovery is $2m - 2km + k \leq 0$. Solving for k in terms of m gives the expression $k \geq 2m/(2m-1)$. Clearly as $m \to \infty$, $k \to 1$ asymptotically but the condition $k = 1$ cannot be satisfied for any value of m. Naively this implies that it would not be possible to measure the particle masses given this assumption. Here we present a technique that defies this apparent restriction and demonstrate a particle mass measurement technique using only the condition $k = 1$.

For situations in which the number of unknown quantities is larger than the number of constraint equations available, there exists a novel and unorthodox method of extracting particle masses using a relatively small number of events. The idea behind this method utilizes the fact that even in situations where the number of constraints is not large enough to specify a unique solution to all of the unknown quantities, it may be large enough to reduce the space of solutions down to a lower dimensional subspace where the solution may be inferred. Our toy model is taken again from a GMSB scenario. The process under consideration starts with the direct pair production of right-handed sleptons labeled here by X_2 and Y_2. The sleptons then decay to LSP gravitinos X_1 and Y_1, emitting a leptons a_1 and b_1 in the process. The relevant part of the mass spectrum is summarized in the following table:

Particle	Symbol	Mass
Right-handed Slepton	$\tilde{l}_R$	107.44 GeV
Gravitino	$\tilde{G}$	0 GeV

The central challenge associated with this example is that there are two unknown quantities z_X and z_Y but only one mass constraint equation $m_{X_2}(z_X, z_Y) = m_{Y_2}(z_X, z_Y)$, which means that a unique solution cannot be obtained. However, this constraint allows us to express z_X as a function of z_Y, which we may then use to write down an expression for the mass of a particle in terms of one variable $m_{X_2}(z_X)$. With this one-to-one map from z_X to m_{X_2}, the space of possible solutions has been reduced to a one-dimensional subspace (i.e. a line) and the true value of m_{X_2} must exist as an element of this subspace.

Recall that all of the unknown quantities could be parameterized by the direction of the NLSPs $\hat{p}_{X_2}$ and $\hat{p}_{Y_2}$. Recall further that the direction of an NLSP is given by the location of its secondary vertex $\hat{p}_{X_2} = \vec{r}_X/|\vec{r}_X|$, which is restricted to lie somewhere along the trajectory of the associated displaced track. Recall finally, that a secondary vertex can thus be parameterized by its location along the beam axis $\vec{r}_X \to \vec{r}_X(z_X)$. The powerful observation here is the fact that as the hypothesized location of the displaced vertex along the beam axis approaches infinity ($z_X \to \infty$), the direction of the NLSP will asymptotically approach some fixed unit vector ($\hat{p}_{X_2} \to \hat{p}_{\text{const}}$). This means that as $z_X \to \infty$, the corresponding value of $m_{X_2}(z_X)$ will asymptotically approach some fixed number. In other words for the function $m_{X_2}(z_X)$, the domain $z_X \in (-\infty, \infty)$ maps to a closed finite range for m_{X_2}, and the correct value of m_{X_2} will always be contained in this range. If we plot the elements of this range in a histogram over a small number of events, the histogram will peak around the correct solution since it is an element of every set and should thus have the highest multiplicity across events.

In principle, the correct values for z_X and z_Y can take on any arbitrary value. Since the decay distance of particles has the form of an exponentially decaying function, hypotheses for the location of the displaced vertex that are closer to the primary vertex should carry more weight than ones that are farther away. In order to attenuate contributions from unlikely vertex locations and increase the efficiency of our analysis, we

scan the trajectory of the displaced track and assign a weight to each point accordingly. The weighting function is given by Eq. 9.13

$$f[l] = \frac{e^{-l/l_0}}{g(d_\perp)} \tag{9.13}$$

Here l is the distance between the point on the displaced track and the primary vertex and l_0 is the characteristic decay length of the NLSP. A more detailed discussion of this can be found in Appendix A. Note that we need as input only the rough order of this decay length which can be derived by looking at the distribution of displaced tracks as described in the Appendix B. The result of this weighted histogram is shown in Fig. 9.7. As we can see, this histogram quickly peaks at the value of the correct slepton mass of 107 GeV.

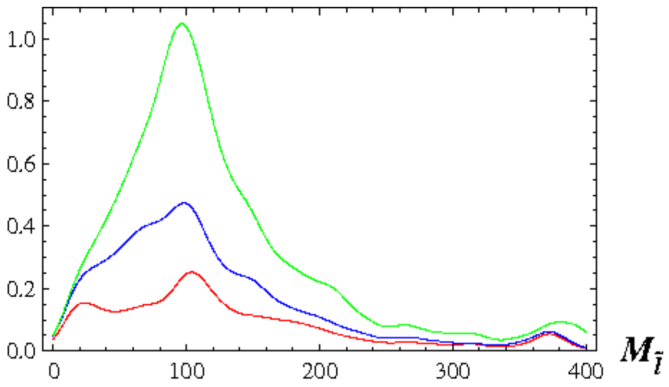

Figure 9.7: Results of the likelihood fit. The red curve indicates an exam ple with 15 events. The blue curve indicates an example with 30 events. The green curve indicates and example with 60 events

9.4 Examples with a Massive LSP

Recall again from the introduction, that for m events and k constraint equations, the general scenario with a massive LSP resulted in a counting of unknown quantities given by Eq. 9.14. In this section we will study such examples, that typically arise in the supersymmetric context when SUSY is broken at the Planck scale via gravity-mediation. The techniques described in this section will all be a straightforward demonstration of matching constraint equations with unknowns.

$$\text{Number of Unknowns for Massive LSP Scenario} = 6m - 2km + k \tag{9.14}$$

9.4.1 Measurable Displaced Vertices

Just as it was with the massless LSP, the requirement for measurable displaced vertices is that the final visible SM particles a_1 and b_1 must each decay promptly to two or more visible particles as depicted in Fig. 9.4. The measurement of displaced vertices will again provide us with a complete measurement of the LSP 3-momenta $\vec{p}_{a_1}$ and $\vec{p}_{b_1}$. The difference is that now the mass of the LSP remains an unknown quantity in the LSP 4-momenta.

In terms of our counting exercise, the measurement of displaced vertices subtracts $4m$ unknown quantities from Eq. 9.14 bringing the total number of unknowns down to $2m - 2km + k$. If we are interested in solving for all masses on an event-by-even t basis ($m = 1$), the minimum number of constraint equations clearly implies $k = 2$. With the LSPs now massive we may take our two constraint equations to be $m_{X_2} = m_{Y_2}$ and $m_{X_1} = m_{Y_1}$. Substituting the second expresion into the first reduces the problem to solving one equation for one unknown $m_{X_2}(m_{X_1}) = m_{Y_2}(m_{X_1})$. Expressions for the masses are given by Eq. 9.15 with solutions for c_1 and c_2 given by Eq. 9.5.

$$\begin{aligned} m_{X_2}^2 &= m_{X_1}^2 + 2E_{a_1}\sqrt{m_{X_1}^2 + c_1^2 + \vec{p}_{a_1}^2 - (\mathbb{P}_{X_2}^{a_1})^2} - 2(\mathbb{P}_{X_2}^{a_1} + c_1)\mathbb{P}_{X_2}^{a_1} + 2\vec{p}_{a_1}^2 \\ m_{Y_2}^2 &= m_{Y_1}^2 + 2E_{b_1}\sqrt{m_{Y_1}^2 + c_2^2 + \vec{p}_{b_1}^2 - (\mathbb{P}_{Y_2}^{b_1})^2} - 2(\mathbb{P}_{Y_2}^{b_1} + c_2)\mathbb{P}_{Y_2}^{b_1} + 2\vec{p}_{b_1}^2 \end{aligned} \tag{9.15}$$

Here we assume that particles a_1 and b_1 are massive, as per our next example where we study a more general GMSB scenario with massive SM particles and a massive gravitino. The process under consideration will be one in which two partons collide to pair produce two right-handed squarks. The squarks then decay to Higgsino-like neutralinos, labeled by X_2 and Y_2, emitting jets in the process. The neutralinos then decay to Z bosons, corresponding to particles a_1 and b_1, as well as a pair of massive gravitinos X_1 and Y_1

[30] P. Meade, M. Reece, D. Shih, JHEP 1005, 105 (2010). [arXiv:0911.4130 [hep-

. We select events in which each Z boson decays promptly to two leptons so that the intersection of the lepton tracks gives the location of the displaced vertex. Because of the extreme precision with which the detectors can track leptons, this should be the scenario in which secondary vertices may be located with the highest degree of precision. The spectrum for our toy model is given by the following table:

Particle	Symbol	Mass
Higgsino	$\tilde{H}$	196.27 GeV
Gravitino	$\tilde{G}$	50 GeV

Although the constraint equation $m_{X_2} = m_{Y_2}$ is highly non-linear and may have multiple solutions, it can be solved relatively easily using numerical techniques. Unforunately, the existence of multiple solutions may necessitate a larger data sample in order to perform a confident mass measurement. Once the equation has been solved, a numerical value for m_{X_1} can be extracted and used to solve for the exact value of m_{Y_1}. Here we show a table of the solutions from 5 events with correct and erroneous solution s separated by columns:

Event	correct (Gravitino,Slepton)	wrong (Gravitino,Slepton)
1	(50, 196.274)	Null
2	(50, 196.274)	Null
3	(50, 196.274)	(120.173, 286.545)
4	(50, 196.274)	(24144.9, 24349.4)
5	(50, 196.274)	Null

Here we see that in this case, gravitino and slepton masses are determined precisely. Though some events evidently contain multiple solutions, the unphysical solutions are sufficiently dispersed about the parameter space so as not to cause confusion in the presence of multiple events when a unique common value can easily be determined by eye.

9.4.2 Measurable Displaced Tracks

The situation is more challenging if particles a_1 and b_1 are stable as in Fig. 9.5. If this is the case, then displaced vertices will not be measurable and only the trajectories of the displaced tracks may be observed. This will allow us to subtract only $2m$ from Eq. 9.14, reducing the condition for total kinematic recovery to $4m - 2km + k \leq 0$. Solving for k in terms of m gives $k = 4m/(2m-1)$ so as $m \to \infty$ we see that $k \to 2$. Thus the minimum number of constraint equations we can demand is $k = 3$, which can be solved using $m = 2$ events. The constraints $m_{X_1} = m_{Y_1}$ and $m_{X_2} = m_{Y_2}$ were combined in Eq. 9.15, so the one additional constraint we require for $k = 3$ is the condition $m_{X_3} = m_{Y_3}$. The equations for these masses are given in Eq. 9.16

$$\begin{aligned} m_{X_3}^2 = m_{X_1}^2 + 2(E_{a_i} + E_{a_j})\sqrt{m_{X_1}^2 + c_1^2 - (\mathbb{P}_{X_2}^{a_i})^2 + \vec{p}_{a_i}^2} \\ -2(c_1 + \mathbb{P}_{X_2}^{a_i})(\mathbb{P}_{X_2}^{a_i} + \mathbb{P}_{X_2}^{a_j}) + 2\vec{p}_{a_i}^2 + 2E_{a_i}E_{a_j} \end{aligned}$$

$$\begin{aligned} m_{Y_3}^2 = m_{Y_1}^2 + 2(E_{b_i} + E_{b_j})\sqrt{m_{Y_1}^2 + c_2^2 - (\mathbb{P}_{Y_2}^{b_i})^2 + \vec{p}_{b_i}^2} \\ -2(c_2 + \mathbb{P}_{Y_2}^{b_i})(\mathbb{P}_{Y_2}^{b_i} + \mathbb{P}_{Y_2}^{b_j}) + 2\vec{p}_{b_i}^2 + 2E_{b_i}E_{b_j} \end{aligned} \tag{9.16}$$

These equations are again calculated assuming massive a_1 and b_1 as per our example, though the assumption of massless particles a_2 and b_2 is still taken for simplicity. It should be noted however, that all equations generalize easily to arbitrary massive SM particles. From the above equations we see that it is possible to construct expressions for m_{X_2}, m_{Y_2}, m_{X_3}, and m_{Y_3} in terms of three unknown quantities z_X, z_Y, and m_{X_1}. For each event we have two constraint equations $m_{X_1} = m_{Y_1}$ and $m_{X_2} = m_{Y_2}$ with which to solve them. First notice that since the LSP 4-momenta can be calculated in terms of z_X, z_Y, and m_{X_1}, we can explicitly express m_{X_2} and m_{X_3} in terms of these variables. This means that we can apply a change of variables and parameterize the three unknown quantities instead as m_{X_1}, m_{X_2}, and m_{X_3}. The fact that there are two constraint equations means that the solution for each event is a curve in parameter space, which in this case is just $\mathbb{R}^3$ with axes labeled $(m_{X_1}, m_{X_2}, m_{X_3})$. Since the trajectories of the displaced tracks are unique for each event, curves generated by different events will be

unique but will always traverse the correct answer. Thus in principle, the correct value for the masses will exist at the intersection of the curves, which is clearly equivalent to the condition of matching particle masses from different events.

Put another way, every hypothesis for the value of m_{X_1} is equivalent to a hypothesis for the values of z_X and z_Y. It is thus also equivalent to a hypothesis for the values of m_{X_2} and m_{X_3}. By considering a range of hypotheses for m_{X_1} over a few events, the correct values of m_{X_2} and m_{X_3} will be the unique intersection of all hypotheses. A demonstration of this scenario has been performed with the following mass spectrum (the Bino and Slepton masses are the same as before but the Gravitino mass is now set to 50 GeV):

Particle	Symbol	Mass
Bino	$\tilde{B}$	199.30 GeV
Right-handed Slepton	$\tilde{l}_R$	107.44 GeV
Gravitino	$\tilde{G}$	50 GeV

As explained, the parameter space for this scenario is $\mathbb{R}^3$ with axes labeled $(m_{\tilde{B}}, m_{\tilde{l}}, m_{\tilde{G}})$. Analyzing three events, we scan values of the gravitino mass from 0 to 100 GeV. As expected, this scan produces a curve in parameter space for each event with the correct answer lying at the intersection of the curves as shown in Fig. 9.8. For reasons given earlier, in practice we do not expect an exact intersection, but rather a localized region in parameter space where the density of such lines achieves a maximum. The optimal method of mass extraction should then involve searching for the slice in the $m_{\tilde{G}}$ plane where the density of solutions for $m_{\tilde{B}}$ and $m_{\tilde{l}}$ achieves a maximum. To this end we compute a probability sum on each slice of equal $m_{\tilde{G}}$ using the Gaussian distribution in Eq. 9.17 as our probability distribution function with $\sigma = 10\,\text{GeV}$.

$$F[m_{\tilde{B}}, m_{\tilde{B},0}, m_{\tilde{l}}, m_{\tilde{l},0}] = \frac{1}{(2\pi\sigma^2)^2} exp(-\frac{(m_{\tilde{B}} - m_{\tilde{B},0})^2 + (m_{\tilde{l}} - m_{\tilde{l},0})^2}{2\sigma^2}) \tag{9.17}$$

Slices of equal $m_{\tilde{G}}$ give a plane parameterized by $m_{\tilde{B}}$ and $m_{\tilde{l}}$. The function in Eq. 9.17 is defined at each point on this plane ($m_{\tilde{B},0}$, $m_{\tilde{l},0}$) and the sum over i takes a contribution

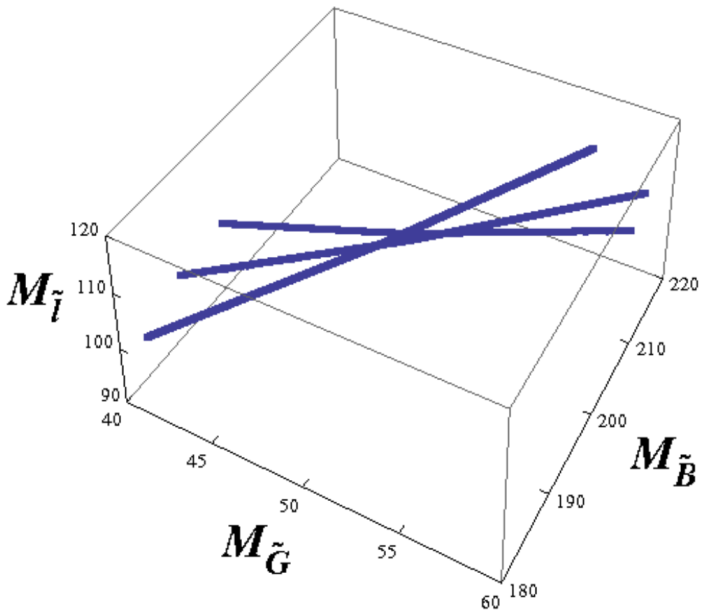

Figure 9.8: With three unknowns ($m_{\tilde{B}}$,$m_{\tilde{l}}$,$m_{\tilde{G}}$) and two equations, the solutions are curves in three dimensional Euclidean space. The intersection of solutions should occur at the correct value of the masses as can be seen in this plot using 3 events as an example.

from each data point ($m_{\tilde{B},i}$, $m_{\tilde{l},i}$), which is just given by the intersection of each line with the equal $m_{\tilde{G}}$ slice. Therefore, Eq. 9.17 should be maximixed at the point in the plane with the highest density of solutions. Furthermore, the maximum height in each plane should achieve its largest absolute magnitude on the slice corresponding to the correct value of $m_{\tilde{G}}$, since it is on this plane that the highest density of solutions resides. Using a sample of 25 events, the probability sum on the correct $m_{\tilde{G}}$ slice is depicted in Fig. 9.9 and we can observe a clear maximum at the correct solution for $m_{\tilde{B}}$ and $m_{\tilde{l}}$. The maximum height for each $m_{\tilde{G}}$ is then plotted as a function of the $m_{\tilde{G}}$ in Fig. 9.10. As expected, the largest absolute magnitude for the probability sum is acheived at the correct value of $m_{\tilde{G}} = 50\,\mathrm{GeV}$.

9.4.3 Can We Do Better

As we saw in the previous section, as the number of events $m \to \infty$, the minimum number of constraint equations needed $k \to 2$. Thus naively it would seem impossible to solve for all particle masses using the condition $k = 2$, with a topology given in Fig.

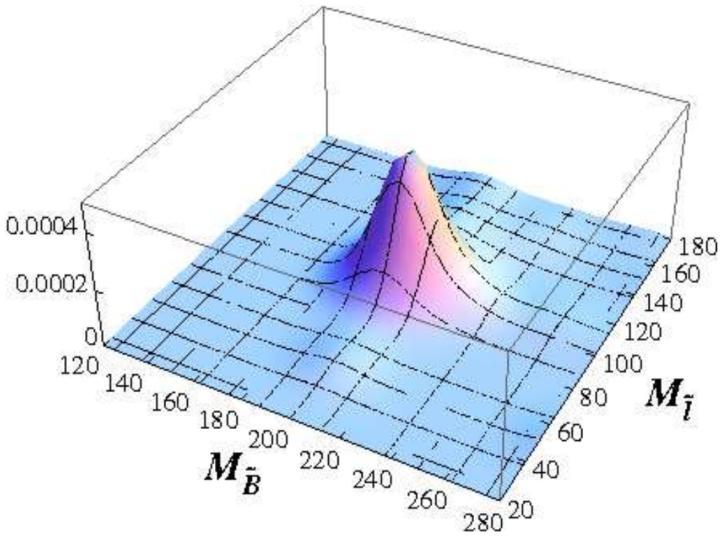

Figure 9.9: The probability sum on the $m_{\widetilde{G}} = 50$ GeV slice. We see that it peaks at the correct value of $m_{\widetilde{B}}$ and $m_{\tilde{l}}$

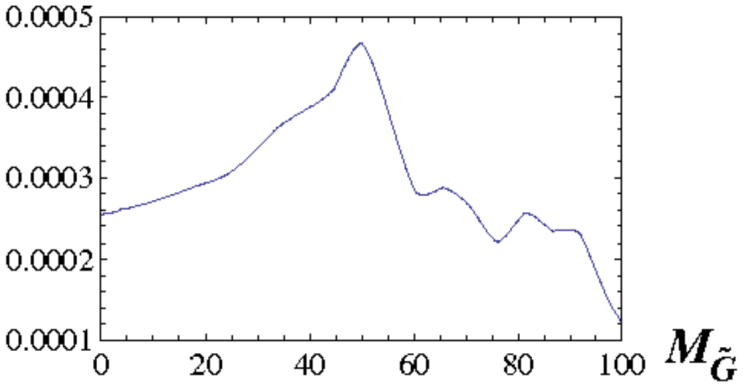

Figure 9.10: A plot of the absolute height of the probability sum as a function of $m_{\widetilde{G}}$. We see that it peaks at the correct value.

9.6. Previously we saw that it was still possible to measure the masses in situations where the unknown quantities outnumbered the constraints, using a very small number of events, by employing the trick of section 4.3. It is thus sensible to ask the question of whether or not it would be possible to perform an analagous measurement on cascade decays with a massive LSP. The spectrum used for this example was as follows:

Particle	Symbol	Mass
Right-handed Slepton	$\tilde{l}_R$	107.44 GeV
Gravitino	$\tilde{G}$	50 GeV

As usual, with a massive LSP we have 4 unknowns which we may take to be z_X, z_Y, m_{X_1}, and m_{Y_1}. Since we are assuming $k = 2$, the available kinematic equations can only remove two unknowns. In analogy with the massless LSP scenario, we choose to eliminate the two LSP masses and can derive an expression for the mass of the NLSP $m_{X_2} \to m_{X_2}(z_X, z_Y)$ We now scan all possible values for $m_{\tilde{G}}$ and play the same trick that was used in the previous section, but in one higher dimension. The result is depicted in Fig. 9.11. Unfortunately, this probability-double-sum produces a ridge-like structure rather than a peak at the correct solution. This result implies that these techniques cannot be used to extract a unique solution for $m_{\tilde{G}}$ when it is non-zero, and can only be used to provide a relation between two mass parameters.

9.5 Going Forward

In this paper we studied scenarios in which heavy new particle states were pair produced and cascaded down to some non-interacting stable particle states generating visible SM particles along the way. Here we assumed the decay length of the last decay was measurable, which resulted in a signature of displaced vertices or tracks. We finally assumed that the LSPs were the only particles that contributed to the transverse missing momentum. Given these assumptions, we described a number of novel techniques for extracting the spectrum of the intermediary particles in the cascade decay that were effective even in the low statistics limit. They would therefore be useful for very early discovery level searches at the LHC.

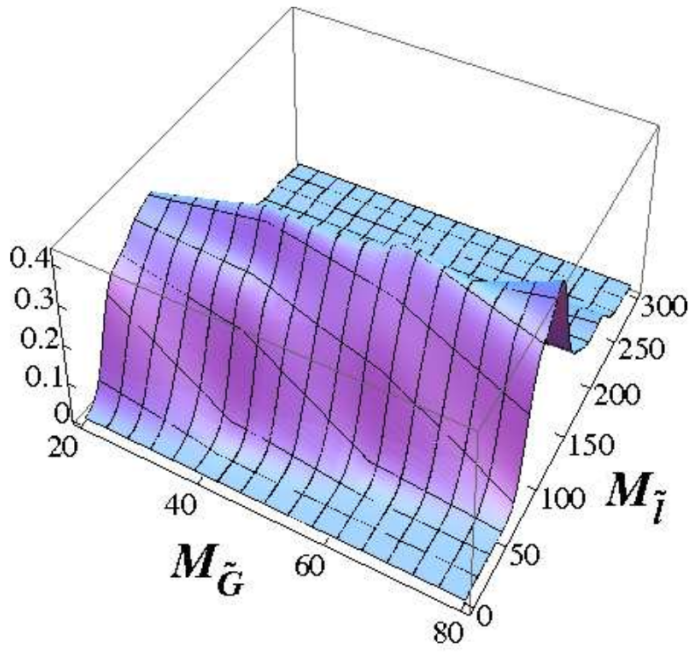

Figure 9.11: The probability double sum for the massive LSP case where unknowns outnumber constraints. The ridge-like structure suggests that no unique solutions exists for the correct value of $m_{\tilde{G}}$ using this technique

It should obvious by now that although this procedure is completely model independent, it was inspired by the phenomenology of supersymmetric models. For any supersymmetric theory on which these methods may be applied, the following conditions must hold:

1. R-parity is preserved, so that the superpartners are pair produced
2. Each of the superpartners decays to gravitino through cascade chain before it reaches to detector
3. Decays to the NLSP occur promptly so that it can effectively be traced back to the primary vertex
4. All transverse missing transverse momentum is contributed by the two gravitinos from the two sides of cascade decay chain
5. The decay of NLSP to LSP happens at a finite distance so that the detectors have enough resolution to isolate the secondary vertices

The first four assumptions are very generic for SUSY models though the fifth assumption is rather specific. Despite this fact it can be generically realized in many models, providing us with additional handles on the kinematics of these events. In our paper, we focus on the scenario in which the final step of decay happens at a reasonable finite distance but before the NLSP hits the detector. In scenarios with gauge-mediated SUSY breaking, the decay length of the NLSP is directly related to NLSP mass and the SUSY breaking scale via the relation $(c\tau)_{NLSP} \sim (\sqrt{F})^4/m^5_{X_2}$. Since all of the techniques presented in this paper also provide a direct measurement of the decay length of the NLSP, if SUSY is realized in nature they could also be used to extract a very early measurement of the SUSY-breaking scale.

Recently there has been a lot of talk about optimizing search strategies for very early discovery level analyses at the LHC. A central theme in these discussions has been the idea of searching under the lamp post. The principle behind this theme is that at the very early stages of a new physics search, especially when data is sparse

and statistics are low, it may be a better strategy to search for that which is easiest to see rather than that which you think is most likely to be true. If new physics manifests itself through the presence of missing energy and dual displaced tracks, with $\mathcal{O}$(few) events these techniques provide the possibility of

1. Providing convincing evidence for the existence of dual cascade decay topologies
2. Measuring the masses of all new particle states participating in the cascade decay
3. Constructing accurate distributions illuminating the spin-structure of the particles
4. Calculating the SUSY breaking scale if nature is supersymmetric

Clearly the methods described in this paper allow for a very large return from a very small investment. In particular, they allow one to extract an enormous amount of information from signatures that would otherwise be left to very late post-discovery analyses to elucidate completely. As such, they present an extremely bright lamp post under which to search inthe coming months.

Chapter 10

Testing Discrete Symmetries of the Higgs Sector

With the discovery of the Higgs now confirmed beyond reasonable doubt, attention to the exploration of this sector has now turned to measuring the properties of the Higgs with ever increasing precision as more data is collected. Indeed there have been a number of analyses conducted since the discovery in Run I dedicated to the measurement of couplings through branching ratios and spin-properties through kinematic variables. But another orthogonal avenue of exploration exists in testing the known symmetries of the Higgs sector. In this chapter, we discuss the possibility of detecting violations of discrete time-reversal symmetry $\mathbb{T}$, equivalent to charge conjugation-parity symmtry ($\mathbb{CP}$) by the $\mathbb{CPT}$ invariance theorem, through an analysis of the kinematics of Higgs decays. The minimal Higgs boson of the Standard Model is known to conserve $\mathbb{T}$, so any evidence implying violations of $\mathbb{T}$ in Higgs processes would potentially serve as an important window into new physics in the electroweak symmetry breaking sector.

The experimentally observed Higgs mass of $m_\varphi \sim 125\,\text{GeV}$ is fortuitous from an experimental stand point, as it presents a large number of Higgs decay channels with which to search for signs of new physics. In particular, the so called "gold-plated" channel Fig. 10.1 has several unique advantages. Although it suffers from an extremely low $\sigma \times$ Br, electrons and muons are by far the most accurately measured objects experimentally. Thus kinematic variables constructed from this four-lepton final state offer a degree of precision that far exceeds the potential of one constructed from any other final state decay. Furthermore, because it is a resonant channel, obtaining a sample with extremely high signal purity is completely straightforward. Below the scale of electroweak symmetry breaking, the Standard Model contribution to the process $\varphi \to ZZ^*$ arises from the tree level operator $\mathcal{O}_{SM}$

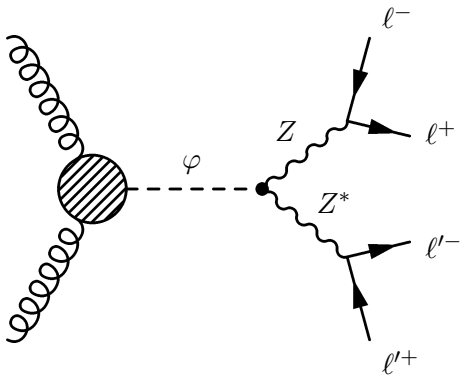

Figure 10.1: The so-called "gold-plated channel", which involves a resonantly produced Higgs boson decaying as $\varphi \to ZZ^* \to \ell^+\ell^-\ell'^+\ell'^-$

$$\mathcal{O}_{SM} = M_Z^2 \, \frac{\varphi}{v} \, Z_\mu Z^\mu \tag{10.1}$$

In this chapter, we consider the possibility that physics beyond the Standard Model could give significant contributions to the couplings of higher dimensional operators. Up to dimension-six, there are exactly two operators that could give contributions to the Higgs-gauge-gauge coupling present in gold-plated channel decays. Labeling them by their transformation properties under parity, there is one scalar operator $\mathcal{O}_S$ and one pseudo-scalar operator $\mathcal{O}_{PS}$

$$\mathcal{O}_S = \frac{M_Z^2 \, S_{ZZ}}{4\pi v^2} \, \frac{\varphi}{v} \, Z_{\mu\nu} Z^{\mu\nu} \tag{10.2}$$

$$\mathcal{O}_{PS} = \frac{M_Z^2 \, \widetilde{S}_{ZZ}}{4\pi v^2} \, \frac{\varphi}{v} \, Z_{\mu\nu} \widetilde{Z}^{\mu\nu} \tag{10.3}$$

The possibility of contributions to $\varphi \to ZZ^*$ from the pseudo-scalar operator $\mathcal{O}_{PS}$ is particularly interesting because of the fact that this operator is odd under $\mathbb{T}$. Thus a measurable enhancement could potentially lead to observable violations of parity and time-reversal symmetry through interference effects parameterized by the strength of the coupling $\widetilde{S}_{ZZ}$. Here we consider the possibility that the observed Standard Model process $\varphi \to ZZ^* \to \ell^+\ell^-\ell'^+\ell'^-$ might be under the receipt of contribution through a small but measurable component of pseudo-scalar decays via the dimension-five effective operator $\mathcal{O}_{PS}$. We introduce a kinematic variable specially tailored to expose the effects of the cross-term between the Standard Model and the leading $\mathbb{T}$-violating interaction

in an effective operator expansion. This observable, which is constructed from the four final-state particle momenta, is sensitive to violations of time-reversal through an asymmetry in its distribution. We will thus explore the potential for measuring such effects at the Large Hadron Collider.

10.1 Four-Body Kinematics

10.1.1 The T-Odd Observable

The gold-plated channel under analysis refers to the 4-body decay $\varphi \to ZZ^* \to \ell^+\ell^-\ell'^+\ell'^-$. In order to restrict our analysis to final states that preserve all of kinematic information from the Higgs-gauge-gauge coupling, we assume here that $\ell = e, \mu$ since prompt τ decays involve at least one ν_τ. To a good approximation we may thus take each of the final state leptons to be massless. With this restriction, a complete kinematic description is given by the 3-momenta of the 4 final-state particles, leaving $3 \times 4 - 1 = 11$ degrees of freedom, where we subtract one due to the arbitrary overall azimuth. If we assume that the Higgs boson as well as one Z boson is always on shell, then the two mass-shell conditions leave only 9 independent kinematic degrees of freedom. One of these may be taken to be the plane angle ϕ, which is the signed angle in the center-of-mass frame of the system between the plane spanned by $\vec{p}_{\ell^+}$, $\vec{p}_{\ell^-}$ and the plane spanned by $\vec{p}_{\ell'^+}$, $\vec{p}_{\ell'^-}$ as shown in Fig. 10.2. It is well known that the plane angle, defined in this way for a four-body final state, is odd under $\mathbb{T}$. Indeed this variable has been used to measure the $\mathbb{CP}$ properties of the Kaon system some years ago.

A more systematic analysis demonstrates that the unique time reversal violating observable for a four-body final state is proportional to the Lorentz invariant product of the four final state lepton 4-momenta constracted with the completely anti-symmetric ϵ tensor:

$$\tau_{\ell^+\ell^-\ell'^+\ell'^-} \equiv \frac{\epsilon_{\mu\nu\rho\sigma}\ p^\mu_{\ell^+} p^\nu_{\ell^-} p^\rho_{\ell'^+} p^\sigma_{\ell'^-}}{m^4_{\ell^+\ell^-\ell'^+\ell'^-}} \tag{10.4}$$

where $m^4_{\ell^+\ell^-\ell'^+\ell'^-} = [(p_{\ell^+} + p_{\ell^-} + p_{\ell'^+} + p_{\ell'^-})^2]^2$, $p_X^2 = p_X \cdot p_X$ and $\epsilon^{0123} = +1$. Since this quantity is odd under time reversal, violations of this symmetry should manifest as an

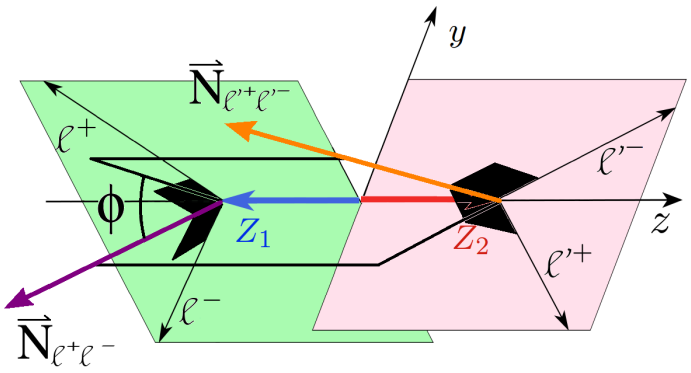

Figure 10.2: The kinematic configuration for a four-body final state decay.

asymmetry in the distribution of this variable across many events. One can see that this variable $\tau_{\ell^+\ell^-\ell'^+\ell'^-}$ is equivalent to the plane angle ϕ in the center-of-mass frame of the total system by writing

$$\sin\phi = (\vec{N}_{\ell^+\ell^-} \times \vec{N}_{\ell'^+\ell'^-}) \cdot \vec{n}_{\ell^+\ell^-}$$

where we have defined the unit vector along any three-momentum vector $\vec{p}_X$ to be $\vec{n}_X \equiv \vec{p}_X/|\vec{p}_X|$. Here $\vec{N}_{\ell^+\ell^-}$ is the unit vector normal to the plane spanned by $\vec{p}_{\ell^+}$, $\vec{p}_{\ell^-}$ as in Fig. 10.2. This can be written in a Lorentz invariant way by defining a relativistic generalization of the cross product that reduces to the ordinary three-dimensional cross product in the center-of-mass frame

$$Q^\mu_{\ell^+\ell^-} = \epsilon^\mu{}_{\nu\rho\sigma}\ p^\nu_{\ell^+}\ p^\rho_{\ell^-}\ n^\sigma_{\ell^+\ell^-\ell'^+\ell'^-} \xrightarrow[c.o.m.]{} \vec{p}_{\ell^+} \times \vec{p}_{\ell^-}$$

where we have also generalized the unit three-vector $\vec{n}_X$ to a normalized four-vector $n^\mu_X \equiv p^\mu_X/\sqrt{p^2_X}$. With this we can define a four-vector that reduces to $\vec{N}_{\ell^+\ell^-}$ in the center-of-mass frame

$$N^\mu_{\ell^+\ell^-} \equiv \frac{Q^\mu_{\ell^+\ell^-}}{\sqrt{Q^2_{\ell^+\ell^-}}} \xrightarrow[c.o.m.]{} \vec{N}_{\ell^+\ell^-}$$

We thus have a compact Lorentz invariant expression for $\sin\phi$

$$\sin\phi = \epsilon_{\mu\nu\rho\sigma}\ N^\mu_{\ell^+\ell^-} N^\nu_{\ell'^+\ell'^-} n^\rho_{\ell^+\ell^-} n^\sigma_{\ell^+\ell^-\ell'^+\ell'^-}$$

This expression for $\sin\phi$ can be expanded and rewritten purely in terms of the $\mathbb{T}$-odd variable $\tau_{\ell^+\ell^-\ell'^+\ell'^-}$ and invariant mass combinations of the final state leptons parameterized by the generic kinematic functions $\lambda(x^2,y^2,z^2) \equiv [x^2-(y-z)^2][x^2-(y+z)^2]$ and $\xi(w^2,x^2,y^2,z^2) \equiv w^2(x^2-z^2)(y^2-z^2)$. As usual the Källen triangle function $\lambda(x^2,y^2,z^2)$ can be interpreted as the squared three momentum of a particle with mass y coming from the two-body decay at rest of a particle with mass x to a particle with mass y and a particle with mass z. By momentum conservation, $\lambda(x^2,y^2,z^2)$ is invariant with respect to an interchange of $y \leftrightarrow z$. The function ξ can be interpreted as the form for the magnitude of our relativistically generalized cross product $\sqrt{Q^2_{\ell^+\ell^-}} = \xi(m^2_{\ell^+\ell^-}, m^2_{\ell^+\ell'^+\ell'^-}, m^2_{\ell^-\ell'^+\ell'^-}, m^2_{\ell'^+\ell'^-})$. We are thus left with the simple expression

$$\sin\phi = -\frac{1}{2}\frac{\lambda^{1/2}(m^2_{\ell^+\ell^-\ell'^+\ell'^-}, m^2_{\ell^+\ell^-}, m^2_{\ell'^+\ell'^-})\; m^4_{\ell^+\ell^-\ell'^+\ell'^-}\tau_{\ell^+\ell^-\ell'^+\ell'^-}}{\xi^{1/2}(m^2_{\ell^+\ell^-}, m^2_{\ell^+\ell'^+\ell'^-}, m^2_{\ell^-\ell'^+\ell'^-}, m^2_{\ell'^+\ell'^-})\;\xi^{1/2}(m^2_{\ell'^+\ell'^-}, m^2_{\ell'^+\ell^+\ell^-}, m^2_{\ell'^-\ell^+\ell^-}, m^2_{\ell^+\ell^-})}$$

10.1.2 Matrix Elements

Any observable effect of the contribution to the diboson decay $\varphi \to Z\,Z^*$ from additional operators can be understood through the dependence of the invariant decay distribution on the matrix element $|\mathcal{M}_{tot}|^2$ for this process. In particular, if $\widetilde{S}_{ZZ}$ is non-zero, then $\mathcal{M}_{tot}$ will receive an additive contribution from the pseudo-scalar matrix element $\mathcal{M}_{PS}$ resulting in the full squared matrix element

$$|\mathcal{M}_{tot}|^2 = |\mathcal{M}_{SM}+\mathcal{M}_{PS}|^2 = |\mathcal{M}_{SM}|^2 + |\mathcal{M}_{PS}|^2 + \mathcal{M}_{SM}\mathcal{M}^*_{PS} + h.c. \tag{10.5}$$

The observable effects of time-reversal violation will require an irreducible contribution from two operators that transform differently under $\mathbb{T}$. Therefore we expect violations of this symmetry to arise only from the interference terms $\mathcal{M}_{SM}\mathcal{M}^*_{PS} + h.c.$. The kinematic observable we propose to measure violations of $\mathbb{T}$ depends only on the distribution of the gauge bosons polarizations, which we infer from the decay plane of their lepton pair daughters. Importantly it is independent of the denominators of the gauge boson propagators. Thus for both notational and conceptual simplicity, we will

henceforth restrict our attention to the matrix element numerators that depend only on the projection operators $P^{\mu\nu}(M_Z^2, p_Z^\sigma)$

$$P^{\mu\nu}(M_Z^2, p_Z) = g^{\mu\nu} - \frac{p_Z^\mu p_Z^\nu}{M_Z^2}$$

rather than considering the full gauge boson propagators. With this simplification, computing the contribution to the matrix element numerators from the Standard Model and pseudo-scalar operators $\mathcal{O}_{SM}$ and $\mathcal{O}_{PS}$ is straightfoward. Taking the lepton assignments $p_Z^\mu = p_{\ell^+}^\mu + p_{\ell^-}^\mu$ and $p_{Z^*}^\mu = p_{\ell'^+}^\mu + p_{\ell'^-}^\mu$, we have

$$\mathcal{M}_{SM} = \frac{2M_Z^2}{v}\ g_{\mu\nu}\ P^{\mu\alpha}(M_Z^2, p_Z^\sigma)\ P^{\nu\beta}(M_{Z^*}^2, p_{Z^*}^\sigma)\ \mathcal{M}_\alpha^{\ell^+\ell^-}\mathcal{M}_\beta^{\ell'^+\ell'^-}$$

$$\mathcal{M}_{PS} = \frac{M_Z^2\ \widetilde{S}_{ZZ}}{\pi v^3}\ \epsilon_{\mu\nu\rho\sigma}\ p_Z^\mu\ P^{\nu\alpha}(M_Z^2, p_Z)\ p_{Z^*}^\rho\ P^{\sigma\beta}(M_{Z^*}^2, p_{Z^*})\ \mathcal{M}_\alpha^{\ell^+\ell^-}\mathcal{M}_\beta^{\ell'^+\ell'^-}$$

Since $g_V^2\ g_A^2 \sim 0.001^{***}$ is numerically small, we can ignore the subleading terms proportional to this quantity and obtain simple expressions for each piece of the total squared matrix element:

$$\frac{1}{4}\sum_{spins}|\mathcal{M}_{SM}|^2 = \frac{8M_Z^4}{v^2}(g_V^2+g_A^2)^2\ (m_{\ell^+\ell'^+}^2 m_{\ell^-\ell'^-}^2 + m_{\ell^+\ell'^-}^2 m_{\ell^-\ell'^+}^2)$$

$$\frac{1}{4}\sum_{spins}|\mathcal{M}_{PS}|^2$$

$$= \frac{\widetilde{S}_{ZZ}M_Z^4}{\pi^2 v^6}(g_V^2+g_A^2)^2\Big(\lambda(m_{\ell^+\ell^-}^2 m_{\ell'^+\ell'^-}^2, m_{\ell^+\ell'^+}^2 m_{\ell^-\ell'^-}^2, m_{\ell^+\ell'^-}^2 m_{\ell^-\ell'^+}^2)$$
$$+ 4m_{\ell^+\ell^-}^2\xi(m_{\ell'^+\ell'^-}^2, m_{\ell'^+\ell^+\ell^-}^2, m_{\ell'^-\ell^+\ell^-}^2, m_{\ell^+\ell^-}^2)$$
$$+4m_{\ell'^+\ell'^-}^2\xi(m_{\ell^+\ell^-}^2, m_{\ell^+\ell'^+\ell'^-}^2, m_{\ell^-\ell'^+\ell'^-}^2, m_{\ell'^+\ell'^-}^2) - 2m_{\ell^+\ell^-}^4 m_{\ell'^+\ell'^-}^4\Big)$$

$$\frac{1}{4}\sum_{spins}\mathcal{M}_{SM}\mathcal{M}_{PS}^* + \text{h.c.}$$

$$= \frac{8\widetilde{S}_{ZZ}M_Z^4}{\pi v^5}\tau_{\ell^+\ell^-\ell'^+\ell'^-}m^4_{\ell^+\ell^-\ell'^+\ell'^-}(g_V^2+g_A^2)^2(m^2_{\ell^+\ell'^+}+m^2_{\ell^-\ell'^-}-m^2_{\ell^+\ell'^-}-m^2_{\ell^-\ell'^+}) \tag{10.6}$$

Since the first two terms in the total squared matrix element are positive definite, and since the cross term is proportional to $\tau_{\ell^+\ell^-\ell'^+\ell'^-}$, we expect a deficit of events when $\tau_{\ell^+\ell^-\ell'^+\ell'^-}$ is negative and a surplus when $\tau_{\ell^+\ell^-\ell'^+\ell'^-}$ is positive. The fact that $\tau_{\ell^+\ell^-\ell'^+\ell'^-}$ is $\mathbb{T}$-odd therefore implies that the distribution of $\tau_{\ell^+\ell^-\ell'^+\ell'^-}$ will be asymmetric in the presence of $\mathbb{T}$ violation, and symmetric when $\mathbb{T}$ is conserved. The zeroth moment of this asymmetry can be quantified in the obvious way by defining the following measure

$$\mathcal{A}_\tau \equiv \frac{N_+ - N_-}{N_+ + N_-} \qquad\qquad N_\pm = \int_0^{\pm\infty} d\tau\ \frac{dN(\varphi \to \ell^+\ell^-\ell'^+\ell'^-)}{d\tau} \tag{10.7}$$

This naive expectation however, fails due to the non-positive-definiteness of the associated kinematic factor in the cross term

$$\widetilde{\mu}_{\ell^+\ell^-\ell'^+\ell'^-} \equiv \frac{m^2_{\ell^+\ell'^+} - m^2_{\ell^+\ell'^-} - m^2_{\ell^-\ell'^+} + m^2_{\ell^-\ell'^-}}{m^2_{\ell^+\ell^-\ell'^+\ell'^-}} \tag{10.8}$$

and instead we find that the asymmetry described above is well correlated with $\widetilde{\mu}_{\ell^+\ell^-\ell'^+\ell'^-}$ as demonstrated in a plot of $\tau_{\ell^+\ell^-\ell'^+\ell'^-}$ vs. $\widetilde{\mu}_{\ell^+\ell^-\ell'^+\ell'^-}$ in Fig. 10.3.

We briefly consider several ways to fold the kinematic factor $\widetilde{\mu}_{\ell^+\ell^-\ell'^+\ell'^-}$ into the $\mathbb{T}$-odd variable $\tau_{\ell^+\ell^-\ell'^+\ell'^-}$ to produce an observable that displays the full asymmetry due to time-reversal violation. The most straightforward way is to compute the product of the two variables,

$$\widetilde{\mathcal{T}}_{\ell^+\ell^-\ell'^+\ell'^-} \equiv \tau_{\ell^+\ell^-\ell'^+\ell'^-}\ \widetilde{\mu}_{\ell^+\ell^-\ell'^+\ell'^-}$$

$$\mathcal{A}_{\widetilde{\mathcal{T}}} \equiv \frac{N_+ - N_-}{N_+ + N_-} \qquad\qquad N_\pm = \int_0^{\pm\infty} d\widetilde{\mathcal{T}}\ \frac{dN(\varphi \to \ell^+\ell^-\ell'^+\ell'^-)}{d\widetilde{\mathcal{T}}} \tag{10.9}$$

which has the conceptual advantage of being proportional to the entire matrix element cross-term

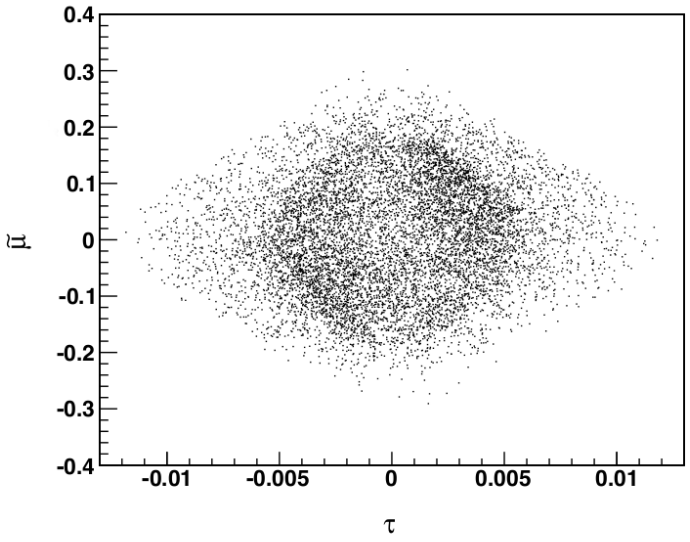

Figure 10.3: The distribution of 10,000 events in the $\tau_{\ell^+\ell^-\ell'^+\ell'^-}$ vs. $\widetilde{\mu}_{\ell^+\ell^-\ell'^+\ell'^-}$ plane. An unrealistically large value of the coupling strength $\widetilde{S}_{ZZ} \sim 250$ is chosen here for illustrative purposes.

$$\frac{1}{4}\sum_{spins}\mathcal{M}_{SM}\mathcal{M}^*_{PS} + \text{h.c.} = \frac{16\widetilde{S}_{ZZ}M_Z^4}{\pi v^5} m^6_{\ell^+\ell^-\ell'^+\ell'^-}(g_V^2+g_A^2)^2\ \widetilde{\mathcal{T}}_{\ell^+\ell^-\ell'^+\ell'^-} \tag{10.10}$$

Since the zeroth moment of the asymmetry in this new variable $\mathcal{A}_{\widetilde{\mathcal{T}}}$ is independent of the details of its distribution, already it displays the maximum possible asymmetry that can arise from $\mathbb{T}$-violation at this order. However, it is possible to define higher moments of the asymmetry weighted by the relative distance of points in the distribution from the origin. For example, the first moment of the asymmetry is

$$\mathcal{A}^{(1)}_{\widetilde{\mathcal{T}}} = \frac{\langle \widetilde{\mathcal{T}}_{\ell^+\ell^-\ell'^+\ell'^-}\rangle}{\langle \widetilde{\mathcal{T}}^2_{\ell^+\ell^-\ell'^+\ell'^-}\rangle^{1/2}} \qquad \langle \widetilde{\mathcal{T}}^n_{\ell^+\ell^-\ell'^+\ell'^-}\rangle = \int_{-\infty}^{+\infty} d\widetilde{\mathcal{T}}\ \widetilde{\mathcal{T}}^n\ \frac{d\mathcal{P}(\varphi\to\ell^+\ell^-\ell'^+\ell'^-)}{d\widetilde{\mathcal{T}}} \tag{10.11}$$

One can therefore consider alternative variables that take the sign of $\widetilde{\mu}_{\ell^+\ell^-\ell'^+\ell'^-}$ into account such as

$$\tau^-_{\ell^+\ell^-\ell'^+\ell'^-} \equiv \tau_{\ell^+\ell^-\ell'^+\ell'^-}\text{sgn}(\widetilde{\mu}_{\ell^+\ell^-\ell'^+\ell'^-}) \qquad \mathcal{A}^{(1)}_{\tau^-} = \frac{\langle \tau^-_{\ell^+\ell^-\ell'^+\ell'^-}\rangle}{\langle \tau^{-2}_{\ell^+\ell^-\ell'^+\ell'^-}\rangle^{1/2}}$$

$$\widetilde{\mu}^{-}_{\ell^+\ell^-\ell'^+\ell'^-} \equiv \widetilde{\mu}_{\ell^+\ell^-\ell'^+\ell'^-}\mathrm{sgn}(\tau_{\ell^+\ell^-\ell'^+\ell'^-}) \qquad \mathcal{A}^{(1)}_{\widetilde{\mu}^-} = \frac{\langle \widetilde{\mu}^{-}_{\ell^+\ell^-\ell'^+\ell'^-} \rangle}{\langle \widetilde{\mu}^{-2}_{\ell^+\ell^-\ell'^+\ell'^-} \rangle^{1/2}}$$

Although all of these variables are equivalent from the perspective of the zeroth moment of asymmetry, they are distinct in their distributions about the origin as in Fig. 10.4 and may have relative advantages from the perspective of higher moments in the asymmetry.

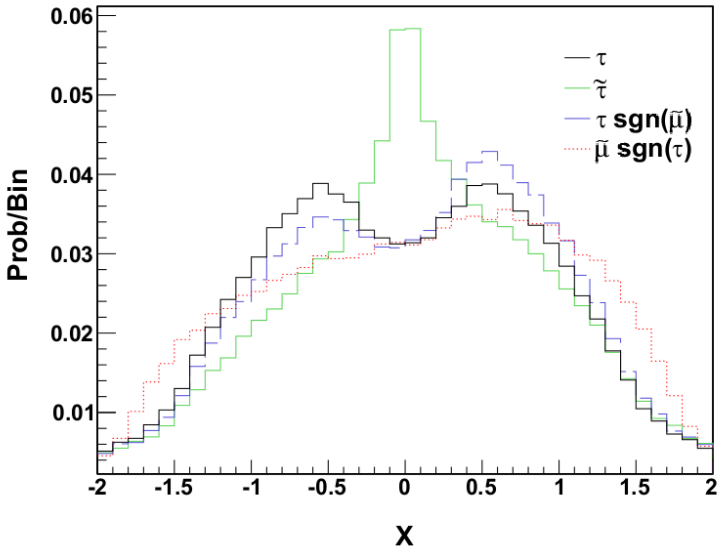

Figure 10.4: Asymmetry variables

10.2 Simulation and Validation

Events are simulated using the full MadGraph4/MadEvent pipeline. Since the generic Higgs effective theory (HEFT) model is not equipped to handle the full range of effects and parameterizations we consider, appropriate modifications are made at each step and the validation procedure is described here. Matrix elements are constructed from modified HELAS subroutines with phase space distributions from MadEvent, showering is simulated with Pythia6 out of the box, and detector simulations are implemented with a modified version of PGS4.

We start with the HEFT model in MadGraph4 with the vector-vector-scalar interaction corresponding to $\mathcal{O}_{SM}$ and fix the Higgs mass at a value of 126 GeV. MadGraph4 does not come with a HELAS subroutine capable of simulating the pseudoscalar effective

operator $\mathcal{O}_{PS}$ out of the box, so modified HELAS subroutines are imported from [93]. A new vector-vector-scalar interaction is added to the model file `interactions.dat` corresponding to $\mathcal{O}_{PS}$, pointing at the modified HELAS subroutines, and events are generated with the full interference effects. The MadEvent file `matrix.f`, responsible for constructing the full matrix element from HELAS subroutines, is then modified by hand with the addition of a new coupling that conforms to our parameterization of the coupling strength Eq. 10.3. Events are generated with different fixed values of the variable $\widetilde{S}_{ZZ}$, with $\log_{10}\widetilde{S}_{ZZ}$ ranging from 0 to 2 in steps of 0.5.

In order to validate the magnitude of the asymmetry $\mathcal{A}_{\widetilde{T}}$ with our analytical expectations, we created a new HELAS subroutine to calculate the effective matrix element corresponding to the full squared matrix element

$$\mathcal{M}_{eff}(\varphi \to e^+e^-\mu^+\mu^-) = \sqrt{|\mathcal{M}_{tot}|^2} \simeq \sqrt{|\mathcal{M}_{SM}|^2 + \mathcal{M}_{SM}\mathcal{M}_{PS}^* + \mathcal{M}_{SM}^*\mathcal{M}_{PS}}$$

We restrict the final state of this validation to $e^+e^-\mu^+\mu^-$ to avoid subtle interference effects and we have ignored here the contribution from $|\mathcal{M}_{PS}|^2$ which is subleading for small values of $\widetilde{S}_{ZZ}$. We input our analytical calculation of the matrix element components in Eq. 10.6 into this subroutine and generate events using MadEvent to fill the phase space. The value of the asymmetry using this effective HELAS subroutine closely matches the asymmetry using the full MadGraph4/MadEvent pipeline for events with a $e^+e^-\mu^+\mu^-$ final state over a wide range of values for the coupling $\widetilde{S}_{ZZ}$. The agreement even diverges for larger values of $\widetilde{S}_{ZZ}$ where the contribution from $|\mathcal{M}_{PS}|^2$ becomes important as expected. This highly non-trivial test offers great confidence that the MadGraph4/MadEvent pipeline is correctly simulating $\mathbb{T}$-violation for the complete matrix element over the full range of final states.

The detector simulation in this study is a version of PGS4 that has also been modified to more accurately reflect the isolation procedure for muons utilized by the CMS collaboration. The isolation procedure for electrons in PGS4 is inextricably tied to the simulation of photon showering, and can thus not be modified without a more detailed understanding of the photon shower and isolation, which is beyond the scope of this

paper. Muon candidates with transverse momentum $p_{T,\mu}$ are identified from an unmodified PGS simulation of muon chamber hits. We then follow CMS by defining a variable $T_{iso,\mu}$ to parameterize the degree of isolation for a muon candidate

$$T_{iso,\mu} = \sum_{0.03 \leq \Delta R_{i,\mu} \leq 0.4} |p_{T,tracks}|_i \times \Theta(|p_{T,tracks}|_i - 0.5 \text{ GeV})$$

Here $\Delta R_{i,\mu}$ is defined to be the distance in $\eta - \phi$ space between an object i and the muon candidate and $\Theta(x)$ is just the usual Heaviside step function. Muons in this analysis are identified with those muon candidates that satisfy $T_{iso,\mu}/p_{T,\mu} < 0.15$, in accordance with the CMS procedure.

10.3 Results

Events are generated with a final state restricted to $e^+e^-\mu^+\mu^-$, $e^+e^-e^+e^-$, and $\mu^+\mu^-\mu^+\mu^-$. For simplicity, we do not consider electrons and muons coming from τ decays or reconstructed hadronically decaying τ's. Such events would likely make small contributions to the asymmetry measurement since they all contain some missing energy in their final states, thus neglecting some of the kinematic degrees of freedom containing information about the violation of $\mathbb{T}$. This simplification is therefore likely to push our estimate of the asymmetry slightly to the conservative side, though a quantitative statement is beyond the scope of this study. A different number of events is generated for different values of $\widetilde{S}_{ZZ}$, so that the error in $\mathcal{A}_{\widetilde{\mathcal{T}}}$ from Poisson statistics $\sigma(\mathcal{A}_{\widetilde{\mathcal{T}}})$ satisfies $\sigma(\mathcal{A}_{\widetilde{\mathcal{T}}}) < \frac{1}{3}\mathcal{A}^{exp}_{\widetilde{\mathcal{T}}}$. Here $\mathcal{A}^{exp}_{\widetilde{\mathcal{T}}}$ is the expected value of the asymmetry from a simple linear fit $\mathcal{A}^{exp}_{\widetilde{\mathcal{T}}} = 0.001 \times \widetilde{S}_{ZZ}$. Since $\sigma(\mathcal{A}_{\widetilde{\mathcal{T}}}) \simeq \sqrt{2/N}$, this gives $N \gtrsim (2/\widetilde{S}_{ZZ}) \times 10^7$. Events with $\log_{10} \widetilde{S}_{ZZ} < 0$ clearly require a computationally infeasible number of events in order to achieve statistical significance and are thus not considered here.

For the analysis and construction of the variable $\tilde{\tau}_{\ell^+\ell^-\ell'^+\ell'^-}$, a set of reasonable cuts are applied that are different in nature from those used by a typical $\varphi \to ZZ^*$ search, since the measurement of $\mathbb{T}$ is not a discovery level analysis. We simply select all events with four leptons in the Higgs mass window $|m_{4\ell} - 126| < 10$ GeV and a flavor pattern $e^+e^-\mu^+\mu^-$, $e^+e^-e^+e^-$, or $\mu^+\mu^-\mu^+\mu^-$, with each lepton satisfying $p_T > 10$

GeV and $|\eta| < 2.5$. This simple set of cuts should be enough to guarantee a sufficiently pure signal sample due to the extremely low Standard Model background for events with four leptons inside the Higgs mass window. For events with a flavor pattern $e^+e^-\mu^+\mu^-$, the variable $\tilde{\tau}_{\ell^+\ell^-\ell'^+\ell'^-}$ can be constructed without ambiguity. For events with a flavor pattern $e^+e^-e^+e^-$ or $\mu^+\mu^-\mu^+\mu^-$, there is a discrete binary ambiguity for which opposite sign leptons to assign as daughters of the same Z boson. Note that since $\tilde{\tau}_{\ell^+\ell^-\ell'^+\ell'^-}$ is proportional to an $\epsilon_{\mu\nu\rho\sigma}$ contraction of the four lepton momenta, it is invariant with respect to the exchange of $Z \leftrightarrow Z^*$. Thus once the discrete binary ambiguity is resolved, $\tilde{\tau}_{\ell^+\ell^-\ell'^+\ell'^-}$ can then be constructed unambiguously. We resolve this ambiguity by assuming that most events contain one on-shell and one off-shell Z boson, so the correct assignment should contain one pair of leptons with an invariant mass within the Z mass window $|m_{\ell^+\ell^-} - m_Z| < 15$ GeV and one pair of leptons with an invariant mass below this Z mass window $m_{\ell'^+\ell'^-} < m_Z - 15$ GeV. We thus consider each of the two ambiguous lepton assignments and if only one assignment satisfies this criteria, then this assignment is assumed to be the correct one and $\tilde{\tau}_{\ell^+\ell^-\ell'^+\ell'^-}$ is constructed accordingly. If both or neither of the two lepton assignments satisfies this criteria, then the assignment that contains the largest invariant mass lepton pair $m^{max}_{\ell^+\ell^-}$ is simply taken to be the correct assignment, and the leptons that make up this maximum invariant mass pair are associated with each other. This asymmetry as a function of the coupling $\widetilde{S}_{ZZ}$ is shown in Fig. 10.5.

10.4 Fermion Electric Dipole Moments

The analysis proposed here would be complementary and orthogonal to existing low energy precision measurements of the electric dipole moment (EDM) of the electron d_e. The electron EDM, which corresponds to an asymmetric charge distribution along the direction of the electron spin ($\vec{S}$), arises from the dimension-five Lagrangian electric dipole operator

$$d_e \, \frac{\vec{S}}{|\mathbf{S}|} \cdot \vec{E} = -\frac{d_e}{2} \, \bar{e}\sigma^{\mu\nu} e \, \widetilde{F}_{\mu\nu}$$

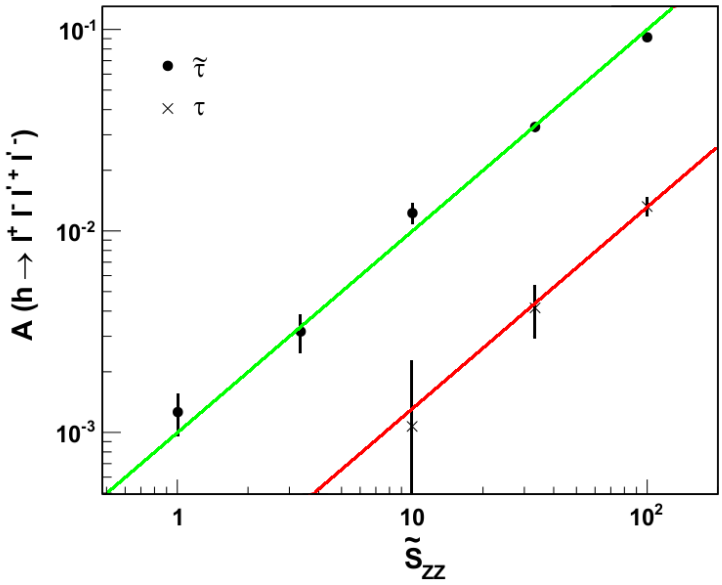

Figure 10.5: Zeroth moment asymmetry

where $\sigma^{\mu\nu} = \frac{i}{2}[\gamma^\mu, \gamma^\nu] = \frac{i}{2}(\gamma^\mu\gamma^\nu - \gamma^\nu\gamma^\mu)$ and $\widetilde{F}^{\mu\nu} = \frac{1}{2}\epsilon^{\mu\nu\rho\sigma}F_{\rho\sigma}$and $\epsilon^{0123} = +1$. This charge distribution is odd with respect to $\mathbb{T}$ due to the spin-dependence and is predicted in the Standard Model to be $|d_e| \lesssim 10^{-38}$ e cm. However, it has long been known that the existence of new particles and interactions that are asymmetric under $\mathbb{T}$ could lead to potentially measurable contributions to d_e. In particular, [145] demonstrated that the pseudo-scalar operators Eq. 10.12, of the same type considered in this analysis, could produce a contribution to d_e through the 1-loop diagram in Fig. 10.6.

$$\frac{e^2\widetilde{S}_{AA}}{16\pi}\frac{\varphi}{v}F_{\mu\nu}\widetilde{F}^{\mu\nu} \qquad\qquad \frac{eg_Z\widetilde{S}_{AZ}}{8\pi}\frac{\varphi}{v}F_{\mu\nu}\widetilde{Z}^{\mu\nu} \tag{10.12}$$

Thus an explicit bound on $|d_e|$ would translate to a bound on the couplings $\widetilde{S}_{AA}$ and $\widetilde{S}_{AZ}$. The explicit calculation at 1-loop yields

$$\frac{d_e}{e} = \frac{\alpha}{32\pi^2}\frac{m_e}{v^2}\left[\widetilde{S}_{AA}\ f(\mu^2/m_h^2) - \frac{1-4\sin^2\theta_W}{2\cos^2\theta_W\sin^2\theta_W}\ \widetilde{S}_{AZ}\ g(\mu^2/m_h^2, \mu^2/m_Z^2)\right] \tag{10.13}$$

where $f(x) = \ln(1+x)$ and $g(x,y) = [\ln(1+x) - (x/y)\ln(1+y)]/(1-x/y)$, and for reference $(\alpha/32\pi^2)(m_e/v^2) \simeq 4\times10^{-26}$ cm. Recently, the ACME collaboration [148] used spin precession measurements on a pulse of ThO molecules from a cryogenic buffer

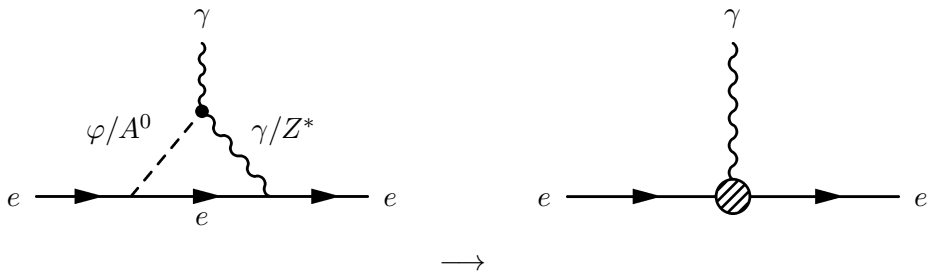

Figure 10.6: Contribution to the electric dipole moment of the electron from the 1-loop Barr Zee diagram.

gas beam source, to produce the most stringent bound yet on $|d_e| \lesssim 9 \times 10^{-29}$ e cm. This was an order of magnitude improvement on the previous bound $|d_e| \lesssim 1 \times 10^{-27}$ e cm, from nuclear magnetic resonant measurements of YbF molecules [146, 147].

Despite this exceedingly stringent bound on $\widetilde{S}_{AA}$ and $\widetilde{S}_{AZ}$, to date there exists no bound whatsoever on the coupling $\widetilde{S}_{ZZ}$, which is the subject of this analysis. Furthermore, there is no model-independent theoretical restriction on the value of $\widetilde{S}_{ZZ}$ that can be derived based on the EDM bound. Because these are all electroweak couplings on the same class of operators, the doctrine of naturalness may imply that these three couplings ($\widetilde{S}_{AA}$, $\widetilde{S}_{AZ}$, $\widetilde{S}_{ZZ}$) should be at least within an order of magnitude of each other. However, currently there exist at least some strong reasons to cast suspicion on our understanding of naturalness, especially as it pertains to the Higgs sector. Thus motivating this first ever measurement of the coupling for the effective operator $\widetilde{S}_{ZZ}$.

Bibliography

[1] J. Alwall, P. Schuster and N. Toro, Phys. Rev. D **79**, 075020 (2009) [arXiv:0810.3921 [hep-ph]].

[2] B. Knuteson and S. Mrenna, hep-ph/0602101.

[3] N. Arkani-Hamed, P. Schuster, N. Toro, J. Thaler, L. -T. Wang, B. Knuteson and S. Mrenna, hep-ph/0703088 [HEP-PH].

[4] D. S. M. Alves, E. Izaguirre and J. G. Wacker, JHEP **1110**, 012 (2011) [arXiv:1102.5338 [hep-ph]].

[5] K. Cranmer and I. Yavin, JHEP **1104**, 038 (2011) [arXiv:1010.2506 [hep-ex]].

[6] T. Sjostrand, S. Mrenna and P. Z. Skands, JHEP **0605**, 026 (2006) [hep-ph/0603175].

[7] J. Alwall, P. Demin, S. de Visscher, R. Frederix, M. Herquet, F. Maltoni, T. Plehn and D. L. Rainwater *et al.*, JHEP **0709**, 028 (2007) [arXiv:0706.2334 [hep-ph]].

[8] W. Kilian, T. Plehn, P. Richardson and E. Schmidt, Eur. Phys. J. C **39**, 229 (2005) [hep-ph/0408088].

[9] L. E. Ibanez and G. G. Ross, Phys. Lett. B **105** (1981) 439.

[10] A. H. Chamseddine, R. L. Arnowitt and P. Nath, Phys. Rev. Lett. **49**, 970 (1982).

[11] R. Barbieri, S. Ferrara and C. A. Savoy, Phys. Lett. B **119**, 343 (1982).

[12] N. Ohta, Prog. Theor. Phys. **70**, 542 (1983).

[13] L. J. Hall, J. D. Lykken and S. Weinberg, Phys. Rev. D **27**, 2359 (1983).

[14] M. Dine, W. Fischler and M. Srednicki, Nucl. Phys. B **189**, 575 (1981).

[15] S. Dimopoulos and S. Raby, Nucl. Phys. B **192**, 353 (1981).

[16] M. Dine and W. Fischler, Phys. Lett. B **110**, 227 (1982).

[17] M. Dine and W. Fischler, Nucl. Phys. B **204**, 346 (1982).

[18] C. R. Nappi and B. A. Ovrut, Phys. Lett. B **113**, 175 (1982).

[19] L. Alvarez-Gaume, M. Claudson and M. B. Wise, Nucl. Phys. B **207**, 96 (1982).

[20] S. Dimopoulos and S. Raby, Nucl. Phys. B **219**, 479 (1983).

[21] M. Dine and A. E. Nelson, Phys. Rev. D **48**, 1277 (1993) [hep-ph/9303230].

[22] M. Dine, A. E. Nelson and Y. Shirman, Phys. Rev. D **51**, 1362 (1995) [hep-ph/9408384].

[23] M. Dine, A. E. Nelson, Y. Nir and Y. Shirman, Phys. Rev. D **53**, 2658 (1996) [hep-ph/9507378].

[24] G. F. Giudice and R. Rattazzi, Phys. Rept. **322**, 419 (1999) [hep-ph/9801271].

[25] L. Randall and R. Sundrum, Nucl. Phys. B **557**, 79 (1999) [hep-th/9810155].

[26] G. F. Giudice, M. A. Luty, H. Murayama and R. Rattazzi, JHEP **9812**, 027 (1998) [hep-ph/9810442].

[27] A. Pomarol and R. Rattazzi, JHEP **9905**, 013 (1999) [hep-ph/9903448].

[28] T. Gherghetta, G. F. Giudice and J. D. Wells, Nucl. Phys. B **559**, 27 (1999) [hep-ph/9904378].

[29] R. M. Barnett, J. F. Gunion and H. E. Haber, Phys. Rev. D **37**, 1892 (1988).

[30] T. Appelquist, H. -C. Cheng and B. A. Dobrescu, Phys. Rev. D **64**, 035002 (2001) [hep-ph/0012100].

[31] K. R. Dienes, E. Dudas and T. Gherghetta, Phys. Lett. B **436**, 55 (1998) [hep-ph/9803466].

[32] H. -C. Cheng, K. T. Matchev and M. Schmaltz, Phys. Rev. D **66**, 056006 (2002) [hep-ph/0205314].

[33] D. S. M. Alves, E. Izaguirre and J. G. Wacker, Phys. Lett. B **702**, 64 (2011) [arXiv:1008.0407 [hep-ph]].

[34] J. T. Ruderman and D. Shih, JHEP **1208**, 159 (2012) [arXiv:1103.6083 [hep-ph]].

[35] S. P. Martin and J. D. Wells, Phys. Rev. D **59**, 035008 (1999) [hep-ph/9805289].

[36] S. Dimopoulos, M. Dine, S. Raby and S. D. Thomas, Phys. Rev. Lett. **76**, 3494 (1996) [hep-ph/9601367].

[37] R. L. Culbertson *et al.* [SUSY Working Group Collaboration], hep-ph/0008070.

[38] P. Meade, N. Seiberg and D. Shih, Prog. Theor. Phys. Suppl. **177**, 143 (2009) [arXiv:0801.3278 [hep-ph]].

[39] M. Buican, P. Meade, N. Seiberg and D. Shih, JHEP **0903**, 016 (2009) [arXiv:0812.3668 [hep-ph]].

[40] P. Meade, M. Reece and D. Shih, JHEP **1005**, 105 (2010) [arXiv:0911.4130 [hep-ph]].

[41] S. Dimopoulos, S. D. Thomas and J. D. Wells, Nucl. Phys. B **488**, 39 (1997) [hep-ph/9609434].

[42] G. F. Giudice and R. Rattazzi, Phys. Rept. **322**, 419 (1999) [hep-ph/9801271].

[43] S. Ambrosanio, G. D. Kribs and S. P. Martin, Phys. Rev. D **56**, 1761 (1997) [hep-ph/9703211].

[44] J. T. Ruderman and D. Shih, JHEP **1011**, 046 (2010) [arXiv:1009.1665 [hep-ph]].

[45] K. Nakamura *et al.* [Particle Data Group Collaboration], J. Phys. G **37**, 075021 (2010).

[46] T. Aaltonen *et al.* [CDF Collaboration], Phys. Rev. Lett. **104**, 061803 (2010) [arXiv:1001.4468 [hep-ex]]. V. M. Abazov *et al.* [D0 Collaboration], Phys. Rev.

Lett. **104**, 061804 (2010) [arXiv:1001.4481 [hep-ex]]. T. Aaltonen *et al.* [CDF and D0 Collaborations], Phys. Rev. Lett. **104**, 061802 (2010) [arXiv:1001.4162 [hep-ex]]. S. Chatrchyan *et al.* [CMS Collaboration], Phys. Lett. B **699**, 25 (2011) [arXiv:1102.5429 [hep-ex]]. G. Aad *et al.* [ATLAS Collaboration], Eur. Phys. J. C **71**, 1728 (2011) [arXiv:1106.2748 [hep-ex]].

[47] R. C. Gray, C. Kilic, M. Park, S. Somalwar and S. Thomas, arXiv:1110.1368 [hep-ph].

[48] H. Baer and J. D. Wells, Phys. Rev. D **57**, 4446 (1998) [hep-ph/9710368]. K. Jakobs, ATL-PHYS-2000-008. V. Cavasinni and D. Costanzo, ATL-PHYS-2000-013.

[49] S. Chatrchyan *et al.* [CMS Collaboration], Phys. Lett. B **704**, 411 (2011) [arXiv:1106.0933 [hep-ex]].

[50] S. Chatrchyan *et al.* [CMS Collaboration], JHEP **1106**, 077 (2011) [arXiv:1104.3168 [hep-ex]].

[51] H. E. Haber, G. L. Kane and T. Sterling, Nucl. Phys. B **161**, 493 (1979). A. G. Akeroyd, Phys. Lett. B **368**, 89 (1996) [hep-ph/9511347].

[52] J. F. Gunion, H. E. Haber, G. L. Kane and S. Dawson, Front. Phys. **80**, 1 (2000).

[53] J. F. Gunion and H. E. Haber, Nucl. Phys. B **278**, 449 (1986). M. Spira, A. Djouadi, D. Graudenz and P. M. Zerwas, Phys. Lett. B **318**, 347 (1993). M. S. Carena, S. Mrenna and C. E. M. Wagner, Phys. Rev. D **60**, 075010 (1999) [hep-ph/9808312]. M. S. Carena, S. Mrenna and C. E. M. Wagner, Phys. Rev. D **62**, 055008 (2000) [hep-ph/9907422].

[54] S. Dittmaier *et al.* [LHC Higgs Cross Section Working Group Collaboration], arXiv:1101.0593 [hep-ph].

[55] F. Maltoni and T. Stelzer, JHEP **0302**, 027 (2003) [hep-ph/0208156].

[56] J. Alwall, P. Demin, S. de Visscher, R. Frederix, M. Herquet, F. Maltoni, T. Plehn and D. L. Rainwater *et al.*, JHEP **0709**, 028 (2007) [arXiv:0706.2334 [hep-ph]].

[57] P. Meade and M. Reece, hep-ph/0703031.

[58] T. Sjostrand, S. Mrenna and P. Z. Skands, JHEP **0605**, 026 (2006) [hep-ph/0603175].

[59] S. Chatrchyan *et al.* [CMS Collaboration], "Search for the standard model Higgs boson in the decay channel H to ZZ to 4 leptons in pp collisions at $\sqrt{s} = 7$ TeV," arXiv:1202.1997 [hep-ex]; [CMS Collaboration], "Search for the standard model Higgs boson decaying into two photons in pp collisions at $\sqrt{s} = 7$ TeV," arXiv:1202.1487 [hep-ex]; [CMS Collaboration], "Combined results of searches for the standard model Higgs boson in pp collisions at $\sqrt{s} = 7$ TeV," arXiv:1202.1488 [hep-ex];

[60] G. Aad *et al.* [ATLAS Collaboration], "Search for the Standard Model Higgs boson in the decay channel H→ZZ(*)→4l with 4.8 fb-1 of pp collisions at $\sqrt{s} = 7$ TeV with ATLAS," arXiv:1202.1415 [hep-ex]; [ATLAS Collaboration], "Combined search for the Standard Model Higgs boson using up to 4.9 fb-1 of pp collision data at $\sqrt{s} = 7$ TeV with the ATLAS detector at the LHC," arXiv:1202.1408 [hep-ex]; [ATLAS Collaboration], "Search for the Standard Model Higgs boson in the diphoton decay channel with 4.9 fb-1 of pp collisions at $\sqrt{s} = 7$ TeV with ATLAS," arXiv:1202.1414 [hep-ex].

[61] T. D. Lee, Phys. Rev. **D8** (1973) 12261239; T. D. Lee, Phys. Rept. **9** (1974) 143177; P. Fayet, Nucl. Phys. **B78** (1974) 14; P. Fayet Nucl. Phys. **B90** (1975) 104124; R. A. Flores, M. Sher, Ann. Phys. **148** (1983) 95.

[62] J. F. Gunion, H. E. Haber, "Higgs Bosons in Supersymmetric Models. 2. Implications for Phenomenology," Nucl. Phys. **B278**, 449 (1986); M. Spira, A. Djouadi, D. Graudenz, P. M. Zerwas, "SUSY Higgs production at proton colliders," Phys. Lett. **B318**, 347-353 (1993); M. S. Carena, S. Mrenna, C. E. M. Wagner, "MSSM Higgs boson phenomenology at the Tevatron collider," Phys. Rev. **D60**, 075010 (1999), [hep-ph/9808312]; M. S. Carena, S. Mrenna, C. E. M. Wagner, "The Complementarity of LEP, the Tevatron and the CERN LHC in the search for a

light MSSM Higgs boson," Phys. Rev. **D62**, 055008 (2000), [hep-ph/9907422]; M. Carena, E. Pontón, J. Zurita, "BMSSM Higgs Bosons at the 7 TeV LHC," [arXiv:1111.2049 [hep-ph]];

[63] J. F. Gunion, H. E. Haber, G. L. Kane, S. Dawson, "The Higgs Hunter's Guide," Front. Phys. **80**, 1-448 (2000).

[64] G. C. Branco, P. M. Ferreira, L. Lavoura, M. N. Rebelo, M. Sher, J. P. Silva, "Theory and phenomenology of two-Higgs-doublet models", [arXiv:1106.0034 [hep-ph]].

[65] S. Chang, J. A. Evans, M. A. Luty, Phys. Rev. **D84** (2011) 095030, [arXiv:1107.2398 [hep-ph]]; J. A. Evans, B. Kilminster, M. A. Luty, D. Whiteson, [arXiv:1201.3691 [hep-ex]].

[66] S. Chatrchyan *et al.* [CMS Collaboration], "Search for Physics Beyond the Standard Model Using multi-lepton Signatures in pp Collisions at $\sqrt{s} = 7$ TeV," Phys. Lett. B **704**, 411 (2011) [arXiv:1106.0933 [hep-ex]].

[67] S. Chatrchyan *et al.* [CMS Collaboration], "Search for anomalous production of multilepton events in pp collisions at $\sqrt{s} = 7$ TeV," JHEP **1206**, 169 (2012) [arXiv:1204.5341 [hep-ex]].

[68] E. Contreras-Campana, N. Craig, R. Gray, C. Kilic, M. Park, S. Somalwar, S. Thomas, "Multi-Lepton Signals of the Higgs Boson," arXiv:1112.2298 [hep-ph].

[69] N. Craig, J. A. Evans, R. Gray, M. Park, S. Somalwar, S. Thomas, M. Walker, "Searching for $t \to ch$ with Multi-Leptons," arXiv:1207.6794 [hep-ph].

[70] S. Dube, J. Glatzer, S. Somalwar, A. Sood and S. Thomas, "Addressing the Multi-Channel Inverse Problem at High Energy Colliders: A Model Independent Approach to the Search for New Physics with Trileptons," J. Phys. G G **39**, 085004 (2012) [arXiv:0808.1605 [hep-ph]].

[71] S. Fajfer, J. F. Kamenik, I. Nisandzic and J. Zupan, "Implications of lepton flavor universality violations in B decays," arXiv:1206.1872 [hep-ph].

[72] S. L. Glashow, S. Weinberg, "Natural Conservation Laws for Neutral Currents," Phys. Rev. **D15**, 1958 (1977).

[73] F. Maltoni, T. Stelzer, "MadEvent: Automatic event generation with MadGraph," JHEP **0302**, 027 (2003). [hep-ph/0208156].

[74] J. Alwall, P. Demin, S. de Visscher, R. Frederix, M. Herquet, F. Maltoni, T. Plehn, D. L. Rainwater *et al.*, "MadGraph/MadEvent v4: The New Web Generation," JHEP **0709**, 028 (2007). [arXiv:0706.2334 [hep-ph]].

[75] D. Alves *et al.* [LHC New Physics Working Group Collaboration], "Simplified Models for LHC New Physics Searches," arXiv:1105.2838 [hep-ph].

[76] P. Meade, M. Reece, "BRIDGE: Branching ratio inquiry / decay generated events," [hep-ph/0703031].

[77] T. Sjostrand, S. Mrenna, P. Z. Skands, "PYTHIA 6.4 Physics and Manual," JHEP **0605**, 026 (2006). [hep-ph/0603175].

[78] J. Conway et al., "PGS 4: Pretty Good Simulation of high energy collisions," 2006, `www.physics.ucdavis.edu/~conway/research/software/pgs/pgs4-general.htm`

[79] R. C. Gray, C. Kilic, M. Park, S. Somalwar and S. Thomas, "Backgrounds to Higgs Boson Searches from $W\gamma^* \to \ell\nu\ell(\ell)$ Asymmetric Internal Conversion," arXiv:1110.1368 [hep-ph].

[80] LHC Higgs Cross Section Working Group, S. Dittmaier, C. Mariotti, G. Passarino, and R. Tanaka (Eds.), *Handbook of LHC Higgs Cross Sections: 1. Inclusive Observables*, CERN-2011-002 (CERN, Geneva, 2011), arXiv:1101.0593 [hep-ph].

[81] A. Djouadi, J. Kalinowski and P. M. Zerwas, Z. Phys. C **70**, 435 (1996) [hep-ph/9511342].

[82] S. Chatrchyan *et al.* [CMS Collaboration], "Search for neutral Higgs bosons decaying to tau pairs in pp collisions at $\sqrt{s} = 7$ TeV," Phys. Lett. B **713**, 68 (2012) [arXiv:1202.4083 [hep-ex]].

[83] S. Chatrchyan *et al.* [CMS Collaboration], "Search for high mass resonances decaying into tau-lepton pairs in pp collisions at $\sqrt{s} = 7$ TeV," arXiv:1206.1725 [hep-ex].

[84] S. Chatrchyan *et al.* [CMS Collaboration], "Search for a light charged Higgs boson in top quark decays in pp collisions at $\sqrt{s} = 7$ TeV," JHEP **1207**, 143 (2012) [arXiv:1205.5736 [hep-ex]].

[85] N. Craig and S. Thomas, "Exclusive Signals of an Extended Higgs Sector," arXiv:1207.4835 [hep-ph].

[86] E. Contreras-Campana, N. Craig, R. Gray, C. Kilic, M. Park, S. Somalwar and S. Thomas, JHEP **1204**, 112 (2012) [arXiv:1112.2298 [hep-ph]].

[87] G. Eilam, J. L. Hewett and A. Soni, Phys. Rev. D **44**, 1473 (1991) [Erratum-ibid. D **59**, 039901 (1999)].

[88] B. Mele, S. Petrarca and A. Soddu, Phys. Lett. B **435**, 401 (1998) [hep-ph/9805498].

[89] J. A. Aguilar-Saavedra, Acta Phys. Polon. B **35**, 2695 (2004) [hep-ph/0409342].

[90] S. Chatrchyan *et al.* [CMS Collaboration], JHEP **1206**, 169 (2012) [arXiv:1204.5341 [hep-ex]].

[91] S. Chatrchyan *et al.* [CMS Collaboration], Phys. Lett. B **704**, 411 (2011) [arXiv:1106.0933 [hep-ex]].

[92] F. Maltoni and T. Stelzer, JHEP **0302**, 027 (2003) [hep-ph/0208156].

[93] J. Alwall, P. Demin, S. de Visscher, R. Frederix, M. Herquet, F. Maltoni, T. Plehn and D. L. Rainwater *et al.*, JHEP **0709**, 028 (2007) [arXiv:0706.2334 [hep-ph]].

[94] S. Moch and P. Uwer, Nucl. Phys. Proc. Suppl. **183**, 75 (2008) [arXiv:0807.2794 [hep-ph]]. U. Langenfeld, S. Moch and P. Uwer, arXiv:0907.2527 [hep-ph].

[95] P. Meade and M. Reece, hep-ph/0703031.

[96] S. Dittmaier *et al.* [LHC Higgs Cross Section Working Group Collaboration], arXiv:1101.0593 [hep-ph].

[97] T. Sjostrand, S. Mrenna and P. Z. Skands, JHEP **0605**, 026 (2006) [hep-ph/0603175].

[98] R. C. Gray, C. Kilic, M. Park, S. Somalwar and S. Thomas, arXiv:1110.1368 [hep-ph].

[99] S. Chatrchyan *et al.* [CMS Collaboration], JHEP **1208**, 110 (2012) [arXiv:1205.3933 [hep-ex]].

[100] K. T. Matchev and S. D. Thomas, Phys. Rev. D **62**, 077702 (2000) [hep-ph/9908482].

[101] C. G. Lester and D. J. Summers, Phys. Lett. B **463**, 99 (1999) [arXiv:hep-ph/9906349].

[102] C. Lester and A. Barr, JHEP **0712**, 102 (2007) [arXiv:0708.1028 [hep-ph]].

[103] D. R. Tovey, JHEP **0804**, 034 (2008) [arXiv:0802.2879 [hep-ph]].

[104] G. G. Ross and M. Serna, Phys. Lett. B **665**, 212 (2008) [arXiv:0712.0943 [hep-ph]].

[105] I. Hinchliffe, F. E. Paige, M. D. Shapiro, J. Soderqvist and W. Yao, Phys. Rev. D **55**, 5520 (1997) [arXiv:hep-ph/9610544].

[106] H. Bachacou, I. Hinchliffe and F. E. Paige, Phys. Rev. D **62**, 015009 (2000) [arXiv:hep-ph/9907518].

[107] P. Huang, N. Kersting and H. H. Yang, Phys. Rev. D **77**, 075011 (2008) [arXiv:0801.0041 [hep-ph]].

[108] K. T. Matchev, F. Moortgat, L. Pape and M. Park, arXiv:0906.2417 [hep-ph].

[109] D. Costanzo and D. R. Tovey, JHEP **0904**, 084 (2009) [arXiv:0902.2331 [hep-ph]].

[110] M. Burns, K. T. Matchev and M. Park, JHEP **0905**, 094 (2009) [arXiv:0903.4371 [hep-ph]].

[111] D. J. . Miller, P. Osland and A. R. Raklev, JHEP **0603**, 034 (2006) [arXiv:hep-ph/0510356].

[112] C. G. Lester, Phys. Lett. B **655**, 39 (2007) [arXiv:hep-ph/0603171].

[113] B. K. Gjelsten, D. J. . Miller, P. Osland and A. R. Raklev, AIP Conf. Proc. **903**, 257 (2007) [arXiv:hep-ph/0611259].

[114] G. L. Bayatian *et al.* [CMS Collaboration], J. Phys. G **34**, 995 (2007).

[115] I. Hinchliffe, F. E. Paige, M. D. Shapiro, J. Soderqvist and W. Yao, Phys. Rev. D **55**, 5520 (1997) [hep-ph/9610544].

[116] C. G. Lester and D. J. Summers, Phys. Lett. B **463**, 99 (1999) [hep-ph/9906349].

[117] A. Barr, C. Lester and P. Stephens, J. Phys. G **29**, 2343 (2003) [hep-ph/0304226].

[118] D. R. Tovey, JHEP **0804**, 034 (2008) [arXiv:0802.2879 [hep-ph]].

[119] K. T. Matchev and M. Park, Phys. Rev. Lett. **107**, 061801 (2011) [arXiv:0910.1584 [hep-ph]].

[120] P. Konar, K. Kong, K. T. Matchev and M. Park, JHEP **1106**, 041 (2011) [arXiv:1006.0653 [hep-ph]].

[121] K. Kawagoe, T. Kobayashi, M. M. Nojiri and A. Ochi, Phys. Rev. D **69**, 035003 (2004) [hep-ph/0309031].

[122] P. Meade, M. Reece and D. Shih, JHEP **1010**, 067 (2010) [arXiv:1006.4575 [hep-ph]].

[123] I. -W. Kim, Phys. Rev. Lett. **104**, 081601 (2010) [arXiv:0910.1149 [hep-ph]].

[124] H. Bachacou, I. Hinchliffe and F. E. Paige, Phys. Rev. D **62**, 015009 (2000) [hep-ph/9907518].

[125] M. G. Jackson, JHEP **0109**, 004 (2001) [hep-th/0103217].

[126] L. Covi, H. -B. Kim, J. E. Kim and L. Roszkowski, JHEP **0105**, 033 (2001) [hep-ph/0101009].

[127] B. C. Allanach, C. G. Lester, M. A. Parker and B. R. Webber, JHEP **0009**, 004 (2000) [hep-ph/0007009].

[128] B. K. Gjelsten, D. J. Miller and P. Osland, JHEP **0412**, 003 (2004) [hep-ph/0410303].

[129] K. Kawagoe, M. M. Nojiri and G. Polesello, Phys. Rev. D **71**, 035008 (2005) [hep-ph/0410160].

[130] C. G. Lester, M. A. Parker and M. J. White, JHEP **0601**, 080 (2006) [hep-ph/0508143].

[131] N. Arkani-Hamed, G. L. Kane, J. Thaler and L. -T. Wang, JHEP **0608**, 070 (2006) [hep-ph/0512190].

[132] M. Baumgart, T. Hartman, C. Kilic and L. -T. Wang, JHEP **0711**, 084 (2007) [hep-ph/0608172].

[133] J. M. Butterworth, J. R. Ellis and A. R. Raklev, JHEP **0705**, 033 (2007) [hep-ph/0702150 [HEP-PH]].

[134] H. -C. Cheng, J. F. Gunion, Z. Han, G. Marandella and B. McElrath, JHEP **0712**, 076 (2007) [arXiv:0707.0030 [hep-ph]].

[135] M. M. Nojiri, G. Polesello and D. R. Tovey, JHEP **0805**, 014 (2008) [arXiv:0712.2718 [hep-ph]].

[136] R. Horsky, M. Kramer, 1, A. Muck and P. M. Zerwas, Phys. Rev. D **78**, 035004 (2008) [arXiv:0803.2603 [hep-ph]].

[137] A. J. Barr and C. Gwenlan, Phys. Rev. D **80**, 074007 (2009) [arXiv:0907.2713 [hep-ph]].

[138] T. Cohen, E. Kuflik and K. M. Zurek, JHEP **1011**, 008 (2010) [arXiv:1003.2204 [hep-ph]].

[139] A. J. Barr and C. G. Lester, J. Phys. G **37**, 123001 (2010) [arXiv:1004.2732 [hep-ph]].

[140] H. -C. Cheng, D. Engelhardt, J. F. Gunion, Z. Han and B. McElrath, Phys. Rev. Lett. **100**, 252001 (2008) [arXiv:0802.4290 [hep-ph]].

[141] H. -C. Cheng, J. F. Gunion, Z. Han and B. McElrath, Phys. Rev. D **80**, 035020 (2009) [arXiv:0905.1344 [hep-ph]].

[142] B. Webber, JHEP **0909**, 124 (2009) [arXiv:0907.5307 [hep-ph]].

[143] P. Meade, M. Reece and D. Shih, JHEP **1005**, 105 (2010) [arXiv:0911.4130 [hep-ph]].

[144] N. Arkani-Hamed and S. Dimopoulos, JHEP **0506**, 073 (2005) [hep-th/0405159].

[145] S. M. Barr and A. Zee, Phys. Rev. Lett. **65**, 21 (1990) [Erratum-ibid. **65**, 2920 (1990)].

[146] J. J. Hudson, D. M. Kara, I. J. Smallman, B. E. Sauer, M. R. Tarbutt and E. A. Hinds, Nature **473**, 493 (2011).

[147] D. M. Kara, I. J. Smallman, J. J. Hudson, B. E. Sauer, M. R. Tarbutt and E. A. Hinds, New J. Phys. **14**, 103051 (2012) [arXiv:1208.4507 [physics.atom-ph]].

[148] J. Baron *et al.* [ACME Collaboration], Science **343**, no. 6168, 269 (2014) [arXiv:1310.7534 [physics.atom-ph]].